Photochemical and dynamics studies of oxygen isotope exchange reactions of CO_2

Thesis by

Laurence Yip-Lun Yeung

In Partial Fulfillment of the Requirements

for the Degree of

Doctor of Philosophy

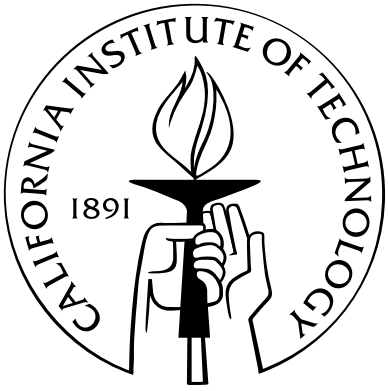

California Institute of Technology

Pasadena, California

2010

(Defended December 10, 2009)

Small quantities of different gases were added to separate portions of a non-inflammable mixture of dry carbonic oxide and oxygen, and the spark was then passed. In all cases where a gas containing hydrogen was introduced, the mixture exploded; in all cases where a gas containing no hydrogen was introduced, the mixture did not explode.

— Harold Dixon, *The Combustion of Carbonic Oxide and Hydrogen*, 1886.

Acknowledgements

This body of work would not have been possible without the intellectual, spiritual, and financial support from professor Mitchio Okumura, professor John Eiler, and Dr. William Davidow. Mitchio and John have taught me how to think critically and quantitatively about scientific problems; their unending creativity, enthusiasm, and wisdom continue to inspire me. Dr. Davidow's generous endowment funded all of this research and much more not documented here. Only with his support was I able to pursue these risky projects.

To my collaborators, professors Hagit Affek, Kristie Boering, Elliot Atlas, Tim Minton, Jon Camden, and George Schatz; Drs. Sue Schauffler, Jeff Paci, Weifu Guo, Kate Hoag, and Jianming Zhang; and Mr. Aaron Wiegel: This work was a collective effort, and I dare not take the credit for any more than my own modest contribution to it. Thank you for your time, patience, lab equipment, and fishing lessons.

To the Okumura group, the Eiler group, and other mentors, professors Jack Beauchamp, Rudy Marcus, Geoff Blake, Yuk Yung, Zhengrong Wang, Julie Fry, Rose Came, Kate Huntington, Ben Passey, Naomi Levin, and Aradhna Tripathi; Drs. Pin Chen, Joe Hodges, Chip Miller, Linda Brown, Andrew Mollner, David Robichaud, Aaron Noell, Nathan Eddingsaas, and Mathieu Daëron; Mr. Bill Bing; fellow students Kana Takematsu, Matt Sprague, Kathleen Spencer, Dave Long, Sigrid Barklund, Aileen Hui, Thinh Bui, Nathan Honsowetz, and Heather Widgren: Most of my education here has been at your hands. Thank you for your time, wisdom, skepticism, and coffee.

Finally, to my friends and family: You are the music of my life. You are the rhythm, the harmony, and melody. *If music be the food of love, play on.* Nothing I could say would ever be enough to express my gratitude. I am excited for whatever misadventures lie ahead.

Abstract

This dissertation describes laboratory studies of three oxygen isotope exchange reactions — $O(^1D)$ + CO_2, O_2 + CO_2, and $O(^3P)$ + CO_2 — and their importance to oxygen cycling in the upper atmosphere. First, we studied the isotope exchange reaction $O(^1D)$ + CO_2, which is believed to govern the oxygen-isotope budget of CO_2 in the stratosphere. Our combined field, laboratory, and modeling study of the exceptionally rare $^{16}O^{13}C^{18}O$ isotopologue revealed that $O(^1D)$ + CO_2 explains only part of the stratospheric CO_2 isotopologue budget, not all of it as previously thought: $O(^1D)$ + CO_2 could not explain the large enrichments of $^{16}O^{13}C^{18}O$ (i.e., of the "Δ_{47}" tracer) at high Northern latitudes. Mesospheric and heterogeneous chemistry of CO_2 were proposed as possible sources of this meridional variation in $^{16}O^{13}C^{18}O$. Therefore, we performed crossed-molecular-beam experiments to investigate the chemistry of CO_2 at hyperthermal collision energies; this class of reaction could be important in the upper atmosphere, where low gas densities and high rates of photochemistry increase the relative probability of hyperthermal reactions. Our experimental and theoretical study of the O_2 + CO_2 isotope exchange reaction showed that the reaction can occur through a short-lived CO_4 reaction complex, which leads to O_2 + CO_2 products that are highly internally excited, but possibly still in their ground electronic state. Our study of $O(^3P)$ + CO_2 collisions at hyperthermal energies showed that $O(^3P)$ + CO_2 isotope exchange can occur in the upper atmosphere, proceeding through a short-lived CO_3 reaction complex. The $O(^3P)$ + $CO_2 \rightarrow O_2$ + CO reaction was also observed, and our data suggest that it can proceed through a 'stripping' mechanism or a CO_3 complex. These reactions demonstrate new ways in which oxygen can be cycled through CO_2 in the atmosphere; their isotope effects, manifest in the isotopic composition of atmospheric CO_2, may impose independent constraints on atmospheric transport and biosphere-atmosphere interactions.

Contents

List of Figures

List of Tables

Chapter 1

Introduction

1.1 CO_2 in the global carbon cycle

Carbon dioxide (CO_2) is the most important anthropogenic greenhouse gas in the earth's atmosphere. Over the past half-century, atmospheric CO_2 concentrations have increased at a rate that correlates with the increase in anthropogenic fossil fuel burning and deforestation [*Solomon et al.*, 2007]. Carbon budget inventories indicate, however, that not all of the CO_2 released into the atmosphere from these activities persists in the atmosphere; approximately half of the anthropogenic CO_2 flux is sequestered in the oceanic and land biospheres [*Ciais et al.*, 1995]. Modeling the fate of anthropogenic CO_2 becomes a considerable technical challenge because of myriad interactions between the atmosphere, the oceans, and the terrestrial biosphere. Our ability to predict future changes in the carbon cycle and their effects on global climate relies on our quantitative understanding of these interactions.

The first step towards understanding these interactions is learning how to differentiate between atmospheric CO_2 molecules derived from various sources and sinks, so we can eventually de-convolve atmospheric observations into their individual components and describe the workings of the global budget through those observations. This task is more complex than it might at first seem because the atmosphere mixes efficiently over the atmospheric lifetime of CO_2; thus each parcel of air contains CO_2 molecules with many different origins and fates (see Figure 1.1). We find some of the needed constraints for these interactions in the variations of naturally occurring stable isotopes.

1.2 Stable isotopes, 'clumped' and otherwise

The stable isotope composition of CO_2 (i.e., the relative abundances of those isotopes that do not decay radioactively: ^{12}C, ^{13}C, ^{16}O, ^{17}O and ^{18}O) varies according to its sources and subsequent atmospheric chemistry and transport. Physical, chemical kinetic, and equilibrium isotope effects act together to determine the stable isotope composition of CO_2 in a given parcel of air. Differences in mass and symmetry of the twelve distinct CO_2 isotopologues (isotopic variants, e.g., $^{12}C^{16}O_2$, $^{13}C^{16}O_2$, $^{16}O^{12}C^{18}O$, $^{16}O^{13}C^{17}O$, etc.) formed from the five stable isotopes lead to subtle, but measurable differences in the rate of chemical transformations such as photosynthesis, respiration, air-sea exchange, or photochemical reactions.

In principle, measuring the stable isotope distribution in CO_2 could lead to an exceptionally detailed analysis of the 'history' of CO_2 in every sample of the atmosphere, as each natural process imparts its own unique isotopic signature; however, only four of these twelve isotopologues ($^{12}C^{16}O_2$, $^{13}C^{16}O_2$, $^{16}O^{12}C^{17}O$, and $^{16}O^{12}C^{18}O$) have been used extensively as tracers in atmospheric chemistry. By themselves, they are insufficient to constrain the relative influences of all the sources and sinks that have acted on a single sample. The remaining eight species (all of which contain two or three heavy rare isotopes) are exceptionally rare and, until recently, were considered to be essentially un-analyzable in natural materials. Measuring these very rare 'clumped' isotopologues would add new and essential independent constraints on the origins of CO_2 in samples of air.

In the laboratory, an equally daunting challenge exists: What are the most important reactions governing the isotopic composition of atmospheric CO_2, and what are the fundamental isotope effects? We wish to know, in the end, if our knowledge of the pertinent atmospheric chemistry is sufficient to explain atmospheric observations.

1.3 Anomalous isotopic enrichments in stratospheric CO_2

Shortly after the discovery of 'mass-independent' enrichments of ^{18}O and ^{17}O in stratospheric ozone [*Mauersberger*, 1981, 1987] and the demonstration of its chemical origin

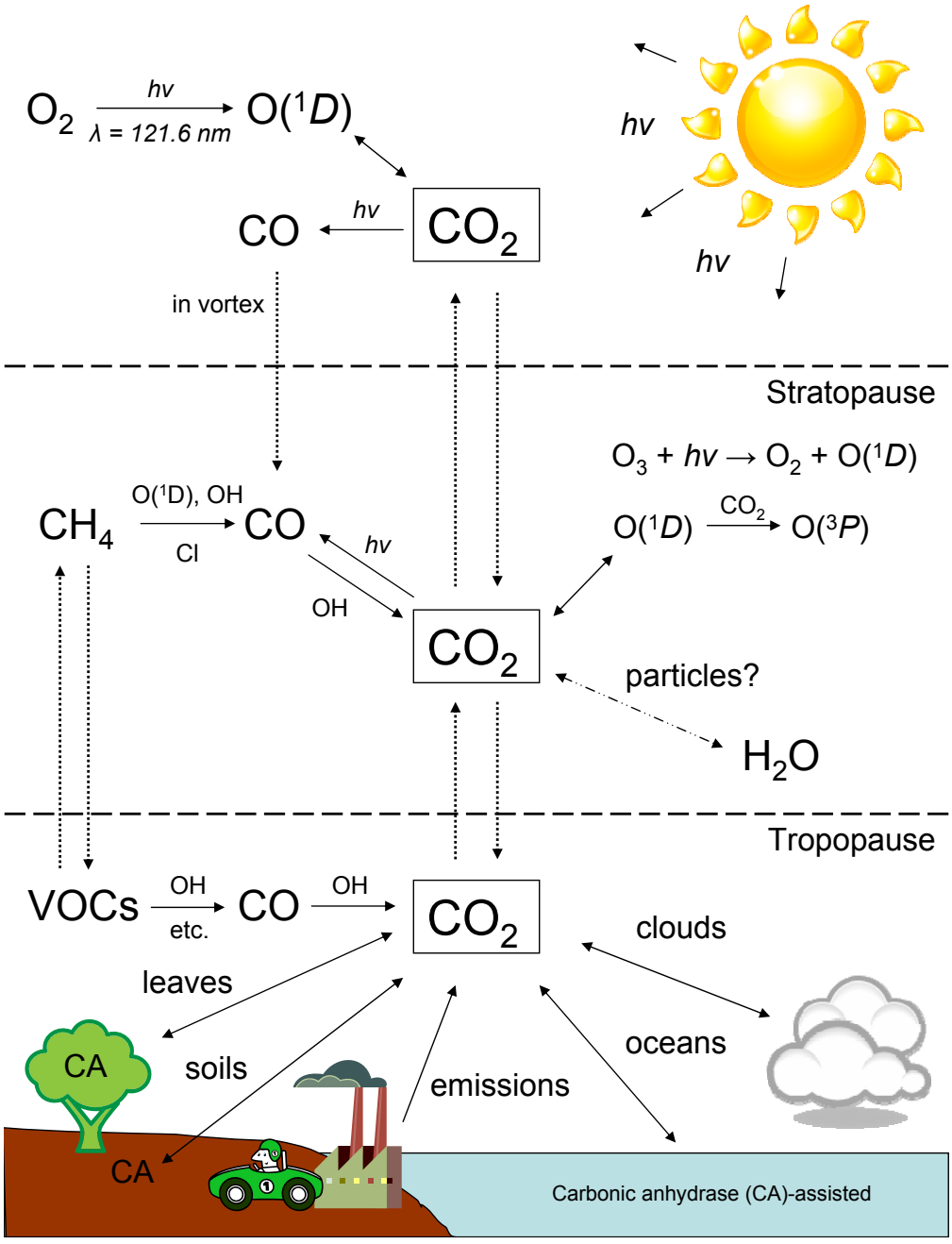

Figure 1.1: **Schematic of atmospheric CO_2 sources and sinks.** Photochemical reactions (single-headed arrows), isotope exchange reactions (double-headed arrows), and atmospheric transport (dotted arrows) are shown. Isotopic exchange on stratospheric liquid water and/or acid particles is uncertain, so its double-headed arrow is dashed.

[*Thiemens and Heidenreich*, 1983], similar enrichments were observed in stratospheric CO_2 (e.g., Figure 1.2) [*Alexander et al.*, 2001; *Boering et al.*, 2004; *Gamo et al.*, 1989; *Kawagucci et al.*, 2008; *Lämmerzahl et al.*, 2002; *Thiemens et al.*, 1991, 1995]. *Yung et al.* [1991] suggested that photochemical transfer of the heavy-isotope signature ($\Delta^{17}O$) from O_3 to CO_2 stratospheric CO_2 was possible after photolysis of O_3:

$$O_3 + h\nu(\lambda < 305 \text{ nm}) \rightarrow O_2 + O(^1D) \tag{1.1}$$

$$\rightarrow O_2 + O(^3P) \tag{1.2}$$

and then subsequent isotope exchange through reaction 1.3:

$$\mathbf{O}(^1D) + CO_2 \rightarrow \mathbf{O}CO_2^* \rightarrow O(^3P) + \mathbf{O}CO \tag{1.3}$$

The authors cited the isotope exchange mechanism in Baulch and Breckenridge's early study of the reaction in which the incident oxygen atom was incorporated into the product CO_2 molecule 2/3 of the time [*Baulch and Breckenridge*, 1966]. While this 'statistical' mechanism could explain the stratospheric ^{18}O and ^{17}O measurements qualitatively, a quantitative discrepancy remained between the observed and modeled $^{17}O/^{16}O$ vs. $^{18}O/^{16}O$ relationships: ^{17}O in CO_2 was more enriched than reaction 1.3 and Yung's model would have predicted. Unfortunately, the isotope effects in O_3 formation and photolysis and in the $O(^1D) + CO_2$ isotope exchange reaction (reaction 1.3) were not yet well understood.

Tests of the 'statistical' isotope exchange hypothesis were first conducted by *Wen and Thiemens* [1993], who photolyzed a mixture of O_3 and CO_2 with a mercury lamp at 254 nm. They observed heavy-atom enrichments in CO_2 that implied a non-statistical isotope exchange mechanism between O_3 and CO_2 (i.e., ^{17}O appeared to be preferentially incorporated into CO_2), but their result was misleading; the isotopic composition of the incident $O(^1D)$ changed significantly over the course of their experiment due to $O(^3P)$ and O_2 recombination. They did not account for these effects and thus were led to a spurious conclusion, as a later study showed [*Johnston et al.*, 2000]. To date, only one of these bulk photochemical experiments has been able to reproduce the relative ^{17}O-to-^{18}O enrichments observed in

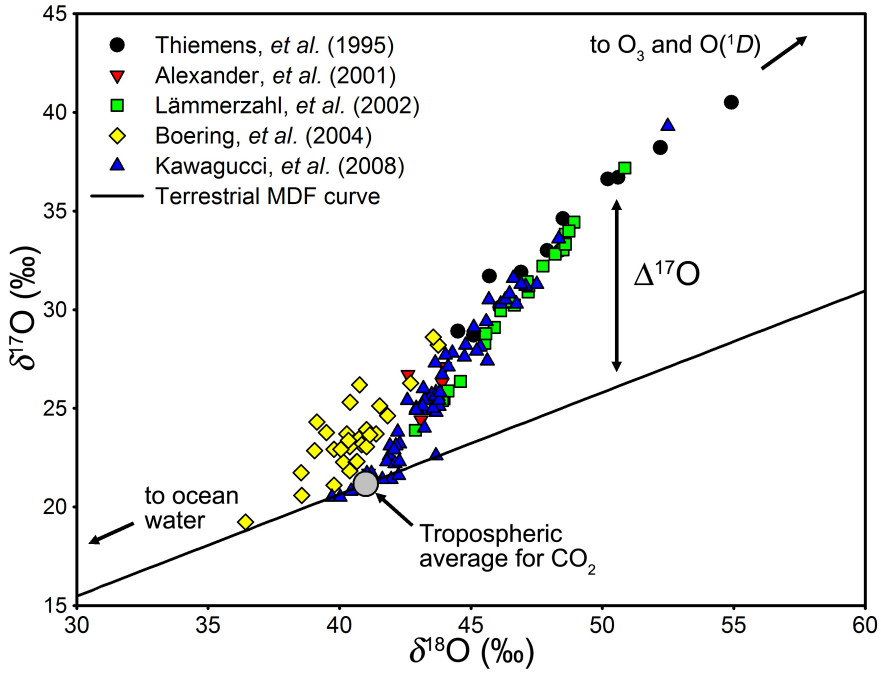

Figure 1.2: **Bulk oxygen isotope composition of stratospheric CO_2.** Departure from 'mass-dependent' compositions ($\Delta^{17}O$; see Appendix 1.A) are observed, owing to oxygen isotope exchange with stratospheric O_3 through reaction 1.3.

the stratosphere [*Chakraborty and Bhattacharya*, 2003], and those results have been controversial [*Shaheen et al.*, 2007]. Mechanistic insights have been limited because bulk stable isotope analysis is not able to differentiate isotope effects in O_3 photolysis and formation from isotope effects in reaction 1.3 unambiguously. Recent theoretical and modeling work on ozone has shed light on the effects of the former [*Babikov et al.*, 2003; *Cole and Boering*, 2006; *Gao and Marcus*, 2001, 2002; *Gao et al.*, 2002; *Hathorn and Marcus*, 1999, 2000; *Schinke et al.*, 2006], but the understanding of the stratospheric CO_2 isotopic distribution remains incomplete. The persistence of this field-laboratory disagreement was the primary inspiration for the 'clumped' isotope studies of reaction 1.3 described in this dissertation.

1.4 Insights from the physical chemist's toolbox

The techniques of physical chemistry have been invaluable for unraveling features in the complex mechanism of reaction 1.3. CO_3^* was believed to play a critical role in the isotope exchange reaction ever since the first experiments of *Katakis and Taube* [1962].

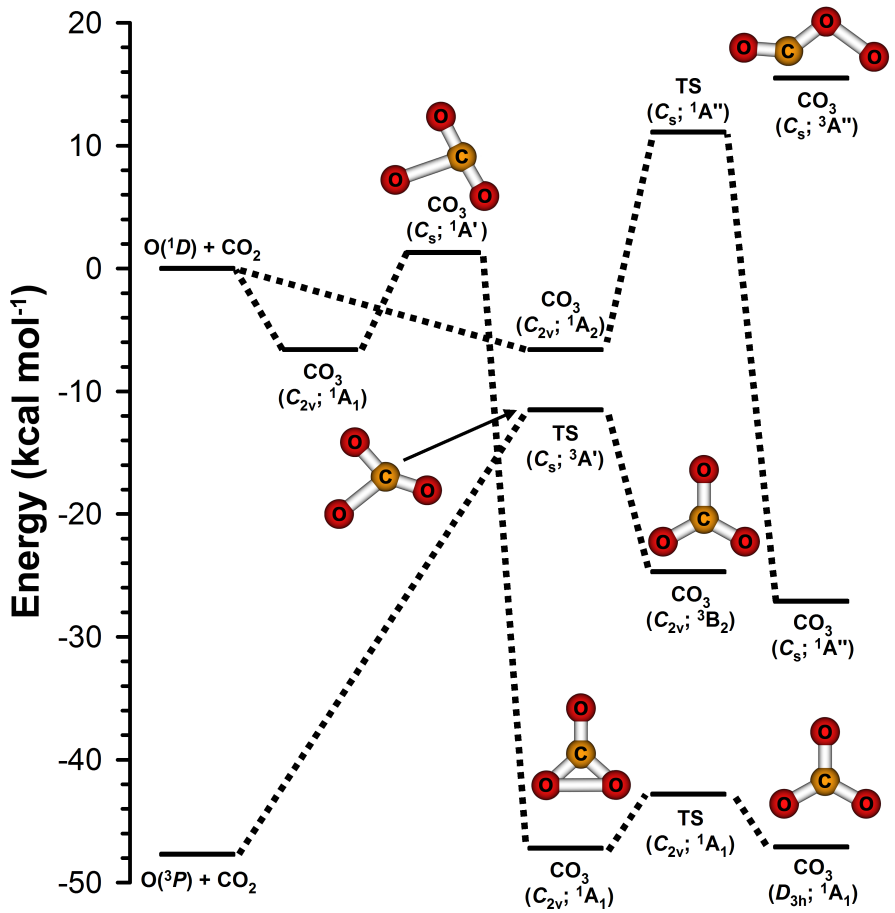

Figure 1.3: **Potential energy surface for $CO_3(^3A'')$ from *Mebel et al.* [2004].** Geometries were optimized at the CASSCF(16,13)/6-311G(d) level of theory. Energies were calculated at the MRCI+Q(16,13)/6-311+G(3df) level of theory.

Moll et al. [1966] first identified a CO_3 molecule spectroscopically upon irradiating CO_2 ice with vacuum-UV light. Although their data implied that stable CO_3 had C_{2v} symmetry, their experiments with ^{18}O-labeled CO_2 ices indicated that a $CO_3(D_{3h})$ species might be important in a reaction between atomic oxygen and CO_2, as was implied by the statistical mechanism of *Baulch and Breckenridge* [1966].

The $O(^1D)$ + CO_2 potential energy surface (PES) calculated by *Mebel et al.* [2004] is shown in Figure 1.3. On the $^1A_1$ surface ($^1A'$ dynamically), the association reaction has an early barrier at 1 kcal mol^{-1}, which is consistent with its collision-limited reaction rate coefficient (1×10^{-10} cm^3 molecule^{-1} s^{-1}) [*Sander et al.*, 2006]. The binding energy of $CO_3(^1A_1)$ is nearly 50 kcal mol^{-1}, and two structures (C_{2v} and D_{3h}) were predicted as bound

species at the bottom of the potential well. $CO_3(C_{2v})$ was detected shortly thereafter in a low-temperature CO_2 matrix [*Bennett et al.*, 2004]; the presence of a true $CO_3(D_{3h})$ minimum on the PES had been debated (see *Kaiser and Mebel* [2008]; *Kowalczyk and Krylov* [2007]; *Liu et al.* [2009] and references therein), but it was recently detected experimentally in a 10 K CO_2 ice bombarded with high-energy electrons [*Jamieson et al.*, 2006].

Intersystem crossing (ISC) from the singlet to the triplet PESs is believed to occur through nonradiative transitions rather than through the minimum of the intersection seam (near the $^3A'$ transition state); the product $O(^3P_j)$ spin-orbit state distribution is consistent with an adiabatic CO_3 dissociation [*Matsumi et al.*, 1994a]. The ISC rate was also calculated to be ten times faster through a radiationless transition than through the singlet-triplet crossing seam [*Mebel et al.*, 2004]. *Yang et al.* [2005] later proposed that a direct quenching mechanism (i.e., not through a CO_3 complex) might also be important.

Gas-phase studies of reaction 1.3 show evidence for CO_3, though none have detected it directly. *Perri et al.* [2003, 2004] reported evidence for a long-lived CO_3^* reaction complex in their crossed-molecular-beam experiments. This long-lived (1 – 10 ps lifetime) intermediate had been suggested in previous temperature- and pressure-dependent studies [*Clerc and Reiffsteck*, 1968; *DeMore and Dede*, 1970; *Weissberger et al.*, 1967], but never directly confirmed; its lifetime was later confirmed to be long enough for nearly statistical intramolecular vibrational redistribution [*Chen et al.*, 2009]. The structure and dynamics of CO_3 are not yet completely understood, however. For instance, $O(^1D)$ + CO_2 collision energy appears to be important dynamically; *Perri et al.* [2003, 2004] reported that $O(^1D)$ + CO_2 collisions yielded spin-conserving, isotopically exchanged products (1.4):

$$\mathbf{O}(^1D) + CO_2 \rightarrow \mathbf{O}CO_2^* \rightarrow O(^1D) + \mathbf{O}CO \tag{1.4}$$

Their crossed-molecular-beam experiments were performed at elevated collision energies (4.2 and 7.7 kcal mol^{-1}) so the importance of reaction 1.4 to the stratosphere is unknown. *Mebel et al.*'s companion computation study suggested that reaction 1.4 has a ~5% branching fraction at stratospheric collision energies, but this prediction has not been tested. Still, *Perri et al.*'s experimental result casts significant doubt on the applicability of the previous

bulk photochemical experiments. All the recent studies of the $O_2/O_3/CO_2$ photochemical system used O_2/O_3 as a source of $O(^1D)$ with a significant mixing fraction of CO_2, so the $O(^1D)$ atoms reacting with CO_2 probably had an elevated average kinetic energy as high as $\sim$9 kcal mol^{-1} [*Thelen et al.*, 1995], six times the calculated average in the stratosphere [*Kharchenko and Dalgarno*, 2004; *Takahashi et al.*, 2002].

1.5 Executive summary

This dissertation describes studies of three oxygen isotope exchange reactions involving CO_2 — one well-studied and two we discovered — and their potential implications for oxygen cycling in the upper atmosphere. First, I will describe the meridional (latitudinal) variations of stratospheric $^{16}O^{13}C^{18}O$ relative to those of $^{12}C^{16}O_2$, $^{13}C^{16}O_2$, $^{16}O^{12}C^{18}O$, and $^{16}O^{12}C^{17}O$; we identified a meridional gradient, with $^{16}O^{13}C^{18}O$ most enriched at the Arctic polar vortex. Our experimental and modeling study revealed that the variations in $^{16}O^{13}C^{18}O$ proportions cannot be explained in full by the known stratospheric chemistry affecting CO_2. Instead, we propose — because of the localization of a $^{16}O^{13}C^{18}O$ anomaly in the wintertime pole — that the chemistry either in the mesosphere or on stratospheric particles leads to the newly discovered isotopic enrichments. Second, I will describe crossed-molecular-beam experiments that led to the discovery of the isotope exchange reaction O_2 + CO_2. We show that the isotope exchange reaction occurs through a short-lived CO_4 intermediate, and that an adiabatic reaction mechanism exists despite a variety of energetically accessible product channels. Third, I will discuss a computational and laboratory dynamics study of hyperthermal collisions between ground-state oxygen-atoms and CO_2. We identified two reactions: oxygen-atom isotope exchange and abstraction. The isotope exchange reaction proceeds through a short-lived CO_3^* reaction complex, and it may have implications for the oxygen-isotope budget in the upper atmosphere and/or the stratospheric polar vortex. The oxygen-atom abstraction reaction may proceed through either a 'stripping'-type mechanism or a CO_3 complex, although the data cannot distinguish between the two mechanisms definitively. In the final chapter, I will attempt to synthesize what we have learned from these three studies, and what questions have emerged as a result.

Appendices

1.A Isotopic notation

The natural abundance of the rare isotopes that are the focus of this thesis are 1.1% (^{13}C), 0.02% (^{18}O), and 0.038% (^{17}O). Variations in these stable isotope abundances are typically $\leq 10^{-3}$. Consequently, bulk stable isotope abundances are commonly reported in δ-notation, in units of per mil (‰):

$$\delta^{13}\mathrm{C} = \left(\frac{R^{13}_{\mathrm{sample}}}{R^{13}_{\mathrm{VPDB}}} - 1 \right) \times 1000 \tag{1.5}$$

$$\delta^{18}\mathrm{O} = \left(\frac{R^{18}_{\mathrm{sample}}}{R^{18}_{\mathrm{VSMOW}}} - 1 \right) \times 1000 \tag{1.6}$$

where R^n is the abundance ratio of a rare isotope or isotopologue of mass n to its most abundant analogue, i.e.,

$$R^{13} = \frac{[^{13}\mathrm{C}]}{[^{12}\mathrm{C}]} \qquad R^{18} = \frac{[^{18}\mathrm{O}]}{[^{16}\mathrm{O}]} \qquad R^{17} = \frac{[^{17}\mathrm{O}]}{[^{16}\mathrm{O}]} \tag{1.7}$$

δ^{17}O is defined similarly to δ^{18}O in Eq. 1.6. δ^{13}C, δ^{18}O, and δ^{17}O are reported relative to the international standards VPDB (Vienna Pee Dee Belemnite; $R^{13} = 0.0112372$) and VSMOW (Vienna Standard Mean Ocean Water; $R^{18} = 0.0020052$ and $R^{17} = 0.0003799$). These standards were established under the International Atomic Energy Agency, but are otherwise arbitrary. They represent convenient reference points against which all isotopic measurements can be compared. Positive δ-values mean that the sample bulk isotope composition is enriched relative to the standard, and negative δ-values mean that the sample bulk isotope composition is depleted relative to the standard.

Within bulk stable isotope geochemistry, a second family of notation has emerged since the discovery of 'mass-independent' oxygen isotope fractionation (MIF) in carbonaceous chondrites [*Clayton et al.*, 1973] and during the formation of ozone (O_3) [*Thiemens and Heidenreich*, 1983]. The magnitude of MIF in oxygen (Δ^{17}O) is defined in Eq. 1.8:

$$\Delta^{17}\mathrm{O} = \delta^{17}\mathrm{O} - 0.516 \times \delta^{18}\mathrm{O} \tag{1.8}$$

This terminology is used to describe deviations from the canonical mass-dependent isotopic relationships derived by *Urey* [1947] and Bigeleisen [*Bigeleisen and Mayer*, 1947; *Bigeleisen and Wolfsberg*, 1958]. Most equilibrium and kinetic isotope effects are half as pronounced for $^{17}O/^{16}O$ ratios vs. $^{18}O/^{16}O$ ratios, so the slope of a $\delta^{17}O$ vs. $\delta^{18}O$ plot (similar to $^{17}O/^{16}O$ vs. $^{18}O/^{16}O$) is nominally 0.5. Departures from mass-dependent fractionation in oxygen are calculated using Eq. 1.8: $\Delta^{17}O > 0$ represents a 'mass-independent' enrichment in ^{17}O, whereas $\Delta^{17}O < 0$ represents a "mass-independent" depletion in ^{17}O. Several excellent reviews of this topic have been published, e.g., *Weston* [1999] and *Thiemens* [2006].

The language of 'clumped' isotope geochemistry is potentially even more confusing because the reference isotopic ratio (e.g., the denominator in Eq. 1.6) is no longer a constant:

$$R^{47} = \frac{[^{47}CO_2]}{[^{44}CO_2]} \qquad \Delta_{47} = \left(\frac{R^{47}_{\text{sample}}}{R^{47}_{\text{stochastic}}}) - 1 \right) \times 1000 \tag{1.9}$$

In Eq. 1.9, $R^{47}_{\text{stochastic}} = 2R^{13}R^{18} + 2R^{17}R^{18} + R^{13}(R^{17})^2$, the distribution of stable carbon and oxygen isotopes if they were randomly distributed among all isotopologues of CO_2 [*Eiler*, 2007]. It is important to recognize that the terms used in 'clumped' isotope geochemistry (Eq. 1.9) differ fundamentally from those in bulk-isotope measurements; the "reference" to which the measured R^{47}_{sample} is compared is a *varying internal* standard (the bulk isotopic composition), rather than the *fixed external* standard used in Eqs. 1.5 and 1.6. This distinction also leads to quirky, yet ultimately useful changes in Δ_{47} when subject to various physical processes such as mixing and diffusion [*Eiler and Schauble*, 2004].

A common question has been: "What is the difference between an isotopo*mer* and an isotopo*logue*?" Two isotopo*mers*, like chemical isomers, share the same isotopic composition, but the stable isotopes themselves are in positions that render the two molecules chemically distinct. A good example can be found in the comparison of isotopically substituted N_2O and CO_2 molecules: ^{14}N–^{15}N–^{16}O and ^{15}N–^{14}N–^{16}O are isotopo*mers* of one another because the N-atom substitutions are not symmetrically equivalent. The two isotopomers, consequently, have differing chemical properties, e.g., vibrational frequencies and rotational constants. In contrast, ^{16}O–^{12}C–^{18}O and ^{18}O–^{12}C–^{16}O are equivalent upon rotation, so they are equivalent structures of a single isotopo*logue*.

1.B Copyright declaration

This thesis contains excerpts from three publications in which the author was involved:

- Huntington, K. W., J. M. Eiler, H. P. Affek, W. Guo, M. Bonafacie, L. Y. Yeung, N. Thiagarajan, B. Passey, A. Tripati, M. Daëron, R. Came (2009), Methods and limitations of 'clumped' CO_2 isotope (Δ_{47}) analysis by gas source isotope ratio mass spectrometry, *J. Mass Spectrom.*, *44*(9), 1318–1329. ©2009 John Wiley & Sons.

- Yeung, L. Y., H. P. Affek, K. J. Hoag, W. Guo, A. A. Wiegel, E. L. Atlas, S. M. Schauffler, M. Okumura, K. A. Boering, and J. M. Eiler (2009), Large and unexpected enrichment in stratospheric $^{16}O^{13}C^{18}O$ and its meridional variation, *Proc. Natl. Acad. Sci. U. S. A.*, *106*(28), 11,496–11,501. ©2009 National Academy of Sciences.

- Yeung, L. Y., M. Okumura, J. T. Paci, G. C. Schatz, J. Zhang, and T. K. Minton (2009), Hyperthermal O-Atom Exchange Reaction O_2 + CO_2 through a CO_4 Intermediate, *J. Am. Chem. Soc.*, *131*(39): 13,940–13,942. ©2009 American Chemical Society Publications.

Chapter 2

Large and unexpected enrichment in stratospheric $^{16}O^{13}C^{18}O$

Adapted from Yeung, L. Y., H. P. Affek, K. J. Hoag, W. Guo, A. A. Wiegel, E. L. Atlas, S. M. Schauffler, M. Okumura, K. A. Boering, and J. M. Eiler (2009), Large and unexpected enrichment in stratospheric $^{16}O^{13}C^{18}O$ and its meridional variation, *Proc. Natl. Acad. Sci. U. S. A.*, *106*(28), 11,496–11,501.

2.1 Abstract

The stratospheric CO_2 oxygen isotope budget is thought to be governed primarily by the $O(^1D)$ + CO_2 isotope exchange reaction. However, there is increasing evidence that other important physical processes may be occurring that standard isotopic tools have been unable to identify. Measuring the distribution of the exceedingly rare CO_2 isotopologue $^{16}O^{13}C^{18}O$, in concert with ^{18}O and ^{17}O abundances, provides sensitivities to these additional processes, and thus is a valuable test of current models. We identify a large and unexpected meridional variation in stratospheric $^{16}O^{13}C^{18}O$, observed as proportions in the polar vortex that are higher than in any naturally derived CO_2 sample to date. We show, through photochemical experiments, that lower $^{16}O^{13}C^{18}O$ proportions observed in the mid-latitudes are determined primarily by the $O(^1D)$ + CO_2 isotope exchange reaction, which promotes a stochastic isotopologue distribution. In contrast, higher $^{16}O^{13}C^{18}O$ proportions in the polar vortex show correlations with long-lived stratospheric tracer and bulk isotope abundances opposite to those observed at mid-latitudes, and thus opposite to those easily explained by $O(^1D)$ + CO_2. We believe the most plausible explanation for this meridional variation is either an unrecognized isotopic fractionation associated with the mesospheric photochemistry of CO_2 or a temperature-dependent isotopic exchange on polar stratospheric clouds (PSCs). Unraveling the ultimate source of stratospheric $^{16}O^{13}C^{18}O$ enrichments may impose additional isotopic constraints on biosphere-atmosphere carbon exchange, biosphere productivity, and their respective responses to climate change.

2.2 Introduction

Predicting future CO_2 concentrations and carbon cycle-climate feedbacks depends on one's ability to quantify the contributions from the sources and sinks governing the global carbon budget and how they may change over time. The bulk stable isotope composition of CO_2 (i.e., its $^{13}C/^{12}C$, $^{18}O/^{16}O$, and $^{17}O/^{16}O$ ratios) plays an important role in constraining this budget (see *Yakir* [2003] and references therein). In the stratosphere, the oxygen-isotope composition of CO_2 is thought to be modified by oxygen isotope exchange reactions with $O(^1D)$ generated by ozone photolysis [*Yung et al.*, 1997], whereas in the troposphere it is controlled by isotope exchange reactions with liquid water in the oceans, soils, and plant leaves [*Ciais and Meijer*, 1998]. The interplay between stratospheric and tropospheric isotope exchange reactions, in principle, could allow the relative abundances of $^{12}C^{16}O_2$, $^{16}O^{12}C^{18}O$, and $^{16}O^{12}C^{17}O$ isotopologues to be used as tracers for gross biosphere productivity [*Hoag et al.*, 2005; *Luz et al.*, 1999], but the stratospheric CO_2 photochemical system is still under-constrained and our understanding of it is incomplete.

Discrepancies between laboratory and stratospheric measurements [*Lämmerzahl et al.*, 2002; *Shaheen et al.*, 2007; *Thiemens et al.*, 1995] have prompted questions about whether the $O(^1D)$ + CO_2 isotope exchange reaction acts alone on stratospheric CO_2 or whether other photochemical [*Bhattacharya et al.*, 2000] or dynamical [*Boering et al.*, 2004] processes significantly affect the stable isotopologue distribution in CO_2. Stratospheric oxygen isotope covariations in CO_2 [*Kawagucci et al.*, 2008; *Lämmerzahl et al.*, 2002; *Liang et al.*, 2008] consistently differ from those found in laboratory experiments simulating stratospheric photochemistry [*Baulch and Breckenridge*, 1966; *Chakraborty and Bhattacharya*, 2003; *Johnston et al.*, 2000; *Shaheen et al.*, 2007; *Wen and Thiemens*, 1993], and the origin of this disagreement is still uncertain because bulk stable isotope measurements alone (i.e., of $\delta^{13}C$, $\delta^{18}O$, and $\delta^{17}O$ values) cannot differentiate extrinsic effects [e.g., the $O(^1D)$ isotope composition] from intrinsic (i.e., photolytic or kinetic isotope) effects on the isotope composition of stratospheric CO_2. Additional constraints arising from analysis of multiply-substituted isotopologues of CO_2 can provide sensitivities to these processes [*Affek and Eiler*, 2006; *Affek et al.*, 2007; *Eiler*, 2007; *Eiler and Schauble*, 2004]. To investigate stratospheric

CO_2 chemistry, we examine here the proportions of $^{16}O^{13}C^{18}O$ (reported as a Δ_{47} value) in stratospheric CO_2 and in laboratory kinetics experiments.

2.3 Field sample collection and analysis

Twelve stratospheric CO_2 samples were analyzed for bulk stable isotope compositions and Δ_{47} values: Six samples of stratospheric CO_2 were collected from the NASA ER-2 aircraft during the 1999/2000 Arctic winter Stratospheric Aerosol and Gas Experiment III (SAGE III) Ozone Loss and Validation Experiment (SOLVE) campaign [*Newman et al.*, 2002], and six samples were collected from a balloon flight from Fort Sumner, New Mexico on 29 September 2004. SOLVE mission samples (January – March 2000, 29 – 79°N, 11 – 20 km) were collected as whole air samples [*Flocke et al.*, 1999]. CO_2 was then isolated from the ~5 L STP of air by a combination of liquid N_2 and ethanol-dry ice traps, then separated into aliquots of 12 – 18 μmol CO_2 each and sealed into glass ampoules. Balloon samples were collected using a cryogenic whole air sampler (34.5°N, 103.6°W, 27 – 33 km) [*Froidevaux et al.*, 2006; *Lueb et al.*, 1975] and purified and stored as above.

$\delta^{13}C$, $\delta^{18}O$, and $\delta^{17}O$ of CO_2 were measured on a Finnigan MAT 252 isotope ratio mass spectrometer (IRMS) at UC-Berkeley. $\Delta^{17}O$ was measured using the CeO_2 technique with a precision of ± 0.5‰ [*Assonov and Brenninkmeijer*, 2001]. Aliquots of the same CO_2 samples were analyzed for Δ_{47} using a Finnigan MAT 253 IRMS at Caltech configured to collect masses 44 – 49, inclusive, and standardized by comparison with CO_2 gases of known bulk isotopic composition that had been heated for two hours at 1000°C to achieve a stochastic isotopic distribution [*Eiler and Schauble*, 2004]. Masses 48 and 49 were used to detect residual hydrocarbon contamination. For Δ_{47} analysis, the 12 – 18 μmol aliquots of SOLVE-mission and balloon CO_2 samples were purified of potential contaminants, such as hydrocarbons, by a pentane-liquid N_2 slush (–120°C) as well as by passing it through a gas chromatographic (GC) column (Supleco Qplot, 530 μm ID, 30 m length) at –20°C, with column baking at 150°C between samples [*Affek and Eiler*, 2006; *Ghosh et al.*, 2006]. All data were corrected for the presence of N_2O using the method described previously [*Affek and Eiler*, 2006]. Each measurement consisted of 5 – 9 acquisitions (of 10 measurement

Table 2.1: Stratospheric air sample data

Air Type*	Sample Name	Altitude (km)	Latitude (°N)	θ (K)	CH_4 (ppbv)	N_2O (ppbv)	CFC-11 (pptv)	CFC-12 (pptv)	$\delta^{13}C$ (‰)	$\delta^{18}O$ (‰)	$\Delta^{17}O$ (‰)	Δ_{47} (‰)
ER-2 samples												
V	20000312(25)1120	19.33	79.2	443.61	948	111.5	19.	147.	-8.11	44.55	5.76	1.614
V	20000131(30)1001	19.85	73.5	448.08	1066	142.1	31.	198.	-8.08	43.62	4.38	1.555
V	20000203(10)1173	17.63	70.4	409.37	1250	192.8	72.	293.	-8.06	43.06	3.69	1.436
VE	20000127(5)1060	19.45	57.7	445.10	1385	227.6	112.	362.	-8.07	42.79	2.45	1.233
M	20000106(30)1169	19.40	29.3	467.43	1495	256.4	157.	421.	-8.08	42.50	2.13	1.071
M	20000111(25)2021	11.40	43.5	358.26	1726	307.9	246.	526.	-8.06	40.98	0.18	1.075
Balloon samples												
M	1-A010-R (2035)	33.34	34.5	931.14	835	54.0	0.13	46.0	-8.07	45.14	6.46	0.976
M	3-A01-R (1141)	32.22	34.6	896.15	843	56.7	0.23	51.2	-7.99	45.44	6.29	0.923
M	5-A013-R (2079)	30.78	34.6	861.84	913	77.8	0.15	78.2	-8.03	45.14	5.91	0.913
M	7-A026-R (1057)	29.26	34.6	778.08	957	92.1	0.63	100.2	-8.07	44.98	6.12	0.912
M	8-A017-E (1113)	28.73	34.6	757.89	1014	107.9	1.10	78.2	-8.04	44.79	5.00	1.004
M	10-A022-E (1186)	27.27	34.6	709.67	1176	155.9	5.90	123.6	-8.03	44.09	4.26	0.916

*Air type is abbreviated as V = vortex, VE = vortex edge, and M = mid-latitude based on N_2O:θ correlations, where θ is potential temperature in Kelvin. Non-isotopic tracer measurement methodology can be found in *Flocke et al.* [1999] and *Froidevaux et al.* [2006].

cycles each), with typical standard deviations (acquisition-to-acquisition) of 0.06‰ in Δ_{47}.

2.4 Field results

The stratospheric samples (see Table 2.1) display Δ_{47} values both higher and more variable than those exhibited by tropospheric air at the surface, which has an average Δ_{47} value of 0.92 ± 0.01‰ in remote regions (Cape Grim, Tasmania and Barrow, Alaska) [*Affek et al.*, 2007]. The high-latitude (> 57°N) stratospheric samples, in particular, are significantly more enriched in Δ_{47} than any material analyzed before in nature (see Figure 2.1 and see *Affek et al.* [2007] and *Eiler* [2007]). At high latitudes, Δ_{47} varies strongly and increases monotonically with decreasing mixing ratios of long-lived trace gases that have tropospheric sources and stratospheric sinks, such as N_2O and CH_4. At mid-latitudes, Δ_{47} varies relatively little and shows correlations with trace gas mixing ratios having the opposite sign of those observed at high latitudes (see Figure 2.2 and Table 2.1). Using the correlation between simultaneously measured N_2O mixing ratios and potential temperature [*Greenblatt et al.*, 2002], we found that the high-latitude samples were collected in inner polar vortex air (three samples) or vortex edge air (one sample). Thus, differences in the sign and magnitude of Δ_{47} variations with N_2O mixing ratio in the two subsets of

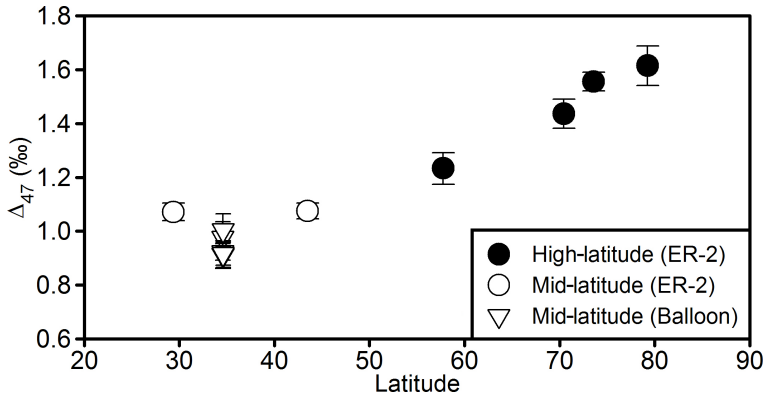

Figure 2.1: **Meridional variation of Δ_{47} measured in stratospheric samples.** Typical values in the troposphere are $\Delta_{47} \sim 0.9$‰. Error bars show 2σ standard errors.

samples are presumably due to differences between vortex and non-vortex processes. In contrast to these Δ_{47} trends, covariations of $\Delta^{17}O$ with $\delta^{18}O$ and mixing ratios of long-lived trace gases for our mid-latitude samples resemble those of our polar vortex samples (or show the expected differences for slightly shorter-lived tracers, e.g., CFC-11) and also those reported in earlier studies of high-latitude [*Boering et al.*, 2004; *Kawagucci et al.*, 2008] and polar vortex air (see Figure 2.3) [*Alexander et al.*, 2001]. This suggests that Δ_{47} records a process to which $\Delta^{17}O$ is not sensitive.

In order to rule out the possibility that the observed high Δ_{47} values result from sample contamination by organic compounds in the stratospheric samples, one of the samples [20000131(30)1001] was exposed to water at 25°C for 24 hours to reach CO_2–water isotopic equilibrium. The exchanged sample had a Δ_{47} value of 0.862 ± 0.078‰, identical to the cylinder CO_2 working standard, whose Δ_{47} value reflects CO_2 isotopic equilibrium at room temperature [*Wang et al.*, 2004]. In contrast, the presence of contaminants would have resulted in a high Δ_{47} value even after isotopic equilibrium was reached. Hence, no evidence for contamination was observed in the high-latitude samples.

2.5 Laboratory photochemical experiments

To gain further insight into the correlations we observed between Δ_{47}, $\Delta^{17}O$, and $\delta^{18}O$, we conducted several laboratory photochemistry experiments. Enrichments of $\Delta^{17}O$ and $\delta^{18}O$

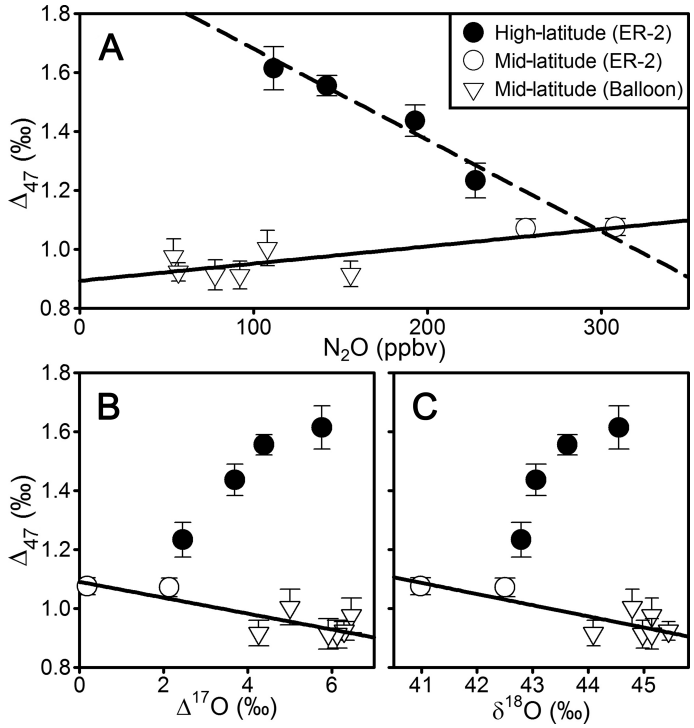

Figure 2.2: **Correlation between Δ_{47} and stratospheric tracers.** (**A**), best-fit lines are shown for mid-latitude (solid line) and high-latitude (dashed line) Δ_{47} vs. N_2O mixing ratio. Correlations between Δ_{47} and other tracers with tropospheric sources and stratospheric sinks are similar (see Figure 2.3). Also shown is the best-fit line of (**B**), Δ_{47} vs. $\Delta^{17}O$, and (**C**), Δ_{47} vs. $\delta^{18}O$ in mid-latitude air, which is used to estimate the integrated effective isotopic composition of stratospheric $O(^1D)$ (see text). Error bars represent 2σ standard errors.

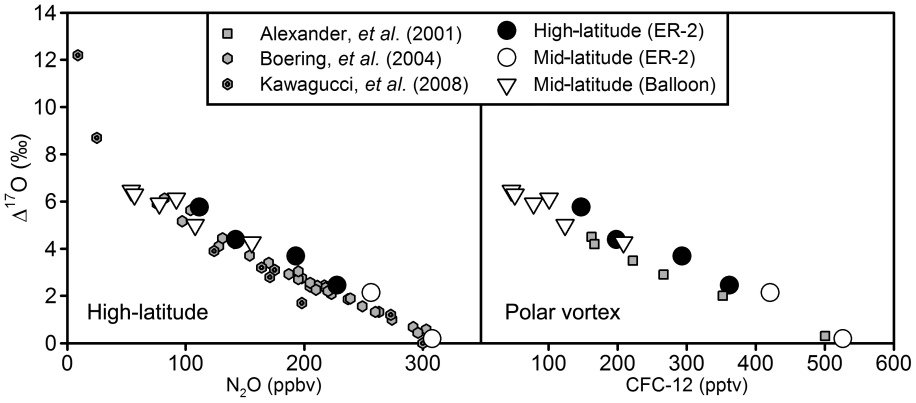

Figure 2.3: **$\Delta^{17}O$ values vs. long-lived stratospheric tracer mixing ratios.** In both panels, measurements reported in this work (ER-2 and Balloon data) are compared with previous high-latitude ($> 48^\circ$N; left panel) and polar vortex (right panel) measurements. The measured $\Delta^{17}O$ correlations with N_2O and CFC-12 do not reveal obvious distinctions among the mid- and high-latitude CO_2 samples; Δ_{47} measurements, in contrast, reveal strong mesospheric or other polar vortex influence.

in stratospheric CO_2 are generally understood to arise from isotope exchange with $O(^1D)$, which is produced by photolysis of ^{18}O- and ^{17}O-enriched stratospheric ozone [*Liang et al.*, 2007; *Yung et al.*, 1997], but the kinetics of the isotope exchange reactions for multiply-substituted isotopologues of CO_2, and their effects on Δ_{47}, have not yet been explored. Changes in Δ_{47} caused by these reactions should principally reflect relative changes in $^{16}O^{13}C^{18}O$ and $^{16}O^{12}C^{18}O$ abundances because the ^{13}C composition is not affected by isotope exchange with $O(^1D)$; variations in $^{17}O^{12}C^{18}O$ and $^{13}C^{17}O_2$ abundances will change Δ_{47} more subtly. Thus, reactions 2.1 and 2.2 are most relevant.

$$^{18}O(^1D) + {}^{12}C^{16}O_2 \rightarrow {}^{18}O^{12}C^{16}O_2^* \rightarrow {}^{16}O + {}^{16}O^{12}C^{18}O \quad (2.1)$$

$$^{18}O(^1D) + {}^{13}C^{16}O_2 \rightarrow {}^{18}O^{13}C^{16}O_2^* \rightarrow {}^{16}O + {}^{16}O^{13}C^{18}O \quad (2.2)$$

Statistical partitioning of isotope exchange products, through a process governed by random chance such that $^{18}O(^1D)$ has a 2/3 probability of being incorporated into the product CO_2, would drive the CO_2 isotopologues towards a stochastic distribution (i.e., $\Delta_{47} = 0$). If any one (or more) of the isotope exchange reactions does not partition products statistically, however, Δ_{47} can increase [e.g., if $^{18}O(^1D)$ exchanges isotopes with $^{13}C^{16}O_2$ more readily than with $^{12}C^{16}O_2$] or decrease accordingly.

Two sets of laboratory experiments were conducted. First, the relative rates of reactions 2.1 and 2.2 were probed directly to obtain the $^{13}C/^{12}C$ kinetic isotope effect (KIE) for the $^{18}O(^1D)$ + CO_2 isotope exchange reaction at 300 K and 229 K. These experiments used pulsed photolysis of 97% $N_2{}^{18}O$ at 193 nm as a source of $^{18}O(^1D)$, and the extent of isotope exchange was minimized. Second, we performed continuous-irradiation experiments, using a mercury lamp, on mixtures of isotopically unlabeled O_2, O_3, and CO_2 as a function of different irradiation times to determine the aggregate effects of the $O_2/O_3/CO_2$ photochemical system on Δ_{47}.

2.5.1 $^{13}C/^{12}C$ kinetic isotope effect experiments

2.5.1.1 Methods overview

For experiments performed at 300 K, a 15 cm-long stainless steel conflat chamber with quartz windows was used as a reaction chamber. Low-temperature experiments were performed in a 25 cm-long, all-quartz chamber, cooled to 229 K under vacuum via direct conduction with a cold copper jacket (see Appendix 2.C). Experiments were initiated with pulsed excimer laser photolysis of $N_2{}^{18}O$ (193 nm, 50 – 100 mJ pulse^{-1}, 1 Hz repetition rate, $<$ 200 pulses), producing $^{18}O(^1D)$, in $\sim$1:100:3000 static mixtures of $N_2{}^{18}O$:CO_2:He (100 Torr total pressure). $N_2{}^{18}O$ was synthesized from the acid-catalyzed reduction of ^{18}O-labeled aqueous $NaNO_2$ [*McIlvin and Altabet*, 2005; *Samuel and Wassermann*, 1971]; a detailed description of its synthesis and characterization can be found in Section 2.5.1.2. A schematic of the reaction scheme is shown in Figure 2.4.

Starting samples of CO_2 contained a stochastic distribution of isotopologues, generated in the manner described in Section 2.3. The initial CO_2 isotopic composition was measured and CO_2 was recollected cryogenically for use in the reaction chamber. Residence time in the reaction chamber had a negligible effect on Δ_{47} in the 300 K experiments, whereas the chamber cooling process alone was observed to enrich the starting material in $\delta^{18}O$ and Δ_{47}, by 0.5‰ and 0.13‰, respectively. These offset values were subtracted from final $\delta^{18}O$

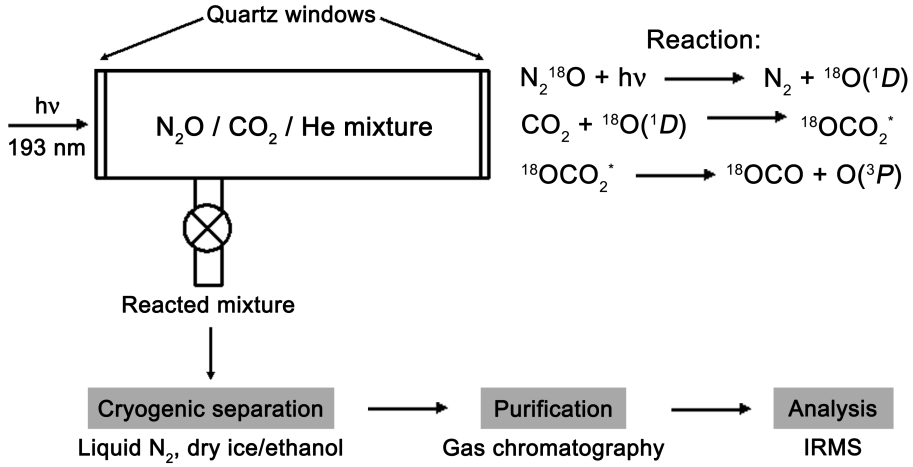

Figure 2.4: **Schematic of O(^1D) + CO_2 reaction-purification-analysis procedure.**

and Δ_{47} values in 229 K experiments. The reaction products were recollected cryogenically and purified in two GC steps. Separation of residual $N_2{}^{18}O$ and reacted CO_2 was achieved through a packed-column (PoraPak Q) GC separation at 25°C, after which the samples were purified with a capillary GC as described above. Due to the presence of $N_2{}^{18}O$ isobars with CO_2 at masses 46 – 49, mass 14 was also monitored to measure the extent of $N_2{}^{18}O$ contamination. Differences in mass-14 signal between the starting and product material of greater than 5 mV (a variation typical of 'clean' laboratory standards) were deemed contaminated, and the data points were rejected.

The difference between the initial and final $\delta^{18}O$ (hereafter referred to as $\Delta\delta^{18}O$) and Δ_{47} compositions was calculated assuming that $\delta^{13}C$ was unchanged, since there was no external carbon reservoir in the reaction. GC separation of $N_2{}^{18}O$ and CO_2 yielded a small, yet reproducible Δ_{47} change of +0.13‰, which was present both when gases of stochastic isotope composition were analyzed as well as when aliquots of cylinder CO_2 working standard (Δ_{47} = 0.86‰) were analyzed. The source of this offset may be a small amount of diffusive or adsorptive fractionation on the GC column, but it was not investigated further. Because of the apparent insensitivity of the Δ_{47} change to initial isotopic composition, the sample purification step was treated as a small additive effect on the measured Δ_{47}, with no effect on the overall kinetics measured.

The following sections, 2.5.1.2 and 2.5.1.3, provide a detailed description of the materials and methods utilized to obtain the results summarized in Section 2.5.1.4.

2.5.1.2 $N_2{}^{18}O$ synthesis

Precursor samples of $N_2{}^{18}O$ were synthesized from the acid-catalyzed reduction of aqueous nitrite ($NO_2{}^-$) [*McIlvin and Altabet*, 2005; *Samuel and Wassermann*, 1971]. A description of a synthesis and characterization follows. First, a solution of 0.4 mmol sodium nitrite ($NaNO_2$) in 800 μl >97% $H_2{}^{18}O$ (Isonics) was placed in a three-neck round-bottom flask and flushed with He at 30 mL min^{-1} for 20 minutes to remove any dissolved gases. The flow was then stopped and the flask closed off and put in an ice bath. 350 μl glacial acetic acid was then added through a rubber septum with a syringe to acidify the water. For 3 minutes,

the nitrite was allowed to exchange oxygen atoms fully with $H_2{}^{18}O$ in the acidic environment [*Ott*, 1981]. Then, the nitrite was reacted with 220 μl of a solution of 1.5 mmol sodium azide (NaN_3), 100 μl glacial acetic acid, and 150 μl $H_2{}^{18}O$, also added through the septum, for 40 minutes with stirring. Due to the high concentration of acid, the dominant reaction was expected to be that between nitrous acid (HNO_2) and hydrazoic acid (HN_3) to produce $N_2{}^{18}O$:

$$HNO_2 + HN_3 \rightarrow N_2O + N_2 + H_2O \tag{2.3}$$

After the 40-minute reaction time, 1 mL of a ~17 M NaOH solution was added through the septum to stop the reaction and remove any residual CO_2. The gas-phase products were collected by flowing He through the flask at 5 mL min^{-1} for 1 h into a "U-trap" held at liquid nitrogen temperature (77 K). Synthesized $N_2{}^{18}O$ was dried cryogenically using a pentane slush (–120 °C), then a dry ice/ethanol slush (–76 °C), and recollected in a trap at liquid nitrogen temperature. Chemical yield in the $N_2{}^{18}O$ was determined by expanding the product gas into a calibrated volume on a vacuum line, and the total product yield was determined to be 53% (0.195 mmol).

Table 2.2: IR band assignments for the spectra in Figure 2.5

Frequency (cm^{-1})	Band	Frequency (cm^{-1})	Band
1155	$2\nu_2$	1285	ν_1 ($^{14}N_2{}^{16}O$)
1247	ν_1	1595	ν_2 ($H_2{}^{16}O$)
1840	$\nu_1 + \nu_2{}^*$	2350	ν_3 (CO_2)
2217	ν_3	2563	$2\nu_1$ ($^{14}N_2{}^{16}O$)
2295	$4\nu_2$	3481	$\nu_1 + \nu_3$ ($^{14}N_2{}^{16}O$)
2412	$\nu_1 + 2\nu_2{}^*$	3657	ν_1 ($H_2{}^{16}O$)
2491	$2\nu_1$	3756	ν_3 ($H_2{}^{16}O$)
2787	$\nu_2 + \nu_3$		
3345	$2\nu_2 + \nu_3{}^*$		
3435	$\nu_1 + \nu_3$		
3663	$2\nu_1 + 2\nu_2{}^*$		
3737	$3\nu_1{}^*$		

Assignments taken from *Łapiński et al.*, and references therein. Literature values are ν_1 = 1247 cm^{-1}, ν_2 = 571 cm^{-1}, and ν_1 = 2217 cm^{-1} for $N_2{}^{18}O$.

*Temporary assignment because band has yet not been reported in the literature.

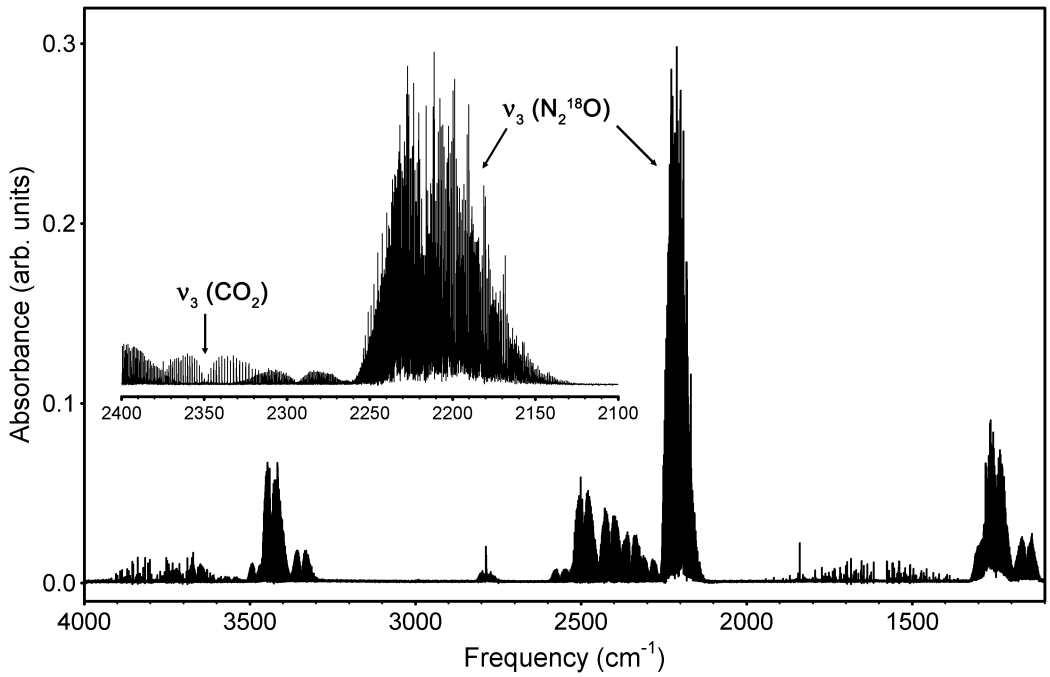

Figure 2.5: **FT-IR spectrum of synthesized $N_2{}^{18}O$ between 1100 cm^{-1} and 4000 cm^{-1}.** Inset shows the zoomed-in area between 2100–2400 cm^{-1}.

Samples were then measured on a Fourier-transform infrared spectrometer (FT-IR) for chemical purity and a IRMS for isotopic purity. FT-IR analysis was conducted on a Nicolet FT-IR spectrometer with 3 Torr $N_2{}^{18}O$, 0.125 cm^{-1} resolution, and 2000 scans in an 18 cm-pathlength cell with CaF_2 windows. Table 2.2 contains the band assignments for the $N_2{}^{18}O$ IR spectrum shown in Figure 2.5. The IR spectrum (see inset of Figure 2.5) contains a small amount of CO_2, but it is considered too small an amount to affect isotopic measurements. The absorption cross-section of the $CO_2(\nu_3)$ band is three times that of the $N_2O(\nu_3)$ band [*Rothman et al.*, 2009], yet in the experimental spectrum, the N_2O band is stronger than the CO_2 band by an order of magnitude; consequently, the concentration of CO_2 in the $N_2{}^{18}O$ sample is estimated to be 3%. Because $N_2{}^{18}O$ was used as a 1% mixture in CO_2 for the photolysis experiments, the estimated mixing ratio of contaminant CO_2 is 3×10^{-4} in the sample CO_2. This mixing ratio amounts to a maximum absolute error less than 0.001‰ in the observed $\delta^{18}O$ at natural abundance (0.2% ^{18}O), and it is therefore negligible. H_2O lines in the spectrum are believed to come from atmospheric water vapor, as they are consistent with $H_2{}^{16}O$ instead of the $H_2{}^{18}O$ used in the synthesis. Because all of the $H_2{}^{18}O$ appears

Table 2.3: IRMS ion signals from the synthesized $N_2{}^{18}O$

m/z	Signal (mV)	^{18}O content
44	1276	96.7%
46	37870	
30	482	96.8%
32	14773	

to have been removed by the cryogenic drying steps, and the sample compartment was continuously purged with dry N_2, this water vapor is believed to arise from desorbing water from the FT-IR cell walls.

Mass-spectrometric analysis was performed on a Finnigan MAT 253 using cup position 3 (3×10^{10} Ω resistor). Isotope ratios were determined at two different *m/z* ranges: 46/44 (mainly $^{14}N_2{}^{18}O/^{14}N_2{}^{16}O$) and 32/30 (mainly $^{14}N^{18}O/^{14}N^{16}O$). Table 2.3 contains the observed signals and calculated isotopic purity at 16.5 mbar in the sample bellows. Here we see that the synthesized N_2O is indeed 97% labeled with ^{18}O, and it was used in experiments without further purification.

2.5.1.3 Reaction models

Two models for the $^{13}C/^{12}C$ KIE experiments were constructed. One was a chemical kinetic model designed to calculate the expected trends in Δ_{47} vs. $\Delta\delta^{18}O$ given specific KIEs. The second was a hard-sphere collision model designed to model the velocity relaxation of the nascent $^{18}O(^1D)$, from which a collision energy distribution for each experiment could be calculated.

CHEMICAL KINETIC MODEL. A comprehensive, isotopologue-specific kinetics model of the $O(^1D)$-CO_2 photochemical experiment (144 isotope exchange reactions) was constructed in the FACSIMILE kinetics modeling package. Stochastic isotope exchange branching fractions [*Baulch and Breckenridge*, 1966; *Yung et al.*, 1997] were used: Incident $O(^1D)$ atoms had a 2/3 probability of isotope exchange, regardless of the isotope exchange reaction. The isotopic composition of the initial $O(^1D)$ was treated as a constant; for these ^{18}O-labeled

experiments, trace ^{17}O and ^{16}O abundances had negligible effects on the measured $^{13}C/^{12}C$ KIE.

We expect to observe subtle isotope effects due to differences in the $^{18}O(^1D)$–CO_2 collision frequencies between different isotopologues in the helium-buffer-gas experiments because the collision-limited rate of reaction for $O(^1D)$ + CO_2 [*Sander et al.*, 2006] implies that the reaction probability for any given $O(^1D)$–CO_2 collision is near unity. For instance, more $^{18}O(^1D)$ + $^{12}C^{16}O_2$ collisions than $^{18}O(^1D)$ + $^{13}C^{16}O_2$ collisions occur because the average velocity for $^{12}C^{16}O_2$ is higher than that for $^{13}C^{16}O_2$ at a given temperature. This reduces the rate at which reaction 2.2 occurs relative to reaction 2.1 in the laboratory by about 5%. The $O(^1D)$-CO_2 collision frequencies in these experiments scale directly with the collision pair's relative velocity, which depends inversely on the pair's reduced mass (μ) according to equation 2.4:

$$k_{2.2} = \sqrt{\frac{\mu_{^{18}O + {}^{44}CO_2}}{\mu_{^{18}O + {}^{45}CO_2}}} \times k_{2.1} = \mu_{eff} k_{2.1} \tag{2.4}$$

k represents the rate coefficient for the subscripted reaction, and μ represents the reduced mass of the subscripted reactant pair. Analogous relationships can be computed for each unique reactant pair. Δ_{47} is expected to decrease with increasing $\Delta\delta^{18}O$ because the collision frequency for $^{18}O(^1D)$ + $^{44}CO_2$ is ~5% larger than that for $^{18}O(^1D)$ + $^{45}CO_2$. Such biases are expected to be small in the atmosphere due to competing electronic quenching reactions (e.g., $O(^1D)$ + $N_2 \rightarrow O(^3P)$ + N_2) [*Johnston et al.*, 2000]. These electronic quenching reactions were minimized in our pulsed photolysis experiments because He was used as the buffer gas [*Heidner and Husain*, 1974; *Shi and Barker*, 1990]. Thus a $^{13}C/^{12}C$ KIE = $k_{2.2}/k_{2.1} = 1$ in our laboratory experiment will appear as an anti-correlation in a plot of Δ_{47} vs. $\Delta\delta^{18}O$. A $^{13}C/^{12}C$ KIE ≈ 1.01 and an $O(^1D)$ source with $\delta^{18}O = \delta^{17}O \approx 100‰$ would be required to generate the polar vortex Δ_{47} enrichment and also the polar vortex Δ_{47} vs. $\Delta^{17}O$ correlation. On the Δ_{47} vs. $\Delta\delta^{18}O$ plot, the slope would be +0.0055 using $k_{2.2}/k_{2.1} = 1.01$.

$O(^1D)$ + CO_2 COLLISION ENERGY DISTRIBUTION. The $^{13}C/^{12}C$ experiment was also modeled on the collision-by-collision level because the $O(^1D)$ + CO_2 isotope exchange reaction occurs through two reaction channels whose branching ratio depends on collision energy

[*Perri et al.*, 2003]:

$$O(^1D) + CO_2 \rightarrow O(^3P) + CO_2 \quad (2.5)$$

$$\rightarrow O(^1D) + CO_2 \quad (2.6)$$

The branching fraction of the non-quenching channel (2.6) increases significantly with reaction collision energy, E_{coll} [*Mebel et al.*, 2004; *Perri et al.*, 2004]. Observed isotope effects, then, may also depend on the distribution of E_{coll}. Nascent $O(^1D)$ atoms from the N_2O photolysis scheme employed in this study had a high average translational energy, so He was chosen as buffer gas to lower the average collision energy, $\langle E_{coll} \rangle$, to a stratospherically relevant value; He quenches the translational energy of $O(^1D)$ atoms efficiently while quenching the electronic energy inefficiently [*Heidner and Husain*, 1974; *Shi and Barker*, 1990]. Furthermore, the translational energy transfer during $O(^1D)$ + He collisions can be modeled well using a hard-sphere collision model [*Matsumi et al.*, 1994b].

We constructed a Monte Carlo hard-sphere collision model in the MATLAB programming environment based on the solution to the general elastic hard-sphere problem; the mathematical derivation can be found in the literature [*Nan and Houston*, 1992], and the program code can be found in Appendix 2.D. The basic function of the program was to calculate the final velocity vectors for two colliding hard spheres of masses m_1 (the O-atom) and m_2 (the He-atom) with initial velocity vectors (v_{1i}, θ_{1i}, ϕ_{1i}) and (v_{2i}, θ_{2i}, ϕ_{2i}), respectively.

The elastic hard-sphere calculation was performed for a distribution of initial O-atom velocities in a He bath gas at thermal equilibrium (e.g., at 298 K). First, O-atom velocity vectors, ($v_{O,i}$, $\theta_{O,i}$, $\phi_{O,i}$), were sampled according to a velocity distribution for $O(^1D)$ ejected from the photolysis of $^{14}N_2{}^{16}O$ at 193 nm [*Felder et al.*, 1991; *Hanisco and Kummel*, 1993; *Springsteen et al.*, 1993] centered at $E_T = 18.2$ kcal mol^{-1}. In the absence of experimental data for $^{14}N_2{}^{18}O$ photodissociation, the $^{18}O(^1D)$ velocity distribution was approximated by a gaussian distribution centered at $\sim$2900 m s^{-1} with a full-width at half-maximum (FWHM) of $\sim$1000 m s^{-1} (i.e., $\langle E_T \rangle \sim 18 \pm 7$ kcal mol^{-1}). Second, a He-atom velocity vector, ($v_{He,i}$, $\theta_{He,i}$, $\phi_{He,i}$), was selected randomly from a Maxwell-Boltzmann velocity distribution. Using this pair of initial conditions and a random impact parameter b (sampled with a probability proportional to itself), the final velocity vector of the O-atom after one collision, ($v_{O,f}$, $\theta_{O,f}$,

$\phi_{O,f}$), was computed and stored. The final velocity was then *re-used as an initial velocity* for the next collision with a second He-atom, whose velocity was randomly sampled as above. This calculation was repeated for up to 200 total collisions and N = 50,000 initial O(^1D) velocities, a total of 10^6 – 10^7 calculations. After 200 collisions, $>$ 96% of the O(^1D) would have reacted with CO_2 under our experimental conditions.

Using the O(^1D) velocity distribution after each O(^1D)–He collision, the distribution of O(^1D)–CO_2 collision energies, $P_j(E_{\text{coll}})$, for the jth collision could then be calculated similarly. The relative CO_2 concentration, i.e., $\rho_{CO_2} \sim 0.03$, was then used to weight the $P_j(E_{\text{coll}})$ distribution at the jth collision to obtain a O(^1D)–CO_2 collision energy distribution over the whole experiment. The results were summed according to equation 2.7:

$$P_{\text{total}}(E_{\text{coll}}) = \rho_{CO_2} \sum_j P_j(E_{\text{coll}}) \tag{2.7}$$

The model was tested by confirming that the average kinetic energy approached (and remained at) the value expected at thermal equilibrium by the equipartition theorem, e.g., $\frac{3}{2}$RT = 0.89 kcal mol^{-1} at 300 K. Calculated $P_{\text{total}}(E_{\text{coll}})$ distributions for several different experimental conditions are shown in Figure 2.6. Our simulation of the initial O(^1D) collision cascade shows that 81% of all O(^1D) + CO_2 collisions occur with $E_{\text{coll}} < 2$ kcal mol^{-1}, with $\langle E_{\text{coll}} \rangle$ = 1.6 kcal mol^{-1}, similar to the E_{coll} distribution expected in the stratosphere [*Kharchenko and Dalgarno*, 2004; *Takahashi et al.*, 2002]. As we noted earlier, the nascent ^{18}O(^1D) translational energy distribution is somewhat uncertain because the existing photodissociaton dynamics studies focused on the $^{14}N_2{}^{16}O$ molecule, not the $^{14}N_2{}^{18}O$ used in these experiments. Changing the peak of the nascent ^{18}O(^1D) translational energy distribution by 1 – 2 kcal mol^{-1} changed the average O(^1D)-CO_2 collision energy by $<$ 0.1 kcal mol^{-1}.

The shape of the laboratory $P_{\text{total}}(E_{\text{coll}})$ distribution appears different from that modeled in conditions resembling the stratosphere [*Kharchenko and Dalgarno*, 2004]; this difference is due to O(^1D) having a slower nascent O(^1D) velocity distribution (O_3 vs. N_2O photolysis) [*Thelen et al.*, 1995] and more efficient electronic quenchers (N_2/O_2 vs. He bath gas) [*Sander et al.*, 2006] in the stratosphere. In addition, minor O(^1D)-producing channels

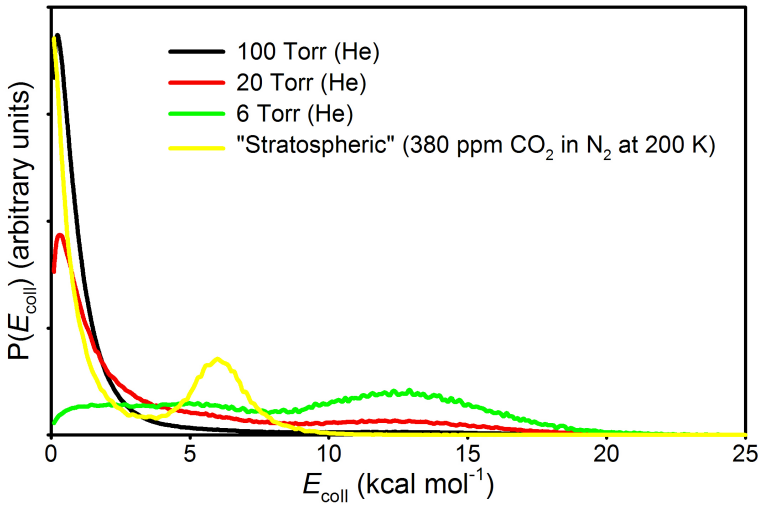

Figure 2.6: **Modeled O(^1D) + CO_2 reaction collision energy distributions at different He bath gas pressure (T = 300 K).** Also shown is the modeled $P(E_{coll})$ under conditions resembling the stratosphere, using O_3 as a source of O(^1D).

important to the stratosphere have not been included in this model (see *Taniguchi et al.* [2000]). Last, the velocity relaxation problem is only qualitatively represented by the hard-sphere model; inelastic collisions are not necessarily described well by the hard-sphere cross-sections, especially when the collision partners are diatomic, and spin-orbit coupling is important [*Kharchenko and Dalgarno*, 2004]. Thus, the "stratospheric" O(^1D) collision model results are only intended for qualitative comparison with the laboratory O(^1D)–He results.

2.5.1.4 Pulsed-photolysis results

The results of the pulsed laser experiments are plotted in Figure 2.7 and shown in Table 2.4. At both temperatures, Δ_{47} of CO_2 decreases with increasing extent of photochemical isotope exchange ($\Delta\delta^{18}O$), indicating the O(^1D) + CO_2 reaction does not selectively enrich $^{16}O^{13}C^{18}O$ relative to $^{16}O^{12}C^{18}O$. Additionally, no significant temperature dependence was observed in Δ_{47} vs. $\Delta\delta^{18}O$, as the 300 K and 229 K data are indistinguishable within our experimental uncertainty; consequently, the data were considered together in the subsequent determination of the $^{13}C/^{12}C$ KIE. The best-fit slope of the Δ_{47} vs. $\Delta\delta^{18}O$ relationship in the experimental data was calculated to be –0.0036 ± 0.0008 (2σ), corresponding to a

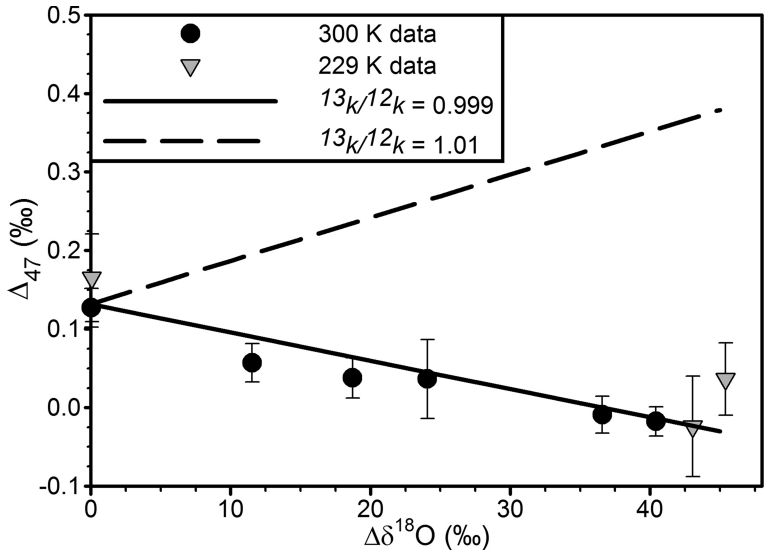

Figure 2.7: **Changes in Δ_{47} vs. $\Delta\delta^{18}$O after pulsed UV photolysis at 300 K (circles) and 229 K (triangles).** $\Delta\delta^{18}O = \delta^{18}O_{final}$ - $\delta^{18}O_{initial}$. Also shown is the modeled Δ_{47} vs. $\Delta\delta^{18}$O dependence for $^{13}C/^{12}C$ KIE = $^{13}k/^{12}k = 0.999$ and 1.01 (offset by $\Delta_{47} = +0.13$‰ for clarity; the significance of this and of the slopes is discussed in the text). Error bars represent 2σ standard errors.

Table 2.4: Results of pulsed photochemical experiments

Temperature	$\delta^{13}C$ (‰)	$\delta^{18}O_i$ (‰)	$\delta^{18}O_f$ (‰)	$\Delta\delta^{18}O^{\dagger}$ (‰)	$\Delta_{47,f}$ (‰)	$\sigma_{\Delta_{47,f}}$ (‰)
Photolysis experiments						
300 K	-10.76	29.84	66.41	36.57	-0.009	0.012
	-10.56	29.95	54.03	24.08	0.036	0.025
	-23.79	15.50	58.44	42.94	0.104	0.017
	-24.24	15.48	55.89	40.41	-0.018	0.009
	-10.69	30.08	48.79	18.71	0.038	0.013
	-10.55	29.63	41.17	11.54	0.057	0.012
229 K	-24.13	15.28	58.33	43.05	-0.024	0.032
	-25.15	14.46	59.86	45.40	0.036	0.023
Blank experiments						
300 K	-10.67	29.81	29.72	-0.09	0.150	0.011
	-19.22	20.84	20.88	0.04	0.127	0.012
229 K	-25.09	14.22	14.29	0.07	0.165	0.028

Blank experiments were run without photolysis step. $^{\dagger}\Delta\delta^{18}O = \delta^{18}O_f$ - $\delta^{18}O_i$

$^{13}C/^{12}C$ KIE of 0.999 $\pm$ 0.001 (2σ). This KIE value was obtained by modeling the $^{13}C/^{12}C$ KIE value corresponding to the best-fit slope of the Δ_{47} vs. $\Delta\delta^{18}O$ data shown in Figure 2.7 (0.999, assuming a $^{13}C/^{12}C$ KIE of 1 in reaction 2.2). Its uncertainty was estimated by varying the $^{13}C/^{12}C$ KIE until the modeled slope varied $\pm$ 0.0008; the upper and lower limits of the $^{13}C/^{12}C$ KIE (1.000 and 0.998, respectively) were then taken as the 2σ uncertainty bounds. In contrast, a $^{13}C/^{12}C$ KIE of 1.01, the KIE required to explain the polar vortex Δ_{47} vs. $\Delta^{17}O$ correlation (see Section 2.5.1.3), would yield a slope of +0.0055 in Figure 2.7. The negative experimental slope, however, rules out this $^{13}C/^{12}C$ KIE > 1 and thus a selective enrichment in $^{16}O^{13}C^{18}O$ resulting from reaction 2.1.

While this experiment was unable to isolate the $^{13}C/^{12}C$ KIEs in reactions 2.5 and 2.6, the laboratory data are consistent with the $^{13}C/^{12}C$ KIE in reaction 2.5 dominating the observed Δ_{47} vs. $\Delta\delta^{18}O$ relationship. Reactions 2.5 and 2.6 are both important in the stratosphere, with the branching ratio between them likely 9:1 (2.5:2.6) at the average stratospheric collision energy (see *Mebel et al.* [2004]) and thus also at the $\langle E_{coll} \rangle$ in our experiments. Using this branching ratio, we calculate that the experiment is approximately three times more sensitive to a $^{13}C/^{12}C$ KIE in reaction 2.5 than in reaction 2.6. A $^{13}C/^{12}C$ KIE $\sim$ 0.993 in reaction 2.6, then, is also consistent with the laboratory Δ_{47} vs. $\delta^{18}O$ slope. If the observed slope were arising exclusively from a $^{13}C/^{12}C$ KIE in reaction 2.6, it would become increasingly negative with increasing initial $\langle E_{coll} \rangle$ because reaction 2.6 is favored at higher E_{coll} [*Mebel et al.*, 2004; *Perri et al.*, 2004]. Several high-collision-energy (no buffer gas, initial $\langle E_{coll} \rangle \approx$ 13.6 kcal mol^{-1}) experiments were performed to test this hypothesis; they also showed depletions in Δ_{47} as the extent of photochemical isotope exchange increased, with no significant (i.e., factor-of-three) change in Δ_{47} vs. $\Delta\delta^{18}O$. Other combinations of $^{13}C/^{12}C$ KIEs in reactions 2.5 and 2.6 could also yield the laboratory Δ_{47} vs. $\Delta\delta^{18}O$ slope, but the absence of significant temperature and collision-energy dependence in the laboratory data, along with negligible $O(^1D)$–CO_2 association and dissociation barriers on the singlet electronic potential energy surface [*Mebel et al.*, 2004], support our attribution of the measured isotope effects to reaction 2.5. As such, we report a $^{13}C/^{12}C$ KIE of 0.999 $\pm$ 0.001 (2σ), which is within the uncertainty of a KIE of 1.000 expected for

stochastic isotope exchange.

2.5.2 Continuous-irradiation experiments

2.5.2.1 Methods

Continuous-irradiation experiments on the $O_2/O_3/CO_2$ photochemical system were performed at UC-Berkeley to examine whether the aggregate isotope effect from all $O(^1D)$–CO_2 reaction pairs would still yield depletions in Δ_{47} with increasing extent of photochemical isotope exchange. A 2 L glass reaction bulb was filled with mixtures of O_2 and CO_2 of known isotopic composition between 100 – 150 Torr total pressure at 295 K, and the mixture was irradiated between 0 – 48 hours with a pen-ray mercury lamp through a MgF_2 window. This scheme generates $O(^1D)$ through narrow-band photolysis of O_2 at 185 nm (6×10^{13} – 1.5×10^{14} photons cm^{-2} s^{-1}) and subsequent photolysis of O_3 at 254 nm (2×10^{15} photons cm^{-2} s^{-1}). Residual O_2 was separated cryogenically from the mixture, and O_3 was catalytically decomposed on hot nickel foil at 333 K for 15 minutes before the CO_2 was purified for isotopic analysis.

A commercially available software program, KINTECUS (Windows version 3.95, 2008; [*Ianni*, 2003]), was used to simulate the kinetics of the photochemical oxygen isotope exchange between O_2 and CO_2 in the continuous-irradiation experiments. The species modeled were O_2, $O_2(^1\Delta)$, $O_2(^1\Sigma_g^+)$, $O(^3P)$, $O(^1D)$, O_3, and CO_2 and included both singly- and doubly-substituted ^{17}O- and ^{18}O- isotopologues as well as ^{13}C isotopologues of CO_2, yielding more than 400 isotope-specific reactions. Rate coefficients for each reaction corresponding to all common isotopologues were from *Sander et al.* [2006], while photolysis rate coefficients (J-values) were calculated from the reported irradiance of the mercury pen-ray lamp at 254 nm [*Reader et al.*, 1996], the geometry of the bulb, and the measured cross sections of O_2 at 185 nm and O_3 at 254 nm [*Sander et al.*, 2006]. The only oxygen KIEs included in the model are in the ozone recombination reaction [*Janssen et al.*, 2001] and in O + O_2 isotope exchange [*Kaye and Strobel*, 1983; *Wiegell et al.*, 1997]. Stochastic scrambling of oxygen was assumed to occur in the $O(^1D)$ + CO_2 isotope exchange reaction [*Baulch and Breckenridge*, 1966; *Yung et al.*, 1997], and scenarios with hypothetical $^{13}C/^{12}C$ KIEs of 1,

Table 2.5: Results of continuous irradiation experiments

Sample name†	Irradiation time (h)	$\delta^{18}O$ (‰)	$\Delta^{17}O$ (‰)	Δ_{47} (‰)
Starting CO_2	0.0	6.4	0.0	1.10
ANOM 1	48.0	67.4	24.8	0.72
ANOM 1	48.0	67.4	24.8	0.85
ANOM 2	4.5	13.1	2.3	0.96
ANOM 2	4.5	13.2	2.3	1.04
ANOM 4	10.0	19.0	4.8	0.75

†Samples with the same names are replicate analyses for Δ_{47}, taken as separate aliquots of the same experiment.

0.999, and 0.998 were considered *a priori*. The model was initialized with the experimental partial pressures, temperature, and starting isotopic compositions of O_2 and CO_2.

2.5.2.2 Continuous-irradiation results

The laboratory results from the continuous-irradiation experiments are shown in Table 2.5 and compared with the modeling results in Figure 2.8. We observed a depletion in Δ_{47} with increasing $\Delta^{17}O$ (a proxy for the extent of photochemical isotope exchange), in agreement with the results from our pulsed photolysis experiments. Within the uncertainty bounds reported for the $^{13}C/^{12}C$ KIE, the continuous irradiation experiments are also generally consistent quantitatively with our pulsed photolysis experiments. There is a noticeable disagreement, however, at the largest $\Delta^{17}O$ value (48-hour irradiation time). Some of this error could be attributed to our assumptions about the initial distribution of CO_2 isotopologues in the model: The initial $\Delta_{47} > 0$ was modeled as an excess of $^{16}O^{13}C^{18}O$ exclusively, although contributions from $^{17}O^{12}C^{18}O$ and $^{13}C^{17}O_2$ may be nontrivial. In addition, trace water in the reaction bulb (in the gas phase or adsorbed onto the glass) could catalyze CO_2–water isotope exchange reactions and drive the distribution of CO_2 isotopologues towards equilibrium, i.e., $\Delta_{47} = 0.86‰$ at 298K. Both of these uncertainties would be exacerbated as the irradiation time increases, leading to a marked deviation from the modeled result at longer irradiation times. Last, the effects of the O_3 decomposition step on Δ_{47} have not been fully elucidated; previous reports have documented some oxygen isotope exchange

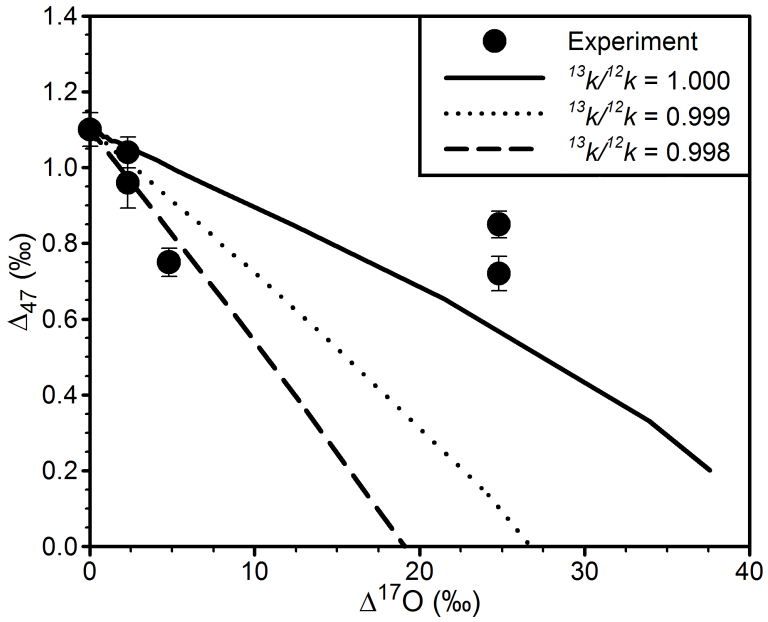

Figure 2.8: **Changes in Δ_{47} vs. Δ^{17}O of CO_2 after continuous UV irradiation of $O_2/O_3/CO_2$ mixtures with a Hg lamp.** Experimental results are compared with calculated results ($^{13}C/^{12}C$ KIE = = $^{13}k/^{12}k$ = 1, 0.999, and 0.998 obtained *a priori* from a kinetics model of the photochemical experiment. Error bars represent 2σ standard errors.

when O_3 is decomposed on hot nickel [*Johnston et al.*, 2000; *Shaheen et al.*, 2007], perhaps with the nickel oxide layer or surface-adsorbed water, so the post-irradiation O_3 decomposition step during CO_2 purification may drive Δ_{47} towards its isotopic equilibrium value ($\Delta_{47} \sim 0.8$‰ at 333 K; see *Wang et al.* [2004]) at the nickel's temperature. We performed experiments to test this hypothesis by heating O_3/CO_2 mixtures (with initial $\Delta_{47} = 0$) in the presence of nickel foil and/or powder at 88, 125, and 155°C. The resulting Δ_{47} values of CO_2 showed 1 – 2‰ changes in δ^{18}O and 0.5 – 0.6‰ increases in Δ_{47}, consistent with isotopic equilibration occurring on the nickel surface.

Still, the continuous irradiation experiments are consistent with the results of the pulsed photolysis experiments. They show that the $O(^1D)$ + CO_2 isotope exchange reaction drives the CO_2 isotopologue distribution towards a stochastic distribution.

2.5.3 Conclusions from laboratory measurements

In both sets of experiments, Δ_{47} of CO_2 decreases with increasing extent of photochemical isotope exchange, as measured by the change in δ^{18}O ($\Delta\delta^{18}$O; see Figure 2.7) or Δ^{17}O

of CO_2 (see Figure 2.8), indicating the $O(^1D)$ + CO_2 reaction does not selectively enrich $^{16}O^{13}C^{18}O$ relative to $^{16}O^{12}C^{18}O$. Furthermore, these results are consistent with a statistical oxygen isotope exchange mechanism; using the results from the ^{18}O-labeled experiments at 300 K and 229 K and the comprehensive kinetics model of the pulsed photolysis experiment, we calculated a $^{13}C/^{12}C$ KIE of 0.999 $\pm$ 0.001 (2σ est.), which is not significantly different from the KIE of 1.000 expected for statistical isotope exchange branching fractions and is quantitatively consistent with the results from the continuous irradiation experiments. Hence, our results are consistent with previous studies asserting that the $O(^1D)$ + CO_2 isotope exchange branching fractions are partitioned statistically [*Baulch and Breckenridge*, 1966; *Johnston et al.*, 2000; *Perri et al.*, 2004]. In contrast, a $^{13}C/^{12}C$ KIE of $\sim$1.01 would be required to explain the high-latitude isotopic correlations shown in Figure 2.2.

A significant Δ_{47} change due to reactions other than 2.1 and 2.2 in the $O(^1D)$–CO_2 photochemical system is unlikely. The KIEs for the other reactions (e.g., the $^{17}O^{12}C^{18}O$-producing channel, which is absent in the pulsed photolysis experiments) would need to be at least 1.01 to be of comparable importance. In addition, the Δ_{47} – $\delta^{18}O$ – $\Delta^{17}O$ covariation observed in the continuous-irradiation experiments (which included the $^{17}O^{12}C^{18}O$-producing channel; see Figure 2.8) agreed well with our laboratory model, which assumes statistical partitioning of isotope exchange products in the $O(^1D)$ + CO_2 reaction. While not all of the relative rates for the $O(^1D)$ + CO_2 isotope exchange reaction were measured directly, the agreement between the pulsed-photolysis and continuous-irradiation experiments suggests that KIEs in the other $O(^1D)$ + CO_2 reactions [e.g., $^{18}O(^1D)$ + $^{16}O^{12}C^{17}O$] are described well using statistical product partitioning in this case. Direct measurements of the other KIEs would be required to determine whether the statistical partitioning of isotope exchange products applies rigorously for all $O(^1D)$–CO_2 reactant pairs. As such, we report a $^{13}C/^{12}C$ KIE of 0.999 $\pm$ 0.001 (2σ), which is within the uncertainty of a KIE of 1.000 expected for stochastic isotope exchange.

2.6 Discussion

2.6.1 $O(^1D)+CO_2$ only explains mid-latitude $^{16}O^{13}C^{18}O$ variations

We conclude that intrinsic isotope effects in $O(^1D)$ + CO_2 isotope exchange cannot produce the elevated values of Δ_{47} observed in stratospheric polar vortex air. Instead, the statistical partitioning of isotope exchange products in the $O(^1D)$ + CO_2 reaction drives the isotopic composition of CO_2 towards a stochastic distribution, thus decreasing Δ_{47}. Indeed, the mid-latitude observations show evidence for decreasing Δ_{47} with increasing extent of photochemical isotope exchange (see Figure 2.2). As photochemical isotope exchange approaches completion (the unlikely, but instructive case in which all the oxygen atoms in CO_2 have been exchanged), the $\Delta^{17}O$ and $\delta^{18}O$ of CO_2 will approach the $\Delta^{17}O$ and $\delta^{18}O$ of $O(^1D)$ because the size of the total oxygen reservoir (i.e., O_2, O_3, etc.) is >500x that of CO_2. Concurrently, the distribution of stable isotopes will become increasingly random, so the Δ_{47} value of CO_2 will approach zero. The slope of this approach, then, reflects the integrated effective isotope composition of $O(^1D)$ with which the CO_2 molecules in the air samples have exchanged since entering the stratosphere; it is possible, however, that other terms in the stratospheric CO_2 budget (e.g., CO oxidation) may, more subtly, change the isotopic composition of CO_2 and thus the isotopic composition of $O(^1D)$ one would infer from such a trend.

We constructed a box model to calculate the effective integrated mid-latitude $O(^1D)$ isotope composition to evaluate this hypothesis quantitatively. The results of our laboratory photochemistry model ($^{13}C/^{12}C$ KIE experiments) were fit to the slope of weighted linear regressions of the mid-latitude Δ_{47} data (Figure 2.2). A quenching (reaction 2.5) and non-quenching (reaction 2.6) branching ratio of 9:1 in the isotope exchange reaction was used. Atmospheric Δ_{47} enrichments (e.g., Δ_{47} = 1.1‰) were treated as $^{16}O^{13}C^{18}O$ enrichments exclusively, since contributions to Δ_{47} from $^{17}O^{12}C^{18}O$ and $^{13}C^{17}O_2$ are $\leq$ 3%. Uncertainties in the fit $\Delta^{17}O$ and $\delta^{18}O$ values were estimated by varying $\delta^{17}O$ and $\delta^{18}O$ to match the 2σ uncertainty in the slope of the weighted linear regressions.

Using this box model and the mid-latitude observations, we estimate $\Delta^{17}O = 80.6^{+59.7}_{-24.1}$‰

and $\delta^{18}O = 98.0^{+43.7}_{-17.1}$‰ ($2\sigma$ est.) as values for the integrated effective isotopic composition of $O(^1D)$, which is consistent with ozone photolysis being the primary $O(^1D)$ source in the stratosphere. While the $\delta^{18}O$ of $O(^1D)$ we calculate is similar to that found in low- and mid-latitude stratospheric ozone, $\Delta^{17}O$ is larger, on average, by 35‰ [*Krankowsky et al.*, 2007]. This is expected because $\Delta^{17}O$ enrichments in ozone are concentrated at terminal atom positions [*Michalski and Bhattacharya*, 2009]; when ozone is photolyzed to $O(^1D)$ and O_2, one of the terminal atoms is ejected [*Dylewski et al.*, 2001], elevating the proportion of heavy oxygen isotopes in $O(^1D)$. We note that the upper and lower uncertainty limits of the reported $\Delta^{17}O$ and $\delta^{18}O$ values are correlated; they correspond to fits that simultaneously match the upper and lower uncertainty limits of the mid-latitude Δ_{47} vs. $\Delta^{17}O$ and Δ_{47} vs. $\delta^{18}O$ weighted linear regressions. They reflect spatial and temporal variations in $O(^1D)$ isotope composition expected to be caused by variations in ozone concentrations, temperature, pressure, actinic flux, and various mass-dependent kinetic and photolytic isotope effects that depend on these variables.

2.6.2 Effects of intra-stratospheric chemistry and mixing

Having experimentally excluded intrinsic isotope effects in the $O(^1D)$ + CO_2 isotope exchange reaction as the source of high stratospheric Δ_{47} in polar vortex air, we consider the possible effects of other gas-phase stratospheric processes on the CO_2 isotopologue budget. CO is produced in the stratosphere by CH_4 oxidation and destroyed with an e-folding time of about two to three months by reaction with OH radicals to form CO_2. We estimate that up to 0.9 ppmv CO_2 could be derived from CH_4 oxidation in our samples based on the difference between the observed CH_4 concentrations (Table 2.1) and the average CH_4 concentration in air entering the stratosphere from the troposphere (1.7 ppmv). $^{12}C/^{13}C$ KIEs for CH_4 + OH, CH_4 + $O(^1D)$, and CH_4 + Cl of 1.004, 1.01, and 1.07, respectively [*Brenninkmeijer et al.*, 2003], should yield ^{13}C-depleted CH_3 radicals at all latitudes, particularly in the polar vortex, where Cl levels are elevated. CH_3 radicals then undergo several rapid oxidation steps to form formaldehyde (CH_2O). Isotope effects in CH_2O photolysis to form CO also favor the light isotopologues [*Feilberg et al.*, 2005a]. These isotope effects, com-

bined with expected ^{13}C compositions for stratospheric CH_4 in these samples ($\delta^{13}C$ = –47 to –35‰) should produce CO that is depleted in ^{13}C relative to background stratospheric CO_2. Small inverse $^{12}C/^{13}C$, $^{16}O/^{18}O$, and $^{16}C/^{17}O$ KIEs (i.e., < 1) in the reaction CO + OH to form CO_2 at low pressures [*Röckmann et al.*, 1998] imply that, in principle, CO + OH reactions could increase Δ_{47} values in the product CO_2, while at higher pressures, the CO + OH reaction yields ^{13}C-, ^{18}O-, and ^{17}O-depleted CO_2 [*Feilberg et al.*, 2005b]. Ultimately, however, the size of Δ_{47} values in the $\leq$ 0.9 ppmv CO_2 derived from CH_4 oxidation would likely be orders of magnitude too small to increase Δ_{47} values significantly in the other $\sim$365 ppmv of background stratospheric CO_2. A possibility remains that unusual timing in the competition between oxidation and photolysis of species in the polar vortex, combined with unexpectedly large carbon and oxygen KIEs in some Cl and Br reactions (e.g., Br + CH_2O; see *Feilberg et al.* [2004]) or other gas-phase processes might be responsible for the mid-latitude-polar vortex differences in Δ_{47} given the large differences in Cl and Br concentrations in polar vortex vs. mid-latitude air, but this seems unlikely in light of the known chemistry and KIEs.

Expected changes in $\delta^{18}O$ and $\delta^{17}O$ due to intra-stratospheric mixing are also too small to yield highly enriched polar vortex Δ_{47}. Effects of CO_2 sources on Δ_{47} can be calculated by solving the three-end-member mixing problem between (*1*) tropospheric CO_2, (*2*) stratospheric CO_2 undergoing photochemical isotope exchange, and (*3*) stratospheric CO_2 derived from a third source and accounting for the non-linearity in mixing (see Appendix 2.A). Therefore, we constructed a mixing model to simulate the effects of mixing isotopically distinct CO_2 sources on stratospheric air. The tropospheric end-member was given an isotopic composition equal to measured 'clean' troposphere values (based on measurements of air sampled from Barrow, Alaska, and Cape Grim, Tasmania; see *Affek et al.* [2007]), namely, $\delta^{13}C_{trop}$ = –8‰, $\delta^{18}O_{trop}$ = 41‰, $\delta^{17}O_{trop}$ = 21‰, and Δ_{47trop} = 0.92‰. Unfortunately, no measurements of Δ_{47} in the tropical troposphere exist, so Δ_{47trop} of the air entering the stratosphere from the tropics is uncertain. The mid-latitude Δ_{47} vs. $\Delta^{17}O$ relationship implies that Δ_{47} may be as high as 1.09‰, but changes of Δ_{47trop} on this order do not affect our qualitative understanding of mixing on stratospheric Δ_{47}. The stratospheric end-

member was $\delta^{13}C_{strat}$ = –8‰, $\Delta^{17}O$ = 80.6‰, and $\delta^{18}O$ = 98.0‰; this was our integrated effective isotopic composition for $O(^1D)$ calculated from the mid-latitude Δ_{47} variations.

We find that two-component mixing between tropospheric and stratospheric air masses does not exhibit sufficient non-linearity to generate the observed Δ_{47} enrichments in high-latitude samples. Mixing non-linearities in Δ_{47} increase as the bulk isotope compositions of the two end-members become more dissimilar, but stratospheric $O(^1D)$–CO_2 isotope exchange alone cannot produce a CO_2 mixture of sufficiently high Δ_{47}. For instance, mixing effects generate Δ_{47} changes < 0.1‰ in the troposphere [*Eiler and Schauble*, 2004], where bulk isotope compositions of major constituents of the CO_2 budget vary typically $<$ 20‰ [*Affek et al.*, 2007; *Ciais and Meijer*, 1998]. A mixture of tropospheric CO_2 and mid-latitude stratospheric CO_2 would generate a similar enrichment because their bulk isotope compositions differ by a similar amount. Even in the extreme case of $\delta^{18}O_{strat}$ = 146‰, $\delta^{17}O_{strat}$ = 142‰ and $\Delta_{47strat}$ = 0‰, the oxygen isotope composition of CO_2 when it is at isotopic equilibrium with excess O_3 (an unlikely case, but an ultimately useful one in illustrating this point; see *Shaheen et al.* [2007]), two-component mixing would yield a maximum Δ_{47} change more than an order of magnitude smaller than, and in the opposite direction of, that which is observed in polar vortex samples over the same range in $\Delta^{17}O$. Bulk isotope compositions of the two CO_2 reservoirs must differ in $\delta^{18}O$ and/or $\delta^{13}C$ by orders of magnitude not previously observed in the stratosphere to generate Δ_{47} enrichments of $\sim$0.7‰ observed in polar vortex samples.

2.6.3 Effects of mesospheric and heterogeneous chemistry

Physical or chemical processes in the mesosphere may yield extreme isotopic enrichments in CO_2 or CO such that subsidence of mesospheric air into the 1999/2000 stratospheric polar vortex [*Plumb et al.*, 2003] could explain the observed meridional variation in Δ_{47}. Thus, we will next consider three mesospheric processes that have been previously studied in other contexts: Gravitational separation of upper atmospheric air, UV photolysis of O_2, and UV photolysis of CO_2.

2.6.3.1 Mixing of gravitationally separated air into the stratosphere

Gravitational separation can concentrate heavy isotopologues of CO_2 into the lower mesosphere [*Ishidoya et al.*, 2008], which could elevate stratospheric Δ_{47} values after mesospheric subsidence and mixing. The expression in Craig [*Craig et al.*, 1988] for the enrichment of a species N_i versus a second species N in per mil is based on the kinetic theory of gases [*Gibbs*, 1948]:

$$\Delta\left(\frac{N_i}{N}\right) = \Delta M \frac{gZ}{RT} \times 10^3 \tag{2.8}$$

where ΔM is the difference in mass, g is the acceleration due to gravity (9.81 m s^{-2}), Z is the column length, R is the gas constant, and T is the temperature. Using a reasonable column length of 50 km at a temperature of 220 K, gravitational separation of CO_2 would increase $\delta^{13}C$, $\delta^{18}O$, and $\delta^{17}O$ by 266‰, 6223‰, and 1113‰, respectively, but would lead to a *decrease* in Δ_{47} by 74‰ at the bottom of the column. In addition, polar vortex $\delta^{13}C$ is not markedly more enriched from mid-latitude $\delta^{13}C$, implying that gravitational separation is generally negligible for the samples in this study.

2.6.3.2 Mixing of mesospheric air highly enriched in ^{17}O and ^{18}O

Isotope effects in the photolysis of O_2 by short-wavelength UV radiation in the upper mesosphere might lead to unusually enriched CO_2 in the mesosphere. *Liang et al.* predicted recently that differences in photolysis cross-sections between light and heavy isotopologues of O_2 in the narrow solar Lyman-α region (121.6 nm) may result in a population of mesospheric $O(^1D)$ enormously enriched in ^{17}O and ^{18}O [*Liang et al.*, 2007]. This extreme enrichment in $O(^1D)$ could then be transferred to mesospheric CO_2 through the $O(^1D)+CO_2$ isotope exchange reaction. CO_2 photolysis in the mesosphere to form CO, followed by oxidation of that same CO by OH in the polar vortex, might also significantly affect the Δ_{47} values of CO_2 in the polar vortex.

To evaluate the effects of ^{17}O- and ^{18}O-enriched mesospheric CO_2 mixing into the stratospheric polar vortex, we constructed a three-component mixing model that included air

Table 2.6: Tropospheric-stratospheric-mesospheric mixing model results

Sample name	f^*_{trop}	f_{strat}	f_{meso}	$\delta^{18}O_{strat}$ (‰)	$\delta^{18}O_{meso}$ (‰)	$\delta^{18}O$ (‰)	$\Delta^{17}O$ (‰)	Δ_{47} (‰)
						Mixing model results		
20000312(25)1120	0.925	0.075	2.6×10^{-6}	82.5	1.76×10^5	44.55	5.76	1.614
20000131(30)1001	0.943	0.057	2.1×10^{-6}	80.0	1.86×10^5	43.62	4.38	1.555
20000203(10)1173	0.952	0.048	1.4×10^{-6}	77.7	2.07×10^5	43.06	3.69	1.436
20000127(5)1060	0.967	0.033	1.7×10^{-6}	87.9	1.47×10^5	42.79	2.45	1.233

*Mixing fraction of tropospheric air, calculated as $1 - f_{strat} - f_{meso}$.

mass contributions from the troposphere, stratosphere, and mesosphere. Each polar vortex datum (i.e., with unique $\Delta^{17}O$, $\delta^{18}O$, and Δ_{47} values) was fit individually because of the presence of mesospheric filaments in the polar vortex [*Plumb et al.*, 2003] and consequent heterogeneity in the mixing fraction and end-member isotopic composition between samples. The multiply-substituted isotopologue distribution was fixed at $\Delta_{47meso} = 0$ for this simple mixing-only scenario because our kinetics experiments and the mid-latitude stratosphere Δ_{47} values indicate that isotope exchange drives the isotopologue distribution towards a stochastic one. No measurements of mesospheric $\delta^{13}C$ exist, so $\delta^{13}C_{meso} = -8‰$ was used; however, the calculated enrichment in mesospheric $\delta^{18}O$ was insensitive to the choice of $\delta^{13}C$.

We were unable to reproduce the polar vortex data in both bulk isotope compositions and Δ_{47} simultaneously when using the mesospheric ^{18}O and ^{17}O enrichments in CO_2 mixing end-member suggested by *Liang et al.* [2007] (i.e., $\delta^{18}O = 10{,}603‰$, $\delta^{17}O = 3{,}149‰$, and $\Delta_{47} = 0$). Only after $\delta^{18}O$ and $\delta^{17}O$ of the mesospheric CO_2 end-member were increased an additional tenfold (i.e., $\delta^{18}O \sim 10^5‰$ and $\delta^{17}O \sim 10^4‰$) were the Δ_{47} – $\delta^{18}O$ – $\Delta^{17}O$ systematics of the polar vortex samples reproduced. Modeled mixing fractions (f_{trop}, f_{strat}, and f_{meso}) and isotopic compositions for each of the high-latitude CO_2 samples are given in Table 2.6.

Due to the uncertainty in our calculated $\Delta^{17}O_{strat}$ and $\delta^{18}O_{strat}$ values (see Section 2.6.1), $\delta^{18}O_{strat}$ was allowed to vary freely about our estimate above; the resulting $\delta^{18}O_{strat}$ values generally fell within the range we predicted. The combined uncertainties introduced by our calculated mid-latitude $O(^1D)$ isotope composition and the other parameters used in these

fits suggest that these results are likely only meaningful to within an order of magnitude.

No laboratory measurements of the isotopic fractionations in O_2 due to Lyman-α photolysis are available to compare with our modeled isotopic compositions, however. Because the Lyman-α lines fall on the edge of the $\tilde{E}^3\Sigma_u^- \leftarrow \tilde{X}^3\Sigma_g^-$ (1,0) absorption band of O_2, a small absolute absorption cross-section error for one O_2 isotopologue can translate into a significant isotopic fractionation error. Relaxing the mesospheric $\delta^{18}O$ vs. $\delta^{17}O$ relationship predicted by *Liang et al.* [2007], i.e, $\delta^{17}O = 0.3 \times \delta^{18}O$, increases the modeled $\delta^{18}O_{strat}$ values and lowers the predicted $\delta^{18}O_{meso}$ values, but the mesospheric CO_2 mixing end-member is still enriched overall to ~100,000‰ in $\delta^{18}O$ and $\delta^{17}O$. A simple calculation (assuming 365 ppm CO_2 and an initial $\delta^{18}O = 23.5$‰ in O_2) predicts that the mesospheric O_2 end-member should have a $\delta^{18}O$ value on the order of –100‰. Furthermore, we note that the $O(^1D)$ + CO_2 reaction may not necessarily partition products statistically (i.e., drive $\Delta_{47} \rightarrow 0$) in the mesosphere, as we assumed here, because the average collision energy there is higher than in the stratosphere.

In principle, measurements of the isotopic composition of mesospheric CO should constrain the isotopic composition of mesospheric CO_2 downwelling into the polar vortex. Large elevations in CO above background stratospheric levels, observed at high altitudes in the polar vortex [*Plumb et al.*, 2003], are due to CO_2 photolysis in the mesosphere and subsequent transport to the stratosphere, so the isotopic composition of CO in these cases should reflect that of the mesospheric CO_2 population and any fractionations arising from CO_2 photolysis there. The bulk isotope composition in mesospheric CO_2 predicted by our three-component mixing model (e.g., tens of percent in ^{18}O-atom abundance, or 100x natural abundance) would result in isotopic enrichments in mesospheric CO that are detectable with remote-sensing spectrometers because CO_2 photolysis isotope effects are expected to be much smaller in magnitude. For example, *Bhattacharya et al.* [2000] measured fractionations of ~100‰ in ^{17}O and ^{18}O in their UV-photolysis experiments; CO_2-photolysis fractionation in the mesosphere could be larger, but the wavelength dependence of these across the actinic spectrum is difficult to estimate because the physical origin of the laboratory fractionations is not understood (see below). Remote-sensing measurements by the JPL

MkIV Fourier-transform spectrometer, however, does not show hundred-fold enrichments in ^{18}O of mesospheric CO observed downwelling to 30 km altitude in the polar vortex (G. C. Toon, personal communication, 2009). On the basis of this observation, mesospheric CO_2 does not appear to possess oxygen isotopic enrichments of sufficient size to produce high Δ_{47} values in the polar vortex upon mixing with stratospheric air masses, although the long path-length and consequent averaging over mesospheric filaments and background stratospheric air of the MkIV instrument will dilute any mesospheric signal. Remote sensing of CO and/or CO_2 isotopologue abundances in the mesosphere are thus needed to constrain this hypothesis.

2.6.3.3 Oxidation of mesospheric CO in the polar vortex

Next, we examine the potential impacts of mesospheric CO_2 photolysis to form CO, followed by mixing and re-oxidation into CO_2, on polar vortex Δ_{47} values. The photolysis of CO_2 in the UV region may result in wavelength-dependent isotope effects, although this contention is based on a single laboratory measurement. *Bhattacharya et al.* [2000] performed laboratory experiments in which they photolyzed CO_2 with either a Kr lamp (120 – 160 nm) or a Hg lamp (185 nm) and measured the ^{17}O and ^{18}O compositions of the product CO and O_2. The 120 – 160 nm results suggest that mass-dependent depletions of order 50‰ and 100‰ in ^{18}O and ^{17}O of CO, respectively, are possible, which would enrich the remaining CO_2 reservoir in ^{18}O and ^{17}O. The 185-nm results were quite different: Photolysis of CO_2 near natural isotopic abundance showed mass-independent enrichments in ^{17}O up to 150‰ with little change in ^{18}O in the CO and O_2 products, while photolysis of ^{13}C-labeled CO_2 showed mass-dependent enrichments in ^{18}O and ^{17}O in the ^{13}CO and O_2 products of $\sim$50 and 100‰, respectively. Taken alone, these latter isotope dependences could result in mesospheric CO that is significantly enriched in ^{18}O, ^{17}O, and ^{13}C, and perhaps even $^{13}C^{18}O$. The remaining mesospheric CO_2 would be correspondingly depleted in heavy isotopologues.

If similar isotopic fractionations occur in CO and CO_2 when CO_2 is photolyzed by UV radiation in the mesosphere, then the population of mesospheric CO downwelling into the

stratospheric polar vortex could have a large impact on the Δ_{47} values of CO_2 in the polar vortex. Once in the stratosphere, mesospheric CO will be oxidized by OH to produce CO_2 in the polar vortex. Oxidation of this CO could, in principle, contribute to the large polar vortex values of Δ_{47} in CO_2 observed because: (*1*) CO mixing ratios as large as 10 ppmv have been observed in mesospheric filaments in the stratosphere (a thousand-fold higher than background stratospheric CO abundances in the polar vortex) [*Plumb et al.*, 2003], (*2*) the known KIEs for the CO + OH reaction are expected to favor formation of $^{13}C^{18}O$-containing CO_2 molecules in the stratosphere [*Feilberg et al.*, 2005b; *Röckmann et al.*, 1998], and (*3*) the lifetime of CO with respect to oxidation is several months, and is therefore not immediately quantitative. These three phenomena could result in a sub-population of CO_2 with elevated concentrations of $^{16}O^{12}C^{17}O$, $^{16}C^{12}C^{18}O$, and $^{16}C^{13}C^{18}O$ (or other mass-47 isotopologues of CO_2), given the sign and magnitude of known KIEs for the CO + OH reaction [*Feilberg et al.*, 2005b; *Röckmann et al.*, 1998]. The slow oxidation of CO may only produce temporary increases of heavy-isotopologue abundances, as large fractionations due to KIEs will decrease in magnitude as CO oxidizes quantitatively to CO_2. Measurements of the $^{13}C^{18}O$ + OH vs. $^{12}C^{18}O$ + OH KIE by *Feilberg et al.* at 298K and 1 atm suggest that the oxidation of mesospheric CO alone could account for elevated Δ_{47} in the stratospheric polar vortex [*Feilberg et al.*, 2005b]. Consequently, CO_2 photolysis in the mesosphere, followed by oxidation of the product CO in the mesosphere and/or stratosphere, may allow the heavy oxygen and carbon isotopes in CO_2 to 'reorganize' in a manner that could elevate Δ_{47} values of CO_2 in the polar vortex. The mixing of the remaining (unphotolyzed) mesospheric CO_2 with stratospheric CO_2 in the polar vortex, however, may have the opposite effect on Δ_{47} values of CO_2. Measurements of all the relevant KIEs of CO + OH reaction at stratospheric temperatures and pressures and a model of the oxidation of mesospheric CO in the stratospheric polar vortex will be required to evaluate the impact of this mechanism quantitatively.

The full impact of this mechanism is not well-constrained, however, because (*1*) the isotopic composition of mesospheric CO_2 has not been measured, (*2*) not all the KIEs for the CO + OH reaction are known at the relevant temperatures and pressures, and (*3*) the

physical origin of the photolytic fractionations associated with CO_2 photolysis are not understood. The first two points were discussed earlier, so they will not be discussed here. For the physical origin of the photolytic fractionations associated with CO_2 photolysis, *Bhattacharya et al.* suggested that dissociation rates for certain CO_2 isotopologues could be enhanced if their excited vibrational states (which get populated when the molecule absorbs UV light) overlap sufficiently with the vibrational states of another CO_2 electronic state. This would facilitate conversion of the electronically excited species $CO_2(^1B_2)$, which is promoted from ground-state CO_2 when it absorbs UV light and does not have enough energy to dissociate into O + CO under the experimental conditions, into the electronically excited species $CO_2(^3B_2)$, which does have enough energy to dissociate. If this mechanism is a general feature of the dynamics of CO_2 photodissociation, it could lead to additional mass-independent fractionations at wavelengths other than at 185 nm. Unfortunately, this hypothesis has not been tested at other wavelengths yet, and without a firm theoretical understanding, or at least an empirical wavelength dependence, of the isotopic fractionations associated with CO_2 photolysis, convolving the 120 – 160 nm results with the 185 nm results from *Bhattacharya et al.*'s experiments, and then convolving those with the actinic flux to make a prediction for Δ_{47} of mesospheric CO and CO_2 is not possible.

2.6.3.4 Heterogeneous chemistry on stratospheric particles

Finally, we consider the potential role stratospheric particles could play in the stratospheric CO_2 isotopic budget. Oxygen isotope exchange on particle surfaces could drive the population of CO_2 towards isotopic equilibrium by catalyzing CO_2–CO_2 isotope exchange reactions (e.g., $^{16}O^{12}C^{18}O + ^{13}C^{16}O_2 \rightleftharpoons {}^{12}C^{16}O_2 + {}^{16}O^{13}C^{18}O$) that are too slow to occur in the gas phase under stratospheric conditions. Zero-point energy isotope effects dominate in these reactions at equilibrium, driving the Δ_{47} value towards its equilibrium value at a given temperature. We calculate that Δ_{47} adopts a value of 1.6‰ if 70% of the CO_2 molecules achieve isotopic equilibrium at temperatures coincident with PSC formation in the polar vortex, $\sim$190 K [*Wang et al.*, 2004] . Thus, in principle, particle-catalyzed equilibration of CO_2, perhaps via CO_2 hydration reactions in quasi-liquid films at the surface of ice particles

[*Dash et al.*, 2006], could produce the observed polar vortex Δ_{47} values. Bulk isotopic compositions would be little-affected by these isotope exchange reactions, consistent with the data presented in Table 2.1 and Figure 2.2, if the catalyst reservoir (e.g., liquid water layers on a surface) is much smaller than the CO_2 reservoir; CO_2 would impart its bulk isotopic composition on the catalyst while the multiply-substituted isotopologue distribution in CO_2, which is insensitive to the isotopic composition of the catalyst, approaches that at isotopic equilibrium. However, CO_2–liquid water isotope exchange may not occur quickly enough at low temperatures and low pH to be the relevant process. Last, we note that, in order for this PSC-catalyzed isotope-exchange mechanism to explain the polar vortex Δ_{47} measurements, the mechanism must result in a strong anti-correlation with N_2O mixing ratios (Figure 2.2a); this would imply that transport is fast compared to isotope exchange on the PSCs, whose distributions are highly variable in space and time in the polar vortex. Future 2-D modeling efforts will examine whether such a mechanism remains consistent with the observations or whether transport and mixing of a mesospheric isotope signal into the polar vortex better explains the observed anti-correlation of Δ_{47} with N_2O.

We conducted preliminary experiments on the kinetics of isotope exchange on PSC-like surfaces (e.g., $H_2SO_4/HNO_3/H_2O$ mixtures; see *Molina et al.* [1993]) to test the PSC-isotope-exchange hypothesis. PSCs made from HNO_3:H_2O mixtures, i.e. 'Type Ia' PSCs, were tested first because they were a major component of the PSCs formed during the 1999/2000 Arctic winter [*Voigt et al.*, 2000] and their crystallization has been studied in the laboratory [*Hanson and Mauersberger*, 1988]. 50% HNO_3 in H_2O was crystallized at 197 K using an ethanol/dry ice bath according to the protocol outlined by *Hanson and Mauersberger* [1988]; the crystal structure and stoichiometry of the ice was not measured. Pure CO_2 of known isotopic composition was then exposed to the HNO_3 ice for 3 hours in a glass reaction vessel held at 197 K. No change in the Δ_{47} values were observed (within statistical uncertainty). Based on the volume of the reaction vessel and the amount CO_2, the root-mean-square (RMS) displacement was 2.5 cm s^{-1}. This RMS displacement was significant compared to the 15-cm length of the reaction vessel; therefore, the reaction's progress was probably not hindered by diffusion. The same experiment was performed also

with 1:1:1 H_2SO_4:HNO_3:H_2O mixtures (similar to 'Type Ib' PSCs) at 197 K, and no isotope exchange was observed in those experiments, either.

These preliminary results imply that CO_2 isotope exchange on PSCs is slow at stratospheric temperatures, although the chemical composition of the surfaces generated in the laboratory may have been different from those of real PSCs. Future studies should explore the isotope exchange reaction on all known PSC surfaces (e.g., types Ia, Ib, and II; see *Zondlo et al.* [2000] and *Prenni and Tolbert* [2001]) and assign upper limits to their rates.

2.7 Conclusions

The signature of a new process preserved in stratospheric $^{16}O^{13}C^{18}O$ proportions reveals that a second mechanism, in addition to the $O(^1D)$ + CO_2 isotope exchange reaction, alters the isotopic composition of stratospheric CO_2 and thus the interpretation of its chemical and transport 'history.' This second mechanism, which elevates Δ_{47} values in the polar vortex, is likely of either mesospheric photochemical or heterogeneous origin. To constrain further the role of each of these mechanisms, isotopic fractionations due to broadband UV photolysis of O_2 and CO_2, the KIEs of the CO + OH reaction under stratospheric conditions, and the kinetics of CO_2 isotope equilibration on the surfaces of PSCs and other stratospheric aerosols need to be studied experimentally. Additionally, kinetic and photolysis-induced isotope effects that may affect CO and CO_2 should be incorporated into atmospheric models to quantify their contributions to both the bulk and multiply-substituted isotopologue budgets of stratospheric CO_2, whose influence on the isotopologue budgets of tropospheric CO_2 may be significant.

2.8 Acknowledgements

We thank R. Lueb for whole-air-sampler and cryogenic whole-air-sampler field support, Y. L. Yung, G. A. Blake, and P. O. Wennberg for manuscript comments, and financial support from the Davidow Fund, the National Science Foundation, the NASA Upper Atmosphere Research Program. K. A. B. was supported by the Camille Dreyfus Teacher-Scholar Award.

Appendices

2.A Mixing effects on isotopic composition

The effects of CO_2 air parcel mixing on isotopic composition have specific relevance for Δ_{47} in Chapter 2, so an example follows below. In general, mixing of two or more reservoirs of CO_2 is linear in $\delta^{13}C$, $\delta^{18}O$, and $\delta^{17}O$ (the mixture has δ-value in between that of the two mixing end-members) because the references against which they are compared are constant (see Eqs. 1.5 and 1.6) Mixing of two reservoirs with the same Δ_{47} and differing bulk isotope distributions, however, can yield Δ_{47} values in the mixture different from those in the end-member gases. This nonlinear dependence of Δ_{47} on mixing arises because both R^{47}_{sample} and the reference against which it is measured ($R^{47}_{\text{stochastic}}$) change upon mixing; the reference is defined by, and therefore varies with, the bulk stable isotope ratios of that mixture. In contrast, the references used in bulk stable isotope measurements are external standards whose values are constant (e.g., VSMOW), so the bulk isotope ratios vary linearly with mixing. The degree of nonlinearity in Δ_{47} is a function of the differences in bulk isotopic composition between the mixing end-member reservoirs and their mixing fractions [*Affek and Eiler*, 2006; *Eiler and Schauble*, 2004].

Because Δ_{47} depends non-linearly on mixing fraction, even for two CO_2 reservoirs with similar Δ_{47} [*Affek and Eiler*, 2006; *Eiler and Schauble*, 2004], mixing relationships are often counterintuitive. An illustrative example is shown in Figure 2.9: The two mixing end-members (given as the bottom-left and bottom-right corners) have different initial $\delta^{18}O$ and $\delta^{17}O$ values, though both have $\delta^{13}C$ = –8‰ and Δ_{47} = 0.92‰. The concentration of $^{47}CO_2$ (i.e., R^{47}_{mix}) varies linearly with mixing fraction, but the stochastic distribution for $^{47}CO_2$ molecules also changes, varying as $\sim 2R^{13}R^{18}$. Consequently, mixing these two isotopically dissimilar CO_2 reservoirs yields a $\Delta_{47\text{mix}} > 0.92$‰ despite each reservoir being initially at Δ_{47} = 0.92‰. This type of relationship is general, and so holds for all Δ_{47}; the sign and magnitude of the resulting Δ_{47} change will depend on the end-member bulk and clumped isotope compositions.

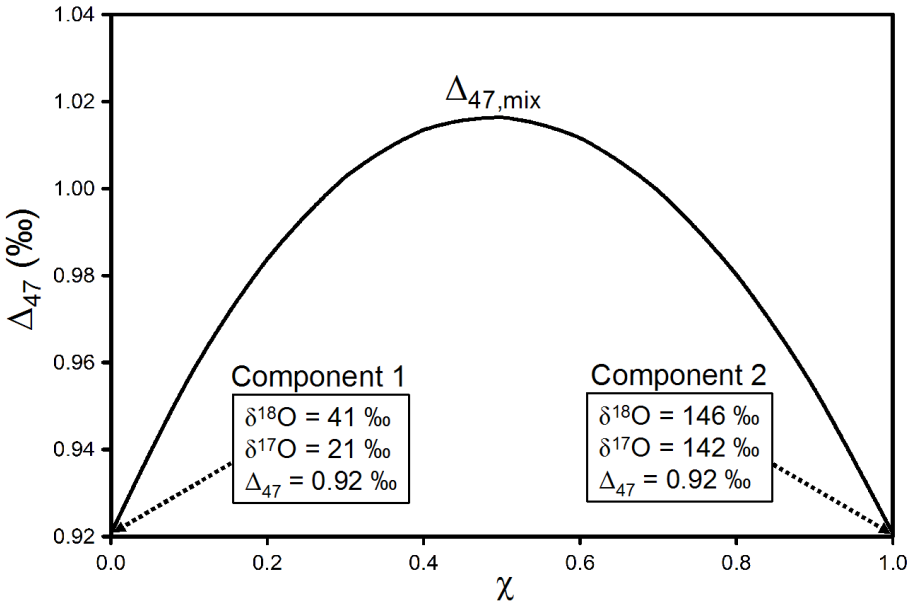

Figure 2.9: **How mixing two arbitrary reservoirs of CO_2 can be nonlinear in Δ_{47}.** The resulting mixture is more enriched in $^{47}CO_2$ relative to its stochastic distribution, as compared to either of the mixing end-members. The isotopic compositions used in this plot are for illustration purposes only; qualitatively similar effects will apply for all mixing relationships.

2.B Practical considerations

2.B.1 IRMS long-term signal stability

Δ_{47} measurements currently take ~4 hours of instrument averaging time per sample analysis. We examined the stability and accuracy of our IRMS system over this time period by using a modified form of the Allan variance technique, originally developed to characterize ultrastable oscillators [*Allan*, 1987]. Instead of using time as the independent variable, here we use individual IRMS acquisitions x:

$$\sigma^2_{\text{Allan}}(x) = \frac{1}{2(N-1)} \sum_i [\langle x \rangle_{i+1} - \langle x \rangle_i]^2 \tag{2.9}$$

Data are first binned into N bins (each consisting of one or more acquisitions), and the average of each bin, $\langle \text{x} \rangle_i$, is taken. The difference between adjacent bins is squared and then summed before being normalized to compute the Allan variance. For example, a data set with six elements [x_1, x_2, x_3, x_4, x_5, x_6] will produce three values of Allan variance corresponding to bins of one ([x_1], [x_2], [x_3], [x_4], [x_5], [x_6]), two ([x_1, x_2], [x_3, x_4], [x_5, x_6]) and three ([x_1, x_2, x_3] and [x_4, x_5, x_6]) elements each. The maximum bin size is therefore half the total number of elements in a data set.

Plotting Allan variance versus bin size, then, conveniently presents both noise- and drift-related effects on single plot. An example of the Δ_{47} Allan variance for a relatively long-duration analysis, consisting of 40 acquisitions of 80 s sample integration each (ten 8 s cycles), is shown in Figure 2.10. An ideal statistical-noise-limited measurement, for which long-term drifts are negligible, will display a power-law relationship $\sigma^2 = Cx^\alpha$ in the Allan variance plot, where α = –0.5, reflecting the Poisson statistics governing the precision of the overall measurement. In contrast, a measurement dominated by long-term, correlated random-walk drifts will have α = 0.5. Consequently, the optimum number of measurements to average together in a given analysis (i.e., the optimum bin size) will occur near where the Allan variance reaches a minimum, i.e. where $d\alpha/dx = 0$. For our instrument, measurements seem to be dominated by statistical noise for $N < 10$ acquisitions, with only a small contribution from long-term drift. The variability of σ^2 appears to increase for

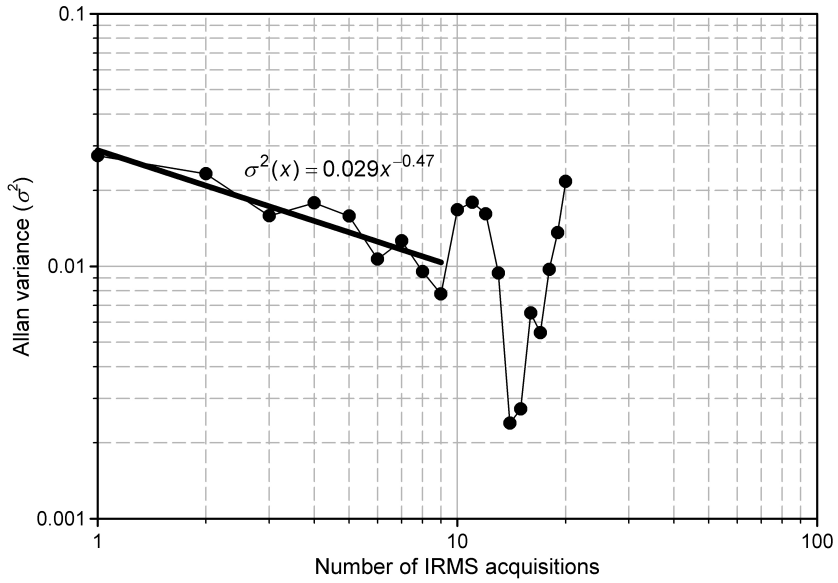

Figure 2.10: **Allan-variance plot of Δ_{47} over 40 IRMS acquisitions.** A power-law regression is shown for bins up to nine acquisitions. α = –0.47 was obtained, indicating that Poisson statistics, not long-term drifts, dominate the uncertainties in the measured Δ_{47} value in this range.

measurements made in excess of nine acquisitions (see Figure 2.10), although we attribute this to the smaller number of bins with greater than nine acquisitions contributing to the Allan variance calculation. More precise values of the Allan variance with these numbers of acquisitions would require a more sustained analytical run by several factors in time. Nevertheless, the ideal precision that should be attainable on a single gas run for measurements that are clearly dominated by statistical noise (nine acquisitions, or 720-s counting time) at the optimal voltage (16 V) is 0.013‰.

2.B.2 IRMS vs. optical methods

The best high-precision isotope-ratio measurements have been made routinely on gas-source mass spectrometers based on Nier's original 1947 design [*Nier*, 1947]. These instruments are fundamentally sensitive to that which makes stable isotopes unique — their mass — so IRMS continues to be the technique-of-choice used for stable isotope abundance measurements. It achieves high precision over a large dynamic range by utilizing multiple Faraday cups with differing amplifier gains (over a factor of 3000 for Δ_{47} measurements)

and rapid sample-standard comparison. However, the relatively poor mass-resolving power ($M/\Delta M \sim 500$) that comes as a consequence of using a magnetic sector and high-sensitivity, electrically stable Faraday-cup detectors leads to well known isobaric (same-nominal-mass) interferences, e.g., between $^{13}CO_2$ and $^{16}O^{12}C^{17}O$ at $m/z = 45$. In 'clumped' isotopologue measurements of CO_2, isobars and other impurities (e.g., N_2O, hydrocarbons) are especially important given the low absolute abundance of $m/z = 47$ isotopologues. A new concern also arises in the study of 'clumped' isotopologues: ion recombination after electron-impact ionization source can alter the measured distribution of stable isotopes vs. that present in the original sample. High-resolution and thermal-ionization mass-spectrometric techniques can potentially address these uncertainties, but none have yet demonstrated the precision and stability necessary for Δ_{47} measurements.

Spectroscopic techniques, however, show great promise for measuring stable isotopologue abundances in natural samples because they are non-destructive, sensitive to both mass and molecular symmetry, and field-deployable. These characteristics are particularly desirable for studying the stable isotope distribution in atmospheric gases, and how they evolve over time. The author has had some experience with these techniques so the following discussion represents a synthesis of his experience. While most examples relate to CO_2, the general considerations presented here should be applicable to spectroscopic stable isotope measurements of other species. More general and thorough reviews of the literature have been published (e.g., *Kerstel* [2004]; *Kerstel and Gianfrani* [2008]), so the references herein are exemplary rather than comprehensive.

Three main instrumental requirements for highly precise optical measurements of rare and/or 'clumped' isotopologues near natural isotopic abundance are apparent: absolute sensitivity, dynamic range, and long-term signal stability. A more subtle problem is the selection of spectral region; the spectral absorption scales not only with analyte concentration, but also the optical pathlength and the size of the transition dipole (i.e., the absorption line strength, S, for the transition). In addition, spectral overlap between isotopologues and also from contaminants will lead to systematic errors. The type of spectroscopic technique, then, will depend on the analyte identity and spectral region. For instance, *Tuzson et al.*

[2008] used the strong CO_2 lines ($S \sim 10^{-18}$ cm molecule^{-1}) near 2300 cm^{-1} and a multi-pass direct absorption cell [*Herriott et al.*, 1964] to measure δ^{13}C and δ^{18}O with better than 0.1‰ precision (100-s averaging). The authors utilized that region because the transitions for $^{12}C^{16}O_2$, $^{13}C^{16}O_2$, and $^{16}O^{12}C^{18}O$ were of nearly equal strengths. *Bergamaschi et al.* [1994] made similar line choices for δ^{13}C and δD measurements in CH_4. *McManus et al.* [2002] surmounted the dynamic range problem for their CO_2 isotopologue measurements by designing an optical cell with differential absorption pathlengths for each isotopologue, allowing CO_2 lines differing in intensity by several orders of magnitude to be measured precisely. In both cases, long-term drifts (e.g., temperature, laser power, frequency jitter etc.) were accounted for by simultaneous measurement of a reference gas.

Other important variables to consider are sample temperature stability and spectral line function. *Bergamaschi et al.* [1994] reported an approximate sensitivity of the measured δ-value and temperature (T) in per-mil units:

$$\frac{\Delta\delta}{\Delta T} \approx \frac{\Delta E}{kT^2} \times 1000 \tag{2.10}$$

where k is Boltzmann's constant and ΔE is the difference in lower-state energies of the corresponding transitions. It is derived from the Taylor series expansion of a normal (Gaussian) distribution [*Schupp*, 1992]. Empirically, this translates to $\pm$ 5‰ K^{-1} for bulk stable isotope measurements of H_2O and CO_2 [*Kerstel and Gianfrani*, 2008], so a temperature stability between the reference gas and the sample of 50 mK would yield temperature-induced errors of 0.1‰. *Kerstel and Gianfrani* [2008] also make the argument that measurement of peak intensities is sufficient so long as the lineshape functions are the same between the sample and standard transitions.

'Clumped' isotope measurements present a new set of concerns due to the more stringent technical demands, e.g., measuring a signal 4.5 $\times$ 10^{-5} with 0.005‰ precision for Δ_{47}-based carbonate thermometry [*Huntington et al.*, 2009]. At present, high-precision IRMS measurements of Δ_{47} involve multiple comparisons between the sample CO_2 gas, bulk stable isotope working standards, and 'clumped' stable isotope standards (CO_2 with a stochastic distribution of isotopologues). Any spectroscopic technique will require similar calibrations

because the instrument response, in general, will not be sufficiently linear over such a large range in concentration. For instance, the required linear dynamic range for rovibrational transitions of $^{12}C^{16}O_2$ and $^{16}O^{13}C^{18}O$ with identical v and J (absolute sensitivity concerns notwithstanding) is $\geq 10^9$. Photoacoustic methods are capable of this dynamic range, in principle, but previous attempts to make high-precision isotopic measurements have been limited by fluctuations in pump laser power [*Samura et al.*, 2002]. On the other hand, if a convenient spectral window is found such that line strengths of the dominant and minor isotopologues are similar, the temperature sensitivity will be large (e.g., due to large differences in the lower-state energies).

From a practical perspective, the line strength of the minor isotopologue will dictate the choice of method; for instance, the strongest $^{16}O^{13}C^{18}O$ transition in the mid-IR has a line intensity $S \sim 10^{-23}$ cm molecule^{-1}, which is out of range for all but the most sensitive spectroscopic techniques. Of the high-sensitivity optical techniques, cavity ringdown spectroscopy (CRDS; *O'Keefe and Deacon* [1988]) with frequency-axis stabilization and single-mode operation (FS-CRDS; [*Hodges et al.*, 2004]) shows the most promise, in this author's opinion. A key feature in FS-CRDS is its ability to average spectra on the timescales of hours; the utility of other ultrasensitive methods, such as the shot-noise-limited NICE-OHMS technique (noise-immune, cavity-enhanced optical heterodyne molecular spectroscopy) [*Ye et al.*, 1998], have been ultimately limited by technical pitfalls and long-term drifts [*Foltynowicz et al.*, 2008]. In contrast, FS-CRDS can be averaged continuously for nearly 10 hours to achieve a signal-to-noise ratio (SNR) of 18,000 (i.e., 0.6‰ precision) on a single line of intensity $S = 1 \times 10^{-24}$ cm molecule^{-1} at 0.5 Torr [*Long et al.*, 2009]. Higher SNRs may be possible with the implementation of single-mode optical feedback [*Motto-Ros et al.*, 2008], optoelectronic laser-locking [*Drever et al.*, 1983], or in combination with rapid (kHz) sample-background ringdown comparison [*Ye and Hall*, 2000]; increasing sample concentration will also improve the SNR, but the dynamic range of the instrument will place an upper limit on the maximum line strength. The choice of lineshape theory used to obtain the integrated intensity might also be important [*Lisak et al.*, 2006, 2009], as the integrated intensity is a more robust measurement of isotopic abundance than

peak height, which increases nonlinearly with gas pressure.

At present, IRMS is the only practical method for measuring 'clumped' isotopologue abundances in in CO_2 with precisions better than 0.1‰. Spectroscopic measurements for CO_2 will be best in the mid-IR region, where the rovibrational transitions are strongest ($S_{^{16}O^{13}C^{18}O} \sim 10^{-23}$ cm molecule^{-1}); single-mode quantum-cascade lasers with $\geq$ 5 mW power are becoming widely available in that region. Another possibility for CO_2 is the 2-μm region, where the strongest $^{16}O^{13}C^{18}O$ line strength is $S_{^{16}O^{13}C^{18}O} \sim 3 \times 10^{-26}$ cm molecule^{-1} (4826.05 cm^{-1}); analysis time will be increased accordingly. The NICE-OHMS method is capable of reducing analysis times significantly, in principle, because it has demonstrated a shot-noise-limited sensitivity for strong laser sources (e.g., SNR = 7700 in 1s for $S = 1 \times 10^{-23}$ cm molecule^{-1} using a 5 mW Nd:YAG) [*Ye and Lynn*, 2003; *Ye et al.*, 1998]. However, technical challenges such as long-term temperature and frequency stability must be addressed.

While examining the possibility for measuring 'clumped' CO_2 isotopologues spectroscopically is useful for illustrating the general principles involved, this approach will ultimately be the most useful for other species of atmospheric and geochemical interest. For instance, isotopic abundances in SO_2 are canonically difficult to measure due to its polarity [*Gao and Thiemens*, 1991, 1993]; high-precision IRMS systems rely on a viscous-flow injection into the ionization region, and high-polarity gases such as SO_2 often display a pronounced 'memory' effect that limits measurement precision and reproducibility [*Ono et al.*, 2006]. SO_2 lines in the mid-IR ($\sim$2500 cm^{-1}) are of comparable strength to those of CO_2 in the 2-μm region (see above), so 'clumped' isotopologue measurements of SO_2 may be possible, with long averaging times, in the near future. These measurements have the potential to establish a link between the ancient atmosphere and the geologic record. For instance, *Lyons* [2009] has proposed that the unique sulfur and oxygen isotope composition of Archaean Fig-tree barites [*Bao et al.*, 2007] may reflect gas-phase SO_2–H_2O isotope exchange reactions; 'clumped' isotope analysis would place additional constraints on the origins of these and other barites, which contain information about the sulfur and oxygen cycles, atmospheric composition, and climate of the ancient past.

2.C Low-temperature cell for $^{13}C/^{12}C$ KIE experiments

For the low-temperature $^{13}C/^{12}C$ KIE experiments, the quartz reaction chamber (filled with N_2O, CO_2, and He) was placed inside a cooling assembly within a conflat vacuum chamber. The vacuum chamber was first pumped down to ∼20 – 50 mTorr, and then liquid N_2 coolant (ΔH_{vap} = 1.33 kcal mol^{-1}) was added through a feedthrough at the top of the chamber. The liquid N_2 cooled a series of metal ("conduction" and "transfer") blocks, which, in turn, cooled the quartz reaction cell along its entire length. Temperature was monitored using a standard type-K thermocouple; active temperature control was possible, though it was not necessary to achieve temperatures near 230 ± 1 K when the liquid N_2 was poured into the feedthrough.

The cooling assembly was designed to fit inside a spare ∼27 × 27 × 21 cm ($l \times w \times h$, interior dimensions) conflat chamber with a 9.5-cm ID (see Figures 2.11, 2.12, and 2.13). Experimental and spatial constraints dictated the design parameters, and the resulting assembly had little flexibility. Use of 193-nm laser radiation to photolyze N_2O meant that quartz (UV-grade fused silica) windows were the most affordable and robust window material; MgF_2 windows can provide ∼10% greater transmission at 193 nm, but quartz was chosen because it was cheaper and could be bonded with a quartz tube to make a monolithic, leak-tight reaction chamber without need for adhesives. During an experiment, the reaction chamber was inserted directly into the oxygen-free, high conductivity (OFHC) copper tube (2.14). This tube was fastened to the "conduction block" (Figure 2.15), which was itself attached to the OFHC copper "heat-transfer block" by a countersunk screw on the rounded underside of the conduction block. A second heat-transfer block (Figure 2.17) was sandwiched between the heat-transfer block and the connection to the liquid N_2 feedthrough (Figure 2.18); this block had a relatively small surface area and was machined out of brass (120 W m^{-1} K^{-1} vs. 401 W m^{-1} K^{-1} for copper at 300 K) to retard heat transfer from the liquid N_2 to the reaction cell. The second heat-transfer block also had a hole drilled through the center so a heating resistor could be inserted, if necessary, to control the temperature in future experiments.

All components were mated with a thin layer of Apiezon "N" grease; this material was

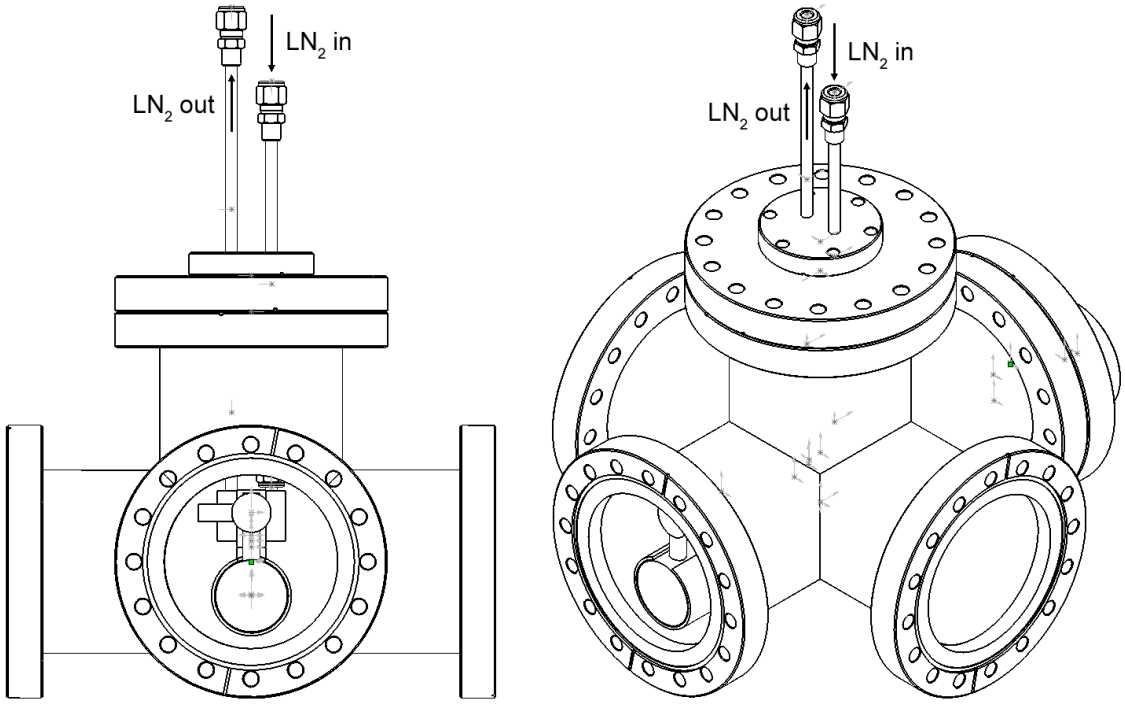

Figure 2.11: **Schematic of conflat chamber used for low-temperature $^{13}C/^{12}C$ KIE experiments.**

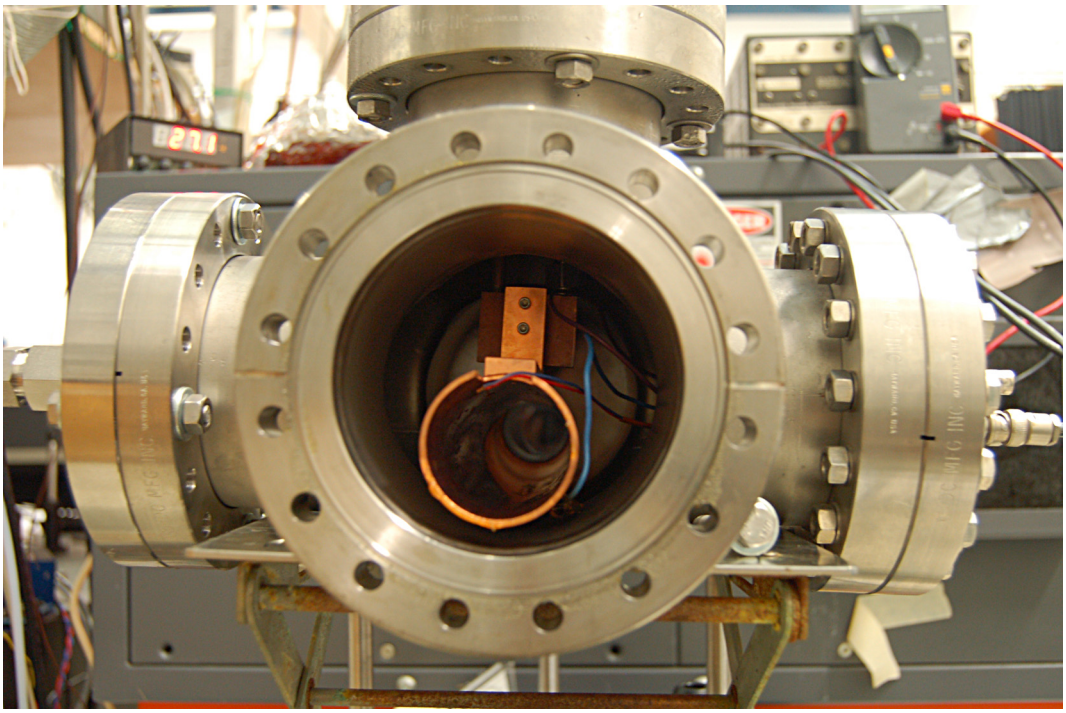

Figure 2.12: **Photograph of conflat chamber used for low-temperature $^{13}C/^{12}C$ KIE experiments.**

chosen over other compounds because of its ability to perform at low temperatures (down to liquid He), low coefficient of thermal expansion ($\leq 10^{-4}$ K^{-1}) and minimal thermal creep. However, it has a very low thermal conductivity (0.1 – 0.2 W m^{-1} K^{-1}), which slowed the cooling process. Typically, the assembly took 40 – 60 min to cool from 300 K to 229 K. While higher-efficiency thermal compounds would have accelerated cooling of the reaction chamber, Apiezon "N" was sufficient to achieve stable temperatures above 200 K.

Small modifications were made to the cooling assembly for planned $O(^1D)$ + CH_4 and OH + CH_4 KIE experiments (see Figure 2.19). Because the target temperatures for those experiments are 140 K $\leq$ T $\leq$ 200 K, the two "heat-transfer" blocks were combined into a single OFHC copper heat-transfer block with a larger contact area with the existing "conduction block" (see Figures 2.20 and 2.21). The primary cooling block was smoothed (the shallow channel removed) to mate well with the new conduction block. Last, metal-to-metal mating surfaces were cleaned and the Apiezon "N" grease replaced with a thermal paste containing silver particles (thermal conductivity $\sim$ 9 W m^{-1} K^{-1}). With this new assembly and the pressurized delivery of liquid N_2 from a free-standing dewar into the feedthrough, the quartz reaction cell was cooled to temperatures of $\sim$140 K within 10 min. Temperature control electronics are currently being designed.

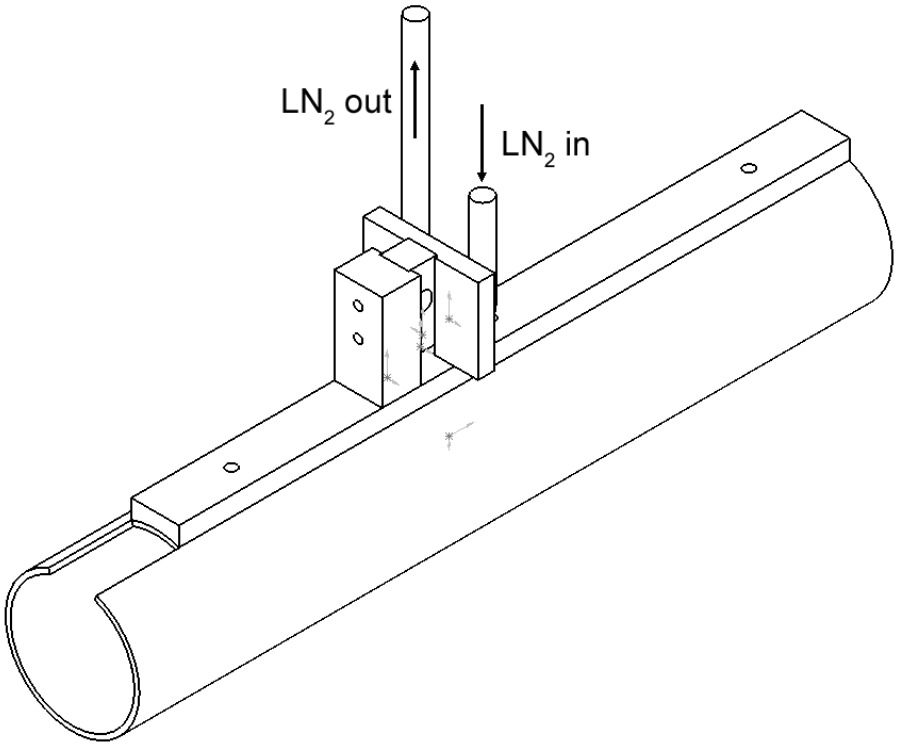

Figure 2.13: **Cold cell assembly.**

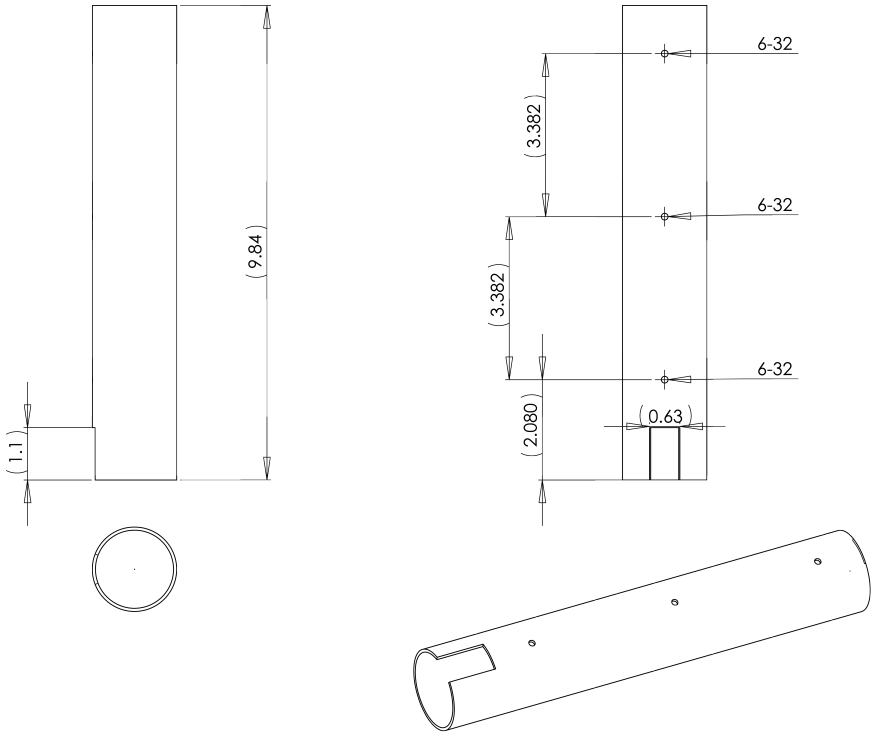

Figure 2.14: **Machining diagram for the OFHC copper tube.**

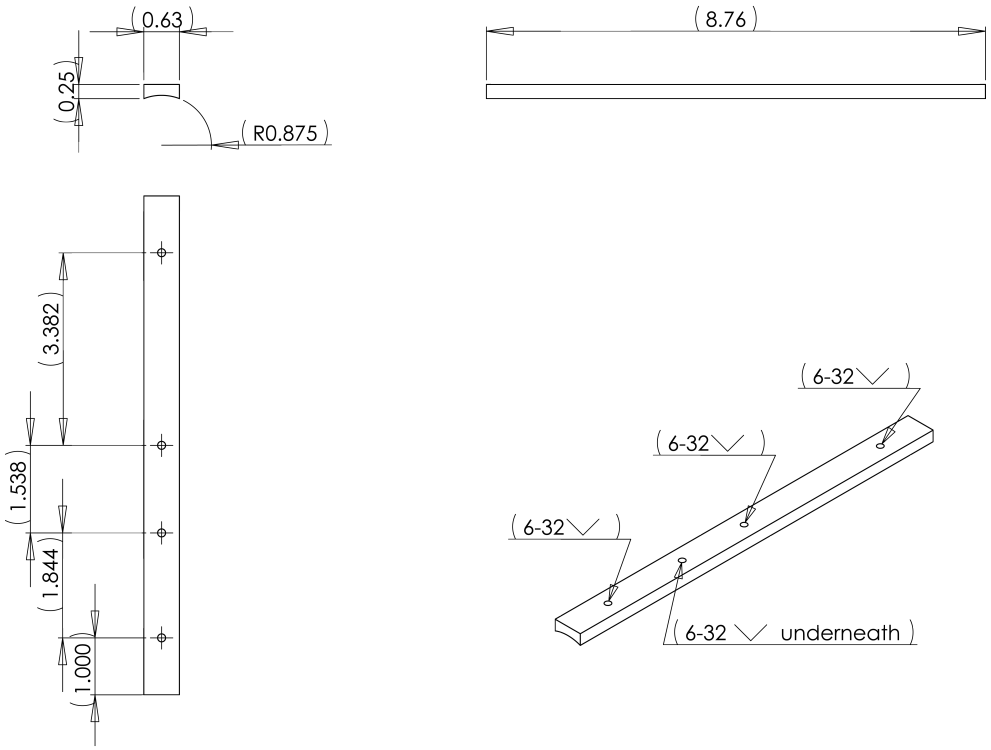

Figure 2.15: **Machining diagram for the OFHC copper conduction block.**

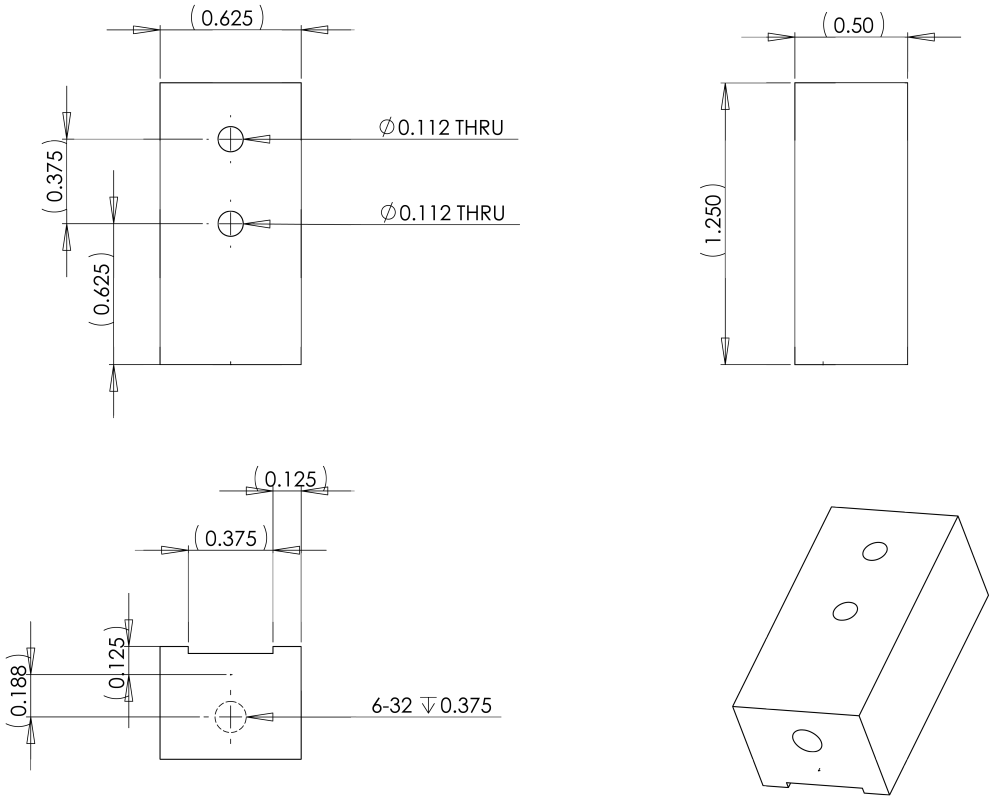

Figure 2.16: **Machining diagram for the OFHC copper heat transfer block.**

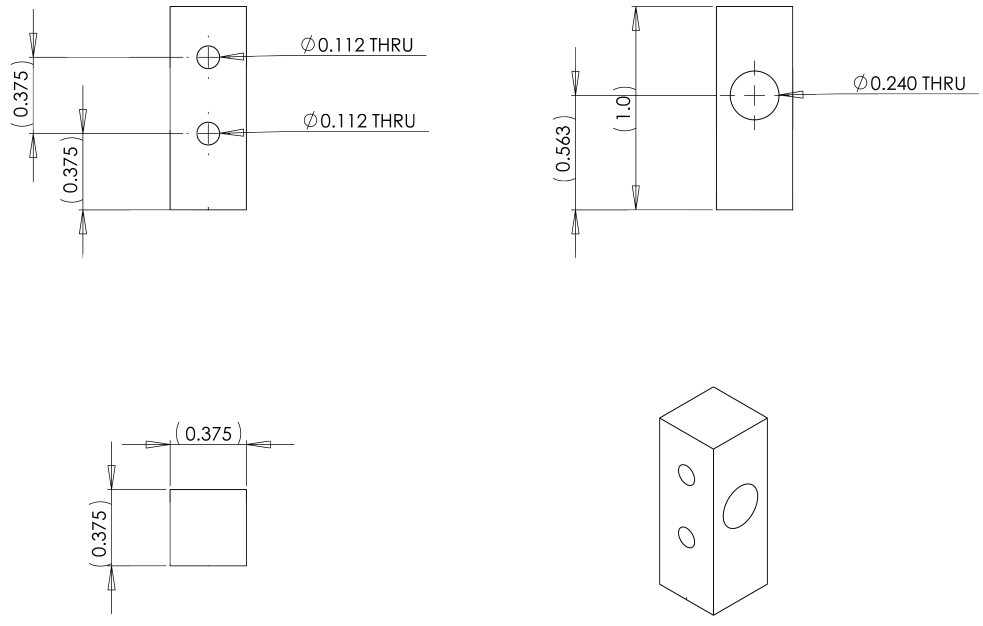

Figure 2.17: **Machining diagram for the brass heat transfer block.**

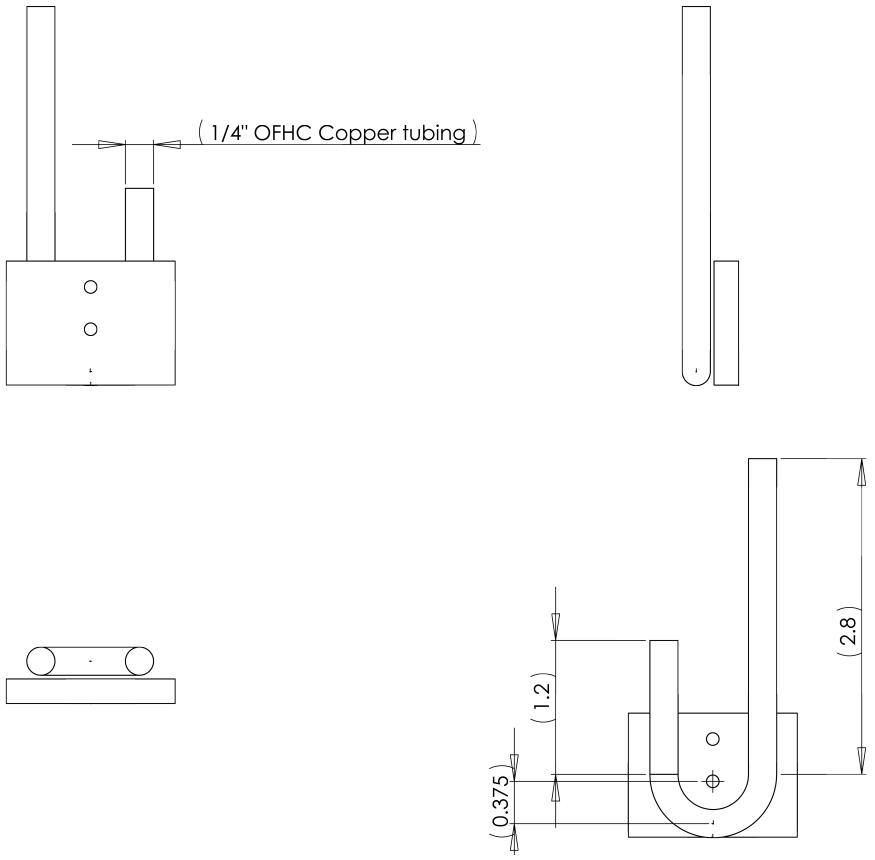

Figure 2.18: **Machining diagram for the OFHC copper connection to the liquid N_2 feedthrough.**

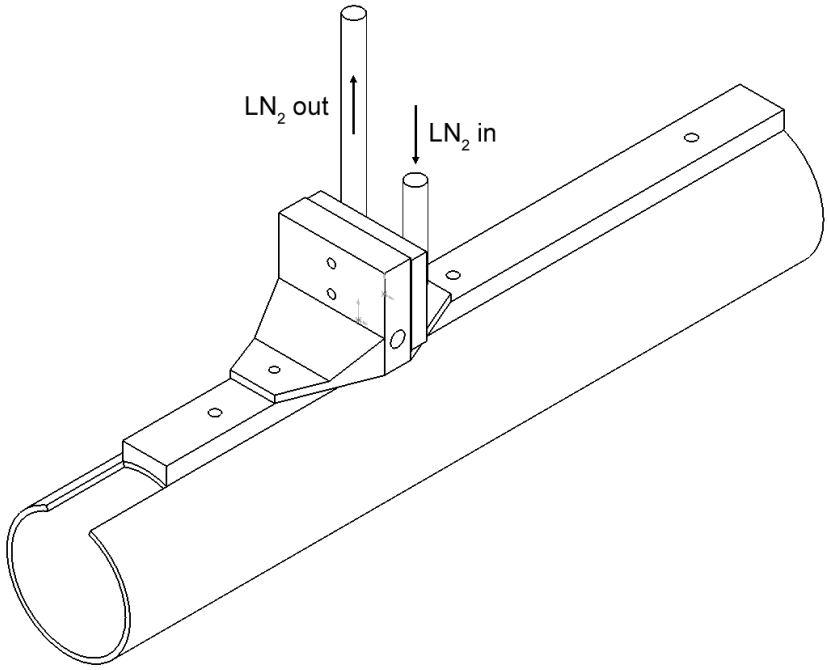

Figure 2.19: **Cold cell assembly for O(^1D), OH + CH_4 KIE experiments.**

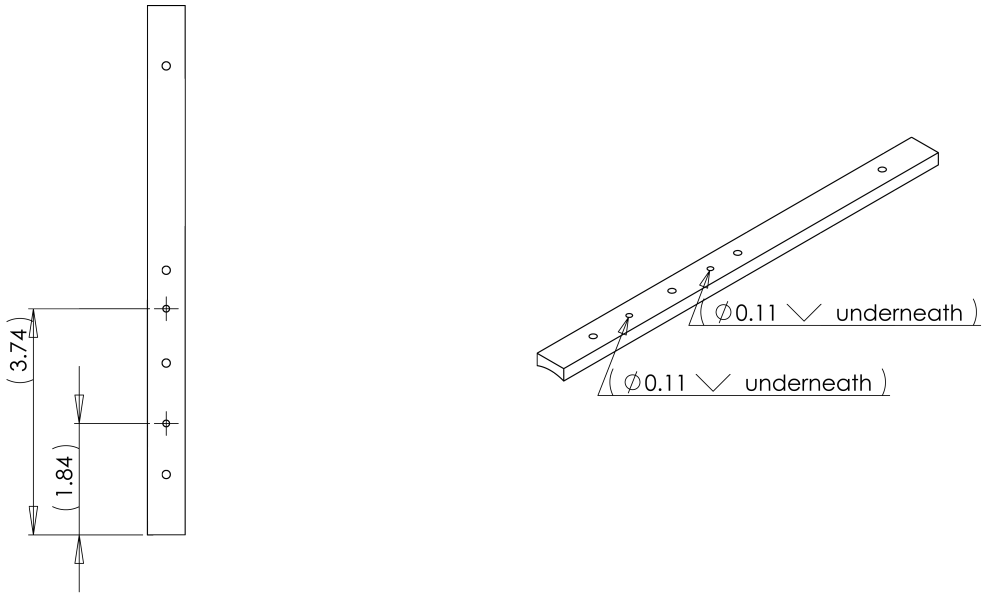

Figure 2.20: **Machining diagram illustrating the modifications made to the conduction block for O(^1D), OH + CH_4 KIE experiments.**

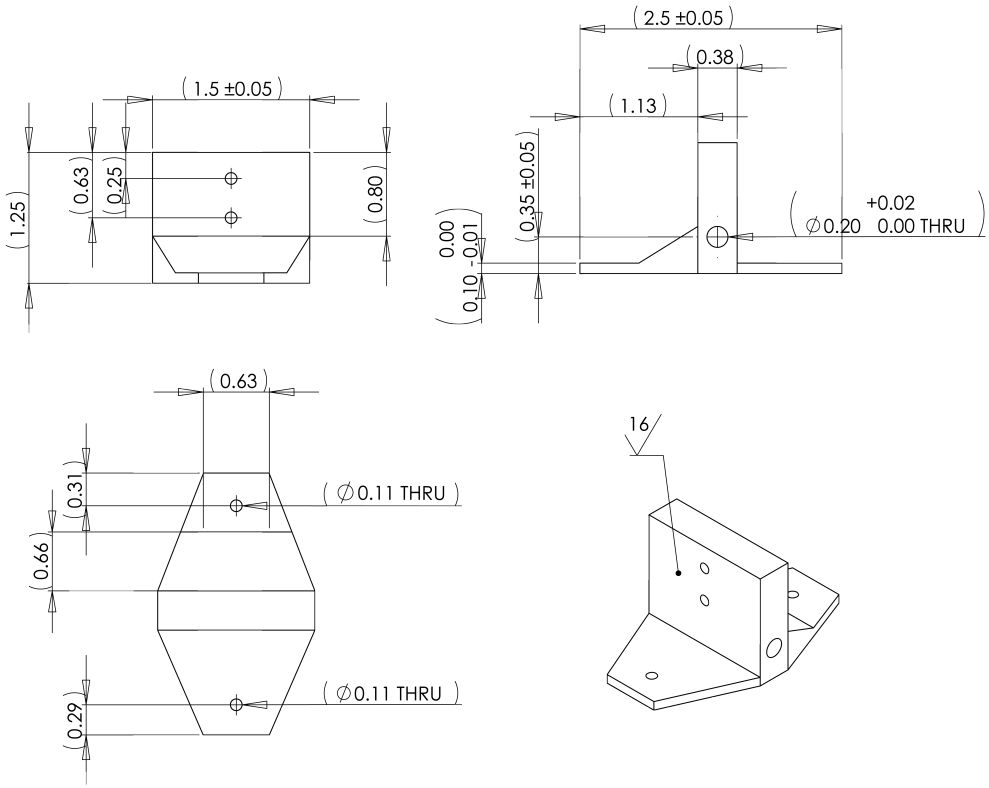

Figure 2.21: **Machining diagram for the OFHC copper heat transfer block designed for O(^1D), OH + CH_4 KIE experiments.**

2.D MATLAB code for hard-sphere collision model

2.D.1 montecarlo.m

```
% Program for calculating 18O(1D)+CO2 collision energy in experiments

clear x y z j v1i v2i r;
points=50000;
% number of points per collision
T=300;
% temperature in K
m1=18;
% mass of O(1D)
m2=4;
% mass of buffer gas (He: 4, N2: 28)
mCO2=44;
ET2lab=18.2; %8.6 for O3 photolysis at 248 nm
% Etrans (kcal/mol) in the Lab frame
Equil=(3/2)*8.314472/4.184/1000*T;
% Equipartition energy
vOpeak=sqrt((ET2lab*1000*4.184*2)/(m1/1000));
% O(1D) atom velocity
vMreduced=vOpeak/sqrt((Equil*1000*4.184*2)/(m2/1000));
% buffer gas velocity in units of O(1D) velocity
%vMreducedCO2=vOpeak/sqrt((Equil*1000*4.18*2)/(mCO2/1000));
ncolltot=200;
% Number of collisions
zz=zeros(points,ncolltot);
% distribution of final O(1D) velocities
zzz=zeros(points,1);
% distribution of initial O(1D) velocities
CO2=zeros(points,ncolltot);
% distribution of collision energies with CO2
dist=zeros(points,ncolltot);
% distribution of buffer gas velocities
PM=97; %1-380e-6 for 'stratospheric'
% pressure of buffer gas in Torr
PCO2=3; %380e-6 for 'stratospheric'
% pressure of CO2 in Torr
Pcoll=PCO2/(PCO2+PM);
% ratio of CO2 to buffer gas (reaction probability per collision)

for l=1:ncolltot
    nPcoll(l)= Pcoll*(1-Pcoll)^(l-1);
    % multiplied by (1-(3.1e-11/1e-10))^(l-1) for 'stratospheric'
    % fraction of O(1D) that reacts at each collision
end
digits(10);
nPcoll=vpa(nPcoll);
for j=1:points
    ncoll=1;
    v1i=randn*exp(-1.5)+vMreduced;
% pick a random v for O(1D) from a gaussian distribution about vMreduced
    zzz(j)=v1i;
% record the velocity in a matrix
```

```
    theta1i=rand*3.14159265359;
% pick a random azimuthal angle between 0 and pi for O(1D)
    phi1i=rand*2*3.14159265359;
% pick a random azimuthal angle between 0 and 2pi for O(1D)
    v2i=randn;%metropolis([v2i,5]);
    theta2i=rand*3.14159265359;
% pick a random azimuthal angle between 0 and pi for M
    phi2i=rand*2*3.14159265359;
% pick a random azimuthal angle between 0 and 2pi for M
    while (phi1i < phi2i)
        phi2i=rand*2*3.14159265359;
% prevents imaginary results in scatter function
    end
    impact=rand^2;
% pick a random (b/bmax) with probability proportional to itself
    omega=rand*3.14159265359;
% pick a random azimuthal angle for b between 0 and pi
    while (ncoll ≤ ncolltot)
% calculate O(1D) trajectory for n collisions
        vrel=sqrt((v1i*sqrt(mCO2/m2))^2+v2i^2-2*v1i*v2i*(sin(theta1i)*
            sin(theta2i)*cos(phi1i-phi2i)+cos(theta1i)*cos(theta2i)));
        % calculating initial relative velocity
        CO2(j,ncoll)=((1/2)*((mCO2*m1/(mCO2+m1))/1000)*(vrel*
            sqrt((Equil*1000*4.184*2)/(mCO2/1000)))^2)/(4.184*1000);
            % calculate initial collision energy w/CO2
        v1f=scatter(m1, m2, v1i, theta1i, phi1i, v2i, theta2i,
            phi2i, impact, omega);
        % calculate final velocity after one more collision
        zz(j,ncoll)=real(v1f);
% record the final velocity
        dist(j,ncoll)=v2i;
% record in initial velocity of M
        v1i=real(v1f);
% reset initial velocity as the final velocity after a collision
        theta1i=rand*3.14159265359;
% pick a new azimuthal angle for O(1D)
        phi1i=rand*2*3.14159265359;
% pick a new polar angle for O(1D)
        v2i=randn;
% pick a new velocity for M
        theta2i=rand*3.14159265359;
% pick a new azimuthal angle for M
        phi2i=rand*2*3.14159265359;
% pick a new polar angle for M
        while (phi1i < phi2i)
% prevents imaginary results in scatter program
            phi2i=rand*2*3.14159265359;
        end
        impact=rand^2;
% pick a new impact parameter (b/bmax)
        omega=rand*3.14159265359;
% pick a new scattering angle
        ncoll=ncoll+1;
% rinse, repeat
    end
end
bins=250;
% number of bins
```

```
upperlimit=25;
% range, 0 — upperlimit
binsvector=zeros(1,upperlimit);
% generating empty histogram bin vector to improve performance
for c=1:bins
    binsvector(1,c)=(upperlimit/bins)*c;
% generating histogram bins
end
[Ppercollision,bin]=histc(CO2,binsvector);
% generating binned histogram matrix of CO2, Ppercollision
for k=1:ncolltot
% each column is reactive probability distribution at that collision
    Ppercollision(:,k)=Ppercollision(:,k)*double(nPcoll(k));
% each column is weighted by the fraction of remaining O(1D) atoms
end
Ecollavg=sum(CO2)/points;
% average collision energy at each collision number
dlmwrite('v1i.csv',zzz);
% write matrix of initial O(1D) velocities to file, v1i.csv
dlmwrite('v1f.csv',zz);
% write matrix of final O(1D) velocities to file, v1f.csv
dlmwrite('Ecollpercollision.csv',CO2);
% write matrix of per—collision collision energies to file
dlmwrite('Ppercollision.csv',Ppercollision);
% write binned histogram matrix of CO2 to file, Ppercollision.csv
```

2.D.2 scatter.m

```
% Function solving the two—particle scattering problem

function v1f=scatter(m1, m2, v1i, theta1i, phi1i, v2i, theta2i, phi2i,
    impact, omega)

vrel=sqrt(v1i^2+v2i^2—2*v1i*v2i*(sin(theta1i)*sin(theta2i)*
    cos(phi1i—phi2i)+cos(theta1i)*cos(theta2i)));
    % relative veocity calculation
v1c=(m2*vrel)/(m1+m2);
% v1 (O(1D)) in the COM frame
v2c=(m1*vrel)/(m1+m2);
% v2 (M) in the COM frame
vcm=sqrt(m1^2*v1i^2+m2^2*v2i^2+2*m1*m2*v1i*v2i*(sin(theta1i)*
    sin(theta2i)*cos(phi1i—phi2i)+cos(theta1i)*cos(theta2i)))/(m1+m2);
    % velocity of the COM
thetacm=acos((m1*v1i*cos(theta1i)+m2*v2i*cos(theta2i))/((m1+m2)*vcm));
% azimuthal angle in the COM frame
phicm=acos((m1*v1i*sin(theta1i)*cos(phi1i)+m2*v2i*sin(theta2i)*
    cos(phi2i))/((m1+m2)*vcm*sin(thetacm)));
    % polar angle in the COM frame
alpha=acos((v1i^2—(vcm^2+v1c^2))/(2*vcm*v1c));
% azimuthal scattering angle in the COM frame
deflect=2*acos(impact);
% polar scattering angle in the COM frame
l=v1c*(cos(deflect)*cos(alpha)—sin(deflect)*sin(alpha)*cos(omega));
v1f=sqrt((vcm+l)^2+v1c^2—l^2);
```

Chapter 3

A hyperthermal O-atom exchange reaction, O_2 + CO_2

Adapted from Yeung, L. Y., M. Okumura, J. T. Paci, G. C. Schatz, J. Zhang, and T. K. Minton (2009), Hyperthermal O-Atom Exchange Reaction O_2 + CO_2 through a CO_4 Intermediate, *J. Am. Chem. Soc.*, *131*(39): 13,940–13,942.

3.1 Abstract

O_2 and CO_2 do not react under ordinary conditions, owing to the thermodynamic stability of CO_2 and the large activation energy required for multiple double-bond cleavage. We present evidence for a gas-phase O-atom exchange reaction between neutral O_2 and CO_2 at elevated collision energies ($\approx$ 160 kcal mol^{-1}) from crossed-molecular-beams experiments. Products were scattered mainly in the forward direction, i.e., in the initial direction of the hyperthermal oxygen beam in the center-of-mass (c.m.) frame, with 16% of the available energy in translation, on average. CCSD(T)/aug-cc-pVTZ calculations demonstrate that isotope exchange can occur on the ground triplet potential energy surface through a short-lived CO_4 intermediate that isomerizes via a symmetric CO_4 transition state containing a bridging oxygen atom. We propose a plausible adiabatic mechanism for this reaction supported by additional spin-density calculations.

3.2 Introduction

O_2 and CO_2 do not react under ordinary conditions. This can be attributed to the large activation energy for multiple double-bond cleavage, as Dixon illustrated in his early experiments in which dry CO–O_2–CO_2 mixtures "did not explode" when subjected to a spark discharge [*Dixon*, 1886]. *Otomo et al.* [2000] later reported a reaction of CO_2 and electronically excited O_2^* when they observed O_3 products after irradiating super- and sub-critical O_2/CO_2 mixtures with UV light. While investigating the isotope exchange reaction

$$^{16}O(^3P) + {}^{12}C{}^{18}O_2 \rightarrow {}^{18}O + {}^{16}O{}^{12}C{}^{18}O \tag{3.1}$$

at hyperthermal collision energies in a crossed-molecular-beams experiment, we found evidence for the gas-phase oxygen isotope exchange reaction

$$^{16}O_2 + {}^{12}C{}^{18}O_2 \rightarrow {}^{18}O{}^{16}O + {}^{16}O{}^{12}C{}^{18}O \tag{3.2}$$

of ground-state reactants at high collision energies ($\sim$160 kcal mol^{-1}). Our observations on the dynamics of this reaction, taken together with *ab initio* calculations of stationary points on the lowest triplet potential energy surface (PES), suggest a plausible adiabatic mechanism for the reaction of O_2 with CO_2 through a CO_4 transition complex.

3.3 Experimental studies

3.3.1 Methods

Crossed-molecular-beam experiments were performed with a hyperthermal oxygen source containing $\sim$87% O(^3P) and $\sim$13% $O_2(^3\Sigma_g^-)$ [*Brunsvold et al.*, 2007, 2008; *Garton et al.*, 2006, 2009]. A diagram of the experimental setup, configured for $^{16}O(^3P)$ + $^{12}C^{18}O_2$ collisions, is shown in Figure 3.1. A pulsed beam of $^{16}O(^3P)$ and $^{16}O_2$ ($^3\Sigma_g^+$; at an unknown vibrational temperature) was generated by laser-induced detonation of $^{16}O_2$ using a high-energy CO_2 TEA laser (6 – 7 J pulse^{-1}) operating at a pulse repetition rate of 2 Hz. Though initially broad in velocity distribution (6 – 9 km s^{-1}), a portion of the overall

beam was velocity-selected for the scattering experiments using a synchronized chopper wheel operating at 300 Hz. This velocity-selected beam was crossed, at a nominal angle of 90°, with a pulsed supersonic expansion of 98% $^{12}C^{18}O_2$ gas (2% $^{16}O^{12}C^{18}O$; Spectra Gas). The molecular beams and scattered products were detected with a rotatable quadrupole mass spectrometer with electron-bombardment ionization [*Brink*, 1966] at 160 eV and a Daly-type ion counter [*Daly*, 1960]. $^{12}C^{18}O_2$ and $^{16}O^{12}C^{18}O$ products were detected at m/z = 48 ($^{12}C^{18}O_2^+$) and 46 ($^{16}O^{12}C^{18}O^+$), respectively, with a rotatable mass spectrometer that collected number density distributions as a function of arrival time, $N(t)$, at a given laboratory angle, Θ, using a multi-channel plate (MCP). Here, Θ is defined as the angle at which the $^{16}O^{12}C^{18}O$ scatters with respect to the direction of the reagent oxygen beam (i.e., Θ = 0°). Time-of-flight (TOF) distributions for $^{16}O(^3P)$, $^{16}O_2$, $^{12}C^{18}O_2$, and $^{16}O^{12}C^{18}O$ were collected over a range of laboratory angles (6° – 54°); at each angle, the TOF distribution for the 33.7-cm distance between the beam interaction region to the ionizer was integrated to give a laboratory angular distribution, $N(\Theta)$. A forward-convolution method was used to derive the center-of-mass (c.m.) translational energy $P(E_T)$ and angular $T(\theta_{c.m.})$ distributions from the laboratory $N(t)$ and $N(\Theta)$ distributions [*Lee*, 1988], where $\theta_{c.m.}$ is the angle at which $^{16}O^{12}C^{18}O$ scatters with respect to the reagent oxygen direction in the c.m. frame. The canonical Newton diagrams used in this analysis are shown in Figure 3.2.

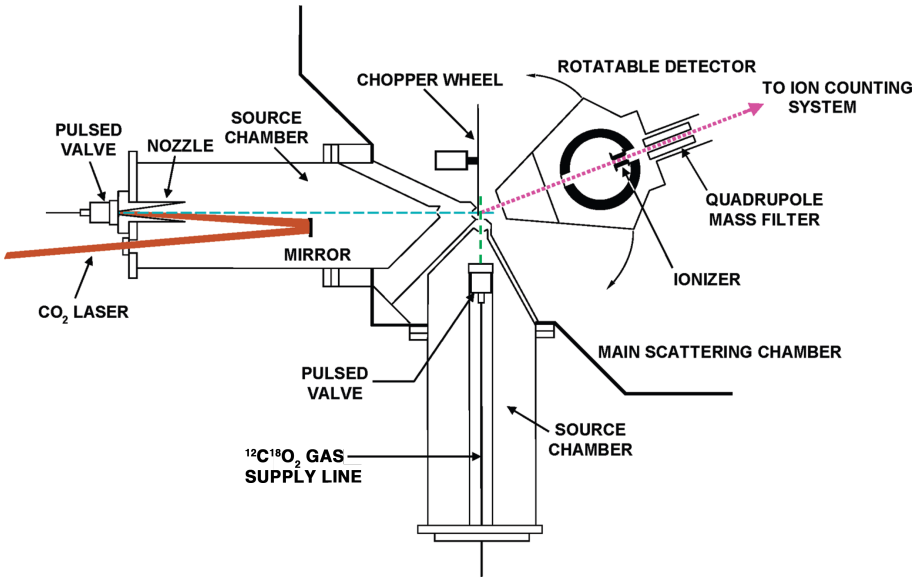

Figure 3.1: **Crossed-molecular-beam apparatus with hyperthermal oxygen source.**

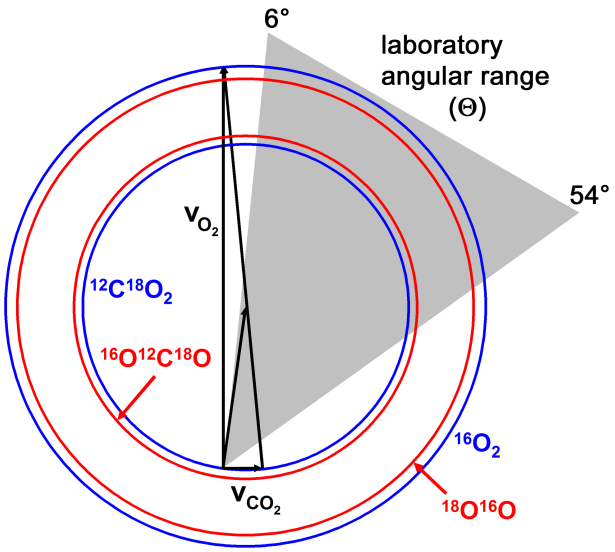

Figure 3.2: **Canonical Newton diagram for hyperthermal $^{16}O_2$ + $^{12}C^{18}O_2$ collisions.** The Newton circles represent the maximum recoil velocities of the products.

The hyperthermal oxygen beam was generated by laser detonation of a pulsed expansion of O_2 gas with 500 psig stagnation pressure using a source based on the design of *Caledonia et al.* [1987]. 174 μs after the pulsed valve is triggered, the CO_2 laser is fired; the laser pulse passed through an antireflection-coated ZnSe window in to the source chamber, whereupon it was reflected back towards the gold-plated, water-cooled copper nozzle with a 1 m radius concave gold mirror. The focused laser pulse initiates a breakdown of the O_2 gas and heats the resulting plasma to $>$ 20,000 K, which accelerates both the atomic and molecular oxygen fractions of the pulsed beam to 6 – 9 km s^{-1}. Use of a conical nozzle allowed for efficient ion-electron recombination and inefficient atom-atom and atom-molecule recombination as the plasma expanded and cooled. The resulting gas pulse was collimated by a 1 cm diameter aperture located 80 cm downstream of the inlet nozzle into a differentially pumped region (10^{-5} – 10^{-6} Torr), after which it passed through a 1.2-mm-diameter skimmer 16 cm further downstream. The beam interaction region was an additional 3 cm downstream in the main chamber (2×10^{-7} Torr), a total distance of 99 cm from the inlet nozzle.

For velocity selection within the hyperthermal oxygen beam, a chopper wheel running at 300 Hz (synchronized with the 2-Hz laser pulses) was placed inside the main scattering

chamber, just downstream of the skimmer. Three equally-spaced slots (1.5 mm wide) of the chopper wheel pass over an LED/photodiode assembly a quarter-turn before each slot enters the beam axis, generating a 900 Hz (3 $\times$ 300 Hz) train of pulses. These chopper wheel pulses are sent to a digital delay generator and used as references for triggering the O_2 gas pulses. The time delay between the chopper wheel pulse and the O_2 pulse determined the portion of the overall hyperthermal oxygen beam allowed to pass through into the interaction region.

We characterized the velocity distribution of the hyperthermal oxygen beam under two conditions: on axis ($\Theta = 0^\circ$) with a small aperture ($\sim$125 μm diameter) to obtain the peak of the distribution, and off axis ($\Theta = 3^\circ$) with a large aperture (4 mm $\times$ 4 mm) to obtain the width of the distribution. For the on-axis configuration, a 2 mA emission current at the ionizer and a –18 kV potential at the secondary emitting electrode of the Daly ion counter was used. For the off-axis configuration, a 10 mA emission current at the ionizer and a –30 kV potential at the secondary emitting electrode was used. Laboratory TOF distributions under both conditions were measured, for both ^{16}O and $^{16}O_2$, to determine the laboratory-frame velocities and translational energy distributions for the hyperthermal oxygen beam. In these experiments, the average velocity of the hyperthermal oxygen beam was thus determined to be 8262 $\pm$ 450 m s^{-1} (i.e., 900 m s^{-1} full width at half maximum; FWHM), which corresponds to average translational energies $\langle E_T \rangle$ = 130.5 $\pm$ 14 kcal mol^{-1} and 261.0 $\pm$ 28 kcal mol^{-1} FWHM for $^{16}O(^3P)$ and $^{16}O_2$, respectively (see Figure 3.3). The relative amounts of atomic ($\sim$87%) and molecular ($\sim$13%) oxygen were determined by integrating the TOF distributions at m/z = 16 ($^{16}O^+$) and 32 ($^{16}O_2{}^+$) at $\Theta = 0^\circ$ and correcting for O_2 fragmentation (11% of the m/z = 32 signal) in the electron-bombardment ionization region.

A pulsed supersonic expansion of $^{12}C^{18}O_2$ was generated using a piezoelectric pulsed general valve with a 1300-Torr stagnation pressure. The expansion passed through a 2 mm diameter skimmer (9.2 cm from the nozzle) into a differential pumping region, and then through a 2.5 mm diameter (2.8 cm downstream of the skimmer) aperture into the main scattering chamber. The distance from this aperture to the interaction region was 1.5 cm.

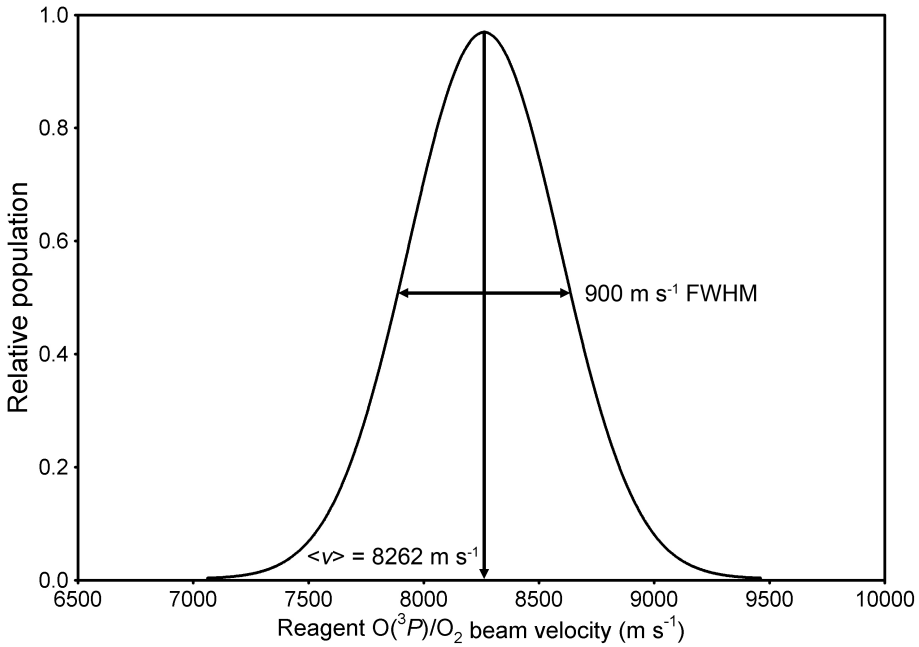

Figure 3.3: **Velocity distribution of hyperthermal oxygen beam.**

The velocity distribution of the $^{12}C^{18}O_2$ beam was not measured directly, and instead was determined iteratively by first estimating the terminal velocity of the supersonic expansion [*Lee*, 1988] and then fitting the $^{12}C^{18}O_2$ velocity to the value that yielded the best Newton circle for non-reactively scattered O-atoms while keeping the measured O-atom velocity distribution fixed at its measured values. This contributes some uncertainty to the measured TOF distributions because the $^{12}C^{18}O_2$ beam velocity is likely only accurate to $\pm$10%. However, because the magnitude of the hyperthermal oxygen beam velocity at the interaction region was ten times that of the $^{12}C^{18}O_2$ beam, and its FWHM was also 4 – 5 times that of the $^{12}C^{18}O_2$ beam, uncertainties in the "time-zero" of the hyperthermal oxygen source dominated the overall uncertainty in the measured translational energy distributions.

Laboratory TOF product distributions were measured every 2° between Θ = 6° – 54°. Scattered product TOF distributions were collected for 200 beam pulses for for m/z = 16 ($^{16}O^+$) and 32 ($^{16}O_2{}^+$), for 1000 beam pulses for m/z = 46 ($^{16}O^{12}C^{18}O^+$), and for 500 beam pulses for m/z = 48 ($^{12}C^{18}O_2{}^+$). Dwell time for each channel at the MCP was 1 μs. At a representative laboratory angle of 10°, integrated count rates were 1.1 $\times$ 10^7 s^{-1} for m/z = 16, 1.3 $\times$ 10^7 s^{-1} for m/z = 32, 1.8 $\times$ 10^5 s^{-1} for m/z = 46 , and 4.2 $\times$ 10^6 s^{-1} for m/z

= 48. Raw flight times were converted to flight times over the 33.7 cm distance between the interaction region and the electron-bombardment ionizer by subtracting the O_2 trigger-pulse-to-laser-fire delay time (174 μs), an electronic-latency delay time (3 μs), the oxygen flight time from the nozzle to the interaction region (120 μs, corresponding to the average velocity of the hyperthermal oxygen beam), and finally the ion flight time between the ionizer and the Daly ion counter. The ion flight time is given by $\alpha(m/z)^{\frac{1}{2}}$, where $\alpha = 2.44$ in these experiments, determined by comparing the relative arrival times of hyperthermal ^{16}O and $^{16}O_2$ at the detector [*Garton et al.*, 2006]. Some uncertainty arises in the product times-of-flight because the exact time- and point-of-origin of the hyperthermal oxygen beam are not well determined; we estimate this uncertainty to be $\sim$2 μs because the laser pulse width in the hyperthermal oxygen source could be as long as 1 μs (a 100 ns-wide peak with a slow tail).

Two signal corrections were made before data analysis. First, we corrected for beam divergence at $\Theta = 6^\circ - 16^\circ$. The divergent intensity with the $^{12}C^{18}O_2$ beam turned off was measured by obtaining TOF distributions at $m/z = 16$ and 32 from $\Theta = 6^\circ - 16^\circ$. These TOF distributions were then scaled and subtracted from the corresponding experimental TOF distributions at $m/z = 16$ and 32 that had the $^{12}C^{18}O_2$ beam turned on. Uncertainties in the inelastic and reactive scattering signals due to collisions of the divergent hyperthermal oxygen could not quantified, however; they were instead considered in the analysis of the laboratory data, where collisions at crossing angles of 88°, 89°, 90°, 91°, and 92° were included during forward-convolution fitting. Adding more crossing angles did not affect the forward-convolution fits significantly. Second, we verified that the $^{12}C^{18}O_2$ beam contained 2% $^{16}O^{12}C^{18}O$ using the instrument's mass spectrometer. Thus, 2% of the inelastic scattering signal ($m/z = 48$) at each laboratory angle ($\Theta = 6^\circ - 54^\circ$) was subtracted from raw $m/z = 46$ ($^{16}O^{12}C^{18}O^+$) TOF distributions to obtain reactive-scattering-only distributions.

A forward-convolution method was employed to perform the laboratory-to-c.m. frame coordinate transformation [*Lee*, 1988] of the data using the MSU XBEAM program (Version 6). Trial $P(E_T)$ and $T(\theta_{c.m.})$ distributions were used to simulate the laboratory-frame TOF distributions using the following relationship derived from the Jacobian transformation:

$$N(t,\Theta)\ \alpha\ \frac{l^3}{ut^3}P(E_{\mathrm{T}})T(\theta_{\mathrm{c.m.}}) \tag{3.3}$$

where l and t are the distance and flight time, respectively, from the interaction region to the ionizer, and u is the product velocity in the c.m. frame. During the fitting process, $^{12}C^{18}O_2$ was assumed to have a single-valued velocity, 800 m s^{-1}, because the large magnitude and width of the hyperthermal oxygen beam velocity distribution is principally responsible (i.e., it contributed $\geq$ 98% of the uncertainty in the c.m. collision energy; see above) for the observed width of the laboratory TOF distributions and the c.m. translational energy distributions. The width of the hyperthermal beam velocity distribution was fit by a Gaussian function centered at 8262 m s^{-1} and a FWHM of 900 m s^{-1}, which was used during data analysis. Note that the data we report for flight times over a 33.7 cm distance were calculated by subtracting the *average* oxygen flight time from the nozzle to the interaction region; the reported product arrival times, then, reflect a convolution of the oxygen beam's wide velocity distribution and the 'true' product translational energy distribution, so the best-fit $P(E_{\mathrm{T}})$ distributions may not be unique. As such, we estimate the uncertainties in the reported $P(E_{\mathrm{T}})$ distribution to be 10 – 20%.

To allow for easy manipulation of the $P(E_{\mathrm{T}})$ and $T(\theta_{\mathrm{c.m.}})$ distributions, parameterized functions were often used. The fitting process often relied on the RRK form of the $P(E_{\mathrm{T}})$ distribution:

$$P(E_{\mathrm{T}})\ =\ (E_{\mathrm{T}}\ -\ B)^p(E_{\mathrm{avail}}\ -\ E_{\mathrm{T}})^q \tag{3.4}$$

where E_{avail} is the available translational energy in the c.m. frame (i.e., the collision energy, E_{coll}, minus the endothermicity, ΔE). The parameters B, p, and q were adjusted to vary the peak and width of the c.m. translational energy distribution when obtaining a best fit to the laboratory data. The $T(\theta_{\mathrm{c.m.}})$ distribution was described by a Legendre polynomial form:

$$T_k(\theta_{\mathrm{c.m.}})\ =\ \frac{a_k}{2^k k!}\frac{c^k(\cos^2\theta_{\mathrm{c.m.}}\ -\ 1)^k}{c(\cos\theta_{\mathrm{c.m.}})} \tag{3.5}$$

where a_k is an adjustable parameter for each of the eleven polynomial terms used, which

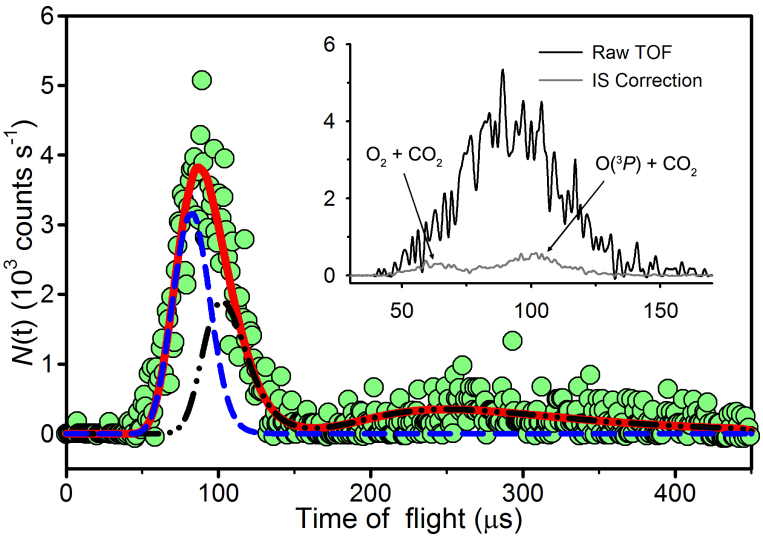

Figure 3.4: **Laboratory TOF distribution of m/z = 46 ($^{16}O^{12}C^{18}O^+$; green circles) at Θ = 6°, with the inelastic scattering signal removed.** The data are shown with the $O(^3P)$ + CO_2 (dot-dashed black line), O_2 + CO_2 (dashed blue line), and summed (solid red line) forward-convolution fits. Flight times less than 72 μs violate energy conservation for $^{16}O(^3P)$ + $^{12}C^{18}O_2$. The inset compares the raw TOF distribution with the IS TOF distribution, which is subtracted.

were denoted by the subscripted k = 0, 1, 2,...10. The functional forms for the $P(E_T)$ and $T(\theta_{c.m.})$ distributions (3.4 and 3.5, respectively), were iterated in XBEAM until they provided satisfactory fits to the laboratory data, though, in some cases, point forms of the $P(E_T)$ and $T(\theta_{c.m.})$ distributions were used. Finally, the "best-fit" $P(E_T)$ and $T(\theta_{c.m.})$ distributions were used to create a c.m. velocity-flux contour map or a differential scattering cross-section plot for the products.

3.3.2 Results

The inset in Figure 3.4 shows a raw m/z = 46 TOF distribution of $^{16}O^{12}C^{18}O$ products recorded at Θ = 6°. A small fraction of the signal can be attributed to inelastic scattering (IS) of $^{16}O^{12}C^{18}O$ impurities in the CO_2 beam by ^{16}O and $^{16}O_2$, and it can be subtracted. The remaining signal, shown in Figure 3.4, represents $^{16}O^{12}C^{18}O$ products from O-atom exchange reactions of $^{12}C^{18}O_2$ (see Chapter 4).

We initially expected the reactive m/z = 46 signal to arise from reactions of $^{12}C^{18}O_2$ with the ^{16}O atoms (reaction 3.1) with a broad distribution of c.m. collision energies (E_{coll})

peaked at 98.8 kcal mol^{-1} and a full width at half maximum (FWHM) of 18 kcal mol^{-1}. However, at small laboratory angles, we observed products with velocities that would violate energy conservation for this O(^3P) + CO_2 reaction (e.g., t $<$ 72 μs in Figure 3.4). $^{12}C^{18}O_2$ was estimated to have a laboratory velocity of 800 $\pm$ 80 m s^{-1} (see *Lee* [1988]). Given the broad velocity distribution in the O(^3P)/O_2 beam (8262 m s^{-1} with 900 m s^{-1} FWHM), the velocity spread in the $^{12}C^{18}O_2$ beam was insignificant by comparison, so the hyperthermal oxygen beam largely determined the broad distribution of collision energies sampled in these experiments. To calculate the maximum available translational energy in the laboratory frame for ^{16}O(^3P) + $^{12}C^{18}O_2$ and $^{16}O_2$ + $^{12}C^{18}O_2$ isotope exchange reactions, an initial ^{16}O(^3P)/$^{16}O_2$ beam velocity of 8862 m s^{-1} was used because $<$ 5% of the O(^3P)/O_2 beam had a greater velocity. A non-negligible population of $^{16}O^{12}C^{18}O$ was observed at translational energies above the maximum allowed for ^{16}O(^3P) + $^{12}C^{18}O_2$ collisions at small laboratory angles.

Despite the uncertainties in the E_{coll} distribution and product flight times (see Section 3.3.1), we observed $^{16}O^{12}C^{18}O$ products arrive 10 – 20 μs faster than the minimum times allowed by the distribution of available energies, E_{avail} ($\approx E_{coll}$; the zero-point energy change is +0.1 kcal mol^{-1}), for reaction 3.1. Forward-convolution best-fits to the TOF distributions that only treat the ^{16}O(^3P) + $^{12}C^{18}O_2$ isotope exchange reaction cannot explain the fastest laboratory data at small laboratory angles (e.g., $\Theta = 6^\circ$ and 8°; see Figure 3.5). Increasing $\langle E_T \rangle$ in the product $P(E_T)$ shifts the fastest part of the fit towards shorter flight times at all laboratory angles. While this improves the TOF fits at small laboratory angles, it decreases the quality of the TOF fits at larger laboratory angles (see $\Theta = 36^\circ$ in Figure 3.6). Introducing the $^{16}O_2$ + $^{12}C^{18}O_2$ isotope exchange reaction yields good fits at all laboratory angles. A sizeable fraction of the products assigned to the $^{16}O_2$ + $^{12}C^{18}O_2$ reaction are slow enough that they do not violate conservation of energy; however, assigning them to the ^{16}O(^3P) + $^{12}C^{18}O_2$ reaction leads to poor fits. Collisions between CO_2 and ions or electronically excited O atoms could also yield $^{16}O^{12}C^{18}O$ products with elevated velocities, previous experience with this hyperthermal source indicates that they are not present in the beam [*Troya et al.*, 2004].

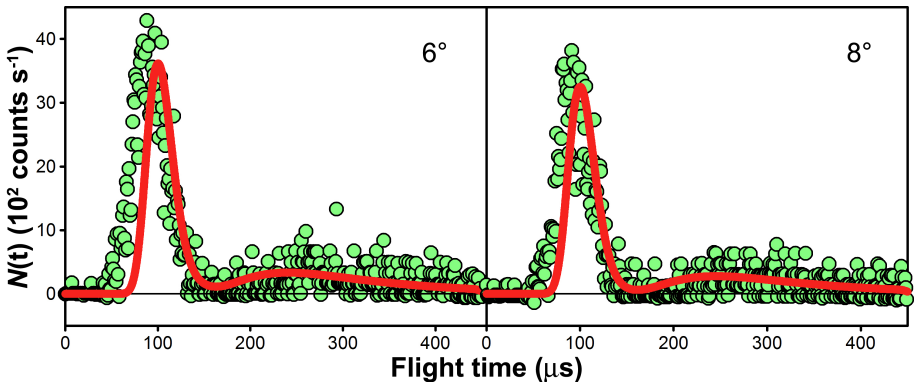

Figure 3.5: **TOF distributions (green dots) for $^{16}O^{12}C^{18}O$ products at laboratory angles $\Theta = 6^\circ$ and 8° with the inelastic scattering signal removed.** Also shown are forward-convolution best fits (solid red line) that treat only one isotope exchange reaction, $^{16}O(^3P)$ + $^{12}C^{18}O_2$ → O + $^{12}C^{18}O_2$. The forward-convolution fits cannot account for the fastest $^{16}O^{12}C^{18}O$ product signals at small laboratory angles.

We therefore hypothesize that the fast $^{16}O^{12}C^{18}O$ products come from reaction of $^{12}C^{18}O_2$ with $^{16}O_2$ in the hyperthermal beam. Because the velocity-selected $^{16}O_2$ molecules have the same laboratory-frame velocity distribution as the ^{16}O atoms, the $^{16}O_2$ molecules collide with the $^{12}C^{18}O_2$ molecules at substantially higher c.m. energies (see Newton diagram in Figure 3.2). The resulting collision energy distribution peaked at E_{coll} = 158 kcal mol^{-1} with FWHM = 28 kcal mol^{-1}. Thus, $^{16}O^{12}C^{18}O$ products from reaction 3.2 have sufficient E_{avail} to account for the fastest products detected. The m/z = 46 signal would then contain products of both reactions 3.1 and 3.2, the fastest products arising exclusively from reaction 3.2.

$P(E_T)$ and $T(\theta_{c.m.})$ distributions for reactions 3.1 and 3.2 were simultaneously obtained from forward-convolution fits of the m/z = 46 TOF distributions. The results for the $^{16}O_2$ + $^{12}C^{18}O_2$ reaction are presented in Figure 3.7; a c.m. velocity-flux contour diagram of $^{16}O^{12}C^{18}O$ products is shown in Figure 3.8, in which the observed product flux is peaked in the forward direction. The presence of signal at flight times violating energy conservation for $^{16}O(^3P)$–$^{12}C^{18}O_2$ collisions was used to guide the fitting process because the TOF distributions do not resolve the products unambiguously. As such, we cannot rule out an additional dynamical channel in reaction 3.1 contributing to some of the signal we attribute to reaction 3.2 because energy conservation in reaction 3.1 is only violated at small lab angles.

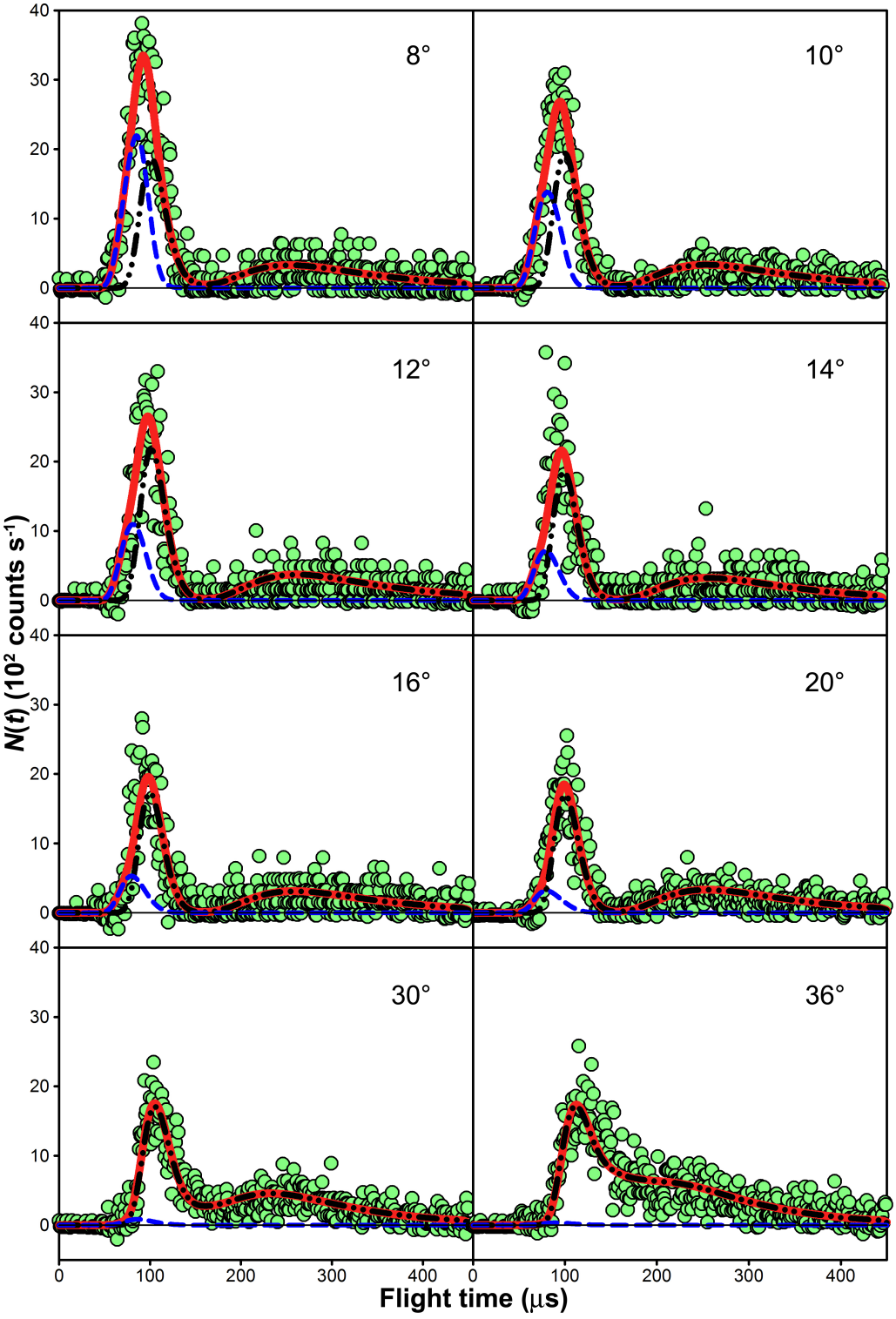

Figure 3.6: **TOF distributions for $^{16}O^{12}C^{18}O$ (m/z = 46) at various laboratory angles Θ with the inelastic scattering signal removed.** The raw data are shown as circles. Forward-convolution fits of the $^{16}O_2$ + $^{12}C^{18}O_2$ (blue dashed curve) and $^{16}O(^3P)$ + $^{12}C^{18}O_2$ (black dot-dashed dashed curve) channels, along with their sum (red solid curve), are also shown.

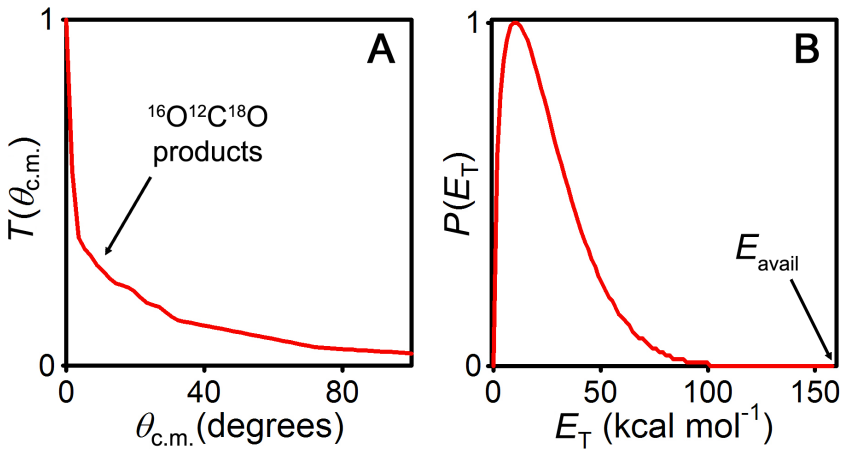

Figure 3.7: **Center-of-mass-frame (A) angular and (B) translational energy distributions from the $^{16}O_2$ + $^{12}C^{18}O_2$ oxygen isotope exchange reaction obtained from TOF fits of m/z = 46.** The peak of the distribution of available energies is E_{avail} = 158 kcal mol^{-1}. Only the experimentally accessible range of c.m. angles ($\theta_{c.m.} < 100°$) is shown.

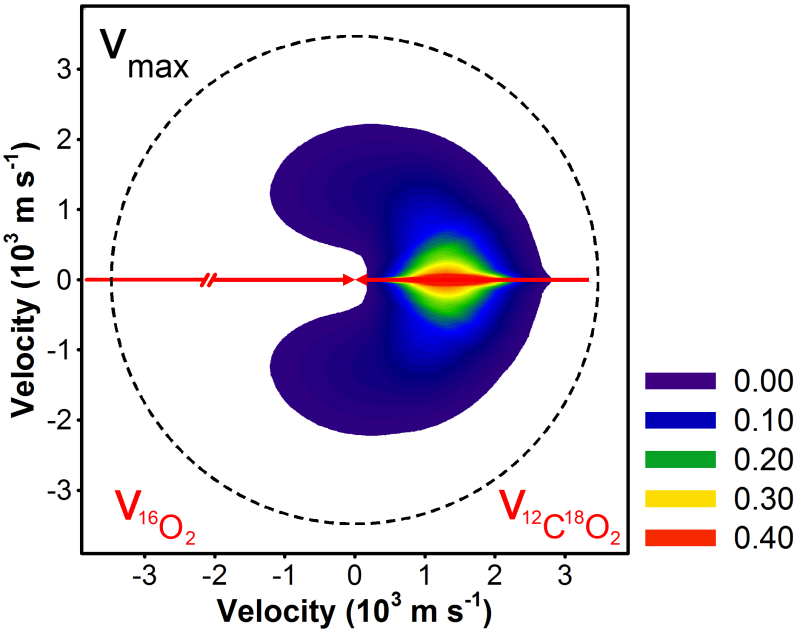

Figure 3.8: **Velocity-flux contour diagram for $^{16}O^{12}C^{18}O$ products of $^{16}O_2$ + $^{12}C^{18}O_2$ collisions in the center-of-mass frame.** The white arrows are the initial $^{16}O_2$ and $^{12}C^{18}O_2$ velocity vectors, and dashed white line is the maximum recoil velocity for $^{16}O^{12}C^{18}O$ (v_{max}). $^{16}O^{12}C^{18}O$ products are scattered opposite the initial direction of the $^{12}C^{18}O_2$ velocity vector.

The $^{16}O^{12}C^{18}O$ products scattered mainly in the forward direction ($\theta_{c.m.} = 0^\circ$), though there was significant sideways scattering. Experimental sensitivity in the backward direction was insufficient to detect backward-scattered $^{16}O^{12}C^{18}O$ products, so forward-backward symmetric scattering (i.e., evidence for a long-lived intermediate complex) could not be ruled out. At these collision energies, however, an intermediate is unlikely to survive for a rotational period. The average total translational energy distribution for the two products was 25 kcal mol^{-1}, or 16% of the available energy; the $P(E_T)$ distribution was peaked at E_T = 10 kcal mol^{-1}. We estimate the yield for reaction 3.2 to be $\leq$ 2% of all O_2–CO_2 collisions. This estimate is an upper limit because the complete Newton circle for inelastically scattered $^{16}O_2$ + $^{12}C^{18}O_2$ products was not observed in these experiments. Vibrational excitation of the O_2 may also be important in promoting reaction, but the vibrational temperature of O_2 present in the expanded plasma is unknown.

Our experimental results are consistent with a $^{16}O^{12}C^{18}O$ product that rebounds from the $^{12}C^{18}O_2$ reactant's initial direction after it collides with O_2; this mechanism is characteristic of reactions with substantial activation energies that require high collision energies. The highly peaked angular distribution is consistent with a direct mechanism or a very short-lived intermediate, but more surprising is the substantial internal energy of the products, which is much greater than that found for similar oxygen isotope exchange reactions between O(^3P) + CO, O(^1D) + CO_2, and O + O_2 [*Brunsvold et al.*, 2008; *Perri et al.*, 2004; *Van Wyngarden et al.*, 2007]. This large translational-to-internal energy conversion suggests that the reaction proceeds through an intermediate species that facilitates efficient translational-to-internal energy transfer or through a non-adiabatic transition to another electronic surface.

On average, 134 kcal mol^{-1} of internal energy is available to both products. This excess energy could be distributed among the five vibrational and four rotational degrees of freedom in O_2 and CO_2. Alternatively, this energy could be in the form of electronically excited products, including the $a^1\Delta_g$, $b^1\Sigma_g^+$, and $A^3\Sigma_u^+$ states of O_2, and the a^3A'' state of CO_2, which lies 119 kcal mol^{-1} above that for $CO_2(^1\Sigma_g^+)$ [*Braunstein and Duff*, 2000]. The mass-spectrometric detection, however, did not allow us to determine the electronic states

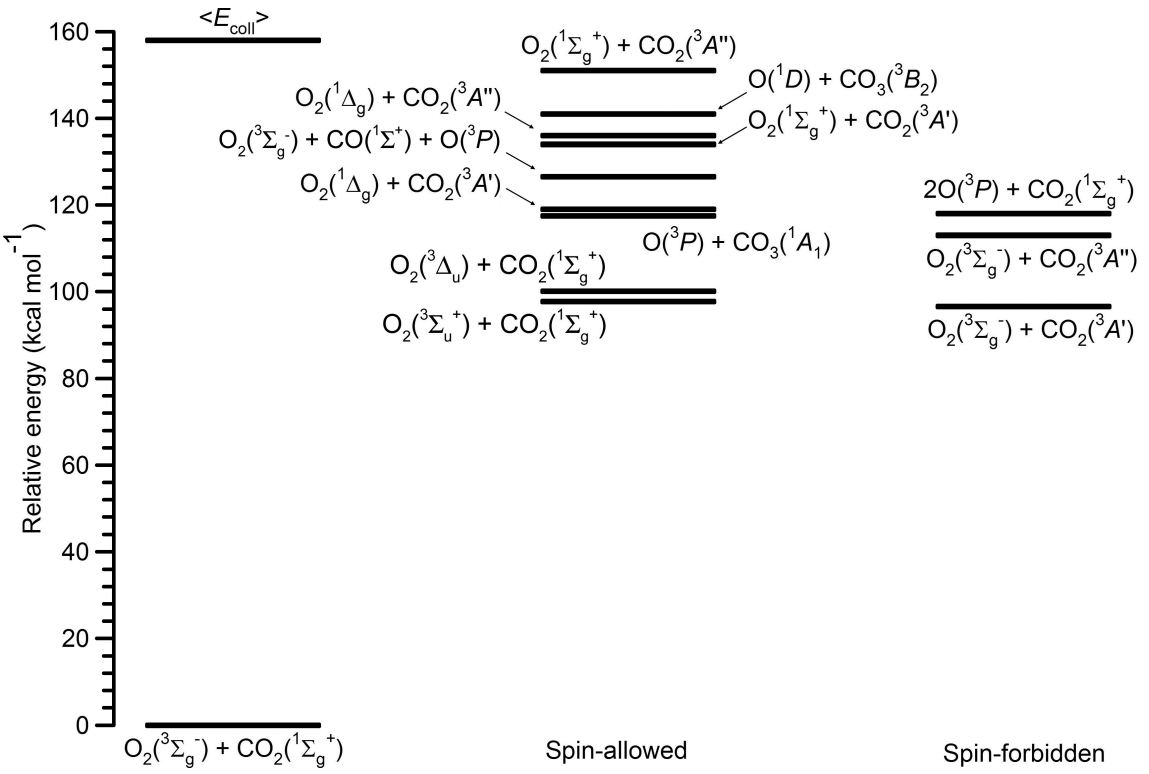

Figure 3.9: **Energetically allowed neutral product channels from O_2 + CO_2 collisions.** Energies are taken from the NIST Webbook [http://webbook.nist.gov], [*Mebel et al.*, 2004], and [*Braunstein and Duff*, 2000].

of the products.

Other reaction channels are possible (see Figure 3.9). We cannot rule out a CO_2 + O + O product channel because we did not collect sufficient data on the counter-fragment $^{18}O^{16}O$. However, the energetically allowed CO_2 + O(^3P) + O(^3P) channel (ΔH = 118 kcal mol^{-1}) is spin-forbidden, and spin conservation would instead favor O(^1D) + O(^3P) products, whose energetic threshold is 163 kcal mol^{-1} and above the average E_{avail} in the experiment. There is also sufficient energy to form O_3 + CO or O + CO_3 [*Mebel et al.*, 2004], and to dissociate CO_2 to form O_2 + O + CO, but because we were not anticipating these reactions, we did not search for the relevant detectable products.

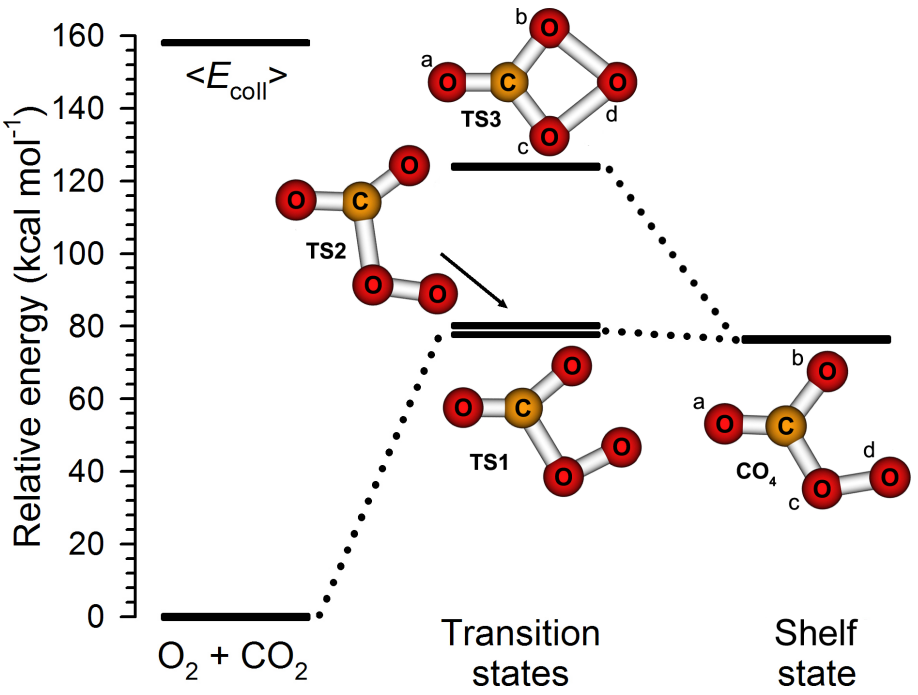

Figure 3.10: **Calculated energies and structures on the lowest triplet PES of O_2 + CO_2.** TS3 connects isoenergetic isomers of the CO_4 shelf.

3.4 Theoretical studies

To investigate whether an adiabatic mechanism exists for the O_2–CO_2 isotope exchange reaction, we performed *ab initio* calculations to find stationary points on the lowest triplet PES for O_2 + CO_2 reaction at the CCSD(T)/aug-cc-pVTZ level of theory using the MOLPRO electronic structure code [*Werner et al.*, 2006]. We identified two transition states (TS1 and TS2) connecting O_2 + CO_2 reactants with a triplet shelf state [$CO_4(^3A'')$; see Figure 3.10 and Table 3.1]. All three structures are planar. One atom of the oxygen molecule approaches the carbon atom of CO_2 and surmounts an activation barrier of 77.9 kcal mol^{-1} over TS1 to form a weak C–O bond and a $CO_4(^3A'')$ shelf (76.4 kcal mol^{-1}, just 1.5 kcal mol^{-1} below TS1) similar to a weakly bound CO_4 complex found at the B3LYP level of theory [*Cacace et al.*, 2003; *Elliott and Boldyrev*, 2005]. At 121.8 kcal mol^{-1}, we identified an effective transition state for $CO_4(^3A'')$ isomerization, TS3, containing a four-membered ring between the carbon atom and three oxygen atoms. A grid-based search revealed that TS3 is bound by 0.02 kcal mol^{-1} when zero-point energy is not considered, and that TS3

Table 3.1: Energies of stationary points associated with the exchange reaction $O_2 + CO_2 \rightarrow O_2 + CO_2$ on the lowest triplet potential energy surface*

	CO_4	TS1	TS2	TS3
$C_{HF}^{\dagger}$	0.973	0.977	0.969	0.945
ΔE [CCSD(T)/aug-cc-pVTZ]	76.0	77.9	80.0	120.9
$\Delta E_{ZPE}^{\ddagger}$ [CCSD(T)/aug-cc-pVTZ]	76.4	77.9	78.3	121.8
ΔE (CASPT2/cc-pVTZ)	91.2	95.6	97.1	137.4

*ΔE in kcal mol^{-1}.

†Coefficient of the Hartree-Fock configuration in the (8,10)-CASSCF expansion of the wave-functions.

‡ZPE-corrected. This calculation was not performed at the CASPT2 level of theory.

is connected to CO_4; a displacement in $O_d < 0.01$ Å towards CO_4 produced CO_4 upon geometry optimization. Thus, it acts as an 'effective' transition state for CO_4 isomerization; it resembles the bound $CO_4(^1A_1)$ structure lying 52.5 kcal mol^{-1} below it, although with a longer O_c–O_d bond length; both structures have C_{2v} symmetry [*Cacace et al.*, 2003; *Elliott and Boldyrev*, 2005; *Jamieson et al.*, 2007].

We observed some evidence for multi-reference character in CO_4. An additional bound state was found 0.8 kcal mol^{-1} above the energy of CO_4 at the MP2/cc-pVTZ level of theory, although it does not exist at the CCSD(T)/aug-cc-pVTZ level; the species is believed to be a resonance structure of $CO_4(^3A'')$. A spin contamination of $\langle S^2 - S_z^2 - S_z \rangle = 0.011$ in the region of the PES near TS3 also suggests some multi-reference character. Thus, CASPT2/cc-pVTZ calculations, which represent resonance qualitatively correctly and do not suffer from spin contamination, were performed to validate the CCSD(T) structures and energies. $CO_4(^3A'')$ was confirmed as a resonance hybrid of two bound-state structures, although the contribution from the single-reference structure to the resonance hybrid dominates the final geometry. The results of those calculations are summarized in Table 3.1 and Figure 3.11.

The uncertainty in the CCSD(T)/aug-cc-pVTZ energies is unknown, although a similar study in which the stationary points of the closely related $O(^3P) + CO_2$ system were characterized was recently completed (see Chapter 4). In addition to CCSD(T)/aug-cc-pVTZ simulations, W4 calculations (close to the full configuration-interaction and infinite-basis-set

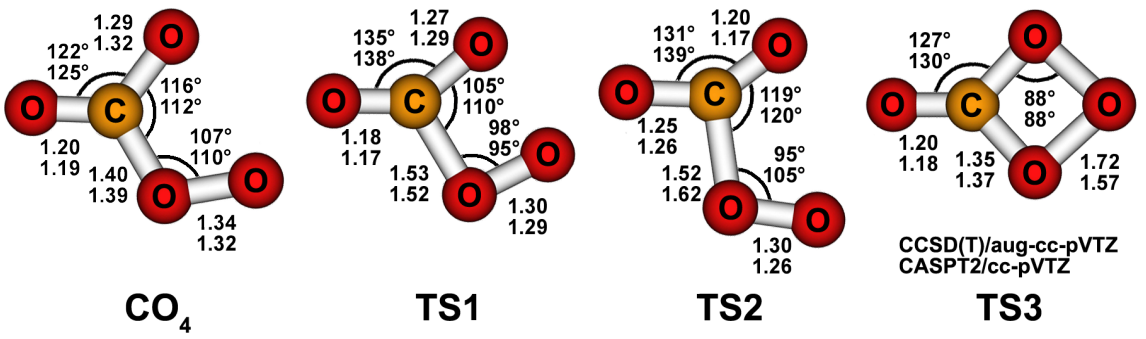

Figure 3.11: **Calculated stationary point geometries on the lowest triplet PES of CO_4.** CCSD(T)/aug-cc-pVTZ values (upper) and CASPT2/cc-pVTZ (lower) values are shown.

limits; see [*Karton et al.*, 2006]) were also performed, as they were found to be affordable, albeit marginally. The differences between the CCSD(T) and W4 results for the transition and bound states indicated a mean-unsigned error of 2.2 kcal mol^{-1}. We expect the errors in the analogous O_2 + CO_2 energies to be approximately the same.

3.5 Proposed mechanism

A possible pathway for oxygen isotope exchange occurs through the forward and reverse directions of the following three steps: O_2 + CO_2 → $[CO_4]^{‡}$ (TS1/TS2) → $CO_4(^3A'')$ → $[CO_4]^{‡}$ (TS3); see Figure 3.12. Spin-density maps (Figure 3.13) depicting the singly-occupied molecular orbitals (SOMOs) for CO_4 and TS3 are consistent with this mechanism. $CO_4(^3A'')$ is a diradical with unpaired electron density concentrated in *p*-type orbitals of the

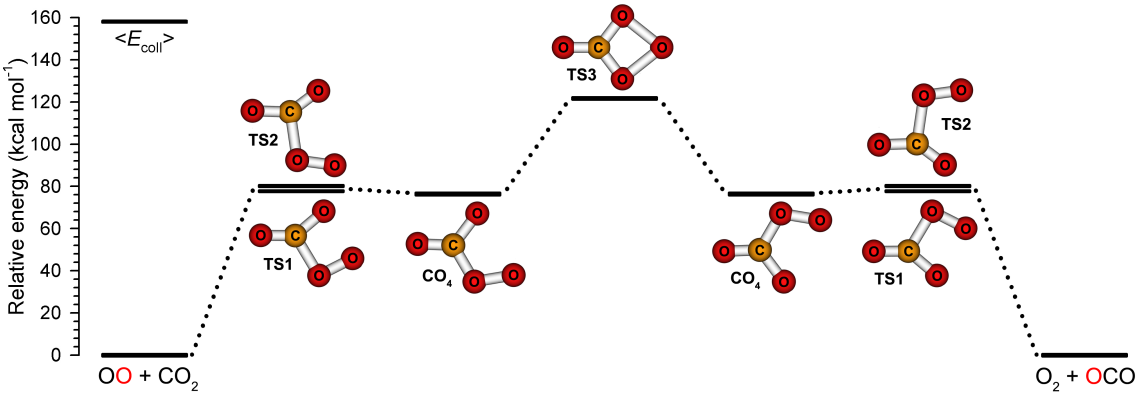

Figure 3.12: **Calculated energies and structures on the lowest triplet PES of O_2 + CO_2.** TS3 connects isoenergetic isomers of the CO_4 shelf.

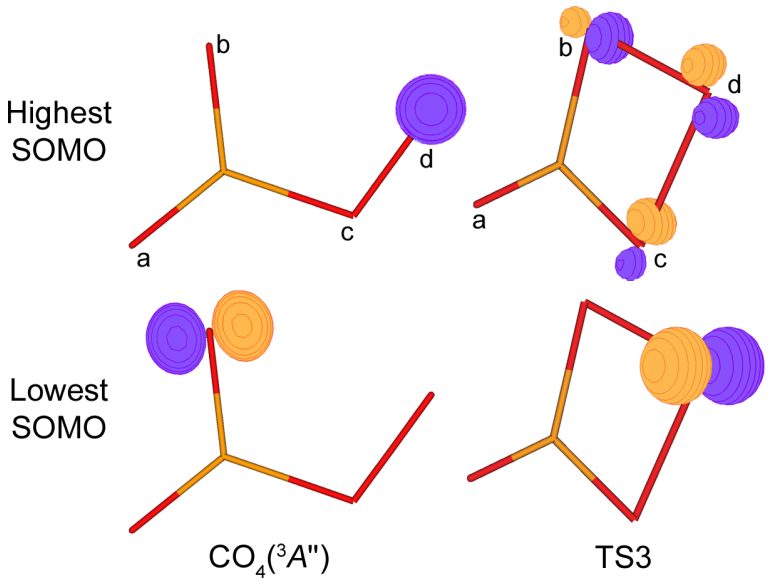

Figure 3.13: **Singly-occupied molecular orbitals (SOMOs) in the $CO_4(^3A'')$ and TS3 structures.** Surfaces containing 70% of the electron density are shown. Note that the highest SOMO of $CO_4(^3A'')$ and the lowest SOMO of TS3 have electron density primarily on O_d, suggesting the SOMO is a spectator during isomerization.

single-bonded oxygens, O_b and O_d. This spin density is consistent with the radical character expected for an association of the O_2 diradical with the carbon atom of CO_2, because the unpaired electrons in O_2 are in orthogonal π_g^* orbitals: As one C–O bond is formed between the in-plane π_g^* orbital of O_2 and the in-plane π_u^b orbital of CO_2 (the higher-energy π_g^{nb} orbital does not interact due to symmetry; see Figure 3.14), the out-of-plane π_g^* orbital on O_2 is a relative spectator to the O_2 radical addition. This interaction, along with the bending of the CO_2, produces the SOMOs for $CO_4(^3A'')$ shown in Figure 3.13. In TS3, the lowest SOMO contains localized electron density on O_d in an out-of-plane *p*-type orbital, suggesting that the unpaired electron on O_d continues to be a spectator during $CO_4(^3A'')$ isomerization. The highest SOMO, however, contains delocalized electron density, of anti-bonding (σ^*) character, in the plane of the molecule. This σ^* character may be interpreted as electron density taken from the lowest SOMO in $CO_4(^3A'')$ while being localized onto O_c during isomerization.

These theoretical results imply that an adiabatic mechanism exists for the oxygen isotope exchange reaction between O_2 and CO_2. During the isomerization of $CO_4(^3A'')$, the O_c–O_d σ-bond is cleaved homolytically (Figure 3.15): One electron moves to a *p*-type orbital on

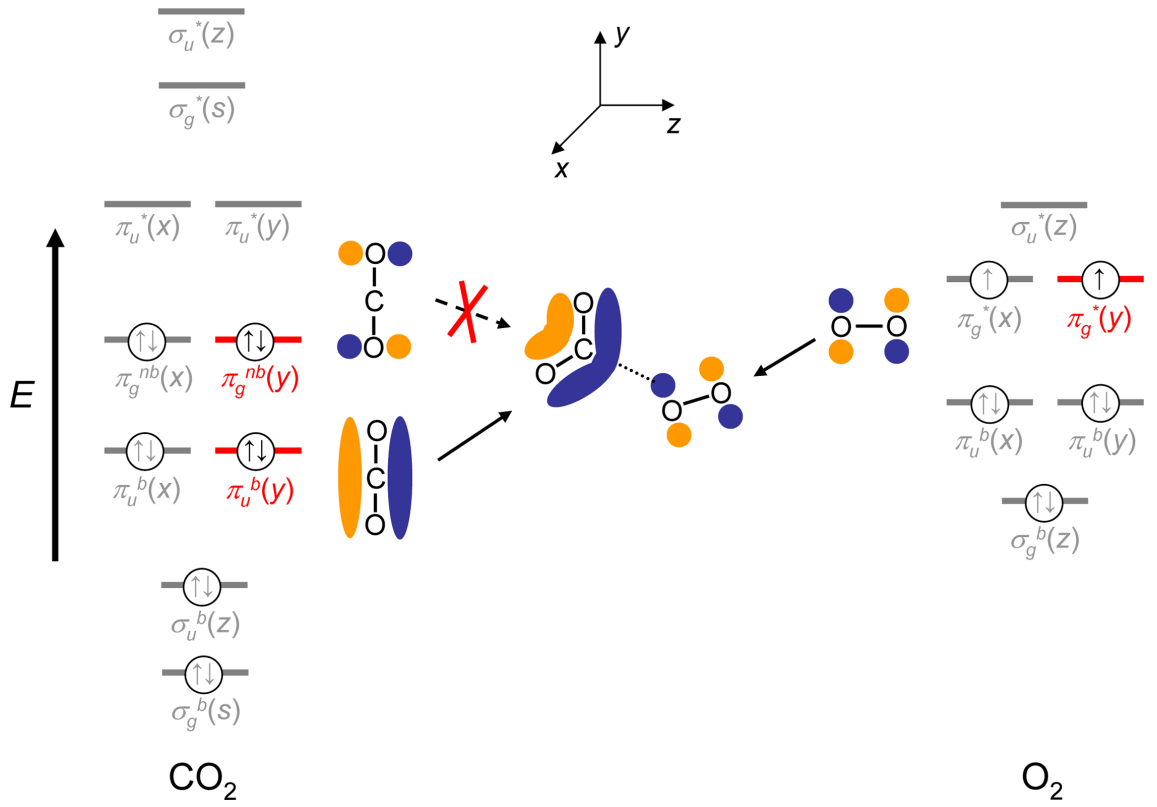

Figure 3.14: **Molecular orbital diagrams for O_2 and CO_2, adapted from *DeKock and Gray* [1980].** Sketches of the highlighted orbitals are shown. As O_2 collides with CO_2, it becomes stretched. In addition, CO_2 bends, increasing the energy of its doubly occupied, in-plane π-orbitals, π_u^b and π_g^{nb}. A weak interaction between the π_g^* orbital on O_2 and the π_u^b orbital on CO_2 is likely responsible for the small (1.5 kcal mol^{-1}) binding energy of CO_4. The π_g^{nb} orbital does not interact, to first approximation, due to symmetry.

O_c, while the other electron forms a bond with the unpaired electron on O_b. This pathway can account for the σ^* character of the highest-energy SOMO in TS3 (the O_b–O_d bond takes an electron from the O_c–O_d bond), and it preserves radical character on O_d. Thus, the $^3A''$ symmetry is preserved throughout the association, isomerization, and dissociation steps.

This mechanism is qualitatively consistent with the small reaction cross-section and a preference for rebounding reactive collisions inferred from the dynamics observed in the experiment. The O_2 must approach the CO_2 at very low impact parameters with high energies to overcome the initial barrier (TS1/TS2) and reach the 'shelf' of the bound $CO_4(^3A'')$. Momentum along the reaction coordinate beyond $CO_4(^3A'')$ with ~80 kcal mol^{-1} excess energy should further compress the C–O_c bond with synchronous bending of the C–O_c–O_d

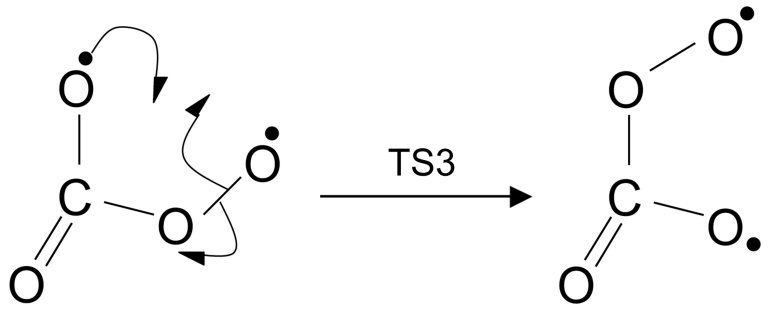

Figure 3.15: **Electron-pushing diagram of an adiabatic $CO_4(^3A'')$ isomerization through TS3.**

angle, stretching of O_c–O_d, and ring formation to form TS3, followed by rapid repulsion from the final TS1/TS2 state. Finally, the large change in geometry from reactants to TS3 should facilitate the transfer of some translational energy into internal degrees of freedom of the products. Reactive scattering should become less 'rebound'-like (forward-scattered) as E_{coll} is increased above the reactive threshold; at 37 kcal mol^{-1} above the reactive barrier, the tight transition state, repulsive exit channel leading out of TS1/TS2, and low angular momentum must limit the extent of sideways scattering. While some sideways scattering is indeed observed in the experiment, the E_{coll} dependence of $T(\theta_{\mathrm{c.m.}})$ is not known.

A non-adiabatic transition to another potential surface cannot be excluded, especially given the high internal energies observed in the products. At these high energies [80 kcal mol^{-1} above even the $CO_4(^3A'')$ shelf state], many excited-state surfaces must exist, and radiationless transitions via conical intersections may occur. While intersystem crossing (ISC) in the exit or entrance channels is unlikely at the high relative velocities of the experiment [*Landau*, 1932], spin transitions could readily occur if a complex is formed. For instance, the bridging oxygen atom in TS3, O_d, must be equivalently bound to O_b and O_c, and chemical intuition suggests that an intersection with a singlet surface may occur by spin-paired $CO_4(^1A_1)$ [*Cacace et al.*, 2003; *Elliott and Boldyrev*, 2005; *Jamieson et al.*, 2007].

3.6 Conclusion

An O_2–CO_2 isotope exchange reaction on the ground triplet electronic surface is possible and is consistent with our laboratory observations. Nevertheless, additional work would

be valuable in the confirmation of this hypothesis. Collision-energy-dependence studies of the product angular distribution may elucidate the mechanistic origins of the low average translational energy of products. Experimental detection of O_2 counter-fragments and a search for products from other channels (e.g., spectroscopic identification of electronically excited states) would also be revealing. Last, a more complete surface, reactive trajectories, and locations of possible surface intersection seams leading to ISC would be vital to a full explanation of the reaction dynamics.

3.7 Acknowledgements

We thank G. B. Ellison, S. L. Mielke, and J. E. Wulff for insightful discussions. This work was supported by the Missile Defense Agency under cooperative agreement HQ0006-05-2-0001. L. Y. Y. was supported by the Davidow Fund, and G. C. S. was supported by AFOSR grant FA955D-07-1-0095.

Appendices

3.A Non-reactive scattering of O_2 and CO_2

The experiment mainly observed signals due to $^{16}O_2$ scattered with little deflection from its initial direction (see Newton diagram in Figure 3.2); these signals corresponded to the sum of elastic and inelastic scattering collisions of $^{16}O_2$, which we could not resolve, so they will be referenced collectively as "scattered $^{16}O_2$." Five representative laboratory-frame TOF distributions (m/z = 32), the c.m. angular and translational energy distributions, and the laboratory-frame angular distribution obtained from $^{16}O_2$ product detection are shown in Figure 3.16. Scattered $^{16}O_2$ had 126.3 kcal mol^{-1} total translational energy, or 80% of the available energy, on average. The experimental translational energy distribution was peaked at ~148 kcal mol^{-1}. The c.m. angular distribution for ^{16}O was highly peaked in the forward direction with little scattered intensity for $\theta_{c.m.} > 30^\circ$; however, the velocity and angular range for $^{16}O_2$ product detection in the experiment prevented the detection of backward-scattered $^{16}O_2$ (see Figure 3.2). Some dependence of the c.m. translational energy distribution on the c.m. angular distribution was observed in the ^{16}O TOF data; the forward-convolution simulations became increasingly faster than the data at larger laboratory and c.m. angles (e.g, $\Theta = 18^\circ$, 28°, and 42° in Figure 3.16). We also note that, like for ^{16}O (see Sections 4.4.2.1 and 4.5.2), the c.m. angular distribution for inelastically scattered $^{16}O_2$ at $\theta_{c.m.} \sim 0^\circ$ is an extrapolation because of high background from the hyperthermal source at the small laboratory angles corresponding to small c.m. angles for $^{16}O_2$. Most of the $^{16}O_2$ probably scatters forward through high-impact-parameter collisions, but the limited constraints on the $\theta_{c.m.} \sim 0^\circ$ angular distribution (e.g., the laboratory-frame angular distribution, which only probes $\Theta = 6^\circ$) increase the uncertainty in that part of the c.m. angular distribution.

The experiment mainly observed $^{12}C^{18}O_2$ scattered opposite its initial direction in the c.m. frame (see Newton diagram in Figure 3.2). Detected $^{12}C^{18}O_2$ products (m/z = 48) showed best-fit c.m. translational energy distributions that were both broader and lower in energy, on average, than that obtained for forward-scattered $^{16}O_2$. A single pair of $P(E_T)$ and $T(\theta_{c.m.})$ distributions was not sufficient to describe the m/z = 48 TOF distributions (see Sections 4.4.2.1 and 4.5.2), and a second pair of $P(E_T)$ and $T(\theta_{c.m.})$ distributions was

included in the fit; five representative laboratory-frame TOF distributions, the c.m. angular and translational energy distributions, and the laboratory-frame angular distribution obtained from $^{12}C^{18}O_2$ product detection are shown in Figure 3.17, along with the c.m. velocity-flux diagram in Figure 3.18. The first $P(E_T)$ and $T(\theta_{c.m.})$ pair for inelastically scattered $^{12}C^{18}O_2$ described the scattering at $\theta_{c.m.} < 125^\circ$. In this region, the angular distribution was peaked near $\theta_{c.m.} = 60^\circ$, though the probability of scattered products was roughly constant for $0^\circ < \theta_{c.m.} < 40^\circ$. The probability of finding these products decayed steadily at $\theta_{c.m.} > 60^\circ$. The corresponding translational energy distribution was peaked at 60 kcal mol^{-1} with an average $\langle E_T \rangle = 62.8$ kcal mol^{-1}, or 40% the available energy. The second $P(E_T)$ and $T(\theta_{c.m.})$ pair for inelastically scattered $^{12}C^{18}O_2$ described the scattering at $60^\circ < \theta_{c.m.} < 125^\circ$ (corresponding to the maximum $\theta_{c.m.}$ observed in the experiment), although there was a small component $0^\circ < \theta_{c.m.} < 60^\circ$. This angular distribution overlapped, in the sideways-scattering region, with the first pair. For $\theta_{c.m.} > 60^\circ$ the distribution increased rapidly until it peaked near $\theta_{c.m.} = 120^\circ$ and decayed quickly at $\theta_{c.m.} > 120^\circ$. This part of the distribution, however, is uncertain because our experiment did not probe it directly. The translational energy distribution was peaked at 103 kcal mol^{-1} with an average $\langle E_T \rangle =$ 100.8 kcal mol^{-1}, or 64% the available energy.

The similarity in product c.m. angular and translational energy distributions in the O_2 + CO_2 system and the $O(^3P)$ + CO_2 system (see Sections 4.4.2.1 and 4.5.2) suggests that the collisional energy transfer mechanism is similar in both cases. *Ryali et al.* [1982] found that CO_2 collisions with N_2, O_2, and Ar near at high collision energies all had similar translational-to-vibrational energy transfer cross-sections for the excitation of $CO_2(\nu_3)$, so they suggested that energy transfer sampled the repulsive part of the intermolecular potential in all cases. Transfer of vibrational energy from O_2 to CO_2 cannot be ruled out in our experiments because we did not characterize the vibrational temperature of the hyperthermal O_2. Consequently, the similarity in inelastic scattering dynamics of $O(^3P)$ and O_2 collisions with CO_2 could also be coincidental.

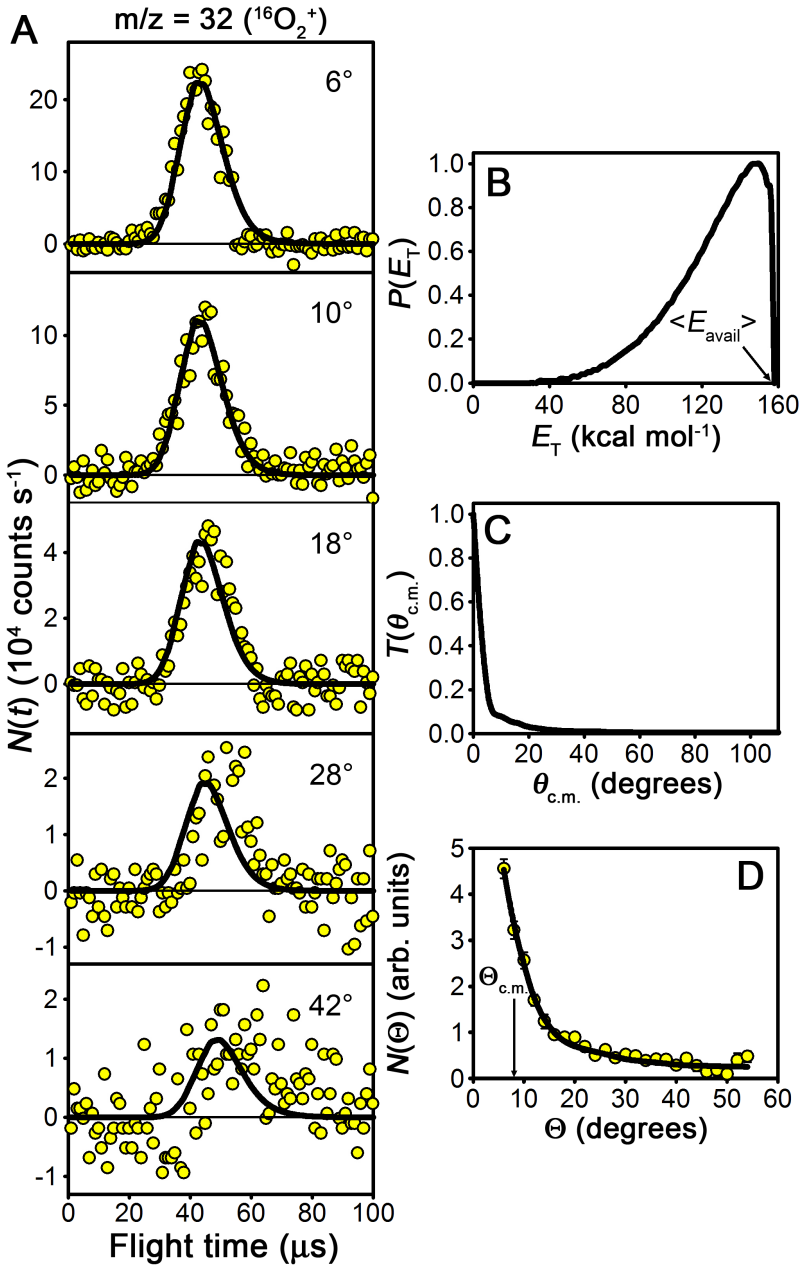

Figure 3.16: **Laboratory scattering data detected at *m/z* = 32.** (**A**) Laboratory TOF, (**B**) c.m. translational energy, and (**C**) c.m. and (**D**) laboratory angular distributions for scattered $^{16}O_2$ products from $^{16}O_2$ + $^{12}C^{18}O_2$ collisions at $\langle E_{coll} \rangle$ = 158.1 kcal mol^{-1}. The circles in (**A**) and (**D**) are experimental data, while the lines (orange and brown) are the best-fit forward-convolution simulations of the experimental data derived from the c.m. translational energy and angular distributions shown in (**B**) and (**C**), respectively. The error bars in (**D**) represent 2σ uncertainties in the integrated experimental TOF distributions (see Appendix 4.7). These data indicate that $^{16}O_2$ is scattered mainly in the forward direction with little change in its initial direction or velocity.

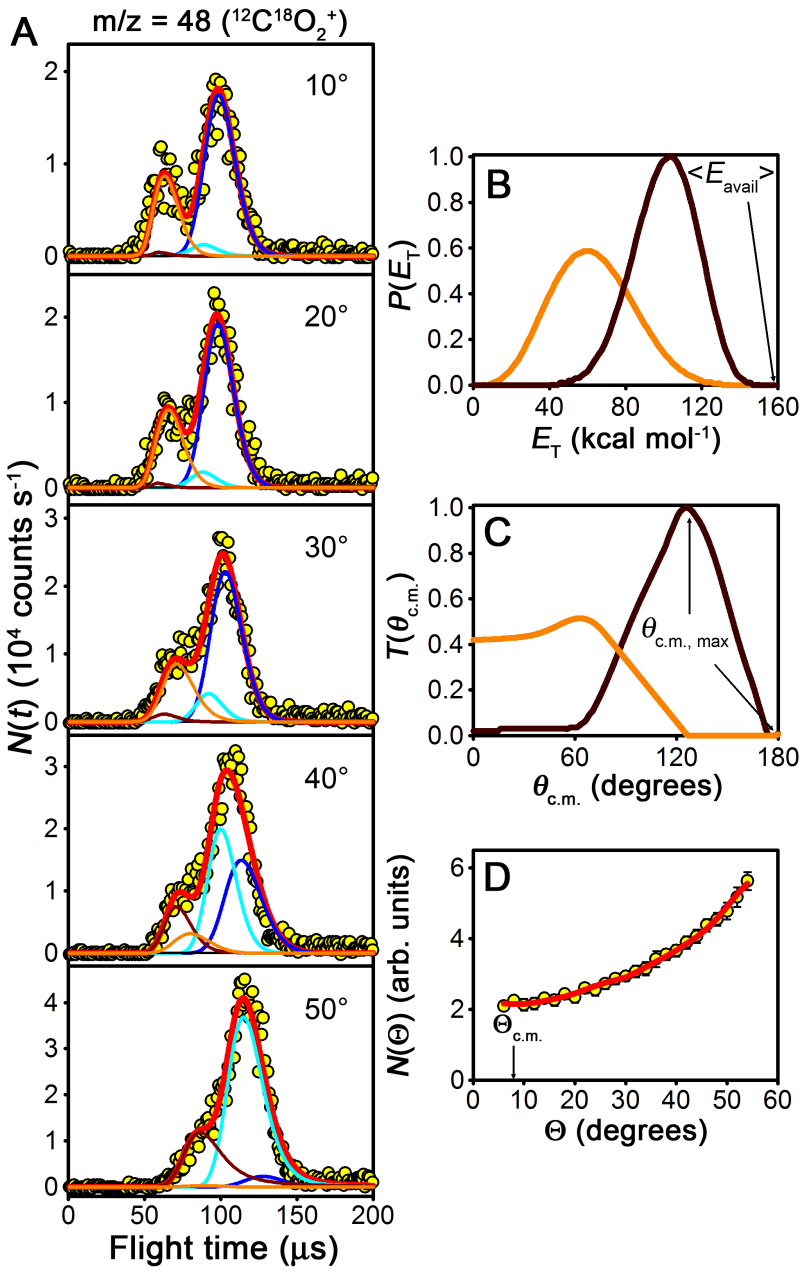

Figure 3.17: **Laboratory inelastic scattering data detected at *m/z* = 48.** (**A**) Laboratory TOF, (**B**) c.m. translational energy, and (**C**) c.m. and (**D**) laboratory angular distributions for inelastically scattered $^{12}C^{18}O_2$ products from $^{16}O_2$ + $^{12}C^{18}O_2$ collisions at $\langle E_{coll} \rangle$ = 158.1 kcal mol^{-1}. The circles in (**A**) and (**D**) are experimental data, while the lines are the best-fit forward-convolution simulations of the experimental data derived from the c.m. translational energy and angular distributions shown in (**B**) and (**C**), respectively. The error bars in (**D**) represent 2σ uncertainties in the integrated experimental TOF distributions (see Appendix 4.7). The dark blue and cyan lines correspond to products of $^{16}O(^3P)$ + $^{12}C^{18}O_2$ collisions, and they are discussed in Section 4.4.2.1. A single c.m. translational energy and angular distribution for each collision partner was insufficient to describe the TOF distributions of inelastically scattered $^{12}C^{18}O_2$, suggesting a scattering dependence on impact parameter.

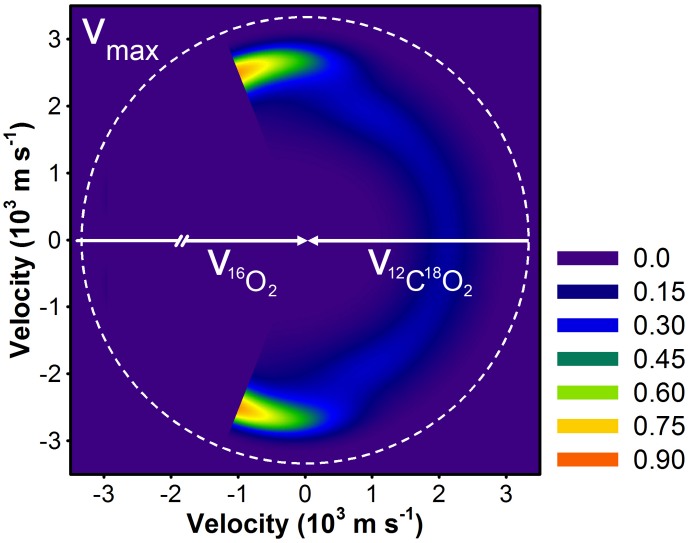

Figure 3.18: **Velocity-flux contour diagram for inelastically scattered $^{12}C^{18}O_2$ from $^{16}O_2$ + $^{12}C^{18}O_2$ collisions in the center-of-mass frame.** The white arrows are the initial $^{16}O_2$ and $^{12}C^{18}O_2$ velocity vectors and dashed white line is the maximum recoil velocity for $^{12}C^{18}O_2$ (v_{max}). Only the c.m. angles for which the experiment were sensitive are shown; inelastically scattered $^{12}C^{18}O_2$ from high-impact-parameter collisions are not shown, as their flux would be off-scale. Strong coupling of the $P(E_T)$ and $T(\theta_{c.m.})$ distributions was observed.

3.B MATLAB program for generating Newton diagrams

A series of programs (linked as functions) was written in MATLAB so meaningful Newton diagrams could be generated with little effort. This proved to be quite useful during data analysis because the program could display expected product times-of-flight, speeding up the forward-convolution fitting process considerably. The programs included here (*NewtonD.m*, *NewtonDcalc.m*, and *NewtonDplot.m*) use parameters specific to the MSU crossed-beam apparatus, but the code is general and the parameters adjustable for use with any crossed-beam apparatus with arbitrary crossing angle. Figure 3.19 shows a sample input and output.

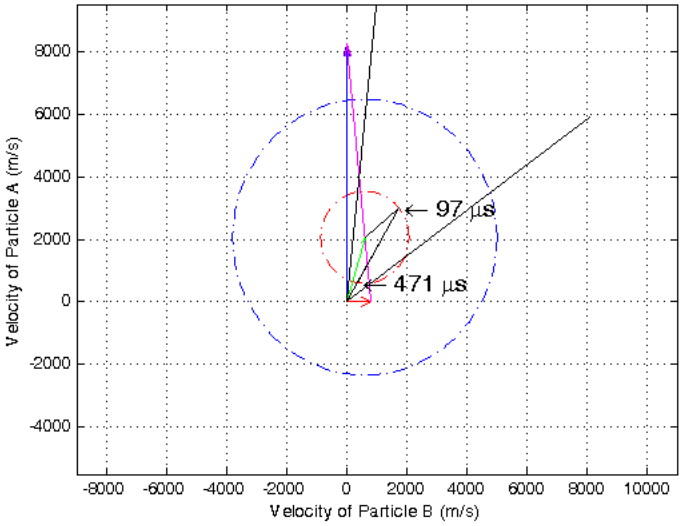


```
>> NewtonD(2,30)
Observed m/z
    48

Lab angle (degrees)
    30

Predicted center-of-mass angles (degrees)
   Fast channel | Slow channel
          124       -15.062
```

Figure 3.19: **Sample output of the *NewtonD.m* program.** Predicted c.m. angles are defined relative to the slow product's c.m. velocity vector.

3.B.1 NewtonD.m

```
% Program for generating Newton diagrams for molecular scattering.
% Command line input is NewtonD(observed,labangle)

function NewtonD(observed, labangle)
clear m1 m2 v1 v2 theta e DEint

observed=observed;     % observed product (1 or 2) as inputted below
labangle=labangle;     % lab angle of observation relative to initial v1
                       % vector, in degrees
```

```
% Begin input section

m1=16;      % mass of particle 1 in g/mol
v1=8262;    % initial velocity of particle 1 in m/s

m2=48;      % mass of particle 2 in g/mol
v2=800;     % initial velocity of particle 2 in m/s

theta=0.5;  % angle between v1 and v2 in pi radians, e.g. 0.5 --> 0.5*pi
            % = 90 degrees

e=0.5;      % elastic scattering efficiency 0 < e ≤ 1)
DEint=0;    % gain of internal energy upon reaction in kcal/mol

mp1=16;     % mass of product 1 in g/mol
mp2=48;     % mass of product 2 in g/mol

minangle=6;     % minimum lab angle relative to v1 vector, in degrees
maxangle=54;    % maximum lab angle relative to v1 vector, in degrees

length=33.66;   % distance between interaction region and ionizer in cm

if observed == 1
    IFT=0;2.44*sqrt(mp1);    % ion flight time (delay) in microseconds
else if observed == 2
        IFT=0;2.44*sqrt(mp2);
    end
end

delec=0;3;               % electronics delay in microseconds
dlaser=0;174;            % laser firing delay in microseconds
otravel=0;(0.99/v1)*10^6;       % O-atom travel time from nozzle to
                                % interaction region in microseconds

% End input section

% Input error check

if observed ≠ 1 && observed ≠ 2
    disp('Invalid input, "observed" must equal 1 or 2');
    return;
end

% Begin calculations

hold off
format short g

disp('Observed m/z');   % Display observed mass
if observed == 1
    disp(mp1);
else if observed == 2
        disp(mp2);
    end
end
disp('Lab angle (degrees)');
disp(labangle);
```

```
disp('Predicted center-of-mass angles (degrees)');
disp('   Fast channel | Slow channel');

% Iterate; first round includes specified change in internal energy,
% second round sets the internal energy change to zero, i.e.
% elastic scattering.
for i = 1:2
    [vc, thetavc, vrel, u1, u2, vrelp, up1, up2, Ecoll, phi, vd, chi]=
        NewtonDcalc(m1, m2, v1, v2, theta, e, DEint, mp1, mp2, labangle,
        observed);
    NewtonDplot(v1, v2, vc, thetavc, up1, up2, e, minangle, maxangle,
        labangle, vd, length, IFT, delec, dlaser, otravel, chi);
    if DEint == 0
        return;
    else
        DEint=0;
    end
end

disp('Collision Energy (kcal/mol)');
disp(Ecoll);
```

3.B.2 NewtonDcalc.m

```
% Function for calculating center-of-mass quantities

function [vc, thetavc, vrel, u1, u2, vrelp, up1, up2, Ecoll, phi, vd,
    chi]=NewtonDcalc(m1, m2, v1, v2, theta, e, DEint, mp1, mp2,
    labangle, observed)

% reactant parameters
mu=m1*m2/(m1+m2);                                   % reduced mass
vc=sqrt((m1/(m1+m2)*v1)^2+(m2/(m1+m2)*v2)^2);       % CM velocity
vrel=sqrt(v1^2+v2^2-2*v1*v2*cos(theta*pi));         % relative velocity
u1=m2/(m1+m2)*vrel;                                 % velocity of particle 1
                                                    % in CM frame
u2=m1/(m1+m2)*vrel;                                 % velocity of particle 2
                                                    % in CM frame
thetavc=asin((u2/vc)*(v1/vrel)*sin(theta*pi));      % angle between CM
                                                    % velocity and v2
Ecoll=(1/2)*mu/1000*vrel^2/4.184/1000;              % CM collision energy

% reactive product parameters
mup=mp1*mp2/(mp1+mp2);                              % reduced mass
vrelp=sqrt(((mu/1000)*vrel^2-2*(DEint*1000*4.184))/(mup/1000));
    %relative velocity
up1=mp2/(mp1+mp2)*vrelp;                            % velocity of product 1
                                                    % in CM frame
up2=mp1/(mp1+mp2)*vrelp;                            % velocity of product 2
                                                    % in CM frame

phi=labangle*pi/180-(theta*pi-(thetavc));           % angle between lab
                                                    % detection vector and
                                                    % CM velocity

% case structure determining output parameters
if observed == 1
```

```
    up=up1; u=u1; v=v1;
else if observed == 2
        up=up2; u=u2; v=v2;
    end
end

% product velocity in lab frame with case structure for removal of
% imaginary roots.

if imag(roots([1 -2*vc*cos(phi) vc^2-(up*sqrt(e))^2])) == 0
   vd=roots([1 -2*vc*cos(phi) vc^2-(up*sqrt(e))^2]);
   % Solve for product velocity observed at detector
   if vd(1) <= 0 && vd(2) <= 0
       vd(1)=0;
       vd(2)=0;
   else if vd(1) > 0 && vd(2) <= 0
           vd(2)=0;
       else if vd(1) < 0 && vd(2) > 0
               vd(1)=0;
           end
       end
   end

% Product scattering angle relative to CM velocity vector of reactant 2
   if phi > 0
       chi=(acos((diag(vd*vd')-vc^2-diag(up*up')*e)/(-2*vc*up*sqrt(e)))-
       asin(v2/u2*sin(thetavc)))*180/pi;
   else
       chi=360-(acos((diag(vd*vd')-vc^2-diag(up*up')*e)/(-2*vc*up*sqrt(e)))+
       asin(v2/u2*sin(thetavc)))*180/pi;
   end
   if imag(chi(1)) ~= 0
       chi(1) = 0;
   end
   if imag(chi(2)) ~= 0
       chi(2) = 0;
   end
   if chi(1) > 180
      chi(1)= chi(1)-360;
   end
   if chi(2) > 180
      chi(2)= chi(2)-360;
   end

% In case of imaginary roots
else
    vd(1,1)=10000;
    vd(2,1)=10000;
    chi=1;
    disp('         N/A         N/A')     % Display lack of solutions
end

%((1/2)*(mp1/1000)*(up1)^2*e)/4184       % CM Translational energy of
                                         % product 1
%((1/2)*(mp2/1000)*(up2)^2*e)/4184       % CM Translational energy of
                                         % product 2
```

3.B.3 NewtonDplot.m

```
function NewtonDplot(v1, v2, vc, thetavc, up1, up2, e, minangle,
    maxangle, labangle, vd, length, IFT, delec, dlaser, otravel, chi)

% Messy plotting code for pretty pictures

          x1 = vc*cos(thetavc);
          y1 = vc*sin(thetavc);
          N=256; t=(0:N)*2*pi/N;

plot(sqrt(e)*up2*cos(t)+x1, sqrt(e)*up2*sin(t)+y1, '-.r');
          % Newton circle for product 2
          hold on
          grid on

plot(sqrt(e)*up1*cos(t)+x1, sqrt(e)*up1*sin(t)+y1, '-.b');
          % Newton circle for product 1

legend('Particle 2', 'Particle 1')
% text(1,1,'Collision energy = \Ecoll kcal/mol')

          x0 = 0;
          y0 = 0;
          x1 = 0;
          y1 = v1;
plot([x0;x1],[y0;y1])    % Particle 1
          alpha = 0.05;  % Size of arrow head relative to the length of
                         % the vector
          beta = 0.2;    % Width of the base of the arrow head relative to
                         % the length
          hu = [x1-alpha*((x1-x0)+beta*((y1-y0)+eps)); x1; x1-alpha*
            ((x1-x0)-beta*((y1-y0)+eps))];
          hv = [y1-alpha*((y1-y0)-beta*((x1-x0)+eps)); y1; y1-alpha*
            ((y1-y0)+beta*((x1-x0)+eps))];
          plot(hu(:),hv(:))  % Plot arrow head

          x0 = 0;
          y0 = 0;
          x1 = v2;
          y1 = 0;
plot([x0;x1],[y0;y1],'r') % Particle 2
          alpha = 0.4;    % Size of arrow head relative to the length of
                          % the vector
          beta = 0.5;     % Width of the base of the arrow head relative to
                          % the length
          hu = [x1-alpha*((x1-x0)+beta*((y1-y0)+eps)); x1; x1-alpha*
            ((x1-x0)-beta*((y1-y0)+eps))];
          hv = [y1-alpha*((y1-y0)-beta*((x1-x0)+eps)); y1; y1-alpha*
            ((y1-y0)+beta*((x1-x0)+eps))];
          plot(hu(:),hv(:),'r')  % Plot arrow head

          x0 = v2;
          y0 = 0;
          x1 = 0;
          y1 = v1;
plot([x0;x1],[y0;y1],'m') % vrel
          alpha = 0.05;   % Size of arrow head relative to the length of
                          % the vector
          beta = 0.2;     % Width of the base of the arrow head relative to
```

```
                        % the length
          hu = [x1-alpha*((x1-x0)+beta*((y1-y0)+eps)); x1; x1-alpha*
            ((x1-x0)-beta*((y1-y0)+eps))];
          hv = [y1-alpha*((y1-y0)-beta*((x1-x0)+eps)); y1; y1-alpha*
            ((y1-y0)+beta*((x1-x0)+eps))];
          plot(hu(:),hv(:),'m')  % Plot arrow head

          x0 = 0;
          y0 = 0;
          x1 = vc*cos(thetavc);
          y1 = vc*sin(thetavc);
plot([x0;x1],[y0;y1],'g') % vc
          alpha = 0.1;    % Size of arrow head relative to the length of
                          % the vector
          beta = 0.25;    % Width of the base of the arrow head relative to
                          % the length
          hu = [x1-alpha*((x1-x0)+beta*((y1-y0)+eps)); x1; x1-alpha*
            ((x1-x0)-beta*((y1-y0)+eps))];
          hv = [y1-alpha*((y1-y0)-beta*((x1-x0)+eps)); y1; y1-alpha*
            ((y1-y0)+beta*((x1-x0)+eps))];
          plot(hu(:),hv(:),'g')  % Plot arrow head

          x1=10000*sin(minangle*pi/180);
          y1=10000*cos(minangle*pi/180);
plot([0;x1],[0;y1],'k')     % minimum lab angle

          x1=10000*sin(maxangle*pi/180);
          y1=10000*cos(maxangle*pi/180);
plot([0;x1],[0;y1],'k')     % maximum lab angle

if chi == 1
    return
else if chi ≠ 1
        x1=vd*sin(labangle*pi/180);
        y1=vd*cos(labangle*pi/180);
    plot([0;x1],[0;y1],'k')    % observed lab angle

        x0=vc*cos(thetavc);
        y0=vc*sin(thetavc);
        x1=vd*sin(labangle*pi/180);
        y1=vd*cos(labangle*pi/180);
    plot([x0;x1],[y0;y1],'k')  % center-of-mass scattering
    end
end

xlabel('Velocity of Particle B (m/s)')
ylabel('Velocity of Particle A (m/s)')
axis([-9000 11000 -5500 9500])

% Relevant quantities

disp(chi');

if vd(1) == 0 && vd (2) == 0
    TOF=[0 0];
else if vd(1) == 0
        TOF=[((length/100)/vd(1))*10^6 0];    % Predicted TOF times in
                                              % microseconds
```

```
    else if vd(2) == 0
           TOF=[((length/100)/vd(1))*10^6 0];  % Predicted TOF times in
                                               % microseconds
        else if vd(1) == 10000 && vd(2) == 10000
                TOF=[0 0];
            else if vd(1) > 0 && vd(2) > 0
                    % Predicted TOF times in microseconds
                    TOFfast=((length/100)/vd(1))*10^6;
                    TOFslow=((length/100)/vd(2))*10^6;
                    TOF=[TOFfast TOFslow];
                end
            end
        end
    end
end

% Display TOF on graph next to Newton circle
text(x1(1),y1(1),[' \leftarrow ',num2str(round(TOF(1)+IFT+delec+dlaser+
    otravel)), ' \mus'],'FontSize',14)

% Only display second TOF value if there is a product to display
if TOF(2) ~= 0
    text(x1(2),y1(2),[' \leftarrow ',num2str(round(TOF(2)+IFT+delec+
        dlaser+otravel)), ' \mus'],'FontSize',14)
else
    return
end
```

Chapter 4

Dynamics of $O(^3P)$ + CO_2 collisions at hyperthermal energies

In collaboration with Mitchio Okumura, Jianming Zhang, Timothy K. Minton, Jeffrey T. Paci, Jan M. L. Martin, Jon M. Camden, and George C. Schatz; parts of this will be submitted to *Journal of Physical Chemistry A* for publication.

4.1 Abstract

The dynamics of $O(^3P)$ + CO_2 collisions at hyperthermal collision energies near 100 kcal mol^{-1} were investigated experimentally and theoretically. Crossed-molecular-beam experiments at $\langle E_{coll} \rangle$ = 98.8 kcal mol^{-1} were performed with isotopically labeled $^{12}C^{18}O_2$ to distinguish products of non-reactive scattering [$^{16}O(^3P)$ + $^{12}C^{18}O_2$] from products of reactive scattering (^{18}O + $^{16}O^{12}C^{18}O$ and $^{18}O^{16}O$ + $^{12}C^{18}O$). ^{16}O products were detected mainly in the forward direction, i.e., in the initial direction of the hyperthermal oxygen beam in the center-of-mass (c.m.) frame, and they contained ~87% of the collision energy in translation, on average; the amount of energy transfer during non-reactive scattering depended on impact parameter. $^{16}O^{12}C^{18}O$ products from the oxygen isotope exchange reaction were scattered mainly in the backward direction with 35% of the available energy in translation, on average. $^{18}O^{16}O$ products from the oxygen-atom abstraction reaction were detected in the forward direction, with 56% of the available energy in translation, on average. Stationary points on the lowest triplet potential energy surface of the $O(^3P)$ + CO_2 system were characterized at the CCSD(T)/aug-cc-pVTZ level of theory. Quasi-classical trajectory (QCT) calculations of $O(^3P)$ + CO_2 collisions at energies between 1.0 – 6.5 eV (23 – 150 kcal mol^{-1}) were performed at the B3LYP/6-311G(d) and BMK/6-311G(d) levels of theory, and both reactive channels observed in the experiment were also predicted by the theory. In addition, trajectories leading to the formation of $^{18}O_2$ + $^{12}C^{16}O$ products were predicted. The c.m. translational energy and angular distributions derived from the QCT calculations show qualitative, but not quantitative agreement with experimental results. The theoretical relative product yield for the oxygen isotope exchange reaction also agreed well with the experiment. The isotope exchange reaction demonstrates a new pathway through which oxygen isotopes may be cycled in the upper atmosphere, where $O(^3P)$ atoms with hyperthermal translational energy distributions can be generated through the photolysis of ozone and molecular oxygen.

4.2 Introduction

Atomic oxygen radicals in the atmosphere play an important role in regulating Earth's oxidative and radiative balance. Photodissociation of molecular oxygen and ozone by solar ultraviolet radiation produces not only electronically excited $O(^1D)$ and $O(^1S)$, but also ground-state $O(^3P)$ with velocities as high as 6 km s^{-1} [*Matsumi and Kawasaki*, 2003; *Stranges et al.*, 1995]. $O(^3P)$ has received less attention than $O(^1D)$ and $O(^1S)$, however, because it is less reactive at low collision energies. Yet, its important role in the terrestrial mesosphere and thermosphere is widely recognized; for instance, its collisions with CO_2 significantly influence the population of $CO_2(010)$, whose emission at 15 μm cools the atmosphere and regulates the height of the mesopause [*Sharma and Roble*, 2002]. $O(^3P)$ can also interact with CO_2 from space vehicle exhaust streams at relative velocities near 8 km s^{-1} and collision energies near 100 kcal mol^{-1}, well above those expected at local thermodynamic equilibrium.

These high collision energies exceed barriers to (*1*) CO_3 formation, leading to oxygen isotope exchange, and (*2*) oxygen-atom abstraction on the triplet potential energy surface (PES) [*Averyanov et al.*, 1999; *Bennett et al.*, 2004; *Froese and Goddard*, 1993; *Mebel et al.*, 2004; *Yang et al.*, 2005]. The enthalpies associated with these reactions are:

$$O(^3P) + CO_2(^1\Sigma_g^+) \rightarrow O(^3P) + CO_2(^1\Sigma_g^+) \qquad \Delta H \sim 0 \tag{4.1}$$

$$\rightarrow O_2(^3\Sigma_g^-) + CO(^1\Sigma^+) \qquad \Delta H = 8 \text{ kcal mol}^{-1} \tag{4.2}$$

A reaction analogous to reaction 4.1, between $O(^1D)$ and CO_2 in the stratosphere [*Baulch and Breckenridge*, 1966; *Chakraborty and Bhattacharya*, 2003; *DeMore and Dede*, 1970; *Johnston et al.*, 2000; *Mebel et al.*, 2004; *Perri et al.*, 2003, 2004; *Shaheen et al.*, 2007; *Wen and Thiemens*, 1993; *Yeung et al.*, 2009a], alters the stable isotope composition of stratospheric CO_2, allowing the isotopic composition of stratospheric CO_2 to be used as a tracer of $O(^1D)$ [*Thiemens et al.*, 1995; *Yung et al.*, 1991, 1997] and atmospheric transport [*Boering et al.*, 2004]. The isotopic composition of CO_2 has also been proposed as a tracer of biogeochemical cycles on annual and decadal timescales [*Hoag et al.*, 2005]. Consequently, the dynamics of reactive channels that could alter the isotopic composition of

upper atmospheric CO_2 are also of interest [*Perri et al.*, 2003, 2004].

Early studies on the $O(^3P)$ + CO_2 system were primarily theoretical and focused on the vibrational-state-specific energy transfer [*Bass*, 1974; *Garrett*, 1983; *Harvey*, 1982; *Schatz and Redmon*, 1981]. The mechanism was found to be primarily impulsive at high collision energies, like that of collisions between CO_2 and noble gases [*Billing and Clary*, 1983; *Harvey*, 1982; *Schatz and Redmon*, 1981]. More recent quantum calculations on the $O(^3P_J)$ + $CO_2(010)$ system indicate that vibrational-to-translational energy transfer is sensitive to the total angular momentum J at thermal collision energies, although the importance of spin-orbit coupling decreases with increasing collision energy [*de Lara-Castells et al.*, 2006, 2007]. Two experimental studies also focused on state-specific excitation in $O(^3P)$ + CO_2 collisions, specifically to $CO_2(001)$; both studies also reported evidence that reaction 4.2, which is important in combustion chemistry [*Tsang and Hampson*, 1986] yielded vibrationally excited CO products [*Oakes et al.*, 1994; *Upschulte and Caledonia*, 1992]; no mechanism was proposed, however.

We recently confirmed the presence of reaction 4.1 at hyperthermal collision energies [*Yeung et al.*, 2009b], and we intend now to investigate its dynamics. *Mebel et al.* [2004] suggested that the dynamics of CO_3 formation on the triplet ($^3A'$) PES with hyperthermal $O(^3P)$ atoms might be complicated by a nearby $^3A'$–$^1A'$ intersection seam, which could lead to non-adiabatic effects along reactive trajectories. Indeed, many low-lying electronic states of CO_3 (e.g., $^3A''$) lie within several eV of $CO_3(^3A')$, so vibronic [*Kowalczyk and Krylov*, 2007] and/or spin-orbit [*Mebel et al.*, 2004] coupling could result in unexpected curvature and dynamics on the triplet PES.

Here, the results of theoretical and crossed-molecular-beam studies of $O(^3P)$ + CO_2 collisions at hyperthermal collision energies will be presented. Theoretical direct dynamics calculations using the QCT method on an adiabatic PES were compared with the results from an experimental dynamics study obtained for an average collision energy $\langle E_{\text{coll}} \rangle = 98.8$ kcal mol^{-1}. The oxygen isotope exchange and oxygen-atom abstraction reactions were observed in both the QCT calculations and the laboratory experiment, and center-of-mass (c.m.) angular and translational energy distributions for the oxygen isotope exchange reaction were

obtained. Their implications for atomic oxygen cycling through CO_2 in the atmosphere will be discussed.

4.3 Theoretical studies

4.3.1 Electronic structure calculations

Geometry-optimization, single-point, and vibrational-frequency calculations were performed on stationary points of the lowest triplet PES of CO_3, $^3A''$; a discussion of the relative energetics of the $^3A'$ and $^3A''$ surfaces can be found in Section 4.5. Stationary points for reactions 4.1 and 4.2 were characterized using electronic structure calculations at the B3LYP/6-311G(d) [*Becke*, 1993; *Frisch et al.*, 1984; *Lee et al.*, 1988], BMK/6-311G(d) [*Boese and Martin*, 2004], and CCSD(T)/aug-cc-pVTZ [*Kendall et al.*, 1992; *Raghavachari et al.*, 1989] levels of theory/basis using the MOLPRO electronic structure code [*Werner et al.*, 2006]. Confirmation of transition-state character was achieved by inspection of the associated vibrational frequencies. Other reactive channels were not characterized because reactant energies in excess of 250 kcal mol^{-1} are required to open them, according to our B3LYP/6-311G(d) calculations.

Here, we report three transition-state structures and one bound-state structure on the $CO_3(^3A'')$ PES; the results are shown in Figures 4.1 and 4.2 and Table 4.1 [*Mebel et al.*, 2004]. All structures are planar. One transition state (TS1) and the bound state (CO_3) were associated with the $O(^3P)$ + CO_2 isotope exchange reaction. Two transition states (TS2 and TS3) were associated with the oxygen-atom abstraction reaction producing O_2 and CO. Two additional bound states and two associated transition states were also found; they resemble the C_s minima reported in previous work [*Bennett et al.*, 2004; *Froese and Goddard*, 1993; *Mebel et al.*, 2004], but they will not be discussed here because neither of the bound states were bound when zero-point energy (ZPE) was considered. For this reason, we are also not reporting minima in the van der Waals region of the PES, e.g., the quadrupole-induced minimum ($\Delta E \sim 335$ cm^{-1}) at the RCCSD(T)/aug-cc-pVTZ level of theory [*de Lara-Castells et al.*, 2006, 2007], because the binding energies were below the ZPE of the system. Further

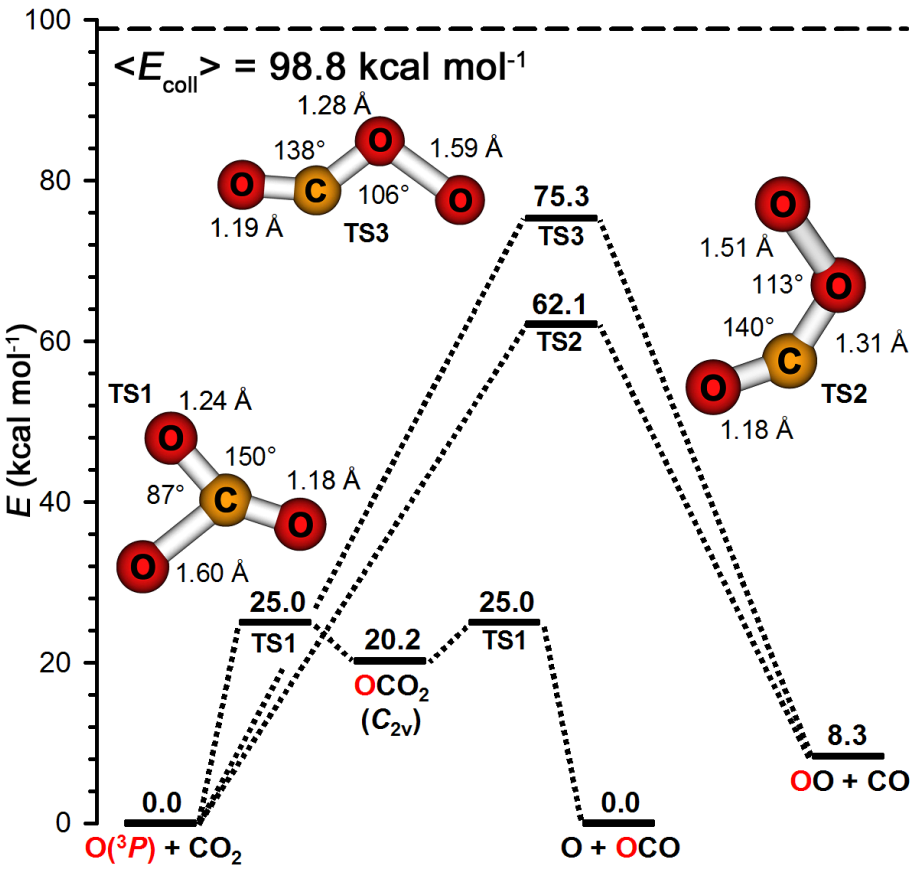

Figure 4.1: **Stationary-point structures for $O(^3P)$ + CO_2 reactions below 100 kcal mol^{-1} calculated at the CCSD(T)/aug-cc-pVTZ level of theory on the $^3A''$.** The relative energies have been corrected for zero-point energy.

comparisons of the structures with previous work on the lowest triplet PES will be presented in Section 4.5.

Of the levels of theory and basis examined in this study, CCSD(T)/aug-cc-pVTZ is probably the most accurate combination; however, multi-reference character in the stationary points may be important because several electronic surfaces are within several eV of the PES that is the subject of this study [*Bennett et al.*, 2004; *Kowalczyk and Krylov*, 2007; *Mebel et al.*, 2004]. Multi-reference CCSD(T) calculations, unfortunately, were not computationally affordable. Still, our CCSD(T)/aug-cc-pVTZ geometries are nearly identical to those obtained in recent calculations using the W4 method [*Karton et al.*, 2006] near the full-configuration-interaction and complete-basis-set limits, with transition-state energies within 2 kcal mol^{-1} and the bound-state energy within 4 kcal mol^{-1} (J. M. L. Martin, per-

Table 4.1: Energies (kcal mol^{-1}) for the stationary points on the lowest triplet CO_3 potential energy surface for $^{16}O(^3P)$ + $^{12}C^{16}O_2 \rightarrow {}^{16}O$ + $^{12}C^{16}O_2$ collisions

	B3LYP 6-311G(d)		**BMK 6-311G(d)**		**CCSD(T) aug-cc-pVTZ**		**CCSD(T) 6-311+G(3df)***
		w/ZPEC†		w/ZPEC†		w/ZPEC†	
$O(^3P)$ + CO_2	0.0	0.0	0.0	0.0	0.0	0.0	0.0
TS1	18.0	17.7	25.2	25.0	25.2	25.0	35.2
CO_3	11.8	11.3	20.2	19.0	21.8	20.2	22.0
TS2	56.2	55.2	65.3	64.5	63.0	62.1	
TS3	70.3	69.2	80.0	78.9	76.5	75.3	
O_2 + CO	9.7	7.9	14.3	12.6	10.2	8.3	

*From *Mebel et al.* [2004] using a $^3A'$ geometry optimized at the CASSCF(16,13)/6-311G(d) level of theory. The authors noted that the more ideal MRCI+Q/6-311+G(3df) energy calculation was not affordable.

†Zero-point-energy correction (ZPEC).

sonal communication). Thus, we used the CCSD(T)/aug-cc-pVTZ geometries and energies as benchmarks for comparison with those calculated by the density-functional methods, which are more affordable for QCT calculations.

In addition to using the B3LYP and BMK levels of theory, we characterized the transition-state structures at the MP2 [*Møller and Plesset*, 1934], M06-2X [*Zhao and Truhlar*, 2008], and CCSD [*Purvis and Bartlett*, 1982] levels using the 6-31G(d,p), 6-311G(d), and cc-pVTZ [*Dunning*, 1989] basis sets during our search for an appropriate level of theory for QCT calculations (optimizing computational cost and accuracy). The density-functional methods B3LYP/6-311G(d) and BMK/6-311G(d), however, were found to have the best balance between computational cost and accuracy, so we will only report the results of those calculations here along with the results of CCSD(T)/aug-cc-pVTZ calculations (see Figure 4.2). The results of the lower-level B3LYP and BMK calculations, along with the MP2, M06-2X, and CCSD calculations, are shown in Figure 4.3.

TS1 had C_s symmetry in all cases. Mild compression of one C–O bond and stretching of the other C–O bond in the parent CO_2, along with moderate bending ($\sim$30°) of the O–C–O bond angle, was found at all levels of theory. The geometries were similar to that calculated at the CCSD(T) level of theory, which had C–O bond lengths of 1.24 Å, 1.18 Å, and 1.60 Å and bond angles of 87°, 123°, and 150° (see Figure 4.2). The B3LYP geometry

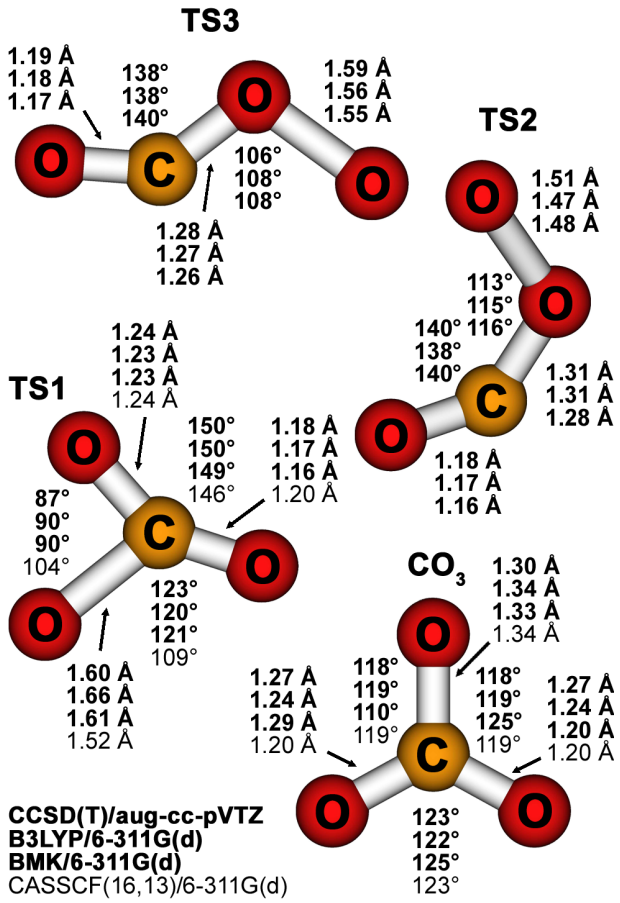

Figure 4.2: **Comparison of CO_3 stationary point geometries relevant to the QCT calculations.** Our geometry optimizations at the CCSD(T)/aug-cc-pVTZ, B3LYP/6-311G(d), and BMK/6-311G(d) levels of theory (bold) are shown with *Mebel et al.*'s CASSCF(16,13)/6-311G(d) geometries for CO_3 and TS1.

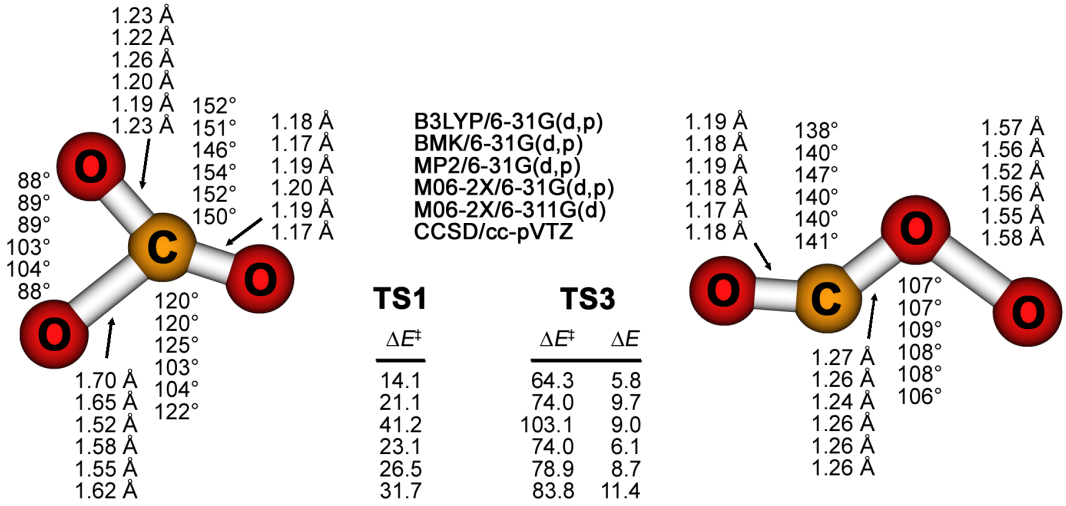

Figure 4.3: **Comparison of TS1 and TS3 geometries and energies at various levels of theory.** ZPE-corrected transition-state ($\Delta E^{\ddagger}$) and reaction (ΔE) energies are shown.

generally agrees well with that at CCSD(T), deviating by < 0.02 Å in the two shorter C–O bond lengths and by $< 3^\circ$ in all the bond angles. The longest bond length, however, is 0.06 Å longer at B3LYP than at CCSD(T). Its ZPE-corrected energy is also 7.3 kcal mol^{-1} lower. At the BMK level of theory, the TS1 geometry agrees with the CCSD(T) geometry within 0.02 Å in all the bond lengths and within 3° in all the bond angles, and with the CCSD(T) energy within 0.1 kcal mol^{-1}.

The CO_3 bound state had C_{2v} symmetry at the B3LYP and CCSD(T) levels of theory and C_s symmetry at the BMK level of theory. C–O bond lengths were larger than typical CO_2 bond lengths (1.21 Å), consistent with an overall decrease in C–O bond order upon CO_3 formation. The B3LYP geometry agreed within 0.04 Å and 1° with the CCSD(T) geometry, which had C–O bond lengths of 1.27 Å, 1.27 Å, and 1.30 Å and bond angles of 118°, 118°, and 123° (see Figure 4.2). The ZPE-corrected B3LYP energy, however, is 8.9 kcal mol^{-1} lower than that at CCSD(T). At the BMK level of theory, moderate agreement in the CCSD(T) geometry was observed; in addition to displaying lower symmetry, the C–O bond lengths calculated at BMK were different from CCSD(T) bond lengths by up to 0.07 Å, while the bond angles were different by up to 8°. The lower symmetry for CO_3 using the BMK functional may be a consequence of the large amount of Hartree-Fock exchange mixed into the functional [*Boese and Martin*, 2004], which can result in orbital symmetry-breaking [*Sherrill et al.*, 1999]. The ZPE corrected CO_3 energy at BMK is in better agreement, however, at 1.2 kcal mol^{-1} below the energy at CCSD(T). Both B3LYP and BMK theories do show a CO_3 potential well of 6.4 and 6.0 kcal mol^{-1}, respectively, in reasonable agreement with the CCSD(T) well depth of 4.8 kcal mol^{-1}.

TS2 and TS3 were associated with an oxygen-atom abstraction reaction producing O_2 + CO. They had C_s symmetry at all levels of theory. In both transition states, one C–O bond on the parent CO_2 was compressed, while the other C–O bond, which is eventually broken, was stretched (see Figure 4.2). The O–C–O bond angle was bent $\sim 40^\circ$, and the only qualitative difference between the structures was the C–O–O bond angle: The C–O–O angle bent inwards to form a 'C'-shape in TS2, whereas it bent outwards to form a 'S'-shape in TS3. Both B3LYP and BMK geometries agreed with the CCSD(T) geometry with a maximum dis-

crepancy of 0.04 Å in the O–O bond length at the BMK level. The two bond angles agreed to within 2°. Resulting ZPE-corrected barrier heights showed larger discrepancies: B3LYP and BMK energies for TS2 differed from CCSD(T) values by –6.9 and +2.4 kcal mol^{-1}, respectively, while they differed from CCSD(T) values by +6.1 and –3.6 kcal mol^{-1}, respectively, in TS3. We note that BMK overpredicted the endothermicity of the O(^3P) + CO_2 → O_2 + CO reaction by ∼4.5 kcal mol^{-1}; this disagreement is again probably a consequence of the large amount of Hartree-Fock exchange mixed into the BMK functional, which was included to improve the performance of the functional when predicting transition state properties.

4.3.2 Reaction dynamics calculations

QCT calculations were run on the $^3A''$ PES with both B3LYP/6-311G(d) and BMK/6-311G(d) methods. Both methods showed reasonable agreement with the geometries and energies of the stationary points calculated at CCSD(T)/aug-cc-pVTZ and were computationally affordable for direct dynamics calculations. Four hundred trajectories were run at collision energies of 1.0, 1.5, 2.5, 3.5, 4.5, 5.5, and 6.5 eV (23.0, 34.6, 57.6, 80.7, 103.7, 126.7, and 149.8 kcal mol^{-1}, respectively) using the B3LYP level of theory for a total of 2800 trajectories. This range of energies was selected because the ZPE-corrected barriers for TS1, TS2, and TS3 according to this level of theory were 17.7, 55.2, and 69.2 kcal mol^{-1} (0.77, 2.4, and 3.0 eV, respectively). In addition, four hundred BMK trajectories were run at collision energies of 1.5, 2.5, 3.5, 4.5, 5.5, and 6.5 eV for a total of 2400 trajectories. At this level of theory, the ZPE-corrected reaction thresholds were 25.0, 64.5, and 78.9 kcal mol^{-1} (1.1, 2.8, and 3.4 eV, respectively) for TS1, TS2, and TS3, respectively. The collision energy of 1.0 eV (23 kcal mol^{-1}) was not considered because it is below the threshold for both reactions 4.1 and 4.2, according to the BMK level of theory. Trajectories were integrated using a standard fifth-order predicator, sixth-order corrector integration algorithm [*Bunker*, 1970; *Press et al.*, 1992] with an integration time-step of 10.0 a.u. (0.24 fs). The energy and gradient were calculated at each point using the Q-Chem software package [*Shao et al.*, 2006], and the initial orientation and impact parameter was sampled randomly. To simulate the ZPE, an intermolecular trajectory starting from CO_2 in its equilibrium configuration was run

with kinetic energy corresponding to the ZPE in each normal mode, and the atomic coordinates along this trajectory were used to sample the initial CO_2 vibrational phase randomly in subsequent trajectories.

An estimate of a reasonable value for the maximum impact parameter for reactive scattering, b_{max}, was calculated using the expression [*Levine*, 2005]:

$$b_{max} = d\left(1 - \frac{E_0}{E_T}\right)^{\frac{1}{2}} \tag{4.3}$$

where d is the distance in the transition-state structure between the center of mass of the reactant CO_2 and the colliding oxygen atom, E_0 is the transition-state energy, and E_T is the collision energy. Because large collision energies were of principal interest, we chose to consider the largest value for b_{max} suitable for trajectories with unlimited collision energy by setting $E_T = \infty$ in Eq. 4.3. Reaction 4.2 had the larger of the two d values, with a value of $d \sim 4.3\ a_0$ (2.3 Å). This d value, combined with a ~15% safety margin, suggested a b_{max} = 5.0 a_0 (2.6 Å); thus, the trajectories were sampled with impact parameters $0 < b < 5.0\ a_0$. Trajectories were stopped when the distance between any two atoms exceeded 12 a_0 (6.3 Å).

Energy conservation and spin contamination were checked at each time-step. Trajectories in which energy was not conserved to within 3 kcal mol^{-1} or spin contamination rose above $\langle S^2 \rangle = 2.5$ were flagged. Less than 1.3% and 10% of the B3LYP and BMK trajectories, respectively, failed to meet these acceptance criteria. Most problems were related to energy conservation, and were attributed to self-consistent field convergence to an excited electronic state. Trajectories that initially did not meet the criteria were run again using a different set of self-consistent field convergence tools, which improved the energy-conservation or spin-contamination problem in many cases. Results of the re-run trajectories were compared to their initial-run analogues, and the one that met or came closest to meeting the acceptance criteria was included in the analysis. To do otherwise would have resulted in an underestimate of the reaction cross-sections, as most of the problematic trajectories were reactive ones.

Reactive cross-sections (σ_R) were calculated from the QCT data using the expression:

$$\sigma_R = \frac{\pi}{p^2} \sum_{i=1}^{N_R} \frac{(2l_i + 1) l_{max}}{N_{total}} \tag{4.4}$$

where $p = (2\mu E_T)^{\frac{1}{2}}$ is the momentum of the reactant system, $l_i = b_i p$ is the angular momentum of the ith trajectory, and $l_{max} = b_{max} p$. N_R is the number of reactive trajectories in the set of N_{total} trajectories run.

The total collision cross-section, σ_{total}, was estimated using the Lennard-Jones parameters for O and CO_2 according to the expression for the total cross-section:

$$\sigma_{total} = \pi b_{total}^2 \tag{4.5}$$

where b_{total} is the radius beyond which no elastic, inelastic, or reactive scattering occurs. This radius can be estimated using the Lennard-Jones potential [*Hirschfelder et al.*, 1964]:

$$V(r) = 4\varepsilon \left[\left(\frac{r_e}{r} \right)^{12} - \left(\frac{r_e}{r} \right)^{6} \right] \tag{4.6}$$

where ε and r_e correspond to the well depth and the separation distance, respectively, at the potential minimum for an interaction between a pair of like atoms or molecules. The separation distance, r_e, is a measure of the atomic or molecular size. The values for the O-atom and for CO_2 have been estimated to be $r_e(O) = 2.78$ Å and $r_e(CO_2) = 3.897$ Å, respectively [*Hirschfelder et al.*, 1964; *Némethy et al.*, 1983]. Combining these radii with the usual method [*Hirschfelder and Meath*, 1967], i.e.,

$$r_e(O + CO_2) = \frac{1}{2} [r_e(O) + r_e(CO_2)] \tag{4.7}$$

we calculated an intermolecular interaction distance $r_e(O + CO_2) = b_{total}$ of 3.34 Å and a total collision cross-section of 125.2 a_0^2, which we used to calculate the relative product yields in Section 4.4.2.4. The theoretical reactive cross-section was divided by three for the comparison with experiment because the $O(^3P) + CO_2$ surface is triply degenerate at large $O(^3P)$–CO_2 separation distances (see Section 4.4.2.4).

Trajectories corresponding to oxygen isotope exchange were observed at all collision

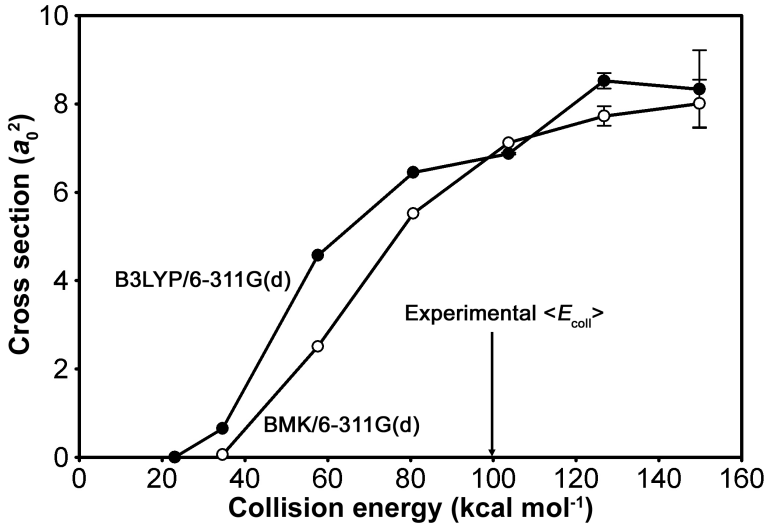

Figure 4.4: **Reactive scattering cross-sections for the O(^3P) + CO_2 isotope exchange reaction obtained from the QCT calculations.**

energies (see Table 4.2), and the resulting excitation functions were calculated from the QCT data (see Figure 4.4). These excitation functions had the same shape at the B3LYP/6-311G(d) and BMK/6-311G(d) levels of theory. The BMK excitation function was shifted to slightly higher energies compared to the B3LYP prediction, consistent with the 7.3 kcal mol^{-1} (0.32 eV) higher ZPE-corrected transition-state barrier for isotope exchange. Opacity functions for the isotope exchange reaction showed a slight decrease in reaction probability at smaller impact parameters as the collision energy increased (see Figure 4.5). $P(b)$ also appeared to reach a maximum near $b \sim 1.5$ – 2 a_0 (1 Å).

The O_2 + CO channel appears to open at higher energies than the exchange channel (see Table 4.2), consistent with the higher ZPE-corrected transition-state barriers for the oxygen-atom abstraction reaction of 37.5 kcal mol^{-1} (1.63 eV) and 39.5 kcal mol^{-1} (1.71

Table 4.2: Number of reactive QCTs observed at different collision energies.

Theory/Basis	**Products**	**Collision energy (eV)**						
		1.0	**1.5**	**2.5**	**3.5**	**4.5**	**5.5**	**6.5**
B3LYP/6-311G(d)	O + CO_2	1	16	54	66	68	80	78
	O_2 + CO	0	0	0	0	1	4	11
BMK/6-311G(d)	O + CO_2		2	37	66	80	76	80
	O_2 + CO		0	0	0	0	5	8

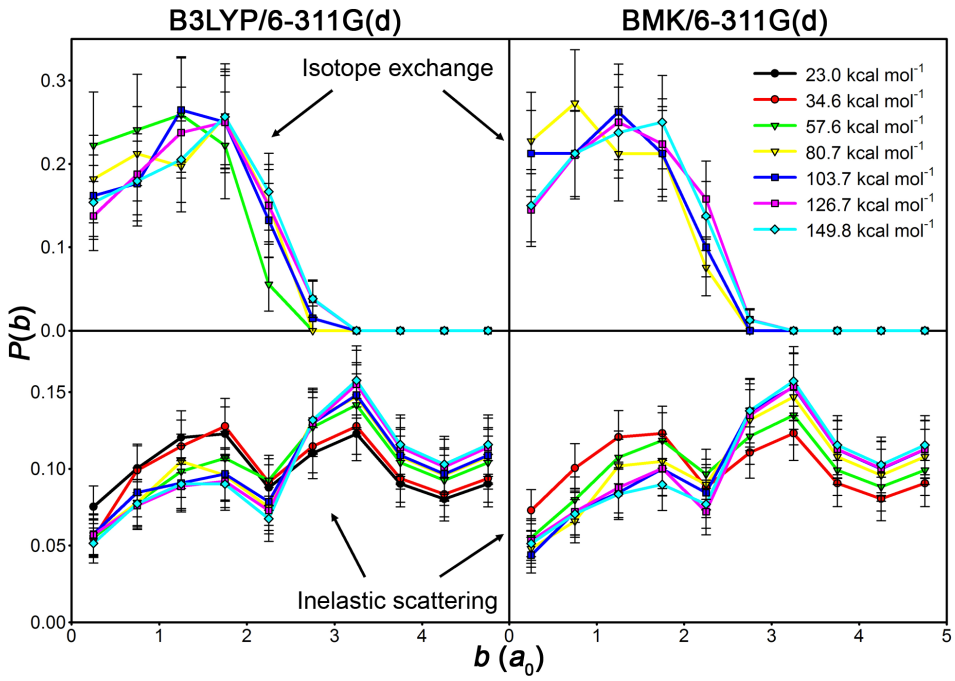

Figure 4.5: **Opacity functions for the $O(^3P)$ + CO_2 isotope exchange reaction and for inelastic scattering of the two reagents obtained from QCT calculations at the B3LYP/6-311G(d) and BMK/6-311G(d) levels of theory.**

eV) higher than the exchange channel barrier according to the B3LYP and BMK predictions, respectively. The B3LYP threshold is slightly higher than that calculated using BMK, which is consistent with a ZPE-corrected barrier 9.3 kcal mol^{-1} (0.40 eV) larger at BMK than at B3LYP. Because only a small number of oxygen-atom abstraction reactions were observed, even at collision energies significantly in excess of the calculated reaction barrier, the amount of mechanistic insight available from the $O(^3P)$ + $CO_2 \rightarrow O_2$ + CO reaction is limited.

A full discussion of the trajectory calculations, including the resulting product angular and translational energy distributions, can be found in Sections 4.4.2 and 4.5; they will be analyzed with the experimental data to elucidate the possible reaction mechanisms for each channel.

4.4 Experimental studies

4.4.1 Methods

Crossed-molecular-beam experiments were performed with an apparatus equipped with a hyperthermal atomic oxygen beam source at Montana State University, which was described in the preceding chapter. Briefly, a pulsed, hyperthermal beam of ~87% $^{16}O(^3P)$ and ~13% $^{16}O_2$ ($^3\Sigma_g^-$) was generated by laser-induced detonation of $^{16}O_2$ using a high-energy CO_2 TEA laser (6 – 7 J pulse^{-1}). Though initially broad in velocity distribution (6 – 9 km s^{-1}), a portion of the overall beam was velocity-selected with a chopper wheel (see Figure 3.1) at an average velocity $\langle v \rangle$ = 8262 m s^{-1}. The resulting beam was crossed at a right angle with a pulsed supersonic expansion of 98% $^{12}C^{18}O_2$. The scattered products were detected with a rotatable quadrupole mass spectrometer that collected number-density distributions for each product as a function of arrival time at the ionizer, $N(t)$, at a given laboratory angle, Θ, the angle at which the product scatters with respect to the direction of the reagent oxygen beam. Time-of-flight (TOF) distributions for ^{16}O, $^{18}O^{16}O$, $^{16}O^{12}C^{18}O$, and $^{12}C^{18}O_2$ were collected over a range of laboratory angles; at each angle, the TOF distribution was integrated to give a laboratory angular distribution, $N(\Theta)$. A forward-convolution method was then used to derive c.m. translational energy $P(E_T)$ and angular $T(\theta_{c.m.})$ distributions from the laboratory $N(t)$ and $N(\Theta)$ distributions [*Lee*, 1988], where $\theta_{c.m.}$ is the angle at which a product scatters with respect to the reagent oxygen direction in the c.m. frame. The canonical Newton diagrams used in this analysis are shown in Figure 4.6.

Laboratory TOF product distributions were measured every 2° between Θ = 6° – 54°. Scattered product TOF distributions were collected for 200 beam pulses for m/z = 16 ($^{16}O^+$) and 32 ($^{16}O_2{}^+$), for 1000 beam pulses for m/z = 46 ($^{16}O^{12}C^{18}O^+$), and for 500 beam pulses for m/z = 48 ($^{12}C^{18}O_2{}^+$). Scattered products at m/z = 34 ($^{18}O^{16}O^+$) were collected for 12000 beam pulses at Θ = 6° and 10° and 6000 beam pulses at Θ = 14°. Dwell time for each channel at the MCP was 1 μs. At a representative laboratory angle of 10°, integrated count rates were 1.1 × 10^7 s^{-1} for m/z = 16, 1.3 × 10^7 s^{-1} for m/z = 32, 1.4 × 10^4 s^{-1} for m/z = 34 ($^{18}O^{16}O^+$), 1.8 × 10^5 s^{-1} for m/z = 46 , and 4.2 × 10^6 s^{-1} for

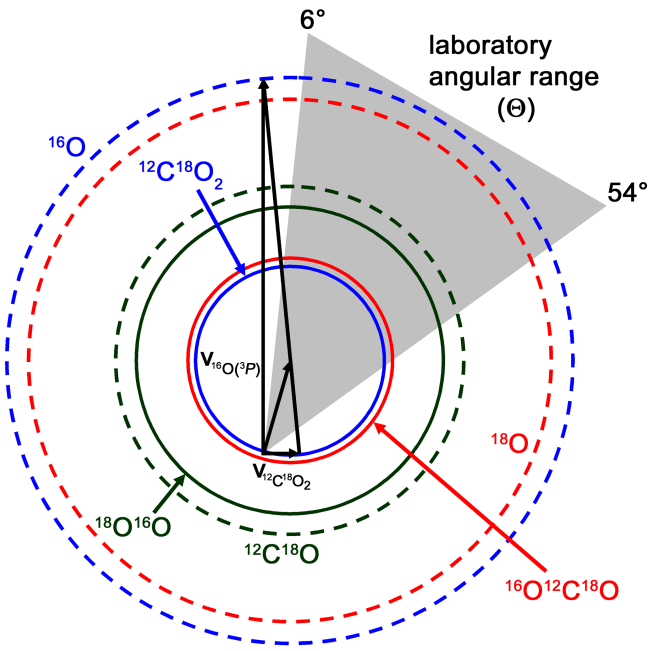

Figure 4.6: **Canonical Newton diagram for ^{16}O + $^{12}C^{18}O_2$ collisions at E_{coll} = 98.8 kcal mol^{-1}** The ^{16}O-atom beam velocity is 8262 m s^{-1} and the $^{12}C^{18}O_2$ beam velocity is 800 m s^{-1}. The shaded region indicates the range of laboratory angles probed. The radii of each circle represent the maximum recoil velocities of the following products of $^{16}O(^3P)$ + $^{12}C^{18}O_2$ collisions: $^{12}C^{18}O_2$ (blue solid) + ^{16}O (blue dashed), $^{16}O^{12}C^{18}O$ (red solid) + ^{18}O (red dashed), and $^{18}O^{16}O$ (green solid) + $^{12}C^{18}O$ (green dashed).

m/z = 48.

Three signal corrections were made before data analysis. First, we corrected for beam divergence at Θ = 6° – 16°. The divergent intensity with the $^{12}C^{18}O_2$ beam turned off was measured by obtaining TOF distributions at m/z = 16 and 32 from Θ = 6° – 16°. These TOF distributions were then scaled and subtracted from the corresponding experimental TOF distributions at m/z = 16 and 32 that had the $^{12}C^{18}O_2$ beam turned on. Uncertainties in the non-reactive and reactive scattering signals due to collisions of the divergent hyperthermal oxygen could not be quantified, however; they were instead considered in the analysis of the laboratory data, where collisions at crossing angles of 88°, 89°, 90°, 91°, and 92° were included during forward-convolution fitting. Adding more crossing angles did not affect the forward-convolution fits significantly. Second, we measured that the $^{12}C^{18}O_2$ beam contained 2% $^{16}O^{12}C^{18}O$ using the instrument's mass spectrometer. Thus, 2% of the inelastic scattering signal (m/z = 48) at each laboratory angle (Θ = 6° – 54°) was subtracted from

raw m/z = 46 ($^{16}O^{12}C^{18}O^+$) TOF distributions to obtain reactive-scattering-only distributions. Last, the hyperthermal O_2 beam contained 0.4% $^{18}O^{16}O$ (at natural isotopic abundances), so 0.4% of the non-reactive scattering signal (m/z = 32) was subtracted from the raw m/z = 34 ($^{18}O^{16}O^+$) TOF distributions to obtain reactive-scattering-only distributions.

4.4.2 Results

4.4.2.1 Non-reactive scattering of $^{16}O(^3P)$ and $^{12}C^{18}O_2$

The experiment mainly observed signals due to ^{16}O scattered with little deflection from its initial direction; these signals corresponded to the sum of elastic and inelastic scattering collisions of ^{16}O, which we could not resolve, so they will be referenced collectively as "scattered ^{16}O." Five representative laboratory-frame TOF distributions (m/z = 16), the c.m. angular and translational energy distributions and the laboratory-frame angular distribution are shown in Figure 4.7. Scattered ^{16}O had 85.6 kcal mol^{-1} total translational energy, or 87% of the available energy (see Figure 4.7B), on average. The experimental translational energy distribution was peaked at ~97 kcal mol^{-1}. The c.m. angular distribution for ^{16}O was highly peaked in the forward direction with little scattered intensity for $\theta_{c.m.} > 20^\circ$; however, the velocity and angular range for ^{16}O product detection in the experiment prevented the detection of backward-scattered ^{16}O (see Newton diagram in Figure 4.6). Some dependence of the c.m. translational energy distribution on the c.m. angular distribution was observed in the ^{16}O TOF data; the forward-convolution simulations became increasingly faster than the data at larger laboratory and c.m. angles (e.g, $\Theta = 20^\circ$, 30°, and 40° in Figure 4.7A). We also note that the c.m. angular distribution for scattered ^{16}O at $\theta_{c.m.} \sim 0^\circ$ is an extrapolation because of high background from the hyperthermal oxygen source at the small laboratory angles corresponding to small c.m. angles for ^{16}O. Most of the ^{16}O probably scatters forward through high-impact-parameter collisions, but the limited constraints on the $\theta_{c.m.} \sim 0^\circ$ angular distribution (e.g., the laboratory-frame angular distribution, which only probes $\Theta = 6^\circ$) increase the uncertainty in that part of the c.m. angular distribution. This extrapolation had a small effect on the relative product yield measurements (see Section 4.4.2.4), but did not alter the results qualitatively.

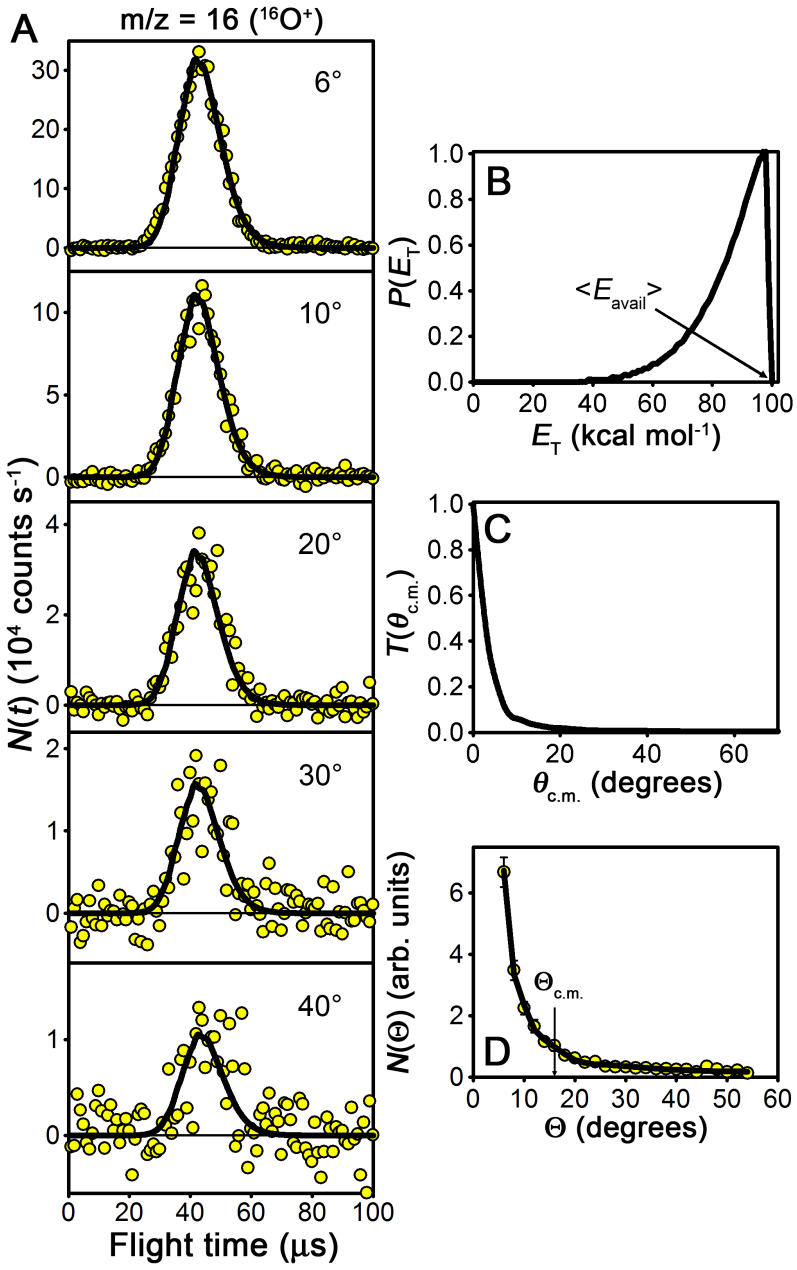

Figure 4.7: **Laboratory inelastic scattering data detected at *m/z* = 16.** (**A**) Laboratory TOF, (**B**) c.m. translational energy, and (**C**) c.m. and (**D**) laboratory angular distributions for inelastically scattered ^{16}O products from ^{16}O + $^{12}C^{18}O_2$ collisions at $\langle E_{coll} \rangle$ = 98.8 kcal mol^{-1}. The circles in (**A**) and (**D**) are experimental data, while the lines are the best-fit forward-convolution simulations of the experimental data derived from the c.m. translational energy and angular distributions shown in (**B**) and (**C**), respectively. The error bars in (**D**) represent 2σ uncertainties in the integrated experimental TOF distributions (see Appendix 4.7). These data indicate that ^{16}O is scattered mainly in the forward direction with little change in its initial direction or velocity.

The experiment mainly observed $^{12}C^{18}O_2$ scattered opposite its initial direction in the c.m. frame (see Newton diagram in Figure 4.6). Detected $^{12}C^{18}O_2$ products (m/z = 48) showed best-fit c.m. translational energy distributions that were both broader and lower in energy, on average, than that obtained for forward-scattered ^{16}O. Furthermore, a single pair of $P(E_T)$ and $T(\theta_{c.m.})$ distributions was not sufficient to describe the m/z = 48 TOF distributions. Consequently, a second pair of $P(E_T)$ and $T(\theta_{c.m.})$ distributions was included in the fit of inelastically scattered $^{12}C^{18}O_2$; five representative laboratory-frame TOF distributions, the c.m. angular and translational energy distributions, and the laboratory-frame angular distribution obtained from $^{12}C^{18}O_2$ product detection are shown in Figure 4.8, along with the c.m. velocity-flux diagram in Figure 4.9. The first $P(E_T)$ and $T(\theta_{c.m.})$ pair for inelastically scattered $^{12}C^{18}O_2$ described the scattering at $\theta_{c.m.} < 120^\circ$. In this region, the angular distribution was peaked near $\theta_{c.m.} = 60^\circ$, though the probability of scattered products was roughly constant for all $\theta_{c.m.} < 60^\circ$ before decaying steadily at $\theta_{c.m.} > 60^\circ$. The corresponding translational energy distribution was peaked at ~39 kcal mol^{-1} with an average $\langle E_T \rangle$ = 40.1 kcal mol^{-1}, or 41% the available energy. The second $P(E_T)$ and $T(\theta_{c.m.})$ pair for inelastically scattered $^{12}C^{18}O_2$ described the scattering at $60^\circ < \theta_{c.m.} < 125^\circ$ (corresponding to the maximum $\theta_{c.m.}$ observed in the experiment); this range overlapped, in the sideways-scattering region, with the first pair. The second $T(\theta_{c.m.})$ distribution increased rapidly from $\theta_{c.m.} = 60^\circ$ peaked near $\theta_{c.m.} = 120^\circ$. It decayed quickly at $\theta_{c.m.} > 120^\circ$, although this part of the distribution is uncertain because our experiment did not probe it directly. The translational energy distribution was peaked at 65 kcal mol^{-1} with an average $\langle E_T \rangle$ = 63.8 kcal mol^{-1}, or 65% the available energy. Mechanistic implications of the additional $P(E_T)$ and $T(\theta_{c.m.})$ distributions will be addressed in Section 4.5.

While the forward-convolution laboratory fitting method produced c.m. angular and translational energy distributions that yielded good fits to the data in Figures 4.7 and 4.8, they may not be unique fits to the data because of the temporal and angular width of the incident O(^3P) source beam and the low resolution and SNR in the resulting TOF distributions. Small changes to the c.m. angular and translational energy distributions still produced good fits to the data that were within the uncertainty bounds of the laboratory-frame

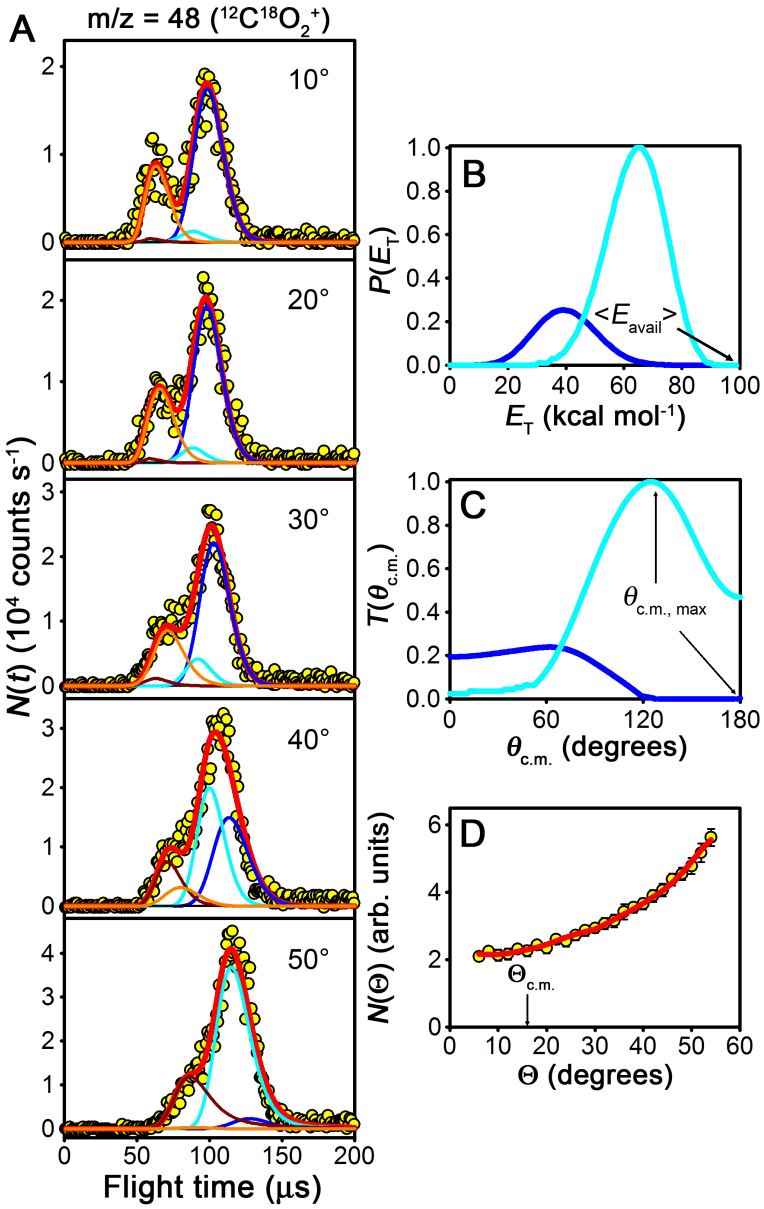

Figure 4.8: **Laboratory inelastic scattering data detected at m/z = 48.** (**A**) Laboratory TOF, (**B**) c.m. translational energy, and (**C**) c.m. and (**D**) laboratory angular distributions for inelastically scattered $^{12}C^{18}O_2$ products from ^{16}O + $^{12}C^{18}O_2$ collisions at $\langle E_{coll} \rangle$ = 98.8 kcal mol^{-1}. The circles in (**A**) and (**D**) are experimental data, while the lines (dark blue and cyan) are the best-fit forward-convolution simulations of the experimental data derived from the c.m. translational energy and angular distributions shown in (**B**) and (**C**), respectively. The error bars in (**D**) represent 2σ uncertainties in the integrated experimental TOF distributions (see Appendix 4.7). The orange and brown lines correspond to products of $^{16}O_2$ + $^{12}C^{18}O_2$ collisions, and they are discussed in Appendix 3.A. A single c.m. translational energy and angular distribution for each collision partner was insufficient to describe the TOF distributions of inelastically scattered $^{12}C^{18}O_2$, suggesting a scattering dependence on impact parameter.

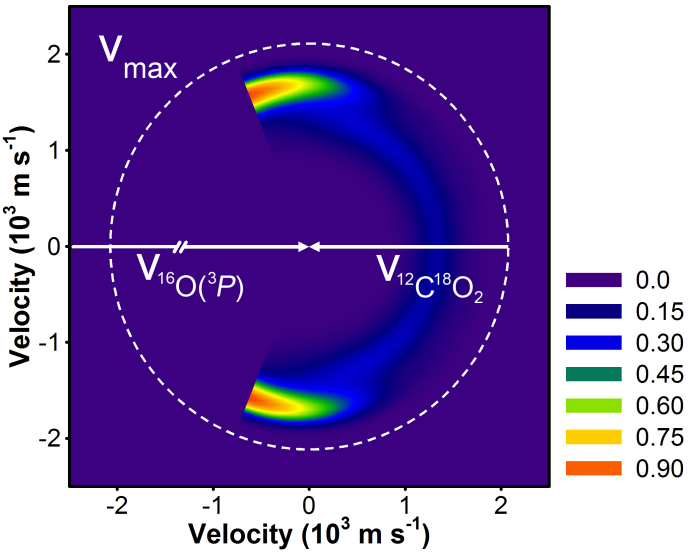

Figure 4.9: **Velocity-flux contour diagram for inelastically scattered $^{12}C^{18}O_2$ from $^{16}O(^3P)$ + $^{12}C^{18}O_2$ collisions in the center-of-mass frame.** The white arrows are the initial $^{16}O(^3P)$ and $^{12}C^{18}O_2$ velocity vectors, and the dashed white line is the maximum recoil velocity for $^{12}C^{18}O_2$ (v_{max}). Only the c.m. angles for which the experiment were sensitive are shown; inelastically scattered $^{12}C^{18}O_2$ from high-impact-parameter collisions are not shown, as their flux would be off-scale. Strong coupling of the $P(E_T)$ and $T(\theta_{c.m.})$ distributions was observed.

angular distribution (see Figures 4.7D and 4.8D), but larger, qualitative changes to the c.m. angular and translational energy distributions did not. Consequently, general statements regarding the scattering direction and degree of energy transfer in the c.m. frame can be made with some certainty.

The c.m. angular and translational energy distributions derived from the QCT calculations at E_{coll} = 4.5 eV (103.7 kcal mol^{-1}) are shown in Figure 4.10 for comparison with the experimental results for scattered ^{16}O. Center-of-mass angular and translational energy distributions for inelastic scattering obtained from the QCT calculations were in qualitative agreement with the laboratory data, although there are noticeable quantitative disagreements. The theoretical c.m. angular distribution showed fewer scattered products at $\theta_{c.m.} < 20^\circ$ and more scattered products at $40^\circ < \theta_{c.m.} < 90^\circ$. In addition, the theoretical c.m. translational energy distribution had a sharper peak at high energies and a broader tail at low energies, although the average translational energies were similar ($\langle E_T \rangle$ = 85 and 86 kcal mol^{-1} for B3LYP and BMK, respectively). However, forward convolution of these dis-

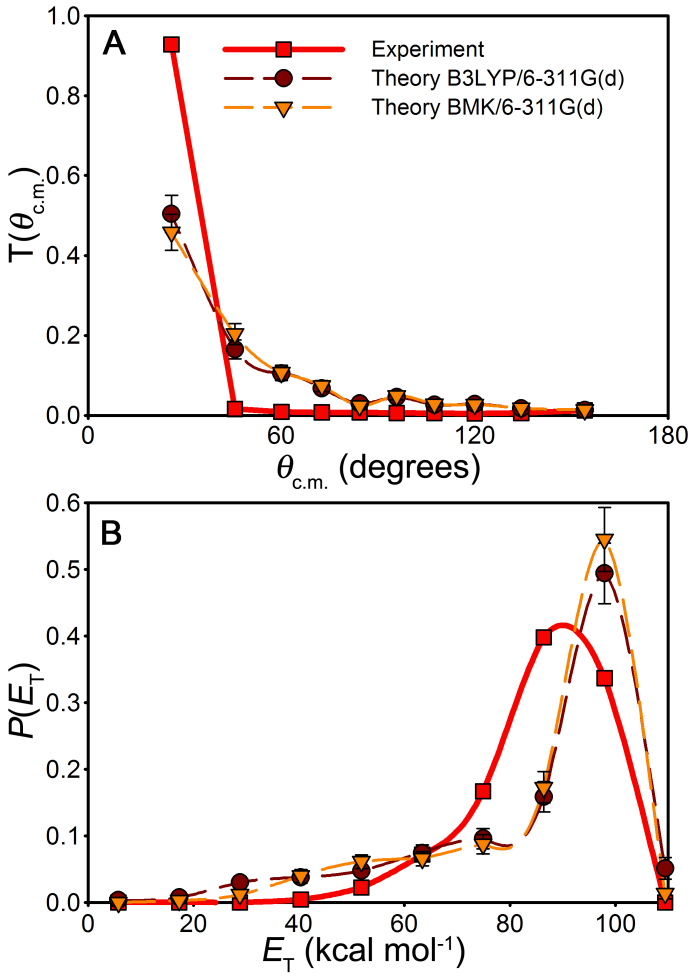

Figure 4.10: **Comparison of laboratory and theoretical c.m. (A) angular and (B) translational energy distributions for inelastic scattering of O(^3P) and CO_2 at $\langle E_{coll} \rangle \approx$ 100 kcal mol^{-1}.** Distributions obtained from the inelastic scattering of ^{16}O and from the QCTs are shown here. They were binned (midpoints are shown, connected by spline curves) to provide better statistics for comparison. Both B3LYP and BMK theories show fewer forward-scattered products than were observed in the experiment. Also, the theories predict a translational energy distribution that is more highly peaked at high energies and that has a longer tail at low energies.

tributions resulted in simulations of the laboratory data that underestimated the proportion of products scattered to low laboratory angles (i.e., $\Theta = 6^\circ$, 8°, and 10°) and overestimated the low-energy tail in the TOF distributions. Some of this disagreement may be attributable to the $\sim$14 kcal mol^{-1} width of the initial collision energy distribution, the inability of the experiment to resolve elastic- from inelastic-scattering contributions to the ^{16}O signal, and the observed coupling between the c.m. angular and translational energy distributions (see Section 4.5). Still, these laboratory results are consistent with previous studies of hyperthermal O(^3P) scattering from small molecules; a forward-scattering preference and minimal energy transfer was also observed in our earlier studies of D_2, CO, and C_2H_6 collisions [*Brunsvold et al.*, 2008; *Garton et al.*, 2006, 2009].

4.4.2.2 $^{16}O(^3P) + {}^{12}C^{18}O_2 \rightarrow {}^{18}O + {}^{16}O^{12}C^{18}O$

As we reported in the preceding chapter, some of the fastest reactively scattered $^{16}O^{12}C^{18}O$ was attributed to an O-atom exchange reaction between fast-moving $^{16}O_2$ and $^{12}C^{18}O_2$ at $E_{\text{coll}} \sim 160$ kcal mol^{-1}. We describe here the results for the remaining product signal at $m/z = 46$, which we attribute to the O(^3P) + CO_2 isotope exchange reaction. Products of the isotope exchange reaction near 100 kcal mol^{-1} scattered mainly in the backward direction ($\theta_{\text{c.m.}} = 180^\circ$), as implied by the five representative laboratory-frame TOF distributions, the c.m. angular and translational energy distributions, and the laboratory-frame angular distribution shown in Figure 4.11. The product c.m. velocity-flux diagram is shown in Figure 4.12. Significant forward and sideways scattering of products was also observed in addition to backward scattering; the $T(\theta_{\text{c.m.}})$ distribution indicates that products scattered to $0^\circ < \theta_{\text{c.m.}} < 90^\circ$ do so with nearly equal probability, and that scattered products become increasingly more probable as $\theta_{\text{c.m.}}$ approaches 180°. On average, the two products had 34.8 kcal mol^{-1} of total translational energy, or 35% of the available energy (see Figure 4.11B). The peak of the experimental translational energy distribution, $P(E_T)$, was $\sim$30 kcal mol^{-1}. These results indicate a significant transfer of translational energy to internal degrees of freedom of the products, which is characteristic of reactions with significant barriers (e.g., $\sim$25 kcal mol^{-1}).

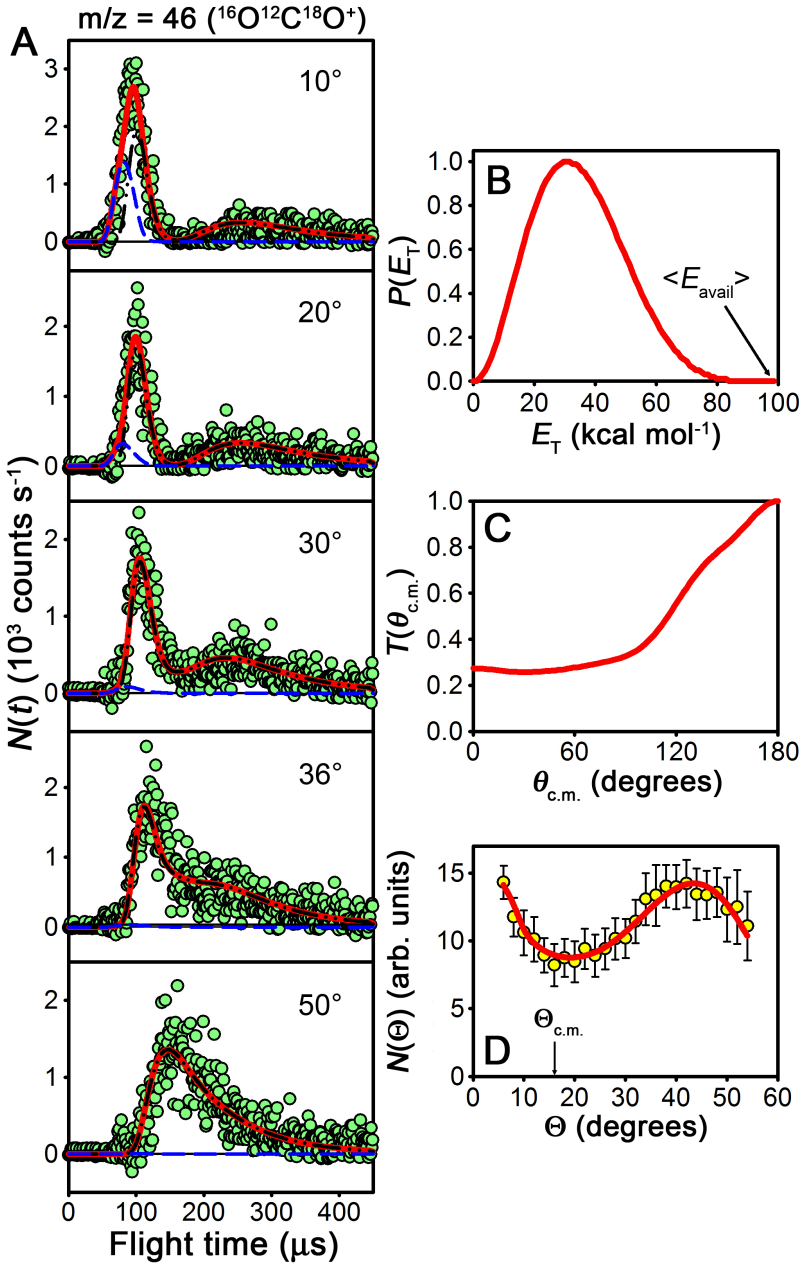

Figure 4.11: **Laboratory reactive scattering data detected at *m/z* = 46.** (**A**) Laboratory TOF, (**B**) c.m. translational energy, and (**C**) c.m. and (**D**) laboratory angular distributions for $^{16}O^{12}C^{18}O$ products of the $^{16}O(^3P)$ + $^{12}C^{18}O_2$ → ^{18}O + $^{16}O^{12}C^{18}O$ reaction at $\langle E_{coll} \rangle$ = 98.8 kcal mol^{-1}. The circles in (**A**) and (**D**) are experimental data, while the lines are the best-fit forward-convolution simulations of the experimental data derived from the c.m. translational energy and angular distributions shown in (**B**) and (**C**), respectively. In (**A**), the best-fit forward-convolution simulations of $^{16}O^{12}C^{18}O$ products from $^{16}O(^3P)$ + $^{12}C^{18}O_2$ collisions (black dot-dashed lines) are shown with those from $^{16}O_2$ + $^{12}C^{18}O_2$ collisions at $\langle E_{coll} \rangle$ = 158.1 kcal mol^{-1} (blue dashed lines). The error bars in (**D**) represent 2σ uncertainties in the integrated experimental TOF distributions (see Appendix 4.7).

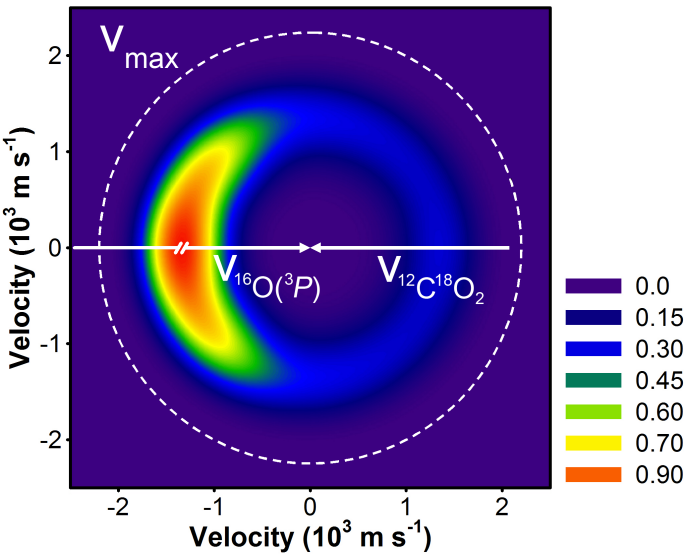

Figure 4.12: **Velocity-flux contour diagram for $^{16}O^{12}C^{18}O$ products of $^{16}O(^3P)$ + $^{12}C^{18}O_2$ collisions in the center-of-mass frame.** The white arrows are the initial $^{16}O(^3P)$ and $^{12}C^{18}O_2$ velocity vectors, and the dashed white line is the maximum recoil velocity for $^{16}O^{12}C^{18}O$ (v_{max}). $^{16}O^{12}C^{18}O$ products are scattered mainly in the same direction as the initial $^{12}C^{18}O_2$ velocity vector.

The theoretical c.m. angular and translational energy distributions derived from the QCT calculations at E_{coll} = 4.5 eV (103.7 kcal mol^{-1}) are plotted with the experimental data for comparison in Figure 4.13. In general, good agreement between experiments and the theoretical predictions was observed. The experimental best-fit c.m. angular distribution agreed nearly quantitatively for products scattered in the forward direction (small $\theta_{c.m.}$), while only qualitative agreement was found for products scattered in the backward direction (large $\theta_{c.m.}$). The preference for backward-scattered $^{16}O^{12}C^{18}O$ products suggested by the QCT calculations is also observed in the experimental data. $\langle E_T \rangle$ for the experimental $P(E_T)$ is in good agreement, within uncertainty, with those obtained from the B3LYP ($\langle E_T \rangle$ = 43 $\pm$ 15%) and BMK ($\langle E_T \rangle$ = 47 $\pm$ 16%) trajectories. Qualitative aspects of the energy transfer during reactive scattering collisions appear to be reproduced in the QCT results, namely, that the product $^{16}O^{12}C^{18}O$ has a significant amount ($\geq$ 50 kcal mol^{-1}) of internal energy, on average. The experimental peak E_T, however, is slightly less than the most probable translational energies predicted by the QCT calculations, $\sim$40 kcal mol^{-1}.

This mild disagreement in the shape of the $P(E_T)$ distribution may arise from uncer-

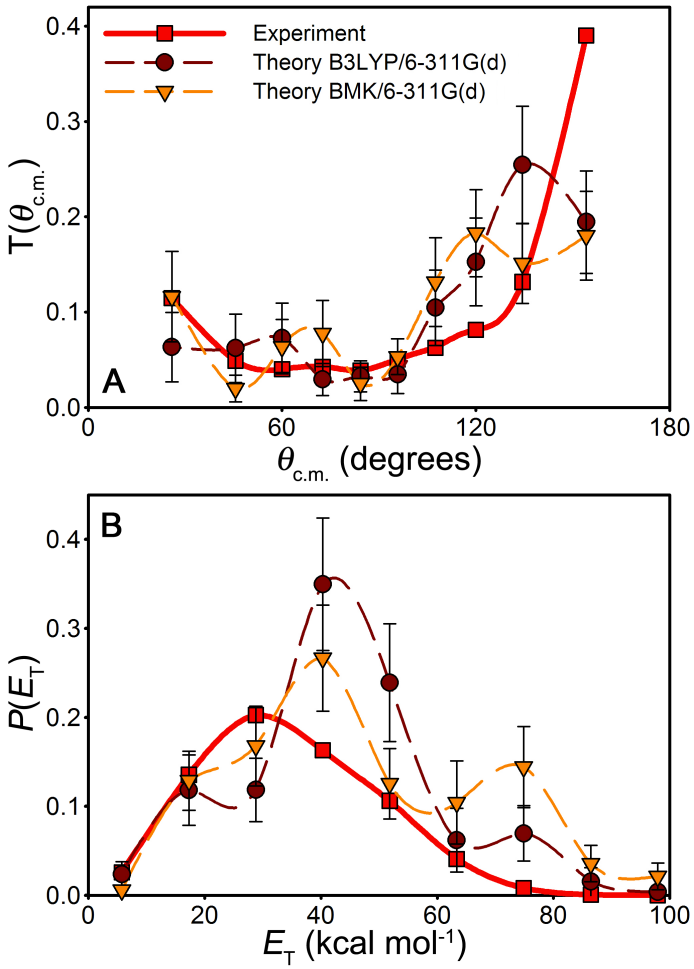

Figure 4.13: **Comparison of laboratory and theoretical c.m. (A) angular and (B) translational energy distributions for the O(^3P) and CO_2 isotope exchange reaction at $\langle E_{\text{coll}} \rangle \approx$ 100 kcal mol^{-1}.** Distributions obtained from the inelastic scattering of ^{16}O and from the QCTs are shown here. They were binned (midpoints are shown, connected by spline curves) to provide better statistics for comparison. Both B3LYP and BMK theories predict fewer backward-scattered products than were observed in the experiment. Also, the theories predict a translational energy distribution that is peaked at slightly higher energies.

tainties in the experiment and in the forward-convolution analysis. First, the broad O(^3P) velocity distribution in the experiment, and the resulting broad collision energy distribution, could mask any underlying structure in the $P(E_T)$ distribution if the location of the peak in the $P(E_T)$ distribution depends on collision energy. Indeed, the theoretical excitation functions indicate that the reaction cross-section is sensitive to collision energy in near E_{coll} = 100 kcal mol^{-1} (see Figure 4.4). Second, the presence of the O_2 + CO_2 isotope exchange channel, which was not resolved from the forward-scattered $^{16}O^{12}C^{18}O$ peak in the laboratory TOF, renders the higher-E_T portion of the $P(E_T)$ less certain. Constraints from the backward-scattered component of the laboratory TOF distributions were also limited due to the t^{-3} dependence of the scattered product intensity in the laboratory-to-c.m.-frame Jacobian transformation (see Eq. 3.3), which reduces the instrument's sensitivity to backward-scattered products. Consequently, the angular distribution of products near $\theta_{c.m.}$ = 180° is less certain, and the observed disagreement between experimental and theoretical c.m. angular and translational distributions could be refined with additional measurements. Last, some uncertainty in the average and peak of the product translational energy distribution in the QCT data arises from the binning process used to obtain better statistics in the distribution; the width of each E_T bin was ~11.5 kcal mol^{-1}, so disagreements in the $P(E_T)$ peak locations between theory and experiment on the order of 10 kcal mol^{-1} are not unreasonable.

4.4.2.3 $^{16}O(^3P)$ + $^{12}C^{18}O_2 \rightarrow {}^{18}O^{16}O$ + $^{12}C^{18}O$

Reactively scattered products at m/z = 34 were clearly resolved at Θ = 6°, barely detectable at Θ = 10°, and not detectable at Θ = 14° (see Figure 4.14). While this laboratory-frame angular dependence may imply that $^{18}O^{16}O$ products are mainly forward-scattered, we cannot rule out backward scattering because the experiment was not sensitive to it (see Newton diagram in Figure 4.6); the signal corresponding to the counterproducts at m/z = 30 ($^{12}C^{18}O^+$) could not be resolved because of high background signal from $^{12}C^{18}O_2$ fragmentation at the ionizer. We obtained a c.m. translational distribution peaked at 56 kcal mol^{-1} from the laboratory data, which indicated that $^{18}O^{16}O$ + $^{12}C^{18}O$ products had 55.0

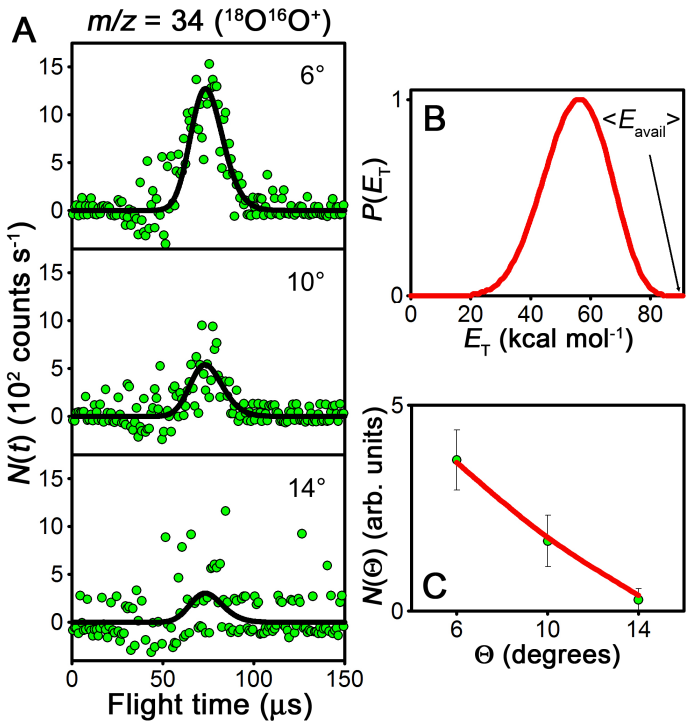

Figure 4.14: **Laboratory reactive scattering data detected at m/z = 34.** (**A**) Laboratory TOF, (**B**) c.m. translational energy, and (**C**) laboratory angular distributions for $^{18}O^{16}O$ products of the $^{16}O(^3P)$ + $^{12}C^{18}O_2 \rightarrow {}^{18}O^{16}O$ + $^{12}C^{18}O$ reaction at $\langle E_{coll} \rangle$ = 98.8 kcal mol^{-1}. The circles in (**A**) and (**C**) are experimental data, while the lines are the best-fit forward-convolution simulations of the experimental data derived from the c.m. translational energy distribution shown in (**B**). Experimental sensitivity was not sufficient to obtain a full c.m. angular distribution, so a $T(\theta_{c.m.})$ distribution is not shown. The error bars in (**C**) represent 2σ uncertainties in the integrated experimental TOF distributions (see Appendix 4.7).

kcal mol^{-1} translational energy, or 61% of the available energy, on average. No products were detected at m/z = 36 ($^{18}O_2{}^+$), which would have corresponded to an oxygen-atom abstraction mechanism more complex than simple stripping. Qualitatively, these results are consistent with the QCT results, which predicted a lower reactive cross-section for the oxygen abstraction channel than for the isotope exchange channel.

4.4.2.4 Relative product yields

Experimental relative product yields for $^{16}O(^3P)$ + $^{12}C^{18}O_2$ collisions at $\langle E_{coll} \rangle$ = 98.8 kcal mol^{-1} were calculated from the integrated cross-sections for each channel, which were obtained from the forward-convolution simulations of the TOF data. Because the signal at m/z = 46 contained contributions from both $^{16}O(^3P)$ + $^{12}C^{18}O_2$ and $^{16}O_2$ + $^{12}C^{18}O_2$ collisions,

Table 4.3: Comparison of experimental and theoretical yields for the products of $O(^3P)$ + CO_2 collisions near 100 kcal mol^{-1}*

	Non-reactive scattering	Oxygen isotope exchange
Experiment	98.4%	1.6%
B3LYP/6-311G(d)	98.2%	1.8%
BMK/6-311G(d)	98.1%	1.9%

*Uncertainty bounds in the experimental estimates are probably less than ± 0.25%, based on the uncertainties in the integrated count rates at m/z = 46. Uncertainties in the QCT-derived relative yields are less than ± 0.1%.

the forward-convolution fits for $^{16}O_2$ + $^{12}C^{18}O_2$ isotope exchange were subtracted from the laboratory TOF data before the $^{16}O(^3P)$ + $^{12}C^{18}O_2$ cross-section was calculated. Resulting integrated cross-sections were scaled by their electron-impact ionization cross-sections and fragmentation patterns for the comparison; the transmission through the quadrupole mass filter was assumed to be similar for all the small molecules examined here. Using this method, we calculated branching fractions for non-reactive scattering (98.5%), oxygen-atom abstraction (0.0004%), and oxygen isotope exchange (1.6%) based on the integrated cross-sections obtained at m/z = 16, 34, and 46, respectively. The oxygen-atom abstraction yield is a lower limit because only a portion of the Newton sphere was observed. The oxygen isotope exchange yield is an upper limit because we compared the integrated cross-section of $^{16}O^{12}C^{18}O$ products to the yield of scattered ^{16}O only; the strongly coupled $P(E_T)$ and $T(\theta_{c.m.})$ distributions for inelastic scattering make momentum-matching of ^{16}O and $^{12}C^{18}O_2$ products difficult.

Our experimental branching fractions for the isotope exchange reaction at $\langle E_{coll} \rangle$ = 98.8 kcal mol^{-1} and those calculated from the QCT calculations at E_{coll} = 4.5 eV (103.7 kcal mol^{-1}) agree within 0.3%, despite a difference of 5 kcal mol^{-1} in the collision energy (see Table 4.3). This agreement could be coincidental because both the theoretical and laboratory data have significant uncertainties when defining the total cross-section, but our analysis suggests that the agreement persists in spite of these uncertainties. First, Eq. 4.4 shows that the theoretical calculation for the total cross-section depends on the square of maximum impact parameter sampled for reactive scattering (b_{max}), but examination of the theoretical opacity function for the oxygen isotope exchange reaction (Figure 4.5) indicates

that no reactions occur beyond $b = 3.5\ a_0$, so the reactive cross-section should be sufficiently converged with a $b_{max} = 5.0\ a_0$. Second, the accuracy of the laboratory integrated cross-sections depends on the accuracy of the best-fit c.m. angular and translational energy distributions, but our sensitivity study on the $\theta_{c.m.} \rightarrow 0^\circ$ extrapolation we used for scattered ^{16}O resulted in the non-reactive scattering and oxygen isotope-exchange branching fractions fluctuating ~0.5% when the scattered intensity at $\theta_{c.m.} < 4^\circ$ was varied between twice the best-fit value and zero. Third, the oxygen-atom abstraction reaction contributes to the overall reactive cross-section, but this channel had a negligible contribution to the overall product yield based on the small number of reactive trajectories observed in the QCT calculations and the small amount of $^{18}O^{16}O$ detected in the experiment. Consequently, the agreement between the theoretically derived and experimental relative product yields for the oxygen isotope exchange reaction should be robust.

The theoretical reactive cross-sections (Eq. 4.4) were divided by three for the comparison with experiment because the $O(^3P)$ + CO_2 surface is triply degenerate at large $O(^3P)$–CO_2 separation distances;. All three electronic states were probed by the experiment, but only one ($^3A''$) was probed in the QCT calculations. Whether the two additional states (e.g., $^3A'$) lead to reaction under our experimental conditions is unknown, but the good agreement between theory and experiment is consistent with the other two electronic surfaces being either repulsive or unimportant for producing $^{16}O^{12}C^{18}O$ at these collision energies. If the barrier to isotope exchange on the $^3A'$ surface is close to the one the $^3A''$ surface, isotope exchange on the $^3A'$ surface could also contribute to the experimental product yield; the current theoretical product yield, therefore, should be treated as a lower limit when compared to the experimental value. Degenerate triplet states were also a concern in our study of $O(^3P)$ + C_2H_6 collisions, but the laboratory relative product yields there also agreed, within uncertainty, with those derived from QCT calculations [*Garton et al.*, 2009].

4.5 Discussion

4.5.1 Theoretical studies

Our electronic structure calculations yielded some disagreements with previous work [*Bennett et al.*, 2004; *Froese and Goddard*, 1993; *Mebel et al.*, 2004; *Yang et al.*, 2005]. First, we reported a geometry and energy for TS1 structure that was significantly different from that predicted by Mebel and coworkers calculated at the CASSCF(16,13)/6-311G(d) level of theory (see Figure 4.2) [*Bennett et al.*, 2004; *Mebel et al.*, 2004]. For example, in *Mebel et al.*'s $^3A'$ TS1 structure, the longest C–O bond was 0.08 Å shorter, the shortest C–O bond was $\sim$0.02 Å longer, and the most acute bond angle was 17° smaller than in our CCSD(T)/aug-cc-pVTZ structure. Interestingly, our $^3A''$ TS1 structure shows smaller disagreements with the $^3A'$ TS1 structures calculated by Froese and Goddard at the HF/6-31G* and MP2/6-31G* levels of theory. These differences in geometries and the difference in symmetry yielded a TS1 energy 11 kcal mol^{-1} higher in *Mebel et al.*'s CCSD(T)/6-311+G(3df) calculation than in our calculation. *Mebel et al.* did note that their truncated (16,13) active space was a clear shortcoming of their study; it was chosen over the full-valence (22,16) active space due to computational limitations. Second, our calculations indicated that the lowest-energy triplet PES near TS1 had $^3A''$ symmetry, not $^3A'$ symmetry, as others had reported [*Bennett et al.*, 2004; *Froese and Goddard*, 1993; *Mebel et al.*, 2004]. We examined this discrepancy first by calculating the single-point CCSD(T)/aug-cc-pVTZ energy of Froese and Goddard's "T9" structure at both orbital symmetries. In this case, the $^3A'$ energy was $\sim$10 kcal mol^{-1} above the $^3A''$ energy. We also attempted to optimize a TS1-like $^3A'$ structure at the CCSD(T)/aug-cc-pVTZ and W4 levels of theory, but we found self-consistent field convergence problems similar to those reported by Froese and Goddard and thus could not locate any stationary points. The $^3A''$ state of CO_3 near TS1, then, appears to be lower in energy than the $^3A'$ state.

We argue that these discrepancies were caused by the differing treatment of dynamical correlation in this study and others. The electronic structure of ground singlet CO_3 displays vibronic coupling with an array of Jahn-Teller states [*Kowalczyk and Krylov*, 2007; *Liu et al.*,

2009], and the resulting energy minima required a high level of dynamical correlation to represent correctly; because of the large number of electronic states within several eV of the lowest triplet PES, vibronic coupling (and therefore dynamical correlation) is likely important here as well. Multiconfigurational self-consistent field methods like CASSCF (used by *Mebel et al.* for geometry optimizations) do not treat dynamical correlation, and this shortcoming has been implicated in the poor representation of the singlet-CO_3, NO_3, and para-benzyne radicals with these methods [*Crawford et al.*, 2001; *Eisfeld and Morokuma*, 2000; *Kowalczyk and Krylov*, 2007]. High-level dynamical correlation is included in coupled-cluster methods, which generally yield more accurate thermochemical properties for this class of problems. Furthermore, the agreement between our TS1, TS2, and CO_3 energies and those calculated using the W4 method (J. M. L. Martin, private communication) suggest that single-reference calculations with high-level treatment of dynamical correlation can describe the triplet stationary points appropriately. Multi-reference character on other regions of the PES could still be important, however, and is not ruled out by the correspondence between the CCSD(T) and W4 calculations at the stationary points.

If strong vibronic coupling on the low-lying electronic states of CO_3 is important during reactive trajectories, it could lead to a misrepresentation of the PES curvature by the B3LYP and BMK methods during the QCT calculations. *Russ et al.* [2004] noted that B3LYP underestimated the magnitude of vibronic interactions in the B–N–B and C_3^+ model systems, and attributed this tendency to the behavior of the Kohm-Sham molecular orbital Hessian near conical intersections. Because the Kohm-Sham Hessian is common to both B3LYP and BMK theories, both functionals are subject to the same tendency. Large fractions of Hartree-Fock exchange mixed into the BMK functional for improved barrier height prediction may also result in unintended symmetry-breaking on the CO_3 PES [*Sherrill et al.*, 1999], as was the case for the CO_3 minimum (see Figure 4.2). The results of these calculations are compared with the experimental results below.

4.5.2 Non-reactive scattering of $O(^3P)$ and CO_2

Non-reactive $^{16}O(^3P)$ + $^{12}C^{18}O_2$ collisions mainly scattered products with little change in the initial direction or speed, although some products scattered in directions sideways and opposite their initial direction; these products had lower average velocities. Products showing little deflection from their initial trajectories probably arise from high-impact-parameter collisions, while products that are highly deflected probably arise from low-impact-parameter collisions. These two molecular regimes were supported qualitatively by the theoretical opacity functions (see Figure 4.5), which display separate peaks at low (1.75 a_0) and high (3.25 a_0) impact parameters. While large impulsive energy transfer was observed for hyperthermal collisions of Ar and $O(^3P)$ with C_2H_6 at low impact parameters [*Brunsvold et al.*, 2004; *Garton et al.*, 2009; *Tasic et al.*, 2007], large energy transfer was also observed for "failed" reactive collisions of hyperthermal $O(^3P)$ and CO; the CO_2* complex resulting from these collisions can dissociate to yield products corresponding to isotope exchange or inelastic scattering, depending on the identity of the dissociating oxygen atom. This mechanism resulted in a low-energy tail in the translational energy distribution for inelastic scattering of $O(^3P)$ + CO [*Brunsvold et al.*, 2008].

Our analysis of inelastically scattered $^{12}C^{18}O_2$ molecules indicated that one pair of $P(E_T)$ and $T(\theta_{c.m.})$ distributions was insufficient to simulate the laboratory data accurately. This observation corresponds to a breakdown of the assumption that the c.m. angular and translational energy distributions are separable. Our use of two pairs of $P(E_T)$ and $T(\theta_{c.m.})$ distributions to fit the laboratory data is similar to previous studies where inelastic scattering of Cl + C_3H_8 and hyperthermal $O(^3P)$ + C_2H_6 were investigated [*Blank et al.*, 1998; *Garton et al.*, 2009]. In both the previous cases and in the present case, the polyatomic species had a large number of degrees of freedom into which translational energy can be transferred upon collision. Consequently, a dependence of energy transfer on the impact parameter is not unexpected; different impact parameters may preferentially excite different degrees of freedom. In the system studied here, the product translational energy decreases as $^{12}C^{18}O_2$ becomes more forward-scattered (small Θ, corresponding to low-impact-parameter collisions), implying that $^{12}C^{18}O_2$ becomes increasingly internally excited as O–CO_2 collisions

become more rebound-like. The type and mechanism of internal excitation are uncertain, however, because the "failed" reaction might also contribute to the observed c.m. angular and translational energy distributions of forward-scattered $^{12}C^{18}O_2$. We note that our experimental data did not display a slow tail in the ^{16}O TOF distributions characteristic of the "failed" reaction in the $O(^3P)$ + CO system.

4.5.3 Oxygen isotope exchange, $O(^3P) + CO_2 \rightarrow O + CO_2$

Laboratory data for the isotope exchange reaction at $\langle E_{coll} \rangle$ = 98.8 kcal mol^{-1} shows a backward-scattering preference, and thus is evidence for a direct reaction mechanism. The isotopically exchanged products also had relatively low translational energy ($\langle E_T \rangle$ = 35% E_{avail}). These two observations suggest that the reaction involves a short-lived CO_3^* intermediate and/or occurs at low impact parameters where the transfer of energy to internal degrees of freedom of the products is efficient. With 74 kcal mol^{-1} excess energy, the $O(^3P)$–CO_2 collision need not be head-on to have enough energy to surmount the TS1 activation barrier. The long C–O bond length (1.6 Å) and mild O–C–O bending angle (150° vs. 180° for CO_2) in TS1 also suggests that the entrance and exit barriers are neither particularly early nor late. Hence, the CO_3^* complex could exist for several vibrational periods. Efficient transfer of energy into vibrational modes of the CO_3^* intermediate would be required for an isotope exchange event to occur because inefficient coupling of that energy would increase the probability of redissociating the incident oxygen atom, resulting in an inelastic collision.

A direct isotope exchange mechanism through a short-lived CO_3 complex is qualitatively in agreement with our QCT calculations (see Figure 4.15). For $O(^3P)$ + CO_2 collisions

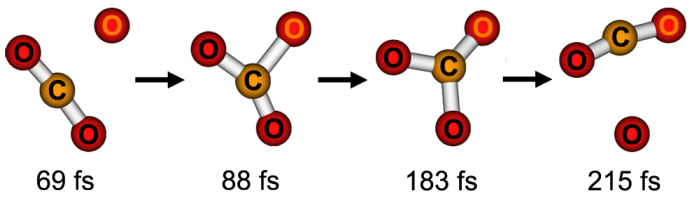

Figure 4.15: **Snapshots of a quasiclassical trajectory for $O(^3P)$ + CO_2 isotope exchange through a short-lived CO_3^* complex at 1.5 eV (34.6 kcal mol^{-1}) collision energy.** The incident oxygen atom is highlighted for clarity.

resulting in oxygen isotope exchange, a CO_3^* complex forms when the incoming oxygen atom interacts with the carbon atom on CO_2 (see also the opacity functions in Figure 4.5). In some cases, the CO_3^* complex existed for less than one vibrational period (the reaction is nearly direct) while in others it existed for many vibrational periods. After some time (typically *leq* 200 fs), one of the oxygen atoms initially part of the CO_2 detaches to leave behind a new CO_2 molecule. Head-on collisions at higher collision energies tended to form complexes existing for shorter times than those formed similarly at lower energies. Higher energies also tended to form CO_3^* complexes that tumbled $\geq 360^\circ$ in the plane of the reaction. In all cases, however, the CO_3^* complex lasted less than a picosecond.

These data support an isotope exchange reaction mechanism that begins with an interaction between $O(^3P)$ and the carbon atom of CO_2 to form a short-lived CO_3^* reaction complex. The identity of the dissociating oxygen atom determines the reaction's classification. If the dissociating oxygen atom is one originally on CO_2, then the trajectory is reactive; if it is the incident oxygen atom, then the trajectory is inelastic. The lifetime of the CO_3 reaction complex determines the c.m. angular and translational energy distributions of product CO_2. Longer-lived CO_3 complexes should yield smaller average translational energies because they will have more time to redistribute the initial translational energy to internal degrees of freedom.

This mechanism for the $O(^3P)$ + CO_2 isotope exchange reaction is different from that observed by *Perri et al.* for the $O(^1D)$ + $CO_2 \rightarrow O(^3P)$ + CO_2 isotope exchange reaction at $E_{\text{coll}} = 4.2$ and 7.7 kcal mol^{-1}, which samples part of the same PES [*Perri et al.*, 2003, 2004]. In those molecular-beam experiments, the reactively scattered CO_2 products had an isotropic (forward-backward symmetric) angular distribution and $\sim$50% of the available energy in translation; these results were evidence for a CO_3^* intermediate complex that lasted for at least several rotational periods ($>$ 1 ps). These dynamics are not inconsistent with our $O(^3P)$ + CO_2 results, however, because the two studies may sample different parts of the $^3A''$ and/or $^3A'$ PESs.

$O(^3P)$ + CO_2 collisions on the $^3A'$ surface could, in principle, cross onto the $^1A'$ surface to yield reactively scattered $O(^1D)$ + CO_2 products. One possible triplet-singlet crossing mech-

anism could be through spin-orbit coupled radiationless transitions, i.e., the reverse of what *Mebel et al.* had suggested for the $O(^1D)$ + CO_2 reaction, because the spin-orbit coupling terms and Franck-Condon factors are favorable [*Mebel et al.*, 2004]. Thus, we evaluated the general possibility of intersystem crossing (ISC) during our experiments by performing forward-convolution fits of the laboratory data that included the ~45 kcal mol^{-1} endothermicity of $O(^1D)$ vs. $O(^3P)$. Satisfactory fits of the laboratory TOF and angular distributions were obtained (see Figure 4.16); the peak and average of the $P(E_T)$ distribution were 34 and 30.7 kcal mol^{-1} (63% and 58% E_{avail}), respectively. Consequently, ISC cannot be explicitly ruled out by the experimental data. The diabatic radiationless transition probability, however, decreases exponentially as a function of velocity [*Landau*, 1932], and no evidence for ISC has been observed during our previous dynamics studies at hyperthermal velocities [*Brunsvold et al.*, 2007]. The qualitative agreement between the experimental and QCT-derived dynamics on the lowest triplet PES is consistent with the oxygen isotope exchange reaction exiting on a triplet surface, although more dynamics studies will be necessary to test this hypothesis.

4.5.4 Oxygen-atom abstraction, $O(^3P)$ + $CO_2 \rightarrow O_2$ + CO

Our laboratory observation of the oxygen abstraction reaction in the forward direction with a moderate amount of energy transfer (~50%) could arise from early-barrier stripping-type mechanisms through TS2 or TS3. Hammond's postulate states that for endothermic reactions, the transition state should be late and product-like. However, the small endothermicity relative to the barrier height (see Figure 4.1 and Table 4.1) for oxygen-atom abstraction suggests that TS2 and TS3 should be more reactant-like. Indeed, the bond lengths of CO and O_2 are significantly longer in TS2 and TS3 than at equilibrium for the isolated molecules, which are 1.14 and 1.21 Å, respectively, at CCSD(T)/aug-cc-pVTZ.

Theoretical trajectories yielding O_2 + CO products occurred generally in one of two ways: through a stripping-type mechanism and through a CO_3^* complex. In the stripping-type mechanism (see Figure 4.17A), the incoming oxygen atom interacts principally with one of the oxygen atoms on CO_2 to form TS3 directly. The C–O bond then breaks, releas-

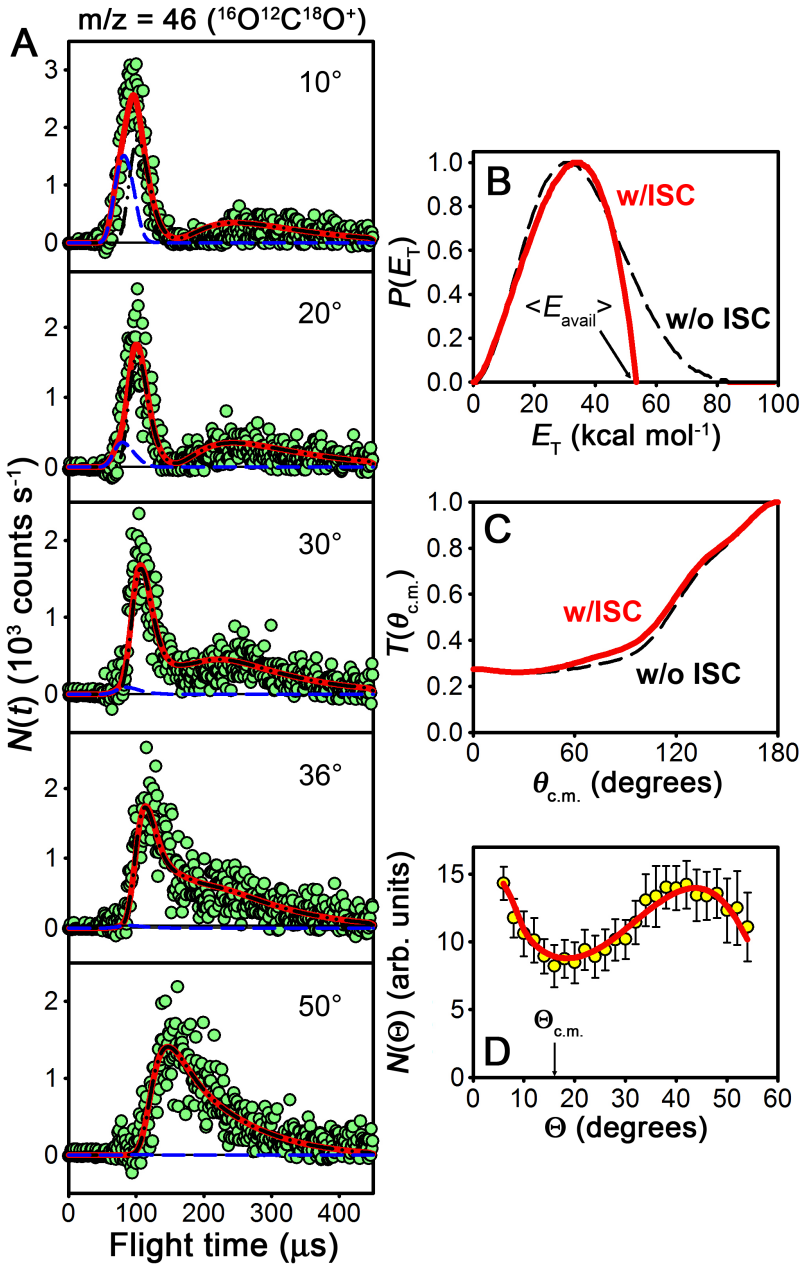

Figure 4.16: **Laboratory reactive scattering data detected at *m/z* = 46, fit assuming an ISC mechanism.** (**A**) Laboratory TOF, (**B**) c.m. translational energy, and (**C**) c.m. and (**D**) laboratory angular distributions for $^{16}O^{12}C^{18}O$ products of the $^{16}O(^3P)$ + $^{12}C^{18}O_2$ → $^{18}O^{16}O(^1D)$ + $^{12}C^{18}O$ reaction at $\langle E_{coll} \rangle$ = 98.8 kcal mol^{-1}. The circles in (**A**) and (**D**) are experimental data, while the lines are the best-fit forward-convolution simulations of the experimental data derived from the c.m. translational energy and angular distributions shown in (**B**) and (**C**), respectively. In (**A**), the best-fit forward-convolution simulations of $^{16}O^{12}C^{18}O$ products from $^{16}O(^3P)$ + $^{12}C^{18}O_2$ collisions (black dot-dashed lines) are shown with those from $^{16}O_2$ + $^{12}C^{18}O_2$ collisions at $\langle E_{coll} \rangle$ = 158.1 kcal mol^{-1} (blue dashed lines). The error bars in (**D**) represent 2σ uncertainties in the integrated experimental TOF distributions (see Appendix 4.7).

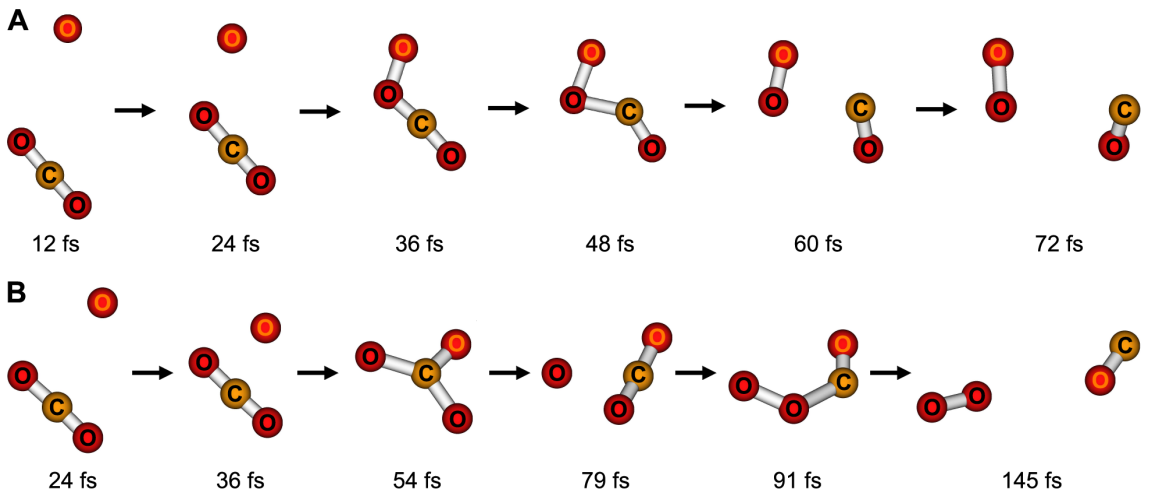

Figure 4.17: **Snapshots of quasiclassical trajectories for the O(^3P) + CO_2 → O_2 + CO reaction.** (**A**) A stripping-type mechanism through TS3 at 6.5 eV (149.8 kcal mol^{-1}) collision energy calculated at the B3LYP/6-311G(d) level of theory. (**B**) A CO_3 reaction-complex mechanism through TS2 at 5.5 eV (126.7 kcal mol^{-1}) collision energy calculated at the BMK/6-311G(d) level of theory. The incident oxygen atoms are highlighted for clarity.

ing O_2 + CO products. Of all the QCTs run, only two of these stripping-type trajectories were observed, and they occurred at E_{coll} = 6.5 eV (149.8 kcal mol^{-1}) using B3LYP/6-311G(d). The remaining 27 O_2 + CO-producing trajectories proceeded through a CO_3^*-complex mechanism (see Figure 4.17B). In that mechanism, the incoming oxygen atom interacts first with the carbon atom of CO_2 to form a short-lived CO_3^* complex, similar to that observed in the isotope-exchange trajectories. This complex rarely survived more than one vibrational period. An oxygen atom is then released and then interacts with a CO_2-bound oxygen atom as the CO_2 rotates. Last, an O–O bond forms as the adjacent C–O bond breaks to form O_2 + CO products.

A key difference between the two O_2 + CO-producing mechanisms is that the CO_3^*-complex mechanism requires a slow recoil of the oxygen atom that dissociated initially. Following complex formation in a high-energy collision, the nascent CO_2 will have sufficient internal energy (∼70 kcal mol^{-1}) to form the O_2 + CO products only if the O atom dissociates with low translational energy. When the O atom escapes the CO_3^* complex with high translational energy, the nascent CO_2 rotates too slowly for any further reaction to take place (in these cases, the trajectory results in either inelastic scattering or isotope

exchange). With so much excess energy, however, the reaction need not take the lowest energy path [*Zhang et al.*, 2008]; the slow recoiling oxygen atom in the CO_3^*-complex mechanism resembles the "roaming' H-atom and methyl group in formaldehyde [*Townsend et al.*, 2004] and acetaldehyde [*Houston and Kable*, 2006] photodissociation, respectively.

We note that the stripping-type mechanism would have produced $^{18}O^{16}O$ molecules in the experiment exclusively, whereas the CO_3^*-complex mechanism can produce $^{18}O_2$ in addition to $^{18}O^{16}O$. Our laboratory observation of $m/z = 34$ products is consistent with both oxygen abstraction mechanisms, but the lack of signal due to $m/z = 36$ products in the forward direction (where there was negligible background) is evidence against the CO_3^*-complex mechanism. The CO_3^*-complex mechanism, however, comprised 27 of the 29 oxygen-atom abstraction trajectories obtained from the QCT calculations, and only one of those trajectories would have produced $m/z = 34$ products. The two remaining trajectories proceeded through the stripping mechanism. This preference for the CO_3^*-complex mechanism observed in the QCT calculations may be a consequence of the $\sim$50 kcal mol^{-1} lower barrier for CO_3 formation and the $\sim$13 kcal mol^{-1} lower energy of TS2, both relative to the energy of TS3. Additional experimental and theoretical studies with a higher SNR, perhaps at higher collision energies, will be required to elucidate the mechanisms of this reaction.

4.6 Conclusions

We have investigated the dynamics of $O(^3P)$ + CO_2 collisions at hyperthermal collision energies. Non-reactive scattering was dominated by high-impact-parameter collisions, which did not perturb the initial velocity of the reactants significantly. Lower impact parameters resulted in increased translational-to-internal energy transfer. Both the oxygen isotope-exchange and the atom-abstraction reaction channels were observed directly by our crossed-molecular-beam apparatus. The oxygen isotope exchange reaction displayed an anisotropic angular distribution with a large amount of translational-to-internal energy transfer, suggesting that the reaction occurs at low impact parameters through a short-lived intermediate CO_3^* complex. The mechanisms for both non-reactive scattering and oxygen isotope exchange were supported qualitatively, but not quantitatively, by the QCT calcula-

tions on the $^3A''$ surface.

Nonadiabaticity during inelastic and reactive trajectories cannot be ruled out and its effects should be investigated; both inelastic and reactive trajectories may be sensitive to the coupling between the lowest triplet ($^3A''$) PES and nearby (e.g., $^3A'$) electronic surfaces. With $\sim$100 kcal mol^{-1} collision energy, the experiment may probe regions of the PES far from the TS1, TS2, TS3, and CO_3 structures; the presence of several other surfaces (both triplet and singlet) within this energy range [*Kowalczyk and Krylov*, 2007; *Liu et al.*, 2009], the possibility of vibronic effects due to Jahn-Teller-like distortion, and the failure of density-functional methods to capture the dynamics quantitatively all suggest that a higher-level treatment of the PES would be desirable. While the transition states and stationary points on the lowest triplet PES may be described well with density-functional calculations, this may not be the case in other regions of the PES where vibronic interactions can affect its curvature. A more complete, high-level description of the PES, along with more dynamics experiments, will be required to describe the dynamics of isotope exchange on the lowest triplet PES quantitatively.

4.7 Acknowledgements

We thank Ned F. Lindholm for experimental assistance. This work was supported by the Missile Defense Agency under cooperative agreement HQ0006-05-2-0001. L. Y. Y. was supported by the Davidow Fund, and G. C. S. was supported by the Air Force Office of Scientific Research grant FA955D-07-1-0095.

Appendices

4.A Differential scattering cross-sections from 1.0 – 6.5 eV

Theoretical center-of-mass differential scattering cross-sections for the oxygen isotope exchange reaction (Figure 4.18) showed a preference for backward scattering at all collision energies. The incident oxygen atom, attached to the product CO_2 molecule, appeared to prefer scattering in a direction opposite its initial direction. As the collision energy increased, however, the angular distribution of products showed little qualitative change: Reactively scattered products showed a slight preference for backward scattering up to E_{coll} = 6.5 eV (149.8 kcal mol^{-1}), the highest collision energy considered in this study.

The theoretical c.m. product translational energy distributions showed significant ($\geq$ 50%) transfer of the available energy into internal degrees of freedom of the products at all collision energies = 2.5 eV (57.6 kcal mol^{-1}). The QCT data below $E_{\text{coll}} \geq$ 2.5 eV did not contain statistically significant number of reactive trajectories, i.e., $>$ 30, so they were not included in this analysis. $P(E_{\text{T}})$ distributions became broader as the collision energy increased, though the proportion of energy remaining translation was similar at all collision energies. A bimodal distribution of translational energies may exist in the products of BMK trajectories run at 2.5, 3.5, and 4.5 eV collision energy (57.6, 80.7, and 103.7 kcal mol^{-1}, respectively); for instance, separate peaks were observed at $\sim$50% and $\sim$80% of the available energy for the 2.5-eV trajectories, although there is considerable uncertainty in the theoretical translational energy distribution (see Figure 4.18). Additional QCT calculations will be required before structure in the product translational energy distributions can be determined conclusively.

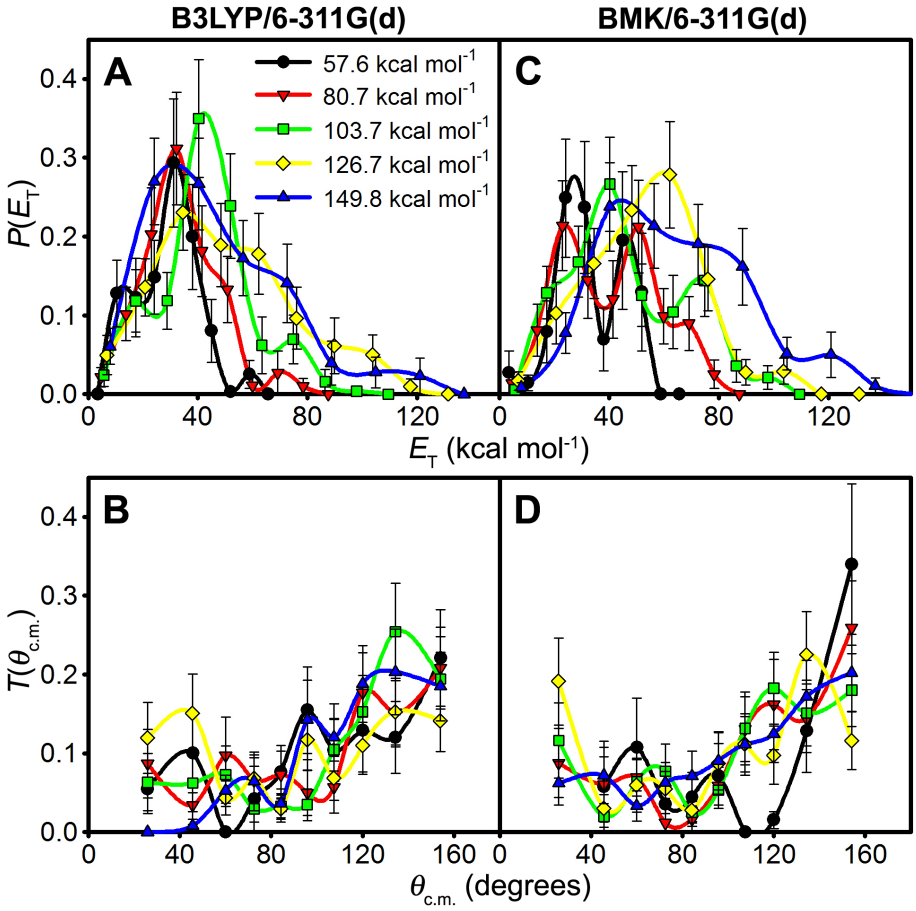

Figure 4.18: **Center-of-mass angular and translational energy distributions for the O(^3P) + CO_2 isotope exchange reaction derived from QCT calculations at the (A and B) B3LYP/6-311G(d) and (C and D) BMK/6-311G(d) levels of theory.** Distributions with more than 30 reactive trajectories are shown. At both levels of theory and all collision energies shown, reactive scattering shows a preference for backward scattering ($\theta_{\text{c.m.}} > 90°$) with a moderate ($\geq 50\%$) transfer of translational energy to internal degrees of freedom of the products.

4.B Estimating uncertainty in the laboratory angular distributions

For this analysis we treat the TOF distribution at a given laboratory angle Θ as a type of Monte Carlo integration of the 'true' TOF distribution, and we estimate the variance in the integrated area accordingly. Under this approximation, the integrated area, $I(\Theta)$, is equivalent to the area of a rectangle with a width equal to the total time range, t_{total}, and height equal to the average number density over that time range, $\langle N(t)\rangle_{\text{total}}$. More formally, this relation can be written as a discrete sum over the channels on the MCP, each of which corresponded to a 1 μs dwell time:

$$I(\Theta) \;=\; \sum_{i=1}^{t_{\text{total}}} N(t_i) \;=\; t_{\text{total}}\Big[\frac{1}{t_{\text{total}}}\sum_{i=1}^{t_{\text{total}}} N(t_i)\Big] \;=\; t_{\text{total}}\langle N(t)\rangle_{\text{total}} \tag{4.8}$$

The variance of $I(\Theta)$, however, must be evaluated as a function of time because the number density at a given arrival time at the detector, $N(t)$, varied with flight time in each TOF distribution. Consequently, the TOF distribution was further divided into a set of bins for which the variance was calculated and summed over the total TOF distribution using the following relation:

$$\sigma^2_{N(t)_{\text{bin}}} \;=\; \frac{1}{t_{\text{bin}}}\sum_{i}^{f}[t_{\text{bin}}N(t_i)]^2 - [t_{\text{bin}}\langle N(t)\rangle_{\text{bin}}]^2 \tag{4.9}$$

$$\sigma^2_{I(\Theta)} \;=\; \sum_{\text{bins}} \sigma^2_{N(t)_{\text{bin}}} \tag{4.10}$$

where i and f represent the first and last members of each data bin. The standard deviation, $\sigma_{I(\Theta)}$, was calculated by taking the square root of the variance. We note some degree of sensitivity in the calculated $\sigma_{I(\Theta)}$ values on t_{bin} because the $N(t)$ distributions show significant structure; consequently, we have reported conservative estimates of $\sigma_{I(\Theta)}$ using the minimum bin size of $t_{\text{bin}} = 3$ μs, or 3 data points per $\sigma^2_{N(t)_{\text{bin}}}$ calculation.

Chapter 5

Summary and outlook

5.1 New signatures, new reactions

Presently, the large enrichment in $^{16}O^{13}C^{18}O$ we found in the stratospheric polar vortex is still unexplained. The laboratory photochemical experiments we reported in Chapter 2 seem to rule out $O(^1D)$ + CO_2 isotope exchange; stratospheric $^{16}O^{13}C^{18}O$ should get more depleted with increasing extent of isotope exchange, not enriched, and we observed this trend as a decrease in Δ_{47} in field samples from the mid-latitude stratosphere. What, then, could enrich $^{16}O^{13}C^{18}O$ in the polar vortex, and what might we be able to learn from future studies?

We suggested in Chapter 2 that fast low-temperature isotopic equilibration of CO_2 on stratospheric particles (e.g., PSCs) could be responsible for the high Δ_{47} values in the polar vortex. Our initial tests of the PSC-isotope-equilibration hypothesis suggested that isotopic equilibration on certain HNO_3 ices and H_2SO_4:HNO_3:H_2O mixtures is slow, and is therefore unlikely to produce $^{16}O^{13}C^{18}O$ enrichments on timescales that would be consistent with our polar vortex data. The CO_2 isotopic equilibration rate, however, could be sensitive to particle structure and composition. PSCs and cirrus clouds form under similar conditions, but they can differ in bulk and surface composition [*Zondlo et al.*, 2000]; the structure, physics, and chemistry of these particles are still not understood [*Dash et al.*, 2006; *Lowe and MacKenzie*, 2008], so the role of CO_2 isotopic equilibration on ice particle surfaces remains uncertain. Future laboratory work on CO_2–ice surface interactions may shed light on the structure and composition of these and other atmospherically important particles.

We also identified three new reactions, O_2 + CO_2 and $O(^3P)$ + CO_2 isotope exchange and $O(^3P)$ + $CO_2 \rightarrow O_2$ + CO, in our crossed-molecular-beam experiments. Because of the $\approx$160 kcal mol^{-1} reaction barrier for O_2 + CO_2 isotope exchange, and the $\approx$75 kcal mol^{-1} barrier for $O(^3P)$ + $CO_2 \rightarrow O_2$ + CO, they are unlikely to be important in the stratosphere. $O(^3P)$ + CO_2, in contrast, has a reaction barrier ($\approx$ 25 kcal mol^{-1}) that is atmospherically accessible, in principle.

5.2 Potential atmospheric importance of $O(^3P)$ + CO_2

The laboratory observation of $O(^3P)$ + CO_2 isotope exchange at hyperthermal energies may have implications for modeling the oxygen isotope cycling in the middle and upper atmosphere because current models do not include $O(^3P)$ + CO_2 reactions explicitly [*Liang et al.*, 2007, 2008; *Thiemens et al.*, 1995; *Yung et al.*, 1991, 1997]. Here, I suggest that $O(^3P)$ + CO_2 reactions in the upper atmosphere could affect the oxygen isotope distribution in CO_2. The $O(^3P)$ + CO_2 isotope exchange reaction could yield isotope effects qualitatively different from those in the $O(^1D)$ + CO_2 reaction because its mechanism is direct, unlike the mechanism involving a long-lived CO_3^* intermediate for the $O(^1D)$ + CO_2 reaction [*Chen et al.*, 2009; *Perri et al.*, 2003, 2004]. Instead, like the O_3^* complex in the $O(^3P)$ + O_2 isotope exchange reaction [*Van Wyngarden et al.*, 2007], the CO_3^* reaction complex formed from $O(^3P)$ + CO_2 does not live long enough for its energy to randomize; thus, dynamical isotope effects are likely to be important to its isotope-specific branching fractions. These types of non-statistical isotope effects are believed to be partly responsible for "anomalous" formation rates of stable O_3 from the O_3^* complex for different isotopologues [*Babikov et al.*, 2003; *Gao and Marcus*, 2001; *Schinke et al.*, 2006]. Due to limitations in our apparatus, however, we were unable to investigate the $O(^3P)$ + CO_2 isotope exchange dynamics near the predicted reaction threshold, which is more relevant to the atmosphere. Our reactive trajectories at E_{coll} = 1.0 and 1.5 eV (23.0 and 34.6 kcal mol^{-1}, respectively), however, suggest that isotope exchange is still direct near the calculated reaction barrier.

The overall importance of the $O(^3P)$ + CO_2 isotope exchange reaction to reactive oxygen cycling in the atmosphere, however, depends on (*1*) the reaction's excitation function

and (*2*) the proportion of $O(^3P)$ in the atmosphere with sufficient translational energy to surmount the reaction barrier. In the absence of experimental data, high-level variational quantum calculations can assign an upper limit to the TS1 barrier. The CCSD(T)/aug-cc-pVTZ energy for TS1 (25 kcal mol^{-1}) reported in this work implies that relative velocities of ≥ 3 km s^{-1} in the ground-state reactants will be required to open the isotope exchange channel; ozone photolysis in the Hartley band (220 – 310 nm) and at shorter wavelengths yields $O(^3P)$ + $O_2(^3\Sigma_g^-)$ photofragments having a total translational energy in excess of 25 kcal mol^{-1} and as high as 100 kcal mol^{-1} [*Fairchild et al.*, 1978; *Kinugawa et al.*, 1990; *Shamsuddin et al.*, 1994; *Stranges et al.*, 1995; *Syage*, 1995; *Takahashi et al.*, 1998]. Our preliminary hard-sphere collision modeling (see Appendix 2.D) using cross-sections for the velocity relaxation of $O(^1D)$ by N_2 [*Matsumi and Chowdhury*, 1996; *Matsumi et al.*, 1994b] suggests that the size of the reactive $O(^3P)$ reservoir could be as high as several percent that of $O(^1D)$. Future theoretical and experimental studies can elucidate the shape of the reaction's excitation function, which is needed before an appropriate simulation can be constructed. Finally, we note that during our laboratory study of the $O_2/O_3/CO_2$ photochemical system using a mercury lamp as an actinic light source (185 and 254 nm), we observed deviations from modeled results at long irradiation times ($t \sim$ days; see Figure 2.8); a minor $O(^3P)$ + CO_2 channel could address part of this discrepancy, as well as some of the disagreements between earlier studies [*Chakraborty and Bhattacharya*, 2003; *Johnston et al.*, 2000; *Shaheen et al.*, 2007; *Wen and Thiemens*, 1993]. The yield of hyperthermal $O(^3P)$ during O_3 photolysis depends on wavelength [*Stranges et al.*, 1995; *Takahashi et al.*, 1998], however, so this hypothesis awaits further testing with systematic studies of the $O_2/O_3/CO_2$ photochemical system.

Claims of hyperthermal $O(^3P)$ + CO_2 chemistry in the atmosphere based on laboratory data must be met with some skepticism, however. Both N_2 and O_2 are efficient energy quenchers for even the most reactive atmospheric species, and the steady-state population of fast-moving $O(^3P)$ will be determined largely by its translational relaxation rate in air. In addition, thermal averaging collapses most reaction rates towards the chemical kinetic limit, so any atmospheric signature of the $O(^3P)$ + CO_2 reaction will be difficult to identify

unless the associated isotope effect is large and unique. Previously published reports of hyperthermal chemistry in the atmosphere based only on laboratory evidence have been controversial due to the lack of an unequivocal signature in the field data [*Li et al.*, 2008; *Miller et al.*, 1994]. The stratospheric $^{16}O^{13}C^{18}O$ enrichment reported in Chapter 2 is a clear signature of *some* heretofore unknown process, but definitive tests of the hyperthermal $O(^3P)$ + CO_2 isotope-exchange hypothesis will have to take the form of well-characterized, rigorously modeled bulk photochemical experiments involving O_3 and CO_2.

Bibliography

Affek, H. P., and J. M. Eiler (2006), Abundance of mass-47 CO_2 in urban air, car exhaust and human breath, *Geochim. Cosmochim. Acta*, *70*(1), 1–12.

Affek, H. P., X. Xu, and J. M. Eiler (2007), Seasonal and diurnal variations of $^{13}C^{18}O^{16}O$ in air: Initial observations from Pasadena, CA, *Geochim. Cosmochim. Acta*, *71*, 5033–5043.

Alexander, B., M. K. Vollmer, T. Jackson, R. F. Weiss, and M. H. Thiemens (2001), Stratospheric CO_2 isotopic anomalies and SF_6 and CFC tracer concentrations in the Arctic polar vortex, *Geophys. Res. Lett.*, *28*(21), 4103–4106.

Allan, D. W. (1987), Time and Frequency (Time-Domain) Characterization, Estimation, and Prediction of Precision Clocks and Oscillators, *IEEE Trans. Ultrason., Ferroelectr., Freq. Control*, *UFFC-34*(6), 647–654.

Assonov, S. S., and C. A. M. Brenninkmeijer (2001), A new method to determine the ^{17}O isotopic abundance in CO_2 using oxygen isotope exchange with a solid oxide, *Rapid Commun. Mass Spectrom.*, *15*, 2426–2437.

Averyanov, A. S., Y. G. Khait, and Y. V. Puzanov (1999), Singlet and triplet states of the CO_3 and CO_4 molecules, *J. Mol. Struct. THEOCHEM*, *459*, 95–102.

Babikov, D., B. K. Kendrick, R. B. Walker, and R. T. Pack (2003), Formation of ozone: Metastable states and the anomalous isotope effect, *J. Chem. Phys.*, *119*(5), 2577–2589.

Bao, H. M., D. Rumble, and D. R. Lowe (2007), The five stable isotope compositions of Fig Tree barites: Implications on sulfur cycle in ca. 3.2 Ga oceans, *Geochim. Cosmochim. Acta*, *71*(20), 4868–4879.

Bass, J. N. (1974), Translation to vibration energy transfer in O + NH_3 and O + CO_2 collisions, *J. Chem. Phys.*, *60*(7), 2913–2921.

Baulch, D. L., and W. H. Breckenridge (1966), Isotopic Exchange of $O(^1D)$ with Carbon Dioxide, *Trans. Faraday Soc.*, *62*, 2768–2773.

Becke, A. D. (1993), Density-functional thermochemistry. III. The role of exact exchange, *J. Chem. Phys.*, *98*(7), 5648–5652.

Bennett, C. J., C. Jamieson, A. M. Mebel, and R. I. Kaiser (2004), Untangling the formation of the cyclic carbon trioxide isomer in low temperature carbon dioxide ices, *Phys. Chem. Chem. Phys.*, *6*(4), 735–746.

Bergamaschi, P., M. Schupp, and G. W. Harris (1994), High-precision direct measurements of $^{13}CH_4/^{12}CH_4$ and $^{12}CH_3D/^{12}CH_4$ ratios in atmospheric methane sources by means of a long-path tunable diode laser absorption spectrometer, *Appl. Opt.*, *33*(33), 7704–7716.

Bhattacharya, S. K., J. Savarino, and M. H. Thiemens (2000), A new class of oxygen isotopic fractionation in photodissociation of carbon dioxide: Potential implications for atmospheres of Mars and Earth, *Geophys. Res. Lett.*, *27*(10), 1459–1462.

Bigeleisen, J., and M. G. Mayer (1947), Calculation of equilibrium constants for isotopic exchange reactions, *J. Chem. Phys.*, *15*(5), 261–267.

Bigeleisen, J., and M. Wolfsberg (1958), Theoretical and experimental aspects of isotope effects in chemical kinetics, *Adv. Chem. Phys.*, *1*, 15–76.

Billing, G. D., and D. C. Clary (1983), Semiclassical calculation of energy transfer in polyatomic molecules. IX. Cross sections for M + CO_2 (000) $\rightarrow$ M + CO_2 (*nml*) (M = He and Ar), *Chem. Phys.*, *80*(3), 213–219.

Blank, D. A., N. Hemmi, A. G. Suits, and Y. T. Lee (1998), A crossed molecular beam investigation of the reaction Cl + propane $\rightarrow$ HCl + C_3H_7 using VUV synchrotron radiation as a product probe, *Chem. Phys.*, *231*(2-3), 261–278.

Boering, K. A., T. Jackson, K. J. Hoag, A. S. Cole, M. J. Perri, M. Thiemens, and E. Atlas (2004), Observations of the anomalous oxygen isotopic composition of carbon dioxide in the lower stratosphere and the flux of the anomaly to the troposphere, *Geophys. Res. Lett.*, *31*(3), l03109.

Boese, A. D., and J. M. L. Martin (2004), Development of density functionals for thermochemical kinetics, *J. Chem. Phys.*, *121*(8), 3405–3416.

Braunstein, M., and J. W. Duff (2000), Electronic structure and dynamics of O(^3P) + CO ($^1\Sigma^+$) collisions, *J. Chem. Phys.*, *112*(6), 2736–2745.

Brenninkmeijer, C. A. M., C. Janssen, J. Kaiser, T. Rckmann, T. S. Rhee, and S. S. Assonov (2003), Isotope Effects in the Chemistry of Atmospheric Trace Compounds, *Chem. Rev.*, *103*(12), 5125–5161.

Brink, G. O. (1966), Electron Bombardment Molecular Beam Detector, *Rev. Sci. Instrum.*, *37*(7), 857–860.

Brunsvold, A. L., D. J. Garton, T. K. Minton, D. Troya, and G. C. Schatz (2004), Crossed beams and theoretical studies of the dynamics of hyperthermal collisions between Ar and ethane, *J. Chem. Phys.*, *121*(23), 11,702–11,714.

Brunsvold, A. L., J. Zhang, H. P. Upadhyaya, T. K. Minton, J. P. Camden, J. T. Paci, and G. C. Schatz (2007), Crossed-Beams and Theoretical Studies of the O(^3P) + H_2O $\rightarrow$ HO_2 + H Reaction Excitation Function, *J. Phys. Chem. A*, *111*(43), 10,907–10,913.

Brunsvold, A. L., H. P. Upadhyaya, J. Zhang, R. Cooper, T. K. Minton, M. Braunstein, and J. W. Duff (2008), Dynamics of Hyperthermal Collisions of O(^3P) with CO, *J. Phys. Chem. A*, *112*, 2192–2205.

Bunker, D. L. (1970), in *Proceedings of the International School of Physics Enrico Fermi Course XLIV: Molecular Beam and Reaction Kinetics*, edited by C. Schlier, pp. 315–319, Academic Press, New York.

Cacace, F., G. de Petris, M. Rosi, and A. Troiani (2003), Carbon Tetraoxide: Theoretically Predicted and Experimentally Detected, *Angew. Chem. Int. Ed.*, *42*, 2985–2990.

Caledonia, G. E., R. H. Kreeh, and B. D. Green (1987), A High Flux Source of Energetic Oxygen Atoms for Material Degradation Studies, *AIAA J.*, *25*(1), 59–63.

Chakraborty, S., and S. K. Bhattacharya (2003), Experimental investigation of oxygen isotope exchange between CO_2 and $O(^1D)$ and its relevance to the stratosphere, *J. Geophys. Res.*, *108*(D23), 4724–4738.

Chen, H.-F., H.-C. Chiang, H. Matsui, S. Tsuchiya, and Y.-P. Lee (2009), Distribution of Vibrational States of CO_2 in the Reaction $O(^1D)$ + CO_2 from Time-Resolved Fourier Transform Infrared Emission Spectra, *J. Phys. Chem. A*, *113*(15), 3431–3437.

Ciais, P., and H. A. J. Meijer (1998), The $^{18}O/^{16}O$ isotope ratio of atmospheric CO_2 and its role in global carbon cycle research, in *Stable Isotopes: integration of biological, ecological and geochemical processes*, edited by H. Griffiths, pp. 409–431, BIOS Scientific Publishers, Ltd., Oxford.

Ciais, P., P. P. Tans, M. Troiler, J. W. C. White, and R. J. Francey (1995), A large northern-hemisphere terrestrial CO_2 sink indicated by the $^{13}C/^{12}C$ ratio of atmospheric CO_2, *Science*, *269*(5277), 1098–1102.

Clayton, R. N., L. Grossman, and T. K. Mayeda (1973), A Component of Primitive Nuclear Composition in Carbonaceous Meteorites, *Science*, *182*(4111), 485–488.

Clerc, M., and A. Reiffsteck (1968), Determination of the Rate Constant of the Gas-Phase Reaction between $O(^1D)$ and CO_2, *J. Chem. Phys.*, *48*(6), 2799–2801.

Cole, A. S., and K. A. Boering (2006), Mass-dependent and non-mass-dependent isotope effects in ozone photolysis: Resolving theory and experiments, *J. Chem. Phys.*, *125*(18), 184301.

Craig, H., Y. Horibe, and T. Sowers (1988), Gravitational Separation of Gases and Isotopes in Polar Ice Caps, *Science*, *242*, 1675–1678.

Crawford, T. D., E. Kraka, J. F. Stanton, and D. Cremer (2001), Problematic *p*-benzyne: Orbital instabilities, biradical character, and broken symmetry, *J. Chem. Phys.*, *114*(24), 10,638–10,650.

Daly, N. R. (1960), Scintillation Type Mass Spectrometer Ion Detector, *Rev. Sci. Instrum.*, *31*(3), 264–267.

Dash, J. G., A. W. Rempel, and J. S. Wettlaufer (2006), The physics of premelted ice and its geophysical consequences, *Rev. Mod. Phys.*, *78*(3), 695–741.

de Lara-Castells, M. P., M. I. Hernández, G. Delgado-Barrio, P. Villarreal, and L. López-Puertas (2006), Vibrational quenching of $CO_2(010)$ by collisions with $O(^3P)$ at thermal energies: A quantum-mechanical study, *J. Chem. Phys.*, *124*(16), 164302.

de Lara-Castells, M. P., M. I. Hernández, G. Delgado-Barrio, P. Villarreal, and L. López-Puertas (2007), Key role of spin-orbit effects in the relaxation of $CO_2(010)$ by thermal collisions with $O(^3P_j)$, *Mol. Phys.*, *105*(9), 1171–1181.

DeKock, R. L., and H. B. Gray (1980), *Chemical Structure and Bonding*, Benjamin/Cummings, Menlo Park, CA.

DeMore, W. B., and C. Dede (1970), Pressure Dependence of Carbon Trioxide Formation in the Gas-Phase Reaction of $O(^1D)$ with Carbon Dioxide, *J. Phys. Chem.*, *74*(18), 2621–2625.

Dixon, H. (1886), XI. – The Combustion of Carbonic Oxide and Hydrogen, *J. Chem. Soc., Trans.*, *49*, 94–112.

Drever, R. W. P., J. L. Hall, F. V. Kowalski, J. Hough, G. M. Ford, A. J. Munley, and H. Ward (1983), Laser phase and frequency stabilization using an optical resonator, *Appl. Phys. B*, *31*(2), 97–105.

Dunning, T. J. (1989), Gaussian basis sets for use in correlated molecular calculations. I. The atoms boron through neon and hydrogen, *J. Chem. Phys.*, *90*(2), 1007–1023.

Dylewski, S. M., J. D. Geiser, and P. L. Houston (2001), The energy distribution, angular distribution, and alignment of the $O(^1D_2)$ fragment from the photodissociation of ozone between 235 and 305 nm, *J. Chem. Phys.*, *115*(16), 7460–7473.

Eiler, J. M. (2007), "Clumped-isotope" geochemistry – The study of naturally-occurring, multiply-substituted isotopologues, *Earth Planet. Sci. Lett.*, *262*, 309–327.

Eiler, J. M., and E. Schauble (2004), $^{18}O^{13}C^{16}O$ in the Earth's atmosphere, *Geochim. Cosmochim. Acta*, *68*(23), 4767–4777.

Eisfeld, W., and K. Morokuma (2000), A detailed study on the symmetry breaking and its effect on the potential surface of NO_3, *J. Chem. Phys.*, *113*(14), 5587–5597.

Elliott, B. M., and A. I. Boldyrev (2005), The Oxygen-Rich Carboxide Series: CO_n (n = 3, 4, 5, 6, 7, or 8), *J. Phys. Chem. A*, *109*(16), 3722–3727.

Fairchild, C. E., E. J. Stone, and G. M. Lawrence (1978), Photfragment spectroscopy of ozone in the uv region 270-310 nm and at 600 nm, *J. Chem. Phys.*, *69*(8), 3632–3638.

Feilberg, K. L., M. S. Johnson, and C. J. Nielsen (2004), Relative Reaction Rates of HCHO, HCDO, DCDO, $H^{13}CHO$, and $HCH^{18}O$ with OH, Cl, Br, and NO_3 Radicals, *J. Phys. Chem. A*, *108*(36), 7393–7398.

Feilberg, K. L., B. D'Anna, M. S. Johnson, and C. J. Nielsen (2005a), Relative Tropospheric Photolysis Rates of HCHO, $H^{13}CHO$, $HCH^{18}O$, and DCDO Measured at the European Photoreactor Facility, *J. Phys. Chem. A*, *109*(37), 8314–8319.

Feilberg, K. L., M. S. Johnson, and C. J. Nielsen (2005b), Relative rates of reaction of $^{13}C^{16}O$, $^{12}C^{18}O$, $^{12}C^{17}O$ and $^{13}C^{18}O$ with OH and OD radicals, *Phys. Chem. Chem. Phys.*, *7*, 2318–2323.

Felder, P., B.-M. Haas, and J. R. Huber (1991), The photoreaction $N_2O \rightarrow O(^1D) + N_2(^1\Sigma)$ studied by photofragment translational spectroscopy, *Chem. Phys. Lett.*, *186*(2-3), 177–182.

Flocke, F., R. L. Herman, R. J. Salawich, E. Atlas, C. R. Webster, S. M. Schauffler, R. A. Lueb, R. D. May, E. J. Moyer, K. H. Rosenlof, D. C. Scott, D. R. Blake, and T. P. Bui (1999), An examination of chemistry and transport processes in the tropical lower stratosphere using observations of long-lived and short-lived compounds obtained during STRAT and POLARIS, *J. Geophys. Res.*, *104*(D21), 26,625–26,642.

Foltynowicz, A., F. M. Schmidt, W. Ma, and O. Axner (2008), Noise-immune cavity-enhanced optical heterodyne molecular spectroscopy: Current status and future potential, *Appl. Phys. B*, *92*(3), 313–326.

Frisch, M. J., J. A. Pople, and J. S. Binkley (1984), Self-consistent molecular orbital methods 25. Supplementary functions for Gaussian basis sets, *J. Chem. Phys.*, *80*(7), 3265–3269.

Froese, R. D. J., and J. D. Goddard (1993), Features of the Lowest Singlet and Triplet Potential Energy Surfaces of CO_3, *J. Phys. Chem.*, *97*(29), 7484–7490.

Froidevaux, L., N. Livesey, W. Read, Y. Jiang, C. Jimenez, M. F. M. Schwartz, M. Santee, H. Pumphrey, J. Jiang, D. Wu, G. Manney, B. Drouin, J. Waters, E. Fetzer, P. Bernath, C. Boone, K. Walker, K. Jucks, G. Toon, J. Margitan, B. Sen, C. Webster, L. Christensen, J. Elkins, E. Atlas, R. Lueb, and R. Hendershot (2006), Early validation analyses of atmospheric profiles from EOS MLS on the Aura satellite, *IEEE Trans. Geosci. Remote Sens.*, *44*(5), 1106–1121.

Gamo, T., M. Tsutsumi, H. Sakai, T. Nakazawa, M. Tanaka, H. Honda, H. Kubo, and T. Itoh (1989), Carbon and oxygen isotopic ratios of carbon dioxide of a stratospheric profile over Japan, *Tellus*, *41B*(2), 127–133.

Gao, X., and M. H. Thiemens (1991), Systematic study of sulfur isotopic composition in iron meteorites and the occurrence of excess ^{33}S and ^{36}S, *Geochim. Cosmochim. Acta*, *55*(9), 2671–2679.

Gao, X., and M. H. Thiemens (1993), Variations of the isotopic composition of sulfur in enstatite and ordinary chondrites, *Geochim. Cosmochim. Acta*, *57*(13), 3171–3176.

Gao, Y. Q., and R. A. Marcus (2001), Strange and Unconventional Isotope Effects in Ozone Formation, *Science*, *293*, 259–263.

Gao, Y. Q., and R. A. Marcus (2002), On the theory of the strange and unconventional isotopic effects in ozone formation, *J. Chem. Phys.*, *116*(1), 137–154.

Gao, Y. Q., W.-C. Chen, and R. A. Marcus (2002), A theoretical study of ozone isotopic effects using a modified *ab initio* potential energy surface, *J. Chem. Phys.*, *117*(4), 1536–1543.

Garrett, B. C. (1983), Basis-set effects in quantum-mechanical calculations of translational-to-vibrational energy transfer in $O(^3P) + CO_2$ collisions, *Chem. Phys.*, *87*(1), 63–71.

Garton, D. J., A. L. Brunsvold, T. K. Minton, D. Troya, B. Maiti, and G. C. Schatz (2006), Experimental and Theoretical Investigations of the Inelastic and Reactive Scattering Dynamics of $O(^3P)$ + D_2, *J. Phys. Chem. A*, *110*, 1327–1341.

Garton, D. J., T. K. Minton, W. Hu, and G. C. Schatz (2009), Experimental and Theoretical Investigations of the Inelastic and Reactive Scattering Dynamics of $O(^3P)$ Collisions with Ethane, *J. Phys. Chem. A*, *113*(16), 4722–4738.

Ghosh, P., J. Adkins, H. Affek, B. Balta, W. Guo, E. Schauble, D. Schrag, and J. M. Eiler (2006), ^{13}C–^{18}O bonds in carbonate materials: A new kind of paleothermometer, *Geochim. Cosmochim. Acta*, *70*(6), 1439–1456.

Gibbs, J. W. (1948), *Collected Works*, Yale University Press, New Haven, CT.

Greenblatt, J. B., H.-J. Jost, M. Leowenstein, J. R. Podolske, T. P. Bui, D. F. Hurst, J. W. Elkins, R. L. Herman, C. R. Webster, S. M. Schauffler, E. L. Atlas, P. A. Newman, L. R. Lait, M. Mller, A. Engel, and U. Schmidt (2002), Defining the polar vortex edge from an N_2O:potential temperature correlation, *J. Geophys. Res.*, *107*(D20), 8268.

Hanisco, T. F., and A. C. Kummel (1993), State-Resolved Photodissociation of N_2O, *J. Phys. Chem.*, *97*(28), 7242–7246.

Hanson, D., and K. Mauersberger (1988), Laboratory studies of the nitric acid trihydrate: Implications for the south polar stratosphere, *Geophys. Res. Lett.*, *15*(8), 855–858.

Harvey, N. M. (1982), A quantum mechanical investigation of vibrational energy transfer in $O(^3P)$ + CO_2 collisions, *Chem. Phys. Lett.*, *88*(6), 553–558.

Hathorn, B. C., and R. A. Marcus (1999), An intramolecular theory of the mass-independent isotope effect for ozone. I., *J. Chem. Phys.*, *111*(9), 4087–4100.

Hathorn, B. C., and R. A. Marcus (2000), An intramolecular theory of the mass-independent isotope effect for ozone. II. Numerical implementation at low pressures using a loose transition state, *J. Chem. Phys.*, *113*(21), 9497–9509.

Heidner, I., R. F., and D. Husain (1974), A study of the collisional quenching of $O(^1D_2)$ by the noble gases employing time-resolved attenuation of atomic resonance radiation in the vacuum ultraviolet, *Int. J. Chem. Kinet.*, *6*, 77–87.

Herriott, D., R. Kompfner, and H. Kogelnik (1964), Off-axis paths in spherical mirror interferometers, *Appl. Opt.*, *3*(4), 523–526.

Hirschfelder, J. O., and W. J. Meath (1967), The Nature of Intermolecular Forces, in *Adv. Chem. Phys.*, vol. 12, edited by J. O. Hirschfelder, Interscience Publishers, New York.

Hirschfelder, J. O., C. F. Curtiss, and R. B. Bird (1964), *Molecular Theory of Gases and Liquids*, John Wiley & Sons, Inc., New York.

Hoag, K. J., C. J. Still, I. Y. Fung, and K. A. Boering (2005), Triple oxygen isotope composition of tropospheric carbon dioxide as a tracer of terrestrial gross carbon fluxes, *Geophys. Res. Lett.*, *32*, l02802.

Hodges, J. T., H. P. Layer, W. W. Miller, and G. E. Scace (2004), Frequency-stabilized single-mode cavity ring-down apparatus for high-resolution absorption spectroscopy, *Rev. Sci. Instrum.*, *75*(4), 849–863.

Houston, P. L., and S. H. Kable (2006), Photodissociation of acetaldehyde as a second example of the roaming mechanism, *Proc. Natl. Acad. Sci. U. S. A.*, *103*(44), 16,079–16,082.

Huntington, K. W., J. M. Eiler, H. P. Affek, W. Guo, M. Bonifacie, L. Y. Yeung, N. Thiagarajan, B. Passey, A. Tripati, M. Daron, and R. Came (2009), Methods and limitations of 'clumped' CO_2 isotope (Δ_47) analysis by gas-source isotope ratio mass spectrometry, *J. Mass. Spectrom.*, *44*(9), 1318–1329.

Ianni, J. C. (2003), A comparison of the Bader-Deuflhard and the Cash-Karp Runge-Kutta integrators for the Gri-Mech 3.0 model based on the chemical kinetics code Kintecus, in *Computational Fluid and Solid Mechanics 2003*, edited by K. J. Bathe, Elsevier Science, Ltd., Oxford.

Ishidoya, S., S. Sugawara, S. Morimoto, S. Aoki, and T. Nakazawa (2008), Gravitational separation of major atmospheric components of nitrogen and oxygen in the stratosphere, *Geophys. Res. Lett.*, *35*, l03811.

Jamieson, C. S., A. M. Mebel, and J. Kaiser (2006), Identification of the D_{3h} isomer of carbon trioxide (CO_3) and its implications for atmospheric chemistry, *ChemPhysChem*, *7*(12), 2508–2513.

Jamieson, C. S., A. M. Mebel, and R. I. Kaiser (2007), Novel detection of the C_{2v} isomer of carbon tetraoxide (CO_4), *Chem. Phys. Lett.*, *440*, 105–109.

Janssen, C., J. Guenther, K. Mauersberger, and D. Krankowsky (2001), Kinetic origin of the ozone isotope effect: A critical analysis of enrichments and rate coefficients, *Phys. Chem. Chem. Phys.*, *3*, 4718–4721.

Johnston, J. C., T. Röckmann, and C. A. M. Brenninkmeijer (2000), CO_2 + O(^1D) isotopic exchange: Laboratory and modeling studies, *J. Geophys. Res.*, *105*(D12), 15,213–15,229.

Kaiser, R. I., and A. M. Mebel (2008), On the formation of higher carbon oxides in extreme environments, *Chem. Phys. Lett.*, *465*, 1–9.

Karton, A., E. Rabinovich, and J. M. L. Martin (2006), W4 theory for computational thermochemistry: In pursuit confident sub-kJ/mol predictions, *J. Chem. Phys.*, *125*(14), 144108.

Katakis, D., and H. Taube (1962), Some photochemical reactions of O_3 in the gas phase, *J. Chem. Phys.*, *36*(2), 416–422.

Kawagucci, S., U. Tsunogai, S. Kudo, F. Nakagawa, H. Honda, S. Aoki, T. Nakazawa, M. Tsutsumi, and T. Gamo (2008), Long-term observation of mass-independent oxygen isotope anomaly in stratospheric CO_2, *Atmos. Chem. Phys.*, *8*, 6189–6197.

Kaye, J. A., and D. F. Strobel (1983), Enhancement of heavy ozone in the Earth's atmosphere?, *J. Geophys. Res.*, *88*(C13), 8447–8452.

Kendall, R. A., T. J. Dunning, and R. J. Harrison (1992), Electron affinities of the first-row atoms revisited. Systematic basis sets and wave functions, *J. Chem. Phys.*, *96*(9), 6796–6806.

Kerstel, E. (2004), Isotope ratio infrared spectrometry, in *Handbook of Stable Isotope Analytical Techniques*, vol. 1, edited by P. A. de Groot, Elsevier, New York.

Kerstel, E., and L. Gianfrani (2008), Advances in laser-based isotope ratio measurements: selected applications, *Appl. Phys. B*, *92*(3), 439–449.

Kharchenko, V., and A. Dalgarno (2004), Thermalization of fast O(^1D) atoms in the stratosphere and mesosphere, *J. Geophys. Res.*, *109*, d18311.

Kinugawa, T., T. Sato, T. Arikawa, Y. Matsumi, and M. Kawasaki (1990), Formation of O(^3P_j) photofragments from the Hartley band photodissociation of ozone at 226 nm, *J. Chem. Phys.*, *93*(5), 3289–3294.

Kowalczyk, T., and A. I. Krylov (2007), Electronic structure of carbon trioxide and vibronic interactions involving Jahn-Teller states, *J. Phys. Chem. A*, *111*, 8271–8276.

Krankowsky, D., P. Lämmerzahl, K. Mauersberger, C. Janssen, B. Tuzson, and T. Röckmann (2007), Stratospheric ozone isotope fractionations derived from collected samples, *J. Geophys. Res.-Atmos.*, *112*, d08301.

Lämmerzahl, P., T. Röckmann, C. A. M. Brenninkmeijer, D. Krankowsky, and K. Mauersberger (2002), Oxygen isotope composition of stratospheric carbon dioxide, *Geophys. Res. Lett.*, *29*(12), 1582.

Landau, L. (1932), Zur Theorie der Energieübertragung. II, *Phys. Z. Sowjetunion*, *2*, 46–51.

Łapiński, A., J. Spanget-Larsen, J. Waluk, and J. G. Radziszewski (2001), Vibrations of nitrous oxide: Matrix isolation Fourier transform infrared spectroscopy of twelve N_2O isotopomers, *J. Chem. Phys.*, *115*(4), 1757–1763.

Lee, C., W. Yang, and R. G. Parr (1988), Development of the Colle-Salvetti correlation-energy formula into a functional of the electron density, *Phys. Rev. B*, *37*(2), 785–789.

Lee, Y. T. (1988), Reactive Scattering I: Nonoptical Methods, in *Atomic and Molecular Beam Methods*, vol. 1, edited by G. Scoles, p. 533, Oxford University Press, New York.

Levine, R. D. (2005), *Molecular Reaction Dynamics*, Cambridge University Press, Cambridge, UK.

Li, S. P., J. Matthews, and A. Sinha (2008), Atmospheric hydroxyl radical production from electronically excited NO_2 and H_2O, *Science*, *319*(5870), 1657–1660.

Liang, M.-C., G. A. Blake, B. R. Lewis, and Y. L. Yung (2007), Oxygen isotopic composition of carbon dioxide in the middle atmosphere, *Proc. Natl. Acad. Sci. U. S. A.*, *104*(1), 21–25.

Liang, M. C., G. A. Blake, and Y. L. Yung (2008), Seasonal cycle of $C^{16}O^{16}O$, $C^{16}O^{17}O$, and $C^{16}O^{18}O$ in the middle atmosphere: Implications for mesospheric dynamics and biogeochemical sources and sinks of CO_2, *J. Geophys. Res.*, *113*(D12), d12305.

Lisak, D., J. T. Hodges, and R. Ciurylo (2006), Comparison of semiclassical line-shape models to rovibrational H_2O spectra measured by frequency-stabilized cavity ring-down spectroscopy, *Phys. Rev. A*, *73*(1), 012507.

Lisak, D., D. K. Havey, and J. T. Hodges (2009), Spectroscopic line parameters of water vapor for rotation-vibration transitions near 7180 cm^{-1}, *Phys. Rev. A*, *79*(5), 052507.

Liu, Y., I. B. Bersuker, W. Zou, and J. E. Boggs (2009), Combined Jahn-Teller and Pseudo-Jahn-Teller Effect in the CO_3 molecule: A Seven-State Six-Mode Problem, *J. Chem. Theory Comput.*, *5*(10), 2679–2686.

Long, D. A., D. K. Havey, M. Okumura, H. M. Pickett, C. E. Miller, and J. T. Hodges (2009), Laboratory measurements and theoretical calculations of O_2 *A* band electric quadrupole transitions, *Phys. Rev. A*, *80*(4), 042513.

Lowe, D., and A. R. MacKenzie (2008), Polar stratospheric cloud microphysics and chemistry, *J. Atmos. Sol.-Terr. Phy.*, *70*(1), 13–40.

Lueb, R., D. H. Ehhalt, and L. E. Heidt (1975), Balloon-borne low temperature air sampler, *Rev. Sci. Instrum.*, *46*(6), 702–705.

Luz, B., E. Barkan, M. L. Bender, M. H. Thiemens, and K. A. Boering (1999), Triple-isotope composition of atmospheric oxygen as a tracer of biosphere productivity, *Nature*, *400*(6744), 547–550.

Lyons, J. R. (2009), Atmospherically-derived mass-independent sulfur isotope signatures, and incorporation into sediments, *Chem. Geol.*, *267*(3-4), 164–174.

Matsumi, Y., and A. M. S. Chowdhury (1996), Translational relaxation and electronic quenching of hot $O(^1D)$ by collisions with N_2, *J. Chem. Phys.*, *104*(18), 7036–7044.

Matsumi, Y., and M. Kawasaki (2003), Photolysis of Atmospheric Ozone in the Ultraviolet Region, *Chem. Rev.*, *103*(12), 4767–4781.

Matsumi, Y., Y. Inagaki, G. P. Morley, and M. Kawasaki (1994a), Fine structure branching ratios and translational energies of $O(^3P_j)$ produced from collision induced intersystem crossing of $O(^1D)$ atoms, *J. Chem. Phys.*, *100*(1), 315–324.

Matsumi, Y., S. M. Shamsuddin, Y. Sato, and M. Kawasaki (1994b), Velocity relaxation of hot $O(^1D)$ atoms by collisions with rare gases, N_2, and O_2, *J. Chem. Phys.*, *101*(11), 9610–9618.

Mauersberger, K. (1981), Measurement of heavy ozone in the stratosphere, *Geophys. Res. Lett.*, *8*(8), 935–937.

Mauersberger, K. (1987), Ozone isotope measurements in the stratosphere, *Geophys. Res. Lett.*, *14*(1), 80–83.

McIlvin, M. R., and M. A. Altabet (2005), Chemical Conversion of Nitrate and Nitrite to Nitrous Oxide for Nitrogen and Oxygen Isotopic Analysis in Freshwater and Seawater, *Anal. Chem.*, *77*(17), 5589–5595.

McManus, J. B., M. S. Zahniser, D. D. Nelson, L. R. Williams, and C. E. Kolb (2002), Infrared laser spectrometer with balanced absorption for measurement of isotopic ratios of carbon gases, *Spectrochim. Acta, Part A*, *58*(11), 2465–2479.

Mebel, A. M., M. Hayashi, V. V. Kislov, and S. H. Lin (2004), Theoretical Study of Oxygen Isotope Exchange and Quenching in the $O(^1D)$ + CO_2 Reaction, *J. Phys. Chem. A*, *108*(39), 7983–7994.

Michalski, G., and S. K. Bhattacharya (2009), The role of symmetry in the mass independent isotope effect in ozone, *Proc. Natl. Acad. Sci. U. S. A.*, *106*(14), 5493–5496.

Miller, R. L., A. G. Suits, P. L. Houston, R. Toumi, J. A. Mack, and A. M. Wodtke (1994), The "Ozone Deficit" Problem: O_2(X, $v \geq 26$) + $O(^3P)$ from 226-nm Ozone Photodissociation, *Science*, *265*, 1831–1838.

Molina, M. J., R. Zhang, P. J. Woolridge, J. R. McMahon, J. E. Kim, H. Y. Chang, and K. D. Beyer (1993), Physical Chemistry of the $H_2SO_4/HNO_3/H_2O$ System: Implications for Polar Stratospheric Clouds, *Science*, *261*(5127), 1418–1423.

Moll, N. G., D. R. Clutter, and W. E. Thompson (1966), Carbon Trioxide: Its Production, Infrared Spectrum, and Structure Studied in a Matrix of Solid CO_2, *J. Chem. Phys.*, *45*(12), 4469–4481.

Møller, C., and M. S. Plesset (1934), Note on an Approximation Treatment for Many-Electron Systems, *Phys. Rev.*, *46*(7), 618.

Motto-Ros, V., M. Durand, and J. Morville (2008), Extensive characterization of the optical feedback cavity enhanced absorption spectroscopy (OF-CEAS) technique: ringdown-time calibration of the absorption scale, *Appl. Phys. B*, *91*(1), 203–211.

Nan, G., and P. L. Houston (1992), Velocity Relaxation of $S(^1D)$ by rare gases measured by Doppler spectroscopy, *J. Chem. Phys.*, *97*(11), 7865–7872.

Némethy, G., M. S. Pottle, and H. A. Scheraga (1983), Energy Parameters in Polypeptides. 9. Updating of Geometrical Parameters, Nonbonded Interactions, and Hydrogen Bond Interactions for the Naturally Occurring Amino Acids, *J. Phys. Chem.*, *87*(11), 1883–1887.

Newman, P., N. Harris, A. Adriani, G. Amanatidis, J. Anderson, G. Braathen, W. Brune, K. Carslaw, M. Craig, P. DeCola, M. Guirlet, R. Hipskind, M. Kurylo, H. Kullmann, N. Larsen, G. Megie, J. Pommereau, L. Poole, M. Schoeberl, F. Stroh, O. Toon, C. Trepte, and M. V. Roozendael (2002), An overview of the SOLVE/THESEO 2000 campaign, *J. Geophys. Res.*, *107*(D20), 8259.

Nier, A. O. (1947), A Mass Spectrometer for Isotope and Gas Analysis, *Rev. Sci. Instrum.*, *18*(6), 398–411.

Oakes, D. B., D. M. Sonnenfroh, G. E. Caledonia, and W. A. M. Blumberg (1994), Velocity dependent O atom IR cross sections: Connections with flight data, *J. Geophys. Res.*, *99*(A12), 23,249–23,255.

O'Keefe, A., and D. A. G. Deacon (1988), Cavity ring-down optical spectrometer for absorption measurements using pulsed laser sources, *Rev. Sci. Instrum.*, *59*(12), 2544–2551.

Ono, S., B. Wing, D. Rumble, and J. Farquhar (2006), High precision analysis of all four stable isotopes of sulfur (^{32}S, ^{33}S, ^{34}S and ^{36}S) at nanomole levels using a laser fluorination isotope-ratio-monitoring gas chromatography-mass spectrometry, *Chem. Geol.*, *225*, 30–39.

Otomo, J., Y. Oshima, A. Takami, and S. Koda (2000), KrF Excimer Laser-induced Ozone Formation in Supercritical Carbon Dioxide, *J. Phys. Chem. A*, *104*(15), 3332–3340.

Ott, D. G. (1981), *Synthesis with stable isotopes of carbon, nitrogen, and oxygen*, John Wiley & Sons, New York.

Perri, M. J., A. L. Van Wyngarden, K. A. Boering, J. J. Lin, and Y. T. Lee (2003), Dynamics of the $O(^1D)+CO_2$ oxygen isotope exchange reaction, *J. Chem. Phys.*, *119*(16), 8213–8216.

Perri, M. J., A. L. Van Wyngarden, J. J. Lin, Y. T. Lee, and K. A. Boering (2004), Energy Dependence of Oxygen Isotope Exchange and Quenching in the $O(^1D)$ + CO_2 Reaction: A Crossed Molecular Beam Study, *J. Phys. Chem. A*, *108*(39), 7995–8001.

Plumb, R. A., W. Heres, J. L. Nei, N. M. Mahowald, J. del Corral, G. C. Toon, E. Ray, F. Moore, and A. E. Andrews (2003), Global tracer modeling during SOLVE: High-latitude descent and mixing, *J. Geophys. Res.-Atmos.*, *108*(D5), 8309.

Prenni, A. J., and M. A. Tolbert (2001), Studies of Polar Stratospheric Cloud Formation, *Acc. Chem. Res.*, *34*(7), 545–553.

Press, W. H., B. P. Flannery, S. A. Teukolsky, and W. T. Vetterling (1992), *Numerical Recipes in FORTRAN: The Art of Scientific Computing*, 2nd ed., Cambridge University Press, Cambridge, UK.

Purvis, G. D., and R. J. Bartlett (1982), A full coupled-cluster singles and doubles model: The inclusion of disconnected triples, *J. Chem. Phys.*, *76*(4), 1910–1918.

Raghavachari, K., G. W. Trucks, M. Head-Gordon, and J. A. Pople (1989), A fifth-order perturbation comparison of electron correlation theories, *Chem. Phys. Lett.*, *157*(6), 479–483.

Reader, J., C. J. Sansonetty, and J. M. Bridges (1996), Irradiances of spectral lines in mercury pencil lamps, *Appl. Opt.*, *35*(1), 78–83.

Röckmann, T., C. A. M. Brenninkmeijer, G. Saueressig, P. Bergamaschi, J. N. Crowley, H. Fischer, and P. J. Crutzen (1998), Mass-Independent Oxygen Isotope Fractionation in Atmospheric CO as a Result of the Reaction CO + OH, *Science*, *281*, 544–546.

Rothman, L. S., I. E. Gordon, A. Barbe, D. C. Benner, P. E. Bernath, M. Birk, V. Boudon, L. R. Brown, A. Campargue, J. P. Champion, K. Chance, L. H. Coudert, V. Dana, V. M. Devi, S. Fally, J. M. Flaud, R. R. Gamache, A. Goldman, D. Jacquemart, I. Kleiner, N. Lacome, W. J. Lafferty, J. Y. Mandin, S. T. Massie, S. N. Mikhailenko, C. E. Miller, N. Moazzen-Ahmadi, O. V. Naumenko, A. V. Nikitin, J. Orphal, V. I. Perevalov, A. Perrin, A. Predoi-Cross, C. P. Rinsland, M. Rotger, M. Simeckova, M. A. H. Smith, K. Sung, S. A. Tashkun, J. Tennyson, R. A. Toth, A. C. Vandaele, and J. Vander Auwera (2009), The HITRAN 2008 molecular spectroscopic database, *J. Quant. Spectrosc. Radiat. Transf.*, *110*(9-10), 533–572.

Russ, N. J., T. D. Crawford, and G. S. Tschumper (2004), Real versus artifactual symmetry-breaking effect in Hartree-Fock, density-functional, and coupled-cluster methods, *J. Chem. Phys.*, *120*(16), 7298–7306.

Ryali, S. B., J. B. Fenn, C. E. Kolb, and J. A. Silver (1982), Collisional excitation of CO_2 by N_2, O_2 and Ar, *J. Chem. Phys.*, *76*(12), 5878–5886.

Samuel, D., and I. Wassermann (1971), A New Method for the Synthesis of ^{18}O-Labelled Potassium Nitrite and Related Compounds, *J. Labelled Compd.*, *7*(3), 355–356.

Samura, K., S. Hashimoto, M. Kawasaki, A. Hayashida, E. Kagi, T. Ishiwata, and Y. Matsumi (2002), Isotope $^{18}O/^{16}O$ Ratio Measurements of Water Vapor by Use of the 950-nm Wavelength Region With Cavity Ring-Down and Photoacoustic Spectroscopic Techniques, *Appl. Opt.*, *41*(12), 2349–2354.

Sander, S. P., R. R. Friedl, A. R. Ravishankara, D. M. Golden, C. E. Kolb, M. J. Kurylo, M. J. Molina, G. K. Moortgat, H. Keller-Rudek, B. J. Finlayson-Pitts, P. H. Wine, R. E. Huie, and V. L. Orkin (2006), *Chemical Kinetics and Photochemical Data for Use in Atmospheric Studies: Evaluation Number 15, JPL Publication 06-2*, Jet Propulsion Laboratory, Pasadena, CA.

Schatz, G. C., and M. J. Redmon (1981), A quasiclassical trajectory study of collisional excitation in $O(^3P)$ + CO_2, *Chem. Phys.*, *58*(2), 195–201.

Schinke, R., S. Y. Grebenshchikov, M. V. Ivanov, and P. Fleurat-Lessard (2006), Dynamical Studies of the Ozone Isotope Effect: A Status Report, *Annu. Rev. Phys. Chem.*, *57*, 625–661.

Schupp, M. (1992), Entwicklung und Demonstration einer laserspektroskopischen Methode zur Messung des Kohlenstoffisotopenverhältnisses in Methan, Ph.D. thesis, Universität Mainz.

Shaheen, R., C. Janssen, and T. Röckmann (2007), Investigations of the photochemical isotope equilibrium between O_2, CO_2, and O_3, *Atmos. Chem. Phys.*, *7*, 495–509.

Shamsuddin, S. M., Y. Inagaki, Y. Matsumi, and M. Kawasaki (1994), $O(^3P_j)$ atom formation from photodissociation of ozone in the visible and ultraviolet region, *Can. J. Chem.*, *72*(3), 637–642.

Shao, Y., L. F. Molnar, Y. Jung, J. Kussmann, C. Ochsenfeld, S. T. Brown, A. T. B. Gilbert, L. V. Slipchenko, S. V. Levchenko, D. P. O'Neill, R. A. DiStasio, R. C. Lochan, T. Wang, G. J. O. Beran, N. A. Besley, J. M. Herbert, C. Y. Lin, T. Van Voorhis, S. H. Chien, A. Sodt, R. P. Steele, V. A. Rassolov, P. E. Maslen, P. P. Korambath, R. D. Adamson, B. Austin, J. Baker, E. F. C. Byrd, H. Dachsel, R. J. Doerksen, A. Dreuw, B. D. Dunietz, A. D. Dutoi, T. R. Furlani, S. R. Gwaltney, A. Heyden, S. Hirata, C. P. Hsu, G. Kedziora, R. Z. Khalliulin, P. Klunzinger, A. M. Lee, M. S. Lee, W. Liang, I. Lotan, N. Nair, B. Peters, E. I. Proynov, P. A. Pieniazek, Y. M. Rhee, J. Ritchie, E. Rosta, C. D. Sherrill, A. C. Simmonett, J. E. Subotnik, H. L. Woodcock, W. Zhang, A. T. Bell, A. K. Chakraborty, D. M. Chipman, F. J. Keil, A. Warshel, W. J. Hehre, H. F. Schaefer, J. Kong, A. I. Krylov, P. M. W. Gill, and M. Head-Gordon (2006), Advances in methods and algorithms in a modern quantum chemistry program package, *Phys. Chem. Chem. Phys.*, *8*(27), 3172–3191.

Sharma, R. D., and R. G. Roble (2002), Cooling Mechanisms of the Planetary Thermospheres: The Key Role of O Atom Vibrational Excitation of CO_2 and NO, *ChemPhysChem*, *3*(10), 841–843.

Sherrill, C. D., M. S. Lee, and M. Head-Gordon (1999), On the performance of density-functional theory for symmetry-breaking problems, *Chem. Phys. Lett.*, *302*(5-6), 425–430.

Shi, J., and J. Barker (1990), Kinetic studies of the deactivation of $O_2(^1\Sigma_g^+)$ and $O(^1D)$, *Int. J. Chem. Kinet.*, *22*, 1283–1301.

Solomon, S., D. Qin, M. Manning, Z. Chen, M. Marquis, K. B. Averyt, M. Tignor, and H. L. Miller (Eds.) (2007), *Climate Change 2007: The Physical Science Basis. Contribution of Working Group I to the Fourth Assessment Report of the Intergovernmental Panel on Climate Change*, Cambridge University Press, New York.

Springsteen, L. L., S. Satyapal, Y. Matsumi, L. M. Dobeck, and P. L. Houston (1993), Anisotropy and Energy Disposal in the 193-nm N_2O Photodissociation Measured by VUV Laser-Induced Fluorescence of $O(^1D)$, *J. Phys. Chem.*, *97*(28), 7239–7241.

Stranges, D., X. Yang, J. D. Chesko, and A. G. Suits (1995), Photodissociation of ozone at 193 nm by high-resolution photofragment translational spectroscopy, *J. Chem. Phys.*, *102*(15), 6067–6077.

Syage, J. A. (1995), Photofragment Imaging of Ozone Photodissociation: $O_3 \rightarrow O(^3P_j) + O_2(\tilde{X}, v)$ at 226 nm, *J. Phys. Chem.*, *99*(45), 16,530–16,533.

Takahashi, K., N. Taniguchi, Y. Matsumi, and M. Kawasaki (1998), Translational energy and angular distributions of $O(^1D)$ and $O(^3P_j)$ fragments in the UV photodissociation of ozone, *Chem. Phys.*, *231*, 171–182.

Takahashi, K., N. Taniguchi, Y. Sato, and Y. Matsumi (2002), Nonthermal steady state translational energy distributions of $O(^1D)$ in the stratosphere, *J. Geophys. Res.*, *107*(D16), 4290–4296.

Taniguchi, N., K. Takahashi, and Y. Matsumi (2000), Photodissociation of O_3 around 309 nm, *J. Phys. Chem. A*, *104*(39), 8936–8944.

Tasic, U., P. Hein, and D. Troya (2007), Theoretical study of the dynamics of Ar collisions with C_2H_6 and C_2F_6 at hyperthermal energy, *J. Phys. Chem. A*, *111*(18), 3618–3632.

Thelen, M.-A., T. Gejo, J. A. Harrison, and J. R. Huber (1995), Photodissociation of ozone in the Hartley band: Fluctuation of the vibrational state distribution in the $O_2(^1D_g)$ fragment, *J. Chem. Phys.*, *103*(18), 7946–7955.

Thiemens, M. H. (2006), History and Applications of Mass-Independent Isotope Effects, *Annu. Rev. Earth Planet. Sci.*, *34*, 217–262.

Thiemens, M. H., and J. E. Heidenreich (1983), The Mass-Independent Fractionation of Oxygen: A Novel Isotope Effect and its Possible Cosmochemical Implications, *Science*, *219*(4588), 1073–1075.

Thiemens, M. H., T. Jackson, K. Mauersberger, B. Schueler, and J. Morton (1991), Oxygen isotope fractionation in stratospheric CO_2, *Geophys. Res. Lett.*, *18*(4), 669–672.

Thiemens, M. H., T. Jackson, E. C. Zipf, P. W. Erdman, and C. van Egmond (1995), Carbon Dioxide and Oxygen Isotope Anomalies in the Mesosphere and Stratosphere, *Science*, *270*(5238), 969–972.

Townsend, D., S. A. Lahankar, S. K. Lee, S. D. Chambreau, A. G. Suits, X. Zhang, J. Rheinecker, L. B. Harding, and J. M. Bowman (2004), The roaming atom: Straying from the reaction path in formaldehyde decomposition, *Science*, *306*(5699), 1158–1161.

Troya, D., G. C. Schatz, D. J. Garton, A. L. Brunsvold, and T. K. Minton (2004), Crossed Beams and theoretical studies of the $O(^3P) + CH_4 \rightarrow H + OCH_3$reaction excitation function, *J. Chem. Phys.*, *120*(2), 731–739.

Tsang, W., and R. F. Hampson (1986), Chemical kinetic data base for combustion chemistry. Part I. Methane and related compounds, *J. Phys. Chem. Ref. Data*, *15*(3), 1087–1279.

Tuzson, B., J. Mohn, M. J. Zeeman, R. A. Werner, W. Eugster, M. S. Zahniser, D. D. Nelson, J. B. McManus, and L. Emmenegger (2008), High precision and continuous field measurements of $\delta^{13}C$ and $\delta^{18}O$ in carbon dioxide with a cryogen-free QCLAS, pp. 451–458.

Upschulte, B. L., and G. E. Caledonia (1992), Laboratory measurements of infrared excitation cross sections of fast O-atom collisions with CO, CO_2, and CH_4, *J. Chem. Phys.*, *96*(3), 2025–2033.

Urey, H. C. (1947), The thermodynamic properties of isotopic substances, *J. Chem. Soc.*, *47*(5), 562–581.

Van Wyngarden, A. L., K. A. Mar, K. A. Boering, J. J. Lin, Y. T. Lee, S.-Y. Lin, H. Guo, and G. Lendvay (2007), Nonstatistical Behavior of Reactive Scattering in the $^{18}O + {}^{32}O_2$ Isotope Exchange Reaction, *J. Am. Chem. Soc.*, *129*(10), 2866–2870.

Voigt, C., J. Schreiner, A. Kohlmann, P. Zink, K. Mauersberger, N. Larsen, T. Deshler, C. Kroger, J. Rosen, A. Adriani, F. Cairo, G. Di Donfrancesco, M. Viterbini, J. Ovarlez, H. Ovarlez, C. David, and A. Dornbrack (2000), Nitric acid trihydrate (NAT) in polar stratospheric clouds, *Science*, *290*(5497), 1756–1758.

Wang, Z., E. A. Schauble, and J. M. Eiler (2004), Equilibrium thermodynamics of multiply substituted isotopologues of molecular gases, *Geochim. Cosmochim. Acta*, *68*(23), 4779–4797.

Weissberger, E., W. H. Breckenridge, and H. Taube (1967), Reaction Of $O(^1D)$ With CO_2 At Low Temperatures, *J. Chem. Phys.*, *47*(5), 1764–1769.

Wen, J., and M. H. Thiemens (1993), Multi-isotope study of the $O(^1D) + CO_2$ exchange and stratospheric consequences, *J. Geophys. Res.*, *98*(D7), 12,801–12,808.

Werner, H.-J., P. J. Knowles, R. Lindh, F. R. Manby, M. Schutz, P. Celani, T. Korona, G. Rauhut, R. D. Amos, A. Bernhardsson, A. Berning, D. L. Cooper, M. J. O. Deegan, A. J. Dobbyn, F. Eckert, C. Hampel, G. Hetzer, A. W. Lloyd, S. J. McNicholas, W. Meyer, M. E. Mura, A. Nicklass, P. Palmieri, R. Pitzer, U. Schumann, H. Stoll, A. J. Stone, R. Tarroni, and T. Thorsteinsson (2006), MOLPRO, a package of *ab initio* programs.

Weston, J., R. E. (1999), Anomalous of Mass-Independent Isotope Effects, *Chem. Rev.*, *99*(8), 2115–2136.

Wiegell, M. R., N. W. Larsen, T. Pedersen, and H. Egsdard (1997), The temperature dependence of the exchange reaction between oxygen atoms and dioxygen molecules studied by means of isotopes and spectroscopy, *Int. J. Chem. Kinet.*, *29*(10), 745–753.

Yakir, D. (2003), The Stable Isotopic Composition of Atmospheric CO_2, in *Treatise on Geochemistry*, vol. 4, edited by K. K. Turekian and H. D. Holland, pp. 175–212, Elsevier, Ltd., Amsterdam.

Yang, G. H., L. Yao, X. Zhang, Q. T. Meng, and K. L. Han (2005), Theoretical Study of the Mechanism for Spin-Forbidden Quenching Process $O(^1D) + CO_2(^1\Sigma_g^+) \rightarrow O(^3P) + CO_2(^1\Sigma_g^+)$, *Int. J. Quantum Chem.*, *105*(2), 154–159.

Ye, J., and J. L. Hall (2000), Cavity ringdown heterodyne spectroscopy: High sensitivity with microwatt light power, *Phys. Rev. A*, *61*(6), 061802.

Ye, J., and T. W. Lynn (2003), Applications of Optical Cavities in Modern Atomic, Molecular, and Optical Physics, in *Adv. At., Mol., Opt. Phys.*, vol. 49, edited by B. Bederson and H. Walther, pp. 1–83, Elsevier Academic Press, San Francisco, CA.

Ye, J., L.-S. Ma, and J. L. Hall (1998), Ultrasensitive detections in atomic and molecular physics: demonstration in molecular overtone spectroscopy, *J. Opt. Soc. Am. B*, *15*(1), 6–15.

Yeung, L. Y., H. P. Affek, K. J. Hoag, W. Guo, A. A. Wiegel, E. L. Atlas, S. M. Schauffler, M. Okumura, K. A. Boering, and J. M. Eiler (2009a), Large and unexpected enrichment in stratospheric $^{16}O^{13}C^{18}O$ and its meridional variation, *Proc. Natl. Acad. Sci. U. S. A.*, *106*(28), 11,496–11,501.

Yeung, L. Y., M. Okumura, J. T. Paci, G. C. Schatz, J. Zhang, and T. K. Minton (2009b), Hyperthermal O-Atom Exchange Reaction $O_2 + CO_2$ through a CO_4 Intermediate, *J. Am. Chem. Soc.*, *131*(39), 13,940–13,942.

Yung, Y. L., W. B. DeMore, and J. P. Pinto (1991), Isotopic Exchange Between Carbon Dioxide and Ozone via $O(^1D)$ in the Stratosphere, *Geophys. Res. Lett.*, *18*(1), 13–16.

Yung, Y. L., A. Y. T. Lee, F. W. Irion, W. B. DeMore, and J. Wen (1997), Carbon dioxide in the atmosphere: Isotopic exchange with ozone and its use as a tracer in the middle atmosphere, *J. Geophys. Res.*, *102*(D9), 10,857–10,866.

Zhang, J., J. P. Camden, A. L. Brunsvold, H. P. Upadhyaya, T. K. Minton, and G. C. Schatz (2008), Unusual Mechanisms Can Dominate Reactions at Hyperthermal Energies: An Example from $O(^3P) + HCl \rightarrow ClO + H$, *J. Am. Chem. Soc.*, *130*(28), 8896–8897.

Zhao, Y., and D. G. Truhlar (2008), The M06 suite of density functionals for main group thermochemistry, thermochemical kinetics, noncovalent interactions, excited states, and transition elements: two new functionals and systematic testing of four M06-class functionals and 12 other functionals, *Theo. Chem. Acc.*, *120*(1-3), 215–241.

Zondlo, M. A., P. K. Hudson, A. J. Prenni, and M. A. Tolbert (2000), Chemistry and Microphysics of Polar Stratospheric Clounds and Cirrus Clouds, *Annu. Rev. Phys. Chem.*, *51*, 473–499.